


Spring 2019

## Chemical and Physical Modification of Thiol-Ene and Epoxy-Amine Networks for Advanced Control of Gas Transport and Flame Retardant Behavior

Vivek Vasagar  
*University of Southern Mississippi*

Follow this and additional works at: <https://aquila.usm.edu/dissertations>

 Part of the [Membrane Science Commons](#), [Polymer Science Commons](#), and the [Transport Phenomena Commons](#)

---

### Recommended Citation

Vasagar, Vivek, "Chemical and Physical Modification of Thiol-Ene and Epoxy-Amine Networks for Advanced Control of Gas Transport and Flame Retardant Behavior" (2019). *Dissertations*. 1651.  
<https://aquila.usm.edu/dissertations/1651>

This Dissertation is brought to you for free and open access by The Aquila Digital Community. It has been accepted for inclusion in Dissertations by an authorized administrator of The Aquila Digital Community. For more information, please contact [Joshua.Cromwell@usm.edu](mailto:Joshua.Cromwell@usm.edu).

CHEMICAL AND PHYSICAL MODIFICATION OF THIOL-ENE AND EPOXY-AMINE  
NETWORKS FOR ADVANCED CONTROL OF  
GAS TRANSPORT AND FLAME RETARDANT BEHAVIOR

by

Vivek Vasagar

A Dissertation  
Submitted to the Graduate School,  
the College of Arts and Sciences  
and the School of Polymer Science and Engineering  
at The University of Southern Mississippi  
in Partial Fulfillment of the Requirements  
for the Degree of Doctor of Philosophy

Approved by:

Dr. Sergei I Nazarenko, Committee Chair

Dr. Robert Y Lochhead

Dr. Sarah E Morgan

Dr. Jeffrey S Wiggins

Dr. Derek L Patton

---

Dr. Sergei I Nazarenko  
Committee Chair

---

Dr. Jeffrey S Wiggins  
Director of School

---

Dr. Karen S. Coats  
Dean of the Graduate School

May 2019

COPYRIGHT BY

Vivek Vasagar

2019

*Published by the Graduate School*



THE UNIVERSITY OF  
**SOUTHERN**  
**MISSISSIPPI**®

## ABSTRACT

Crosslinked polymers are widely used due to its several advantages not limited to high mechanical strength combined with the easy processability. Despite of its popular usage, the fundamental understanding of polymer structure affecting the desired properties is still lacking. This PhD thesis is in two parts, the first part is devoted to the design and developing a basic understanding of structure and chemical composition dependencies of gas transport, whereas in the second part a fundamental relationship between structure to the fire-retardant properties is established.

Membrane based gas separation technique has attracted interest of selective removal of carbon dioxide gas from mixture of light gases such as H<sub>2</sub>, O<sub>2</sub>, N<sub>2</sub> and CH<sub>4</sub>. Polyethylene glycol (PEG) has been employed to improve the solubility of acidic gases such as CO<sub>2</sub> to improve the selective permeation. While conventional research on solubility selective membranes focuses on the strategies to prepare amorphous membrane while incorporating maximum PEG content, to the best of our knowledge, no studies have been focused in determining the effect of increasing PEG units on solubility/selectivity of CO<sub>2</sub>/light gases. This research aims to determine the increasing effect of PEG units in solubility selectivity of UV curable thiol-ene based membranes. We determined the threshold amount of PEG units to achieve maximum CO<sub>2</sub> gas solubility/selectivity. We also examined the effect of network architecture on solubility when PEG units are placed in the backbone or as a dangling chain. The results indicated that CO<sub>2</sub> solubility / selectivity saturated at 10 weight percentage of PEG for these elastomeric networks despite of the placement of the PEG units. Knowing that the required amount of PEG to achieve maximum selectivity is around 10 wt%, several other moieties that

incorporate flexibility such as PDMS can be incorporated to further increase the permeability without compromising the selectivity, thus improving the overall membrane separation process.

Crosslink density affects several properties of a crosslinked network. The effect of network crosslink density on fire retardant performance was examined via cone calorimeter using thiol-ene model networks in chapter 3. A series of networks was designed to vary the rigidity and crosslink density. Rigidity was tuned by using different types of ene monomer from aliphatic to aromatic nature. By crosslinking trifunctional ene with thiol with varying functionality from 2 through 4, it was possible to increase the crosslink density without changing the chemical nature of the network. We determined that fire retardant properties improved with increasing crosslink density and rigidity within the series of networks examined. Pyrolysis behavior was examined via scanning electron microscope on networks constructed with two structurally similar ene monomers, allyl triazine (TOT) and an allyl isocyanurate (TTT). The combustion process was interrupted by quenching in liquid nitrogen at increasing times, and the cross section was examined via SEM. SEM images revealed that the isomers undergo distinct pyrolysis behavior. Networks containing ether linkage had faster bulk pyrolysis, while the monomers with allyl linkage underwent surface pyrolysis. Through cross section elemental analysis, we were able to quantify the composition of different zones and were able to trace the extent of degradation at various times of combustion. This could be an important tool in enhancing the fire-resistant properties of neat polymeric systems.

Since epoxy networks are another class of polymers widely used in aerospace, electrical insulation and construction, special emphasis was given in understanding and

correlating the epoxy resin structure with several fire-retardant properties determined via cone calorimeter in chapter 4. TGA analysis was used to calculate the activation energy of decomposition via fitting in Ozawa plot. The main emphasis was given to relate structural parameters such as glass transition temperature, network crosslink density to the fire performance of these networks. The presence of aromatic content in the networks influenced the char formation which reduced the heat release rate. For the first time, FR properties determined via cone calorimeter was correlated with numerically calculated heat release and heat capacity values predicted via molar group contribution method. Comparative studies of structurally similar isomers, 3,3'-DDS and 4,4'-DDS, revealed the differences in properties arising solely from the differences in configurational entropy between these monomers. Network containing 4,4'-DDS possess higher onset temperature and higher T<sub>g</sub>, but interestingly, the peak heat release rate determined via cone calorimeter was inferior as compared to 3,3'-DDS containing networks. This is mainly due to the higher configurational entropy of 3,3'-DDS making the chain to pack better at elevated temperature during the combustion process.

Following this basic understanding of structure fire retardant properties of epoxy amine networks, a comprehensive comparison of graphene oxide (GO) modified with a phosphorous based compound, DOPO-V and a polysiloxane (PMDA) flame retardant was studied. This was accomplished by two step process: in the first step, GO synthesis via Hummer's method, while in the second step, the GO was functionalized by addition of DOPO and PMDA which were synthesized separately. The chemical modification of GO with DOPO-V and PMDA was verified using FTIR, XPS and AFM. Two separate FR additive, GO-DOPO-V and GO-PMDA was added to a standard DGEBA based

epoxy resin which was cured with a polyether diamine (Jeffamine D230) to form a composite. Thermal stability of the composites were examined using TGA. DSC results showed no change in T<sub>g</sub> which indicated that the added FR additive did not affect the epoxy amine matrix properties. Cone calorimetry was used as a tool to evaluate the flame-retardant properties of composites prepared using GO-DOPO-V and GO-PMDA. The cone results were compared with standard epoxy-amine matrix along with composites made by mixing GO, DOPO-V and PMDA separately which revealed that the presence of grafted GO, ie GO-DOPO-V and GO-PMDA, improved the flame retardancy. The char morphology analyzed via SEM revealed that the presence of GO along with the FR additives led to a honeycomb type morphology. We hypothesize that the modified GO improved the dispersion within the matrix which improved the FR properties.

In the last session of this thesis, a new approach of using dissolved metal in improving flame retardant properties of several polymers including epoxy-amine (EP), polyurethane (PU), polystyrene (PS) and polyethylene oxide (PEO) is presented. Cone calorimeter was used as a standard tool to evaluate the flame retardancy of these metal dissolved composites. It was discovered unexpectedly that dissolution of a divalent metal, which is capable of forming an oxide layer upon combustion, improves the flame retardancy of a polymer matrix by suppressing the smoke formation and reducing the heat release rate. It was discovered that the presence of primary or secondary amine aids in metal dissolution of certain metal salts such as zinc acrylate, but metal salts containing long organic tail such as zinc stearate was readily dissolved upon heating. The dissolution was evidenced from formation of transparent composites and through the loss of crystal

structure of metal salt detected through wide angle X-ray analysis. We discovered that the improvement in flame retardancy was greatly enhanced when the metal was dissolved rather than dispersed in the polymer matrix. A two-step additive approach was followed where in the first step an additive containing dissolved metal in amine was prepared which was subsequently added in to the desired polymer matrix in the second step. The solubility of the additive to a common solvent was chosen as a criterion to disperse in the desired polymer matrix, i.e., the nature of the amine in additive manufacturing was selected such that it solubilizes with a common solvent of the polymer. For instance, a water-soluble additive was prepared using ethylene diamine which was subsequently added to a polyethylene oxide (PEO) which had water as a common solvent. The choice of amine made it possible to add this additive to several polymers which made this approach more versatile in nature. This approach can be termed as “green” technique due to the absence of halogenated, phosphorous or boron containing compounds which releases toxic smoke during suppressing the fire.



## ACKNOWLEDGMENTS

The way leading to a PhD degree is always full of challenges. I would not have reached this point without the people who made it possible. I am greatly indebted to a number of people over the years who have helped me personally and professionally, and oftentimes both. I would never have come so far without the advice, help and support from the people below.

First and foremost, I would like to sincerely thank my advisor, Dr. Sergei I Nazarenko, for his enthusiastic and patient guidance on various aspects including research and life along with the trust he has on me. He is a friend and well-wisher more than an advisor. His pursuance for perfection in research and analytical thinking process set a great example for my professional career. I am also deeply indebted to him for his tremendous effort to improve my skills of oral presentation and article writing. Dr. Nazarenko granted me complete freedom to work with several new ideas and research projects in our lab and have always supported and encouraged me even at the time of failures. He has always given me the freedom to travel, explore several opportunities which molded me as a better researcher.

I would like to also thank Dr. Robert Lochhead for his extreme guidance and constructive inputs during my independent research proposals. The learning curve during the patent filing process thought me so much invaluable things I never expected to learn in graduate school. His constant inputs and thoughts along with encouragement made the flame-retardant project to completion. I would also like to thank my other committee members Dr. Jeffery Wiggins, Dr. Derek Patton and Dr. Sarah Morgan for their suggestions, guidance and support.

I would like to express my gratitude to Dr. Charles Manzi-Nshuti who is a friend, mentor and for his timely support even after he left our lab. I would like to also thank Dr. Jim Goetz for his guidance and training as a mentor when I joined this lab in USM and for the countless advises. His guidance extended from the experimental protocol to devices construction and software developments using LabView. Dr. Luke Kwisnek, was a wonderful resource and despite of not knowing him as a person, his support was tremendous and he was always there to support us when needed. I am also greatly thankful to Dr. Ramesh Ramakrishnan as a good friend, colleague and lab mate. I am very thankful to him to generate several free-volume analysis reported in this thesis work. I would like to also thank Beibei Chen who is a friend, colleague and for endlessly helping me in several experiments reported in this thesis. I am very thankful to every member of Dr. Nazarenko lab, Dr. Kevin Meyers, Dr. Maliha Syed, Jacob Schekman and Karina Reynolds who have helped me in several aspects of research. The great help and dedication from my undergraduate research assistant, Drew Bossier for helping me completing the Constant Volume Variable Pressure apparatus in our lab.

I am greatly thankful for giving me an opportunity to work with high school teachers during almost most summers in these years as a part of NSF-RET. It has been an incredible learning experience to work with Jamie Sorrell, Eric Shows, Giselle Marks, Karen Deniakos, Rebecca Hopper and Robin Lewis and their work helped me to complete certain aspects of the research presented in this thesis. I was also a part of NSF-REU program which game an opportunity to work with highly motivated summer undergraduate researcher, Jason Gunnell who also helped me with my experiments. I am

very grateful that I was a part of REU and RET which taught me how to teach which I never expected to learn in graduate school.

My sincere thanks to all my collaborative works conducted with Dr. John Wong, Dr. Xiangmei Li and Mr. Watari which also helped me to comprehend my research during my graduate school. A great thanks to Jessica in training me on SEM and TEM microscopes and helping me to get accustomed with those instrumentations. I would also thank Christopher Scanlon for helping me use SEM which belongs to Dr. Rawlins research group.

A special thanks to our lab manager Ms. Jody Wiggins who took care of all the supply essentials to our lab. I would like to thank all the professors, staff and students of the Polymer department who have helped me in some way or other during my graduate education.

Last but not least, I would like to thank my parents my brother and my dog for their support and unconditional love. My adorable dog Emma stayed late with me for countless nights and supported me emotionally when I was in need.

Finally, none of this research would have been possible without the financial support from Fusion UV systems and National Science Foundation (NSF) and all the company who generously provided with the raw materials required for my research activities.

## DEDICATION

Dedicated to my father, Pojjeya Vasagar, mother, Rajee Vasagar and brother,  
Vinoth Vasagar for their unconditional love, support and prayers

Also dedicated to my daughter, Hridhisha.

## TABLE OF CONTENTS

ABSTRACT .....	ii
ACKNOWLEDGMENTS .....	vii
DEDICATION .....	x
LIST OF TABLES .....	xviii
LIST OF ILLUSTRATIONS .....	xxii
LIST OF SCHEMES.....	xxxvi
CHAPTER I - GENERAL BACKGROUND AND THESIS ORGANIZATION .....	1
1.1 Introduction.....	1
1.2 Thesis organization .....	1
1.3 Research background and motivation.....	4
1.3.1 Greenhouse gasses and Carbon dioxide (CO <sub>2</sub> ) .....	4
1.3.2 Application of Carbon dioxide gas (CO <sub>2</sub> ).....	6
1.3.3 Electronic properties of CO <sub>2</sub> and its reactivity .....	7
1.4 Carbon Dioxide(CO <sub>2</sub> ) gas separation and capture .....	9
1.4.1 Membrane separation process.....	9
1.4.2 Polymeric Membranes and Solution-Diffusion model .....	11
1.4.3 Solution-Diffusion model .....	11
1.5 UV initiated Thiol-ene click chemistry.....	18
1.5.2 Thio-Micheal addition reactions .....	20

1.6 Fire retardant polymers .....	22
1.6.1 Combustion mechanism.....	23
1.6.2 Concepts of flame retardancy .....	24
1.6.3 Methods to determine the flame retardancy.....	27
1.7 Epoxy resins.....	29
CHAPTER II – PEG MODIFIED THIOL-ENE NETWORKS FOR ADVANCED CONTROL OF CO <sub>2</sub> GAS SEPARATION FROM OTHER LIGHT GASES .....	36
2.1 Background.....	37
2.2 Experimental.....	39
2.2.1 Materials .....	39
2.2.2 Synthesis of PEG modified thiol monomers.....	40
2.2.3 Membrane fabrication and network formation .....	43
2.2.4 Characterization .....	49
2.3 Results and discussion .....	56
2.3.1 Fourier Transform Infrared Spectroscopy (FTIR).....	56
2.3.2 Investigation of Thermal transitions .....	60
2.3.3 Dynamic-mechanical thermal properties .....	64
2.3.4 Investigation of crystallinity of B-3T↓EDDT↑/DDE networks.....	68
2.3.5 Free-volume analysis and dependencies of all networks.....	73
2.3.6 Gas transport analysis .....	75

2.3.7 Selectivity analysis of CO <sub>2</sub> / light gases .....	86
2.3.8 Literature values comparison .....	91
2.3.9 Pressure dependencies .....	96
2.4 Conclusions .....	100
 CHAPTER III – FUNDAMENTAL INVESTIGATION OF FLAMMABILITY OF THIOL-ENE NETWORKS: EFFECT OF NETWORK STRUCTURE AND ARCHITECTURE .....	
3.1 Background .....	104
3.2 Experimental .....	106
3.2.1 Materials .....	106
3.2.2 Membrane fabrication and rationale for the design .....	107
3.2.3 Characterization .....	109
3.3 Results and discussion .....	111
3.3.1 Differential Scanning Calorimetry (DSC) .....	112
3.3.2 Thermal Stability .....	115
3.3.3 Fire resistant properties .....	119
3.3.4 Shapes of heat release rate curves for various thiol-ene networks at 50 kW/m <sup>2</sup> . .....	122
3.3.5 Changes in surface morphology and composition in cone experiments .....	127
3.3.6 Effective heat of combustion and smoke .....	130

3.3.7 Comparative studies: 4T-TTT and 4T-TOT networks.....	133
3.3.7.1 Fire behavior properties of 4T-TTT and 4T-TOT under different fire scenarios.....	134
3.3.8 Investigation of pyrolysis behavior through SEM/EDAX.....	139
3.4 Conclusion .....	144
3.5 Acknowledgements.....	147
 CHAPTER IV – FUNDAMENTAL INVESTIGATION OF FLAMMABILITY OF EPOXY-AMINE NETWORKS: EFFECT OF VARIOUS EPOXY MONOMERS.....	
4.1 Background.....	149
4.2 Experimental.....	152
4.2.1 Materials .....	152
4.2.2 Network formation and rationale for the design.....	156
4.2.2.1 Specimen preparation.....	157
4.2.3 Characterization .....	158
4.3 Results and discussion .....	167
4.3.1 Thermogravimetric analysis (TGA):.....	167
4.3.2 Effect of Curing temperature on fire properties of crosslinked networks: .....	171
4.3.2.1 Activation energy of decomposition via Ozawa Plots.....	171
4.3.2.2 Cone calorimeter results of TGDDM networks cured at varying temperatures.....	175



4.3.3 Differential scanning calorimetry (DSC):.....	176
4.3.4 Density: .....	178
4.3.5 Cone calorimeter:.....	180
4.4 Correlation analysis .....	187
4.5 Molar group contribution method to determine polymer flammability .....	194
4.5.1 Prediction of heat release capacity (HRC):.....	194
4.5.2 Prediction of total heat release (THR): .....	197
4.6 Isomeric effect. ....	200
4.7 Conclusion .....	210
4.8 Acknowledgements.....	211
CHAPTER V – DEVELOPMENT OF NOVEL GRAPHENE OXIDE GRAFTED SILOXANE AND PHOSPHORUS CONTAINING ADDITIVES AS FLAME RETARDANTS FOR EPOXY-AMINE NETWORKS. ....	212
5.1 Background.....	213
5.2 Experimental.....	218
5.2.1 Materials .....	218
5.2.2 Synthesis of graphene oxide .....	221
5.2.3 Synthesis of Polysiloxane (PDMA):.....	222
5.2.4 Synthesis of polysiloxane (GO-PDMA) functionalized graphene oxide.....	223
5.2.5 Synthesis of DOPO-V:.....	224

5.2.6 Synthesis of DOPO-V functionalized graphene oxide .....	225
5.2.7 Preparation of Epoxy Composite: .....	226
5.2.8 Characterization .....	227
5.3 Results and discussion .....	228
5.3.1 Characterization of synthesized monomers .....	228
5.3.2 Analysis of composite materials .....	238
5.4 Conclusion .....	250
5.5 Acknowledgements.....	252
 CHAPTER VI METAL ORGANIC SALTS AS NEW INTUMESCENT FLAME RETARDANT MATERIALS. ....	
6.1 Background.....	253
6.2 Experimental.....	255
6.2.1 Materials .....	265
6.2.2 Synthesis of small molecule additive / $\beta$ -amino complex .....	269
6.2.3 Composite Preparation.....	271
6.2.4 Characterization .....	274
6.3 Experimental findings and discussion .....	276
6.3.1 Effect of different Zinc salts in Flame retardancy of Epoxy-amine networks.....	277
6.3.2 Study of different metal acetates.....	283
6.3.3 Analysis of small molecule additive/ $\beta$ -amino complex.....	286

6.3.4 Effect of small molecule additive on various polymer systems .....	291
6.3.4.1 Flame retardant for Epoxy-amine networks .....	291
6.3.4.2 Flame retardant for polyurethane networks: .....	293
6.3.4.3 Flame retardant for polystyrene polymers: .....	296
6.3.4.4 Flame retardant polyethylene oxide composites:.....	298
6.3.5 Effect of increasing content of small molecule additive.....	301
6.3.6 Effect of processing conditions of zinc stearate on FR properties.....	309
6.3.7 Effect of different stearate salts on FR properties .....	312
6.3.8 Self-healing fire-retardant polymer networks comprising polymer chains crosslinked through coordination bonds with metal ions. ....	317
6.4 Conclusions and future directions.....	320
6.5 Acknowledgements.....	321
CHAPTER VII REFERENCES.....	322

## LIST OF TABLES

Table 1.1 Critical temperature and kinetic diameter of various gases of interest.....	17
Table 2.2 Formulation details for set B-3T↓EDDT↑/DDE-X .....	47
Table 2.3 Formulation details for set B-HDT↓EDDT↑/TTT- X.....	47
Table 2.4 Formulation details for set D-3T↓4TPEG↑/DDE-X.....	48
Table 2.5 Formulation details for set D-3T↓4TPEG↑/DDE-X.....	48
Table 2.6 Glass Transition, melting temperature and enthalpy of fusion of the membranes obtained from second heat cycle of DSC analysis .....	63
Table 2.7 Melting temperature and enthalpy of fusion of the membranes obtained from second heat cycle of DSC analysis. The column on the right indicates the calculated % crystallinity using X-ray .....	71
Table 2.8 Literature values of solubility of N <sub>2</sub> , O <sub>2</sub> , CO <sub>2</sub> in polymers with and without polar group <sup>4</sup> .....	83
Table 2.9 Gas transport (P,D & S) values of all networks with standard error. Reported values are average of 3 individual runs.....	84
Table 2.10 CO <sub>2</sub> / CH <sub>4</sub> , CO <sub>2</sub> /O <sub>2</sub> and CO <sub>2</sub> /N <sub>2</sub> selectivity values of all networks with calculated propagation of error. Reported values are average of 3 individual runs .....	89
Table 2.11 Reported literature values for amorphous PEO membranes on CO <sub>2</sub> permeability and CO <sub>2</sub> /N <sub>2</sub> selectivity.....	92
Table 3.1 Network Description.....	108
Table 3.2 Glass transition temperature values for all the networks in this study. Reported values are the midpoints of inflection from the 2 <sup>nd</sup> heat cycle .....	114
Table 3.3 Temperatures for the mass loss of 10 and 50 wt.% (T <sub>10%</sub> , T <sub>50%</sub> ).....	119

Table 3.4 Cone calorimeter data for TAE, TOT & TTT networks at an external irradiation of 50 kW/m <sup>2</sup> .....	120
Table 3.5 Cone calorimeter smoke and gas related test results .....	129
Table 4.1 List of monomers and oligomers used in this study. The names listed in industry/ product name is the trade names associated with the supplier .....	154
Table 4.2 Curing profile used to prepare network. Calculated quantities of aromatic content for each network when cured with 3,3'-DDS. The aromatic contribution from each monomer is accounted to calculate the aromatic content .....	158
Table 4.3 Bond dissociation energy of several chemical bonds considered in this work	161
Table 4.4 TGA data for all networks in studying structure- FR properties of epoxy amine .....	170
Table 4.5 Glass transition and density of networks crosslinked with 4,4'-DDS.....	177
Table 4.6 Cone calorimeter data for Difunctional (top set) and multi-functional (bottom set) epoxide containing networks.....	184
Table 4.7 Experimentally determined and theoretically calculated fire properties of networks in this study .....	199
Table 4.8 Naming scheme used in this work to represent the networks formed using isomers .....	200
Table 4.9 TGA results listed for isomer networks .....	202
Table 4.10 Physical characteristics of networks crosslinked with isomers 3,3'-DDS and 4,4'-DDS .....	206
Table 4.11 Cone calorimeter results of networks crosslinked with 3,3'-DDS and 4,4'-DDS isomeric amine .....	209

Table 5.1 Network Description.....	227
Table 5.2 TGA data of epoxy-amine / GO-DOPO-V/ GO-PMDA nano-composites ....	241
Table 5.3 Cone calorimeter data for PMDA based nanocomposites (on the top set) and DOPO-V based nanocomposites (on the bottom).....	247
Table 6.1 Cone calorimeter results of epoxy amine composites prepared with several small molecule additive based on zinc salts .....	282
Table 6.2 Solubility check of zinc acrylate with dibutyl amine at different proportions	289
Table 6.3 Solubility analysis of small molecule additive prepared using zinc acrylate and dibutyl amine .....	290
Table 6.4 Cone calorimeter results comparing with and without dibutyl amine as dispersing agent for metal salt in polyurethane systems.....	296
Table 6.5 Cone calorimeter results comparing with and without dibutyl amine as dispersing agent for metal salt in polystyrene systems.....	297
Table 6.6 Cone calorimeter results comparing with and without dibutyl amine as dispersing agent for metal salt in polyethylene oxide systems.....	300
Table 6.7 TGA data for epoxy amine composites with increasing $\beta$ -amino complexes content.....	303
Table 6.8 Effect of $\beta$ -amino complexes of zinc acrylate on the glass transition temperature of epoxy-amine resin as determined by differential scanning calorimetry.	304
Table 6.9 Effect of $\beta$ -amino complexes of zinc acrylate on the Young's Modulus and yield stress of epoxy resin as determined by compressive testing .....	305
Table 6.10 Effect of concentration of $\beta$ -amino complexes of zinc acrylate on fire retardancy of epoxy-amine compositions .....	307

Table 6.11 ASTM method UL-94 HB testing of $\beta$ -amino complexes of zinc acrylate on the standard flammability of epoxy-amine resin. ....	309
Table 6.12 Effects of formulation temperature conditions on epoxy-amine compositions with zinc stearate.....	310
Table 6.13 Flame resistance of stearate-based salts of zinc, nickel and magnesium determined via cone calorimeter .....	313

## LIST OF ILLUSTRATIONS

Figure 1.1 Increasing concentration of CO <sub>2</sub> in Atmosphere. Data obtained from NOAA <sup>5</sup> .5	
Figure 1.2 Application of CO <sub>2</sub> gas in food industry, chemical industry as a raw material and compressed gas for oil extraction.....	6
Figure 1.3 Structure of CO <sub>2</sub> gas showing the electronic properties. ....	8
Figure 1.4 Representation of membrane gas separation. ....	10
Figure 1.5 Diffusivity of several gases through thiol-ene based fluoropolymer. Plot shows the comparison of diffusivity co-efficient of gases with different kinetic diameter. ....	13
Figure 1.6 Dependence of solubility on critical temperature. Shown here is the solubility values for UV-curable thiol-ene fluoro-polymeric networks.....	14
Figure 1.7 Selectivity plotted against permeability of fast moving gas. Red dots indicate selectivity of polymers reported in literature. The black line indicates the hypothetical Robeson upper bond upper bond indicating the commercially attractive region. (Moderate selectivity with high permeability) .....	15
Figure 1.8 Fire triangle emphasizing the importance of three components required for a sustainable fire. ....	24
Figure 1.9 Potential mode of action of Flame retardants (1 to 4) in the combustion cycle. ....	25
Figure 1.10 Typical cone calorimeter cure showing the obtained values. ....	28
Figure 1.11 Three membered epoxide group.....	30
Figure 2.1 Dependence of solubility on critical temperature. Shown here is the solubility values for UV-curable thiol-ene fluoro-polymeric networks.....	40



Figure 2.2 <sup>1</sup> H NMR spectra of unmodified (bottom) and modified (red and blue) thiol monomer .....	42
Figure 2.3 Linear dependence on PEG weight % and PEG molar content.....	45
Figure 2.4 Corresponding network monomers and naming scheme used in chapter 2 ....	49
Figure 2.5 Representative plot of standard upstream and downstream pressure versus time collected during CVVP test .....	53
Figure 2.6 Representative Realtime FTIR plot to calculate the monomer conversion. ....	57
Figure 2.7 Real time FTIR of thiol and Ene monomers. Inset shows the decrease in peak area of monomers upon UV exposure. ....	59
Figure 2.8 DSC thermograms of all networks(2nd heat). Curves are offset vertically for clarity. ....	61
Figure 2.9 DMA curves for B-3T↓EDDT↑/DDE systems.....	65
Figure 2.10 Storage modules (on left) and tan δ (on right) for (a)B-HDT↓EDDT↑/ TTT, (b)D-3T↓4TPEG↑/DDE & (c) D-HDT↓3TPEG↑/TTT. ....	67
Figure 2.11 DSC first heat(on left) and DSC second heat (on the right). Curves are offset vertically for clarity.....	69
Figure 2.12 Wide angle X-ray of B-3T↓EDDT↑/DDE membranes. Curves vertically stacked for comparison. ....	70
Figure 2.13 Wide angle X-ray of B-3T↓EDDT↑/DDE membranes. Curves vertically stacked for comparison. ....	72
Figure 2.14 Optical Microscopic images at room temperature. With increasing PEG content (increasing Mc) the crystal size grows.....	73

Figure 2.15 Digital images of B-3T↓EDDT↑/DDE at room temperature. (a) through (e) (top row) amorphous at room temperature. (f) through (i) opaque at room temperature.	73
Figure 2.16 Free-volume plotted as a function of glass transition temperature.....	74
Figure 2.17 Permeability (P), Diffusivity (D) and Solubility (S) of B-3T↓EDDT↑TEGDVE systems plotted against PEG wt%. Data obtained from Kweisnek work <sup>3</sup> .....	76
Figure 2.18 Permeability (P) of CO <sub>2</sub> , CH <sub>4</sub> , O <sub>2</sub> and N <sub>2</sub> gas of all networks (B-3T↓EDDT↑/DDE, B-HDT↓EDDT↑/TTT, D-3T↓4TPEG↓/DDE and D-HDT↓3TPEG↑/TTT) plotted against PEG wt%..	77
Figure 2.19 Diffusivity (D) of CO <sub>2</sub> , CH <sub>4</sub> , O <sub>2</sub> and N <sub>2</sub> gas of all networks (B-3T↓EDDT↑/DDE, B-HDT↓EDDT↑/TTT, D-3T↓4TPEG↓/DDE and D-HDT↓3TPEG↑/TTT) plotted against PEG wt%.	78
Figure 2.20 Solubility (S) of CO <sub>2</sub> , CH <sub>4</sub> , O <sub>2</sub> and N <sub>2</sub> gas of all networks (B-3T↓EDDT↑/DDE, B-HDT↓EDDT↑/TTT, D-3T↓4TPEG↓/DDE and D-HDT↓3TPEG↑/TTT) plotted against PEG wt%.	81
Figure 2.21 Representative plot showing reduced interaction of non-polar N <sub>2</sub> gas with increasing polar PEG content.....	82
Figure 2.22 (a)Permeability selectivity, (b) Diffusivity selectivity and (c) Solubility selectivity of CO <sub>2</sub> / light gas plotted against PEG wt%.....	87
Figure 2.23 Selectivity of CO <sub>2</sub> /N <sub>2</sub> , CO <sub>2</sub> /O <sub>2</sub> and CO <sub>2</sub> /CH <sub>4</sub> for B-3T↓EDDT↑/DDE, D-3T↓4TPEG↑/DDE, B-HDT↓EDDT↑/TTT and D-HDT↓3TPEG↑/TTT following a master trend. Data from previous work B-3T↓EDDT↑/TGEDVE is presented for comparison.	88

Figure 2.24 Permeability selectivity of CO <sub>2</sub> /N <sub>2</sub> plotted against PEG wt%. Half-filled indicates the reported literature values ( Table 2.11).....	95
Figure 2.25 Permeability of (a)CO <sub>2</sub> , (b)N <sub>2</sub> and (c) CH <sub>4</sub> of D-3T↓4TPEG↑/DDE networks plotted against applied pressure feed pressure. ....	97
Figure 2.26 Sorption isotherm of D-3T↓4TPEG↑/DDE demonstrating the henry mode of sorption at lower feed pressure. Each curve represents the network exposed at varied feed pressure. The lines shown is to guide the eyes .....	98
Figure 2.27 Comparison of solubility co-efficient of D-3T↓4TPEG↑/DDE (a) CO <sub>2</sub> (b) N <sub>2</sub> and (c) CH <sub>4</sub> determined via CVVP and sorption technique.....	99
Figure 2.28 Permeability selectivity of D-3T↓4tPEG↑/DDE networks, at different feed pressures, plotted against PEG wt%. At 2 atm feed pressure, permeability selectivity levels off at around 12 wt%, whereas with 12.45 atm applied feed pressure, the permeability. Lines shown here is only to guide eyes. ....	100
Figure 3.1 Chemical structures of monomers used in investigate FR properties of thiol-ene networks .....	107
Figure 3.2 2 <sup>nd</sup> heating scan DSC thermograms of photopolymerized thiol-ene networks. Curves are stacked vertically for clarity. ....	113
Figure 3.3 TGA curves of (I) TOT-, (II) TTT- and (III) TAE-containing thiol-ene networks. Note: heating ramp rate is 10 °C/min; experiments run in a nitrogen environment from 30-800 °C. ....	116
Figure 3.4 Thermal Stability of networks fabricated using same thiol compound but with different ene. ....	118

Figure 3.5 Cone calorimeter representative time dependent curves of [TAE]-containing thiol-ene networks at an external irradiation of 50 kW/m <sup>2</sup> : (I) heat release (HRR) and (II) mass loss (MLR) curves.....	124
Figure 3.6 Cone calorimeter representative time dependent curves of [TTT]-containing thiol-ene networks at an external irradiation of 50 kW/m <sup>2</sup> : (I) heat release (HRR) and (II) mass loss (MLR) curves.....	124
Figure 3.7 Cone calorimeter representative time dependent curves of [TOT]-containing thiol-ene networks at an external irradiation of 50 kW/m <sup>2</sup> : (I) heat release (HRR) and (II) mass loss (MLR) curves.....	124
Figure 3.8 Representative HRR plots for HRR curves for networks fabricated using the tetrafunctional thiol (4T) monomer. All networks were tested at an external heat flux of 50 kW/m <sup>2</sup> .....	126
Figure 3.9 Optical photographs of incompletely burned thiol-ene networks in cone at an external irradiation of 50 kW/m <sup>2</sup> . (A1) 2T-TAE; (A2) 3T-TAE; (A3) 4T-TAE; (B1) 2T-TOT; (B2) 3T-TOT; (B3) 4T-TAE; (C1) 2T-TTT; (C2) 3T-TTT; and (C3) 4T-TTT. The specimens were combusted for about 60 seconds, and then subsequently extinguished and quenched using liquid nitrogen.....	130
Figure 3.10 Smoke production rates of thiol-ene networks for (I) [TAE], (II) [TTT] and (III) [TOT] containing thiol-ene networks.....	131
Figure 3.11 Cone calorimeter HRR of (I) 4T-TOT and (II) 4T-TTT, for 25, 50, and 75 kW/m <sup>2</sup> irradiation.....	135
Figure 3.12 Pictures showing the residues remaining after combusting (A) 4T-TOT and (B) 4T-TTT at an external irradiation of 25 kW/m <sup>2</sup> .....	135

Figure 3.13 Cone calorimeter peak HRR values for 4T-TTT and 4T-TOT at external irradiations of 25, 50 and 75 kW/m <sup>2</sup> .....	136
Figure 3.14 TGA curves of cone residues (external heat flux 25 kW/m <sup>2</sup> ) for 4T-TTT and 4T-TOT networks performed in a nitrogen environment (I) or in Air (II) at a heating ramp rate of 20 °C/min. The cone residue and the residues collected after burning the two networks in cone calorimeter at an external irradiation of 25 kW/m <sup>2</sup> .....	137
Figure 3.15 SEM images of the residues obtained after combusting 4T-TTT (A <sub>1</sub> , A <sub>2</sub> ) and 4T-TOT (B <sub>1</sub> , B <sub>2</sub> ) networks in cone at an external irradiation of 25 kW/m <sup>2</sup> . The subscript 1 is used to indicate the top surface layer of residue while the subscript 2 is used for the bottom area of sample, in direct contact with aluminum foil sample container. ....	139
Figure 3.16 Cross-sectional image of partially burnt networks. (A) represents 2T-TTT,( B) – 3T-TTT and (C)- 4T-TTT networks. Subscripts indicates the combustion times. (1) – 5 sec, (2)-10 sec, (3)- 15 sec,(4)- 20 sec. ....	140
Figure 3.17 Cross-sectional image of partially burnt networks. (A) represents 2T-TOT,( B) – 3T-TOT and (C)- 4T-TOT networks. Subscripts indicates the combustion times. (1) – 5 sec, (2)-10 sec, (3)- 15 sec,(4)- 20 sec. ....	142
Figure 3.18 Elemental analysis of 4T-TTT networks exposed to combustion for 20 sec. A, B,C,D and E represents the imaginary pyrolysis zone. The composition indicated in the left is an average of 3 scans in that zone. Neat represents the unburnt pristine polymer samples.....	143
Figure 3.19 Elemental analysis of 4T-TOT networks exposed to combustion for 20 sec. A, B,C,D and E represents the imaginary pyrolysis zone. The composition indicated in	

the left is an average of 3 scans in that zone. Neat represents the unburnt pristine polymer samples.....	144
Figure 4.1 Typical epoxy amine chain indicating three possible chain scission sites (indicated in red dotted line), to release small molecule which sustains the combustion .....	150
Figure 4.2 Chemical structures of epoxy monomers used in this work.....	155
Figure 4.3 Chemical structures of amine curing agents used in this work .....	155
Figure 4.4 Representative thermogravimetric curve showing the analyzed parameters ( $T_{onset}$ , $T_d$ and $R_c$ ) .....	160
Figure 4.5 Representative plot showing the significance of average heat release. This plot doesn't show the real data from the instrument and this is hand drawn to show the difference in curve .....	166
Figure 4.6 TGA curves for all networks heated up to 600°C in nitrogen. (B) Plot indicating different networks has different char yield .....	168
Figure 4.7 Representative plot of TGDDM exposed to TGA at different heating rate ..	173
Figure 4.8 Flynn & wall method: Temperature of degradation at various heating rate plotted as a function of heating rate .....	173
Figure 4.9 Activation energies at various partial degradation of TGDDM network .....	174
Figure 4.10 Heat release rate of TGDDM epoxy based networks crosslinked with 4,4'-DDS at different temperatures, 150°C, 180°C and 220°C for 30 min.....	175
Figure 4.11 DSC thermograms of all networks. Second heat reported for $T_g$ determinations. Curves vertically offset for clarity .....	176

Figure 4.12 (a) Epoxy functionality and (b) aromatic content plotted as a function of density of the crosslinked networks.....	179
Figure 4.13 Heat release curves of difunctional epoxide containing monomers .....	181
Figure 4.14 Heat release curves of multi-functional epoxide containing monomers ....	185
Figure 4.15 Average HRR plotted as a function of glass transition (T <sub>g</sub> ) of networks. The graph indicates there is no relationship between the Avg. HRR and the T <sub>g</sub> . The magnitude of $R^2 = 0$ indicating the average HRR is independent of T <sub>g</sub> .....	188
Figure 4.16 Temperature of 5% degradation (from TGA data) plotted as a function of time to ignition (from cone calorimeter).....	189
Figure 4.17 Plot signifying the relationship between THR, aromatic Content and Char yield. Char yield is linearly dependent on aromatic content (Plot 9a on bottom) and inversely proportional to THR (Plot 9b on top).....	192
Figure 4.18 Display of char yield % from two different experiments: TGA on X-axis and Cone calorimeter on Y-axis .....	193
Figure 4.19 Experimental HRC determined via cone calorimeter plotted as a function of calculated HRC. Magnitude of $R^2 = 0.54$ indicating a moderate decency of the experimental HRC and the theoretical HRC.....	196
Figure 4.20 Plot of measured THR (Cone calorimeter) as a function of calculated THR via group contribution method. Shown in red is the imaginary line if the measured THR and calculated THR is in agreement. Magnitude of $R^2 = 0.83$ indicates good agreement. ....	199
Figure 4.21 Chemical structures of epoxy and amine monomers used in analyzing the isomeric effect on flame retardant properties. ....	200

Figure 4.22 Chemical structures of epoxy and amine monomers used in analyzing the isomeric effect on flame retardant properties. ....	201
Figure 4.23 Derivative weight loss plotted as a function of temperature .....	203
Figure 4.24 (a) para substituted 4,4'-DDS monomer showing the possible ring-flip mechanism along the axis of symmetry and (b) meta substituted 3,3'-DDS monomers in the network which can't undergo ring flip due to meta substituted positions.....	204
Figure 4.25 DSC thermograms of networks cured with isomers 3,3'-DDS & 4,4'-DDS	205
Figure 4.26 DMA curves showing storage modulus plotted as a function of temperature .....	206
Figure 4.27 DMA curves showing the dynamic loss tangent plotted as a function of temperature .....	207
Figure 4.28 DSC thermograms of networks cured with isomers 3,3'-DDS & 4,4'-DDS	208
Figure 5.1 Chemical structures of monomers used in this work.....	220
Figure 5.2 Solubility experiments indicating the solubility of hydrophilic GO in water and hydrophobic GO-PMDA and GO-DOPO-V soluble in CHCl <sub>3</sub> .....	230
Figure 5.3 FTIR spectra showing the confirmation of monomer formation.....	231
Figure 5.4 (a)XPS survey scans of GO(black), GO-PMDA(red) and GO-DOPO-V(blue) which confirms the covalent functionalization of GO. (b) high resolution XPS spectra of N1s for GO-PMDA.....	233
Figure 5.5 (a)XPS survey scans of GO (black), GO-PMDA (red) and GO-DOPO-V(blue) which confirms the covalent functionalization of GO. (b) high resolution XPS spectra of N1s for GO-PMDA.....	234
Figure 5.6 AFM images of GO, GO-PMDA and GO-DOPO-V with height profile.....	235



Figure 5.7 3D view of GO-DOPO-V which indicates a non-uniform surface morphology .....	236
Figure 5.8 TGA curves of (a) PMDA, GO-PMDA and (b) DOPO, GO-DOPO displayed with unmodified GO for comparison.....	238
Figure 5.9 TGA curves of (a) PMDA, GO-PMDA and (b) DOPO, GO-DOPO shown along with unmodified GO .....	239
Figure 5.10 TGA curves of (a) PMDA, GO-PMDA and (b) DOPO, GO-DOPO shown along with unmodified GO .....	240
Figure 5.11 DSC thermograms of composites investigated in this work. Curves are offset vertically for clarity.....	241
Figure 5.12 Storage modulus and Tan delta curves for EP, EP/GO and EP/GO-PMDA in the DMA test.....	242
Figure 5.13 Storage modulus and Tan delta curves for EP, EP/GO and EP/GO-DOPO-V in the DMA test.....	243
Figure 5.14 HRR and THR curves of EP, EP/GO, EP/PMDA and EP/GO-PMDA.....	245
Figure 5.15 HRR and THR curves of EP, EP/GO, EP/DOPO-V and EP/GO-DOPO-V	246
Figure 5.16 SEM images of residual char after cone calorimeter measurement .....	247
Figure 5.17 SEM images of residual char after cone calorimeter measurement .....	248
Figure 5.18 FTIR spectra of residual char after cone calorimeter measurement.....	249
Figure 6.1 Phosphate based FR.....	260
Figure 6.2 Monomers used as dispersing agents for small molecule metal based additive .....	266
Figure 6.3 Metal salts used in this work .....	267

Figure 6.4 Monomers / oligomers used as base to prepare composite materials.....	268
Figure 6.5 Monomers used to prepare flame-retardant self-healing material.....	269
Figure 6.6 Wide angle X-ray analysis of prepared composites. Black spectrum indicates the powdered salt of zinc, red indicates the neat epoxy amine networks (without zinc) and blue indicates the composite made with metal salt in epoxy amine systems.....	278
Figure 6.7 Heat release data obtained via cone calorimeter for the prepared composites. EP represents the epoxy amine networks. Small molecule additive was prepared with different metal salts prior to adding to the epoxy amine networks.....	279
Figure 6.8 Pictures indicating the unburnt and burnt mold showing a continuous char formed for transparent composites prepared using zinc acetate, zinc acrylate, zinc undecylenate .....	281
Figure 6.9 Pictures indicating the unburnt and burnt mold showing a continuous char formed for transparent composites prepared using zinc acetate, zinc acrylate, zinc undecylenate .....	281
Figure 6.10 Wide angle X-ray analysis of prepared composites. Black spectrum indicates the powdered salt of zinc, red indicates the neat epoxy amine networks (without zinc) and blue indicates the composite made with metal salt in epoxy amine systems.....	283
Figure 6.11 Heat release data obtained via cone calorimeter for the prepared composites. ....	284
Figure 6.12 Pictures indicating the unburnt and burnt mold showing a continuous char formed for transparent composites prepared using cobalt acetate(left) and nickel acrylate (right) .....	284

Figure 6.13 Comparison of time to ignition and peak heat release rate of the composites in this work .....	285
Figure 6.14 Visual observation of solubility for checking the miscibility of 1°, 2° & 3° amines. ....	287
Figure 6.15 Proton NMR spectrum of the reaction product of zinc acrylate with stoichiometric quantities of dibutylamine.....	288
Figure 6.16 Photographs of samples of (a) epoxy resin, (b) Epoxy resin with zinc oxide, (c) epoxy resin with zinc borate and (d) zinc acrylate in DBA as additive in epoxy resin before and after burning in the cone calorimeter. Samples are shown above, and the corresponding char is shown beneath each sample.....	292
Figure 6.17 Heat release rate of prepared epoxy resins with different additives, zinc oxide, zinc borate and synthesized zinc acrylate in DBA.....	293
Figure 6.18 Cone calorimeter results of polyurethane systems. “PU+ Zinc acrylate” indicates the PU composites with metal dispersed and “small molecule additive in PU” indicates the dissolution of metal. Both composites correspond to an effective metal content to 2.25 wt% zinc.....	295
Figure 6.19 Cone calorimeter results of polystyrene (PS) systems. “PS+ Zinc acrylate” indicates the PU composites with metal dispersed and “small molecule additive in PS” indicates the dissolution of metal. Both composites correspond to an effective metal content to 2.25 wt% zinc.....	298
Figure 6.20 Cone calorimeter results of polyethylene oxide (PEO) systems. “PEO+ Zinc acrylate” indicates the PEO composites with metal dispersed and “small molecule	

additive in PEO” indicates the dissolution of metal. Both composites correspond to an effective metal content to 2.25 wt% zinc.....	299
Figure 6.21 TGA analysis of epoxy amine networks with increasing small molecule additive concentrations. ....	301
Figure 6.22 DSC thermograms of composites prepared using $\beta$ -amino complexes in comparison with the neat epoxy amine networks. Thermograms are vertically offset for clarity .....	303
Figure 6.23 Tensile test (compression mode) of the prepared composites with increasing small molecule additive content.....	304
Figure 6.24 Heat release curves obtained via cone calorimeter for networks containing small molecule additive ranging from 0.1 wt% to 18 wt%. Both a and b curves represent the same serious burnt at similar conditions and separated for clarity. ....	306
Figure 6.25 Wide angle x-ray analysis of obtained char from cone calorimeter. Crystal lattice represents the obtained char is zinc oxide.....	308
Figure 6.26 Heat release curves of composites prepared using zinc stearate prepared via different protocol. Labels A through E indicates different protocol listed in Table.....	311
Figure 6.27 Burnt ( on top) and unburnt (bottom) of compositors containing zinc stearate prepared via different protocol. Transparent composites yielded a continuous char underneath a porous top surface .....	312
Figure 6.28 Heat release rates of stearate based salts examined with epoxy amine systems. Zinc and magnesium stearates resulted in lowest PHRR, whereas stearic acid increased the flammability. ....	314

Figure 6.29 Unburnt (top) and burnt (bottom) pictures of epoxy-amine composites of different stearate salts. .... 315

Figure 6.30 Wide angle x-ray spectrum of (a) miscible Zinc stearate, (b) miscible magnesium stearate & (c) immiscible nickel stearate composites in epoxy amine networks ..... 316

Figure 6.31 Polyurethane composites with (a) no Zinc metal on the left & (b) with zinc metal on the right. The composites without Zinc doesn't show the self-healing property, where is the composites with Zinc compound showed bond reformation..... 318

Figure 6.32 Heat release curves of polyurethane composites prepared with zinc acrylate in increasing concentrations..... 318

Figure 6.33 Heat release curves of polyurethane controls prepared with methyl acrylate and di-acrylate instead of zinc acrylate..... 319

## LIST OF SCHEMES

Scheme 1.1 Schematic of typical radical mediated thiol-ene photoinitiated reaction. ....	19
Scheme 1.2 Schematic of typical radical mediated thiol-ene photoinitiated reaction. ....	21
Scheme 1.3 Generalized reaction for epoxy monomer synthesis .....	30
Scheme 1.4 Synthesis of DGEBA based epoxy from bisphenol A and epichlorohydrin.	30
Scheme 1.5 Reaction mechanism of Lewis based catalyzed homo-polymerization of epoxy resins .....	32
Scheme 1.6 Reaction mechanism of Lewis acid catalyzed homo-polymerization of epoxy resin.....	32
Scheme 1.7 Reaction mechanism of Epoxy resin crosslinked with primary and secondary amine.....	33
Scheme 2.1 Thio-Micheal addition reaction used to attach PEG containing monofunctional acrylate.....	41
Scheme 5.1 Epoxy curing reaction. Epoxide ring opens with any active proton donating monomers.....	214
Scheme 5.2 Synthesis of graphene oxide from graphite via Hummer's method .....	222
Scheme 5.3 Synthesis of reactive polysiloxane Oligomer. Color code is used to differentiate the synthesized oligomer in the rest of this work. ....	223
Scheme 5.4 Functionalization of GO with PDMA .....	224
Scheme 5.5 Synthesis of DOPO-V. Color coded to differentiate the molecule from PMDA.....	225
Scheme 5.6 Synthesis of GO-DOPO-V .....	226

Scheme 5.7 Chemical functionalization of GO with PMDA via oxygen rich carboxyl and epoxide groups available on the surface of GO .....	233
Scheme 6.1 Thermal decomposition of melamine-based products. ....	259
Scheme 6.2 Formation of boroxine networks from boric acid, a precursor for char formation.....	262
Scheme 6.3 Synthesis of small molecule additive using dibutyl amine and zinc acrylate .....	270
Scheme 6.4 Synthesis of small molecule additive with self-healing property .....	270
Scheme 6.5 Synthesis of self-healing flame-retardant compositions .....	273
Scheme 6.6 Neat polyurethane to compare with self-healing flame retardant polyurethane networks .....	273
Scheme 6.7 Chemical structures of primary (1°), secondary (2°) & tertiary (3°) amines. ....	286

## CHAPTER I - GENERAL BACKGROUND AND THESIS ORGANIZATION

### 1.1 Introduction

Use of crosslinked network polymers has dramatically increased over the last several decades due to its inherent advantages not limited to high strength to weight ratios, mechanical properties and processability. However, use of polymers are still in development stage due to the unanswered question in several aspects. For instance, within the context of this thesis, the use of networks in the field of gas separation membranes is still in testing phase and couldn't completely replace the traditional chemical engineering techniques such as solvent adsorption, distillation etc. This is because the polymeric membranes exhibit a trade-off between permeability and selectivity (explained later in the thesis), which makes polymer material less attractive compared to the expensive solvent adsorption techniques. In the aspect of flame retardants, the use of polymeric materials in combustible environment imposes a threat because of its high combustible nature. Polymers ignite when exposed to sufficient heat and oxygen which releases smoke and toxic gases affecting the human life along with loss of property. Thus, a basic understanding of structure dependent properties is essential to use polymer material efficiently and safely.

### 1.2 Thesis organization

In this thesis, we aim to study the effect of structure, concentration of chemical moiety and the placement of the chemical moieties on the properties focusing in gas transport and flame retardancy. Both transport and flame-retardant properties have been evaluated using thiol-ene and epoxy-amine crosslinked systems respectively.



This thesis consists of six chapters. Chapter 1 is a summary of literature review on crosslinked networks, thiol-ene and epoxy-amine polymer systems. This chapter also contains review on gas separation membranes and basics of flame-retardant systems. Chapter 2-6 present the results of the original research.

Chapter 2 explores the structure- gas transport properties of polyethylene glycol (PEG) containing thiol-ene based membranes. Our goal was to improve CO<sub>2</sub> permeability and CO<sub>2</sub>/light gas selectivity by focusing on the materials that achieve high CO<sub>2</sub> selectivity as a result of high CO<sub>2</sub> solubility selectivity. More specifically, we determined the minimum amount of PEG required to achieve the maximum solubility selectivity of CO<sub>2</sub>/ light gases and compared the effect of placement of PEG either in backbone or as dangling chain end.

In chapter 3, cone calorimetry was used to explore the structure- flame retardant properties of thiol-ene networks with varying crosslink density tuned via functionality of thiol monomer. We also compared the fire properties of two similar networks fabricated via structural isomeric ene monomers, 2,4,6-tris(allyloxy)-1,3,5-triazine (TOT) and 1,3,5-triallyl-1,3,5-triazine- 2,4,6-trione (TTT), under different fire scenarios. The samples which were quenched at different time frames (5 sec, 10 sec, 15 sec and 20 sec) were studied in scanning electron microscope to understand the pyrolysis behavior of these thiol-ene based networks.

Chapter 4 reports the results obtained in analyzing the structure- fire retardant properties of epoxy-amine networks. Several commercial epoxy monomers/ oligomers were crosslinked with 4,4'- diamino diphenyl sulfone (4,4'-DDS) amine monomer. Activation energy of network was calculated using Flynn and wall method via TGA

measurements. Several network parameters such as glass transition temperatures ( $T_g$ ), aromatic content, crosslink density was related to the results obtained via cone calorimeter. Interestingly we found the networks containing naphthalene performed the best due to its high char forming capability. The cyclo-aromatic and aliphatic fire performance were the least due to the inability to form char. The performance related to aromatic content was moderate in-between these two families of compounds. Group contribution method was used to theoretically estimate the heat release capacity and total heat release. To the best of our knowledge, it was the first attempt to estimate the heat release capacity values through group contribution method for crosslinked networks. We also compared the isomeric effect on flame retardancy by constructing a matrix of networks containing diglycidyl ether of bisphenol-A (DGEBA), diglycidyl ether of bisphenol-F (DGEBF), and tetra-glycidyl methylene dianiline (TGDDM) crosslinked with 3,3'-DDS and 4,4'-DDS.

In chapter 5, we evaluated the flame-retardant effect of a composite prepared by adding graphene oxide (GO) modified with siloxane and phosphorous compounds to a standard bisphenol A type epoxy system. Results indicated that the modification of GO aided better dispersibility of these composites within the matrix which resulted in a better flame-retardant property when compared with GO itself.

In chapter 6, a new metal-based flame-retardant additive was discovered which was halogen and phosphorus free. These metal additives performed better than the commercially available flame-retardants in terms of reducing the peak heat release rate and smoke release. The new additive was found to be effective at very low metal content and it was found to be effective to most common polymers including epoxy-amine,

polyurethanes, polystyrene and polyethylene oxide. Later we found that by chemically attaching the metal-based salts to the monomer, a self-healing flame retardant polyurethane was developed.

### **1.3 Research background and motivation**

#### **1.3.1 Greenhouse gasses and Carbon dioxide (CO<sub>2</sub>)**

Natural greenhouse gases, such as CO<sub>2</sub>, CH<sub>4</sub>, N<sub>2</sub>O, Ozone (O<sub>3</sub>) and water vapor, transmit the Sun's visible light, absorb and re-emit the earth's infrared thermal radiations which helps maintain the temperature suitable for life.<sup>1</sup> Researchers have estimated that maintaining concentrations of greenhouse gases in the range of 350 ppm to 450 ppm can help stabilize global temperatures close to the ideal range for the ecosystems.<sup>2</sup> Although this value of greenhouse gas is not alarming, the monotonic increase of CO<sub>2</sub> concentration in the atmosphere is of concern.

The concentration of CO<sub>2</sub> gas in the atmosphere has increased at an accelerating rate from decade to decade mainly due to the increasing energy demand and subsequent fuel consumption. On an average, 36% of global CO<sub>2</sub> emissions is accounted for by the electricity generation sector.<sup>3</sup> American Energy Information Administration (EIA) and the international Energy Agency (IEA) has estimated an average annual increase in energy consumption by 2%. Fossil fuel usage is still unavoidable and serves to satisfy the growing energy demand. Combustion of coal or natural gas to produce energy releases vast amounts of carbon dioxide (CO<sub>2</sub>) into the atmosphere which accounts for global warming:<sup>4</sup>

The global temperature increase due to greenhouse effect has urged the international community to take actions to reduce the carbon footprint in the ecosystem.

Several researches has been focused on satisfying both energy demands and reduction in greenhouse gas concentrations.

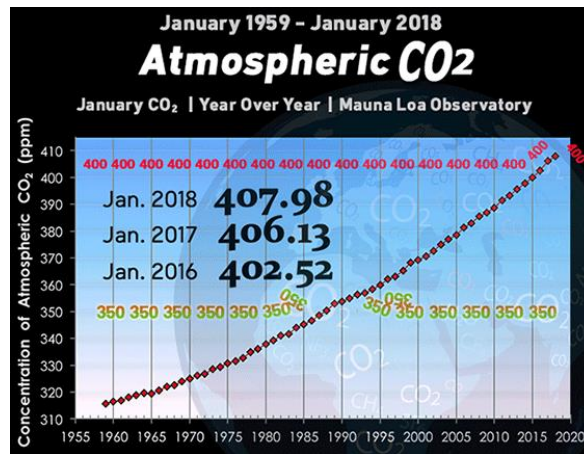


Figure 1.1 Increasing concentration of CO<sub>2</sub> in Atmosphere. Data obtained from NOAA<sup>5</sup>.

Fig. 1.1 shows estimated atmospheric CO<sub>2</sub> concentration in the atmosphere which increases linearly over the past 5 decades without signs of reducing or saturation.<sup>5</sup> The CO<sub>2</sub> concentration as of April 2018 reached 410.31 ppm which is approaching the threshold acceptable concentration of 450 ppm. The raise in CO<sub>2</sub> gas concentration, global temperature increase beyond a certain threshold limit might have serious detrimental effect on the ecosystems.

In addition to contributing to global warming, CO<sub>2</sub> reduces the efficiency of the natural gas.<sup>6</sup> It is acidic and hence corrosive in nature when it gets mixed with water. Removal of CO<sub>2</sub> from natural gas will increase its calorific value, and decrease its volume, prevent pollution of atmosphere and prevent corrosion to the transportation pipe lines.<sup>7</sup> CO<sub>2</sub> is considered to be an impurity in various gases, when it is mixed with CH<sub>4</sub> in natural gas, H<sub>2</sub> with syngas, O<sub>2</sub> in food packaging.<sup>8</sup>

### 1.3.2 Application of Carbon dioxide gas (CO<sub>2</sub>)

In some applications, CO<sub>2</sub> gas is a useful tool mainly due to its abundance, non-flammable nature and low cost, low reactivity along with unique physical properties.<sup>9</sup>

Figure 2 shows a comprehensive uses of CO<sub>2</sub> gas

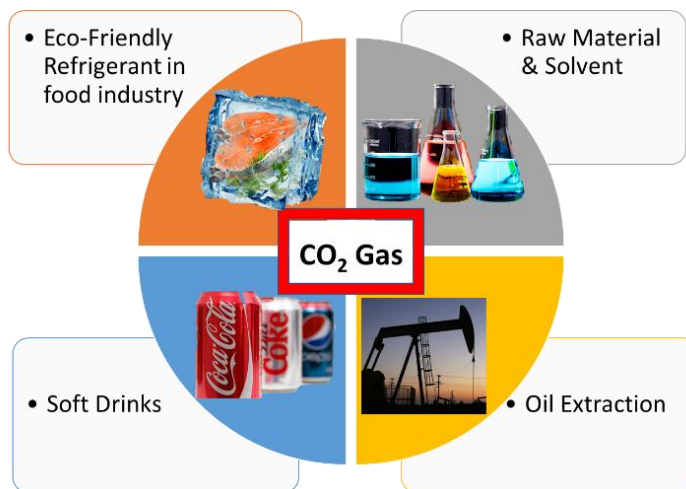


Figure 1.2 Application of CO<sub>2</sub> gas in food industry, chemical industry as a raw material and compressed gas for oil extraction.

Carbon dioxide in its solid and liquid form is used as a quick freezing, surface freezing, chilling and refrigeration in transportation of food.<sup>10</sup> Dry ice pellets are used to replace sandblasting to remove the paint from surfaces aiding in reducing the cost of disposal. Chemical processes sometimes require dry ice due to its inert nature in the storage of carbon powder and in fire extinguishers.<sup>11</sup>

Carbon dioxide is also a raw material for several commodities, especially for methanol and urea production. Liquid and supercritical CO<sub>2</sub> is used in material chemistry for synthesis and processing of polymers, particularly in production of biodegradable polycarbonates from cyclic ethers.<sup>12</sup> CO<sub>2</sub> gas is a good solvent for many organic

compounds. Due to Its solvating potential, it has been employed in dry cleaning as a substitute for conventional solvents.<sup>13</sup>

The most significant usage of CO<sub>2</sub> gas is in the area of oil extraction from wells, where the gas when pumped into the well, it gets dissolved in the oil rendering it less viscous allowing the oil to be extracted more easily from the bedrock.<sup>14</sup>

CO<sub>2</sub> gas is used to carbonate soft drinks, beers and to prevent fungal and bacterial growth. It is also used to de-cafeinate coffee. It is used as a respiration stimulant for medical use when combined with oxygen. It can be used to neutralize water.<sup>15</sup>

Thus, CO<sub>2</sub> gas has the potential of being used in several areas as an alternative owing to its abundance and inexpensiveness. On contrary, several industry releases tons of CO<sub>2</sub> gas as waste to the atmosphere which has detrimental effects on the environment. Thus, it is wise and economical to utilize the abundant, inert CO<sub>2</sub> gas as an alternative thus reducing the carbon foot print and greenhouse gas as well as improved economy. Hence CO<sub>2</sub> separation and capture from other light gases is important not only to mitigate the global climatic changes, but also to improve the efficiency<sup>7,8</sup>. Hence significant controls are implemented to separate and sequester the CO<sub>2</sub> from atmosphere.

### **1.3.3 Electronic properties of CO<sub>2</sub> and its reactivity**

It is essential to understand the electronic properties of CO<sub>2</sub> gas to facilitate the separation and sequestration of the gas on the molecular level. CO<sub>2</sub> is a non-polar, linear and symmetrical gas molecule. Even though the Pauling electronegativity difference between carbon (2.5) and oxygen atoms (3.5) is huge, it has symmetrical dipole with equal magnitude pointing in opposite directions making it a non-polar molecule.<sup>16</sup> The large difference in electronegativity does lead to the presence of partial charges on the

atoms. There is charge separation arising from the partial charges: a partial positive charge ( $+2\delta$ ) is localized on the carbon atom and two partial negative charges of half the magnitude are localized on the oxygen atom ( $-\delta$ ). This arrangement of four unit charges on a molecule is termed as quadrupole.<sup>17</sup>

Due to the presence of partial positive charge on carbon and partial negative charge on oxygen, the atoms become a Lewis-acid and Lewis-bases respectively. Thus  $\text{CO}_2$  molecules can readily participate in Lewis acid-base interactions, H-bonding as an acceptor, along with quadrupole interactions such as quadrupole-dipole, quadrupole-quadrupole and quadrupole ion interactions.

Non-covalent interactions are mainly used in physical adsorption techniques without any chemical reactions occurring between the adsorbant and the gas.<sup>18-20</sup> In addition,  $\text{CO}_2$  is a weak electrophile and it can react with nucleophiles such as amines, hydroxides and it can co-ordinate with transition metals.<sup>21</sup>

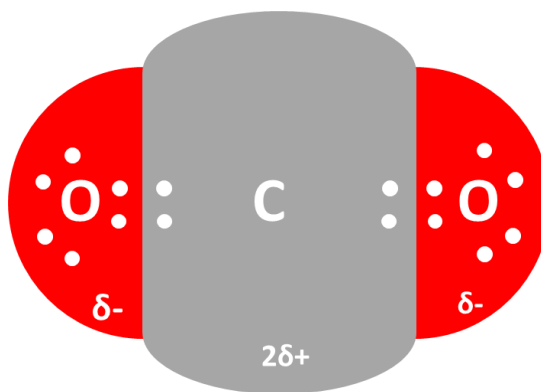


Figure 1.3 Structure of  $\text{CO}_2$  gas showing the electronic properties.

## **1.4 Carbon Dioxide(CO<sub>2</sub>) gas separation and capture**

The process of CO<sub>2</sub> gas capture, separation and storage from fossil fuel combustion and other sources is collectively called *Carbon capture and Storage (CCS)* or *carbon sequestration*. CSS is important because CO<sub>2</sub> gas is generated as mixtures with other gases, for instance, methane and nitrogen in natural gas processing,<sup>22,23</sup> ammonia and hydrogen plants,<sup>24</sup> hydrogen sulfide and sulfur oxides from biogas production<sup>25</sup> etc. In majority of cases, a separation step must be included to capture CO<sub>2</sub> gas. Several processes are available including, cryogenic distillation, absorption processes, pressure swing adsorption and membrane gas separation to achieve CCS.<sup>26</sup> Due to some inherent drawbacks (high operation and recovery cost and lower efficiency) involved in pressure swing adsorption, cryogenic distillation and absorption, membrane technology stand out as a potential candidate for separation of CO<sub>2</sub> from a mixed gas stream<sup>7,27-29</sup>.

### **1.4.1 Membrane separation process**

Membranes are semi-permeable materials which involves the separation of individual components based on the differences in the rate of permeation through them. Recently membrane separation process has become a promising “green” alternative to the traditional separation processes. It has attained significant interest due to its low footprint, competitive energy efficiency and cost-effective approach.<sup>6,30-33</sup>

A mixture of gases on one side of the membrane permeates through to the opposite interface due to the pressure differential. Ideally a single component (retentate) is withheld from transport across the membrane. Membranes can be either porous or non-porous, where the former are made using porous inorganic materials and the later using



polymers. Porous membranes made using zeolite or carbon molecular sieves, follow a size sieving mechanism to separate gases of certain size depending on pore diameter. This mechanism exhibits higher throughput but lower selectivity compared to polymer based membranes.<sup>34,35</sup> Polymer membranes exhibit less permeability but offers good selectivity. Their selectivity can be tuned by adjusting physical or chemical interactions between the polymer membrane and the gases.<sup>35</sup>

Currently, composite organic-inorganic membranes also referred as mixed matrix membranes consists of porous inorganic particles incorporated in a continuous polymer matrix. Several porous inorganic materials with tunable pore size and the particle size has been synthesized targeting the separation of specific gas molecules is size sieving technique.<sup>18,36-38</sup> This is done to combine the advantage of excellent separation properties of porous materials along with the ease of processing of polymeric materials.<sup>39</sup>

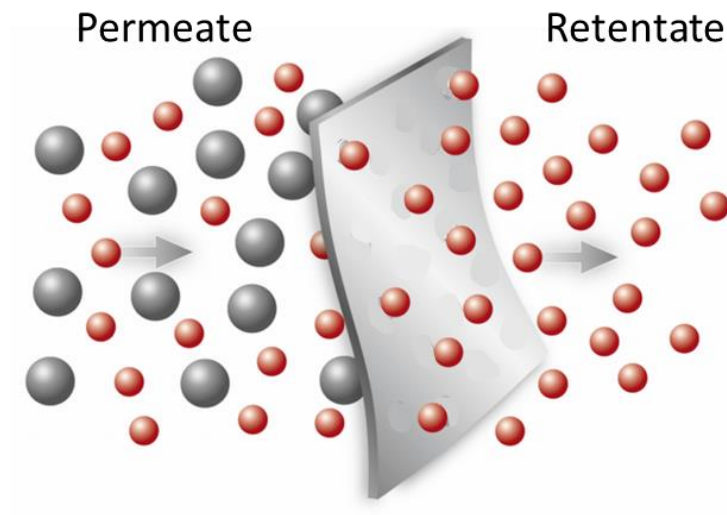


Figure 1.4 Representation of membrane gas separation.

### **1.4.2 Polymeric Membranes and Solution-Diffusion model**

Polymeric materials are the most commonly used in membrane gas separations. Two main parameters, permeability and selectivity (ratio of permeability coefficient of faster moving gas to a slower permeating gas) determines the membrane performance. Low permeable membranes require larger area and subsequently higher capital cost while low selectivity corresponds to higher operating cost. For polymer-based membranes, there is a trade-off between selectivity and permeability. A bench mark was established by Robeson, when he collected experimental permeability values for different polymeric membranes, showed for all gas molecules there exists an “upper-bound” above which no materials exist.<sup>40</sup> Plasticization, mechanical robustness, and physical aging are some additional hurdles facing the commercialization of polymer based membranes.<sup>7</sup>

Polymeric materials can be broadly divided into two categories: rubbery (polymers above glass transition temperature) and glassy (polymers below glass transition temperature). Glassy polymers are known to have high selectivity, excellent thin film forming capabilities coupled with good mechanical properties, but lower permeability. On the other hand, rubbery polymers possess high permeability, but suffer from poor selectivity and tend to plasticization.<sup>41</sup>

Polymeric materials with higher permeability selectivity and mechanical stability would be an ideal candidate for the membrane separation processes to expand the growing demands.

### **1.4.3 Solution-Diffusion model**

The transport of small molecules across the polymeric membrane depends on the molecular motion of the penetrant molecules. The driving force is primarily the

concentration or pressure differences between phases.<sup>42</sup> The permeability coefficient is an intrinsic material property. The amount of gas permeating through a membrane is expressed as a flux of gas at standard temperature and pressure ( $\text{cm}^3(\text{STP})/(\text{cm}^2\text{s})$ ).

$$\text{Equation 1 : } J = \frac{P}{l} * (\Delta p)$$

Where,  $J$  is the flux across the membranes,  $P$  is the permeability coefficient,  $l$  is the thickness of the membrane and  $\Delta p$  is the partial pressure difference across the membrane.

Gas transport through non-porous polymeric membranes can be modeled via the solution-diffusion mechanism in which permeants dissolves in the polymer at the high pressure face and then diffuses through the polymer down a concentration gradient and followed by desorption out of the polymer at the low-pressure face.<sup>43</sup> Using the solution-diffusion model, Barrer described gas permeability through a membrane as a product of diffusivity and solubility as in Equation 2.

$$\text{Equation 2 : } P = D * S$$

Where  $D$  is the diffusion coefficient and  $S$  is the solubility coefficient.

The magnitude of permeability is determined by the diffusivity and the solubility. Diffusivity is a kinetic parameter which depends on the penetrant size, membrane free-volume within the polymer, and temperature. Figure 1.5 demonstrates the relationship between penetrant size and diffusivity, indicating that diffusivity decreases with increasing penetrant size. For amorphous polymeric materials, the diffusion rate will be higher than those of crystalline polymers, like polyethylene oxide, mainly due to the physical barrier posed by the crystalline domains to the gas molecules.

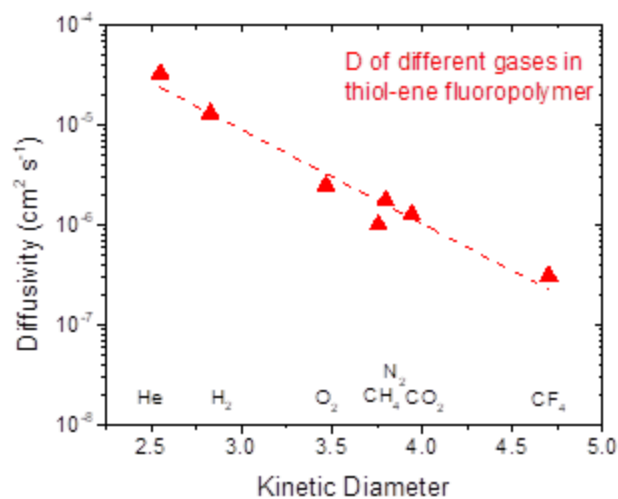


Figure 1.5 Diffusivity of several gases through thiol-ene based fluoropolymer. Plot shows the comparison of diffusivity co-efficient of gases with different kinetic diameter.

Solubility is a thermodynamic behavior which depends on the penetrant critical temperature, sorption sites, and chemical affinity. In general, the higher the critical temperature is the higher the condensability and solubility of the gas in polymer. Figure 6 shows the dependence of critical temperature of several gases on solubility.<sup>31</sup>

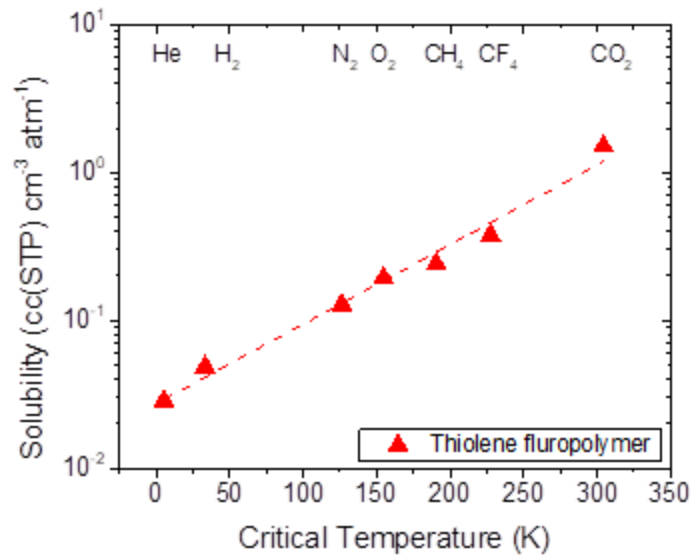


Figure 1.6 Dependence of solubility on critical temperature. Shown here is the solubility values for UV-curable thiol-ene fluoro-polymeric networks

Thus, flux across a membrane is a function of both chemical and physical properties of the penetrant molecules and the membrane.

The ability of a membrane to separate a mixture of gases is called selectivity. Selectivity is achieved between different gas penetrants when there are differences in the solubility and permeability through the membrane.<sup>35,44-46</sup> Selectivity is defined by the ratio of permeability of faster moving gas divided by a slower penetrating gas as shown in Equation 3.

$$\text{Equation 3: Selectivity } \alpha = \frac{P_a}{P_b}$$

Transport properties of a fabricated membranes are determined by building a selectivity plot, where selectivity of a gas pair is plotted against permeability of fast

moving gas as shown in Figure 7. As described earlier, polymeric membranes suffer from a trade-off between selectivity and permeability, i.e., a high permeable membrane has lower selectivity and vice-versa. To achieve a superior separation performance, the membrane should possess higher selectivity along with high permeability. An empirical upper bound relationship was established by Robeson et al.,<sup>40</sup> (Figure 7) from the permeability data of various polymers available in the literature. A hypothetical line called “Robeson upper-bound” was established, below which virtually every experimental data point exists. The ability to achieve a high permeability along with high selectivity or without compromising selectivity, thus surpassing Robeson upper bound is the current target of the gas separation membrane research community.

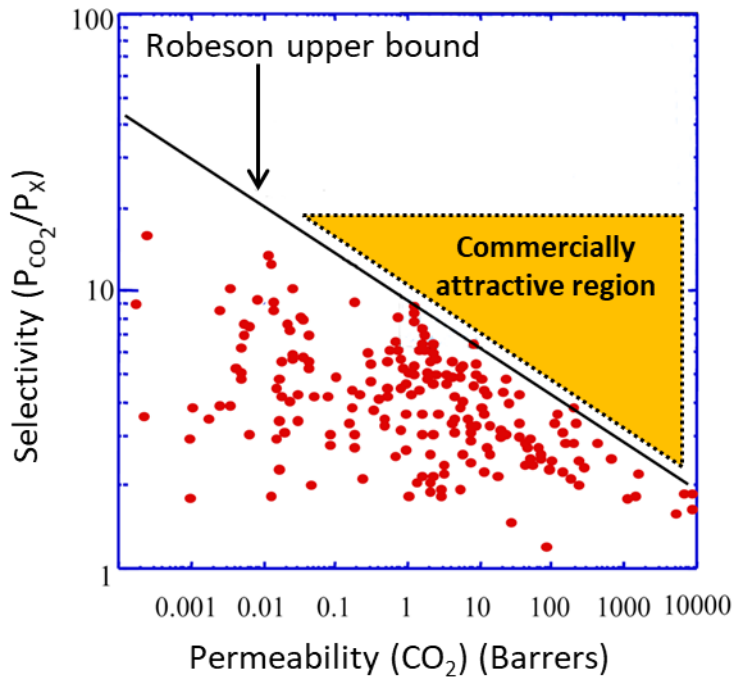


Figure 1.7 Selectivity plotted against permeability of fast moving gas. Red dots indicate selectivity of polymers reported in literature. The black line indicates the hypothetical Robeson upper bound upper bound indicating the commercially attractive region. (Moderate selectivity with high permeability)

Recently, Merkel et al proposed that for post-combustion CO<sub>2</sub> capture, researchers should focus on increasing the permeability of the membranes, and CO<sub>2</sub>/N<sub>2</sub> selectivity values does not need to be higher than 30.<sup>33</sup> Based on energy and cost calculations, the Merkel group demonstrated that moderate CO<sub>2</sub>/N<sub>2</sub> selectivity of around ~30 is only required, and further increase in selectivity is economically less viable, than the membranes having moderate CO<sub>2</sub>/N<sub>2</sub> selectivity values with high permeability.<sup>33</sup>

Considering that permeability is a function of diffusivity and solubility, selectivity can be expressed as a product of diffusivity selectivity and solubility selectivity as shown in Equation 4.

$$\text{Equation 4: Selectivity } \alpha = \frac{P_a}{P_b} = \frac{D_a}{D_b} * \frac{S_a}{S_b}$$

Where D<sub>a</sub>, D<sub>b</sub>, are diffusivities of faster moving gas and slower moving gas respectively and S<sub>a</sub>, S<sub>b</sub> are solubility of faster moving gas and slower moving gas respectively.

Thus, typically polymeric membranes, based on the separation mechanism, can be categorized as diffusive selective membranes, which typically operates through the size sieving technique or solubility selective membranes, which typically achieved by incorporating chemical moieties that interact with penetrant.

*Diffusive selective membranes:* As described earlier in this session, diffusivity based separation is widely employed in separation of chemically similar gas molecules such as O<sub>2</sub> and CH<sub>4</sub> having large differences in kinetic diameter. Separation happens via the differences in diffusion due to difference in size of the molecule, where the smaller molecules diffusive at a faster rate than the other molecule. As seen in the table, the size

sieving effect can only be achieved for gas pairs having large differences in the kinetic diameter. For gases such as CO<sub>2</sub> and O<sub>2</sub> which have similar kinetic diameter, the separation based on size thus becomes nearly impossible leading to have a poor selectivity. Thus research has been focused on separation based on the chemical affinity of the gas molecules.

Table 1.1 Critical temperature and kinetic diameter of various gases of interest

<b>Gas</b>	<b>Critical temperature <math>T_c(K)</math></b>	<b>Kinetic Diameter <math>d_K(\text{Å})</math></b>
<b>He</b>	5.2	2.6
<b>H<sub>2</sub></b>	33.2	2.89
<b>O<sub>2</sub></b>	154.6	3.46
<b>N<sub>2</sub></b>	126.2	3.64
<b>CO</b>	134.5	3.76
<b>CO<sub>2</sub></b>	304.2	3.3
<b>CH<sub>4</sub></b>	190.6	3.8
<b>SF<sub>6</sub></b>	114.08	4.9

*Solubility selective membranes:* Separation by controlling the gas solubility is dictated by the chemical affinity between the gas and the membrane materials. Facilitating preferential interaction between functional groups in the polymer membrane and the retentate gas molecule promotes separation. This phenomenon can be exploited in separating bigger molecules from smaller molecules as well (CO<sub>2</sub> from H<sub>2</sub> gas). These membranes are termed as “reverse selective membranes” where larger molecules can



permeate faster than the smaller molecules ( $\text{CO}_2 - 3.3\text{\AA}$  against  $\text{H}_2 - 2.89\text{\AA}$  gas). A similar chemical interaction strategy can be utilized to make certain gas molecules permeate faster as compared to the other having similar kinetic diameter ( $\text{CO}_2 - 3.3\text{\AA}$  &  $\text{N}_2 - 3.64\text{\AA}$ ).

As mentioned previously,  $\text{CO}_2$  gas is capable of several chemical interactions, and this can facilitate the preferential transport  $\text{CO}_2$  gas through the membrane while retaining the other gas in the high-pressure stream. It is also cost-effective to remove  $\text{CO}_2$  from the high pressure gas mixture which will reduce the cost of pressurizing the gases of interest.<sup>43</sup> In case of  $\text{H}_2$  and  $\text{CH}_4$ , removal of  $\text{CO}_2$  gas from the mixed feed will avoid extensive recompression of the desired gas product. While in case of  $\text{N}_2$  gas, selective removal of  $\text{CO}_2$  gas will reduce the membrane area requirements.

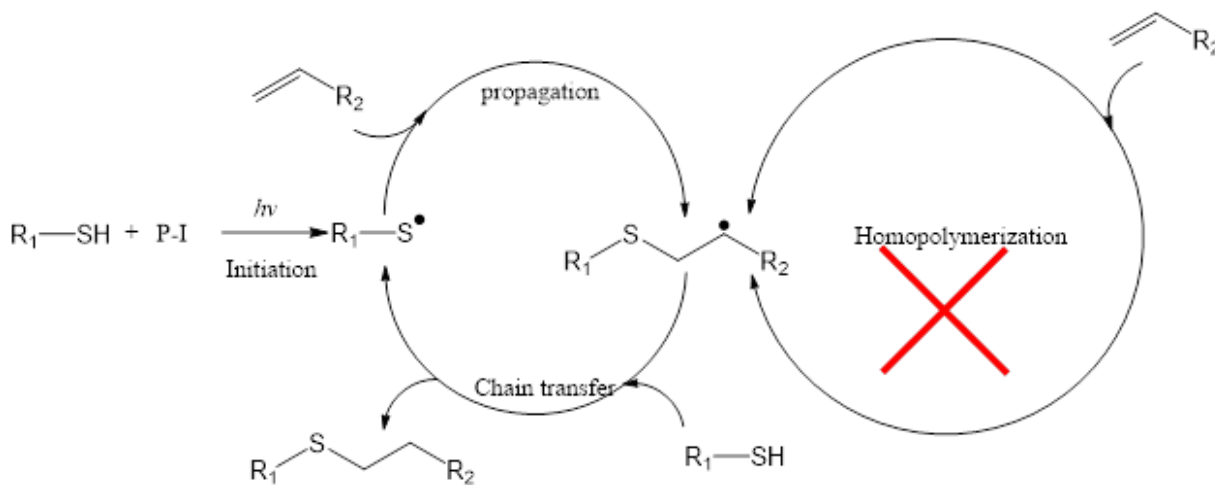
$\text{CO}_2$  gas unique ability to interact with polar groups has attracted several researchers who focus on amine and ether groups for  $\text{CO}_2$  gas separation.<sup>4,36,39,43,47-52</sup> Furthermore several studies have been conducted with ethylene glycol (which has a strong affinity for  $\text{CO}_2$  due to its weak acid base interactions) to improve membrane selectivity through tuning the solubility selectivity.

A detailed literature relating to PEG based membranes has been emphasized in the background session of chapter 2.

### **1.5 UV initiated Thiol-ene click chemistry**

Photopolymerization refers to the technique which utilizes visible or UV light to initiate a polymerization reaction to form either a linear or a crosslinked network. Thiol-ene photopolymerization utilizes UV light to initiate an addition reaction of thiols across unsaturated carbon-carbon double bond for network formation or small molecule

synthesis. Thiol-ene undergoes a step growth reaction and a typical reaction mechanism is shown in Scheme 1.1.<sup>53</sup>



Scheme 1.1 Schematic of typical radical mediated thiol-ene photoinitiated reaction.

Thiols monomers are similar to alcohol analogs except for the presence of sulfur instead of oxygen atom. Thiols exhibit lower hydrogen bonding which leads to low boiling points and lesser polarity compared to alcohols. The low electronegativity of sulfur atoms makes the hydrogen more readily abstractable generating radicals.

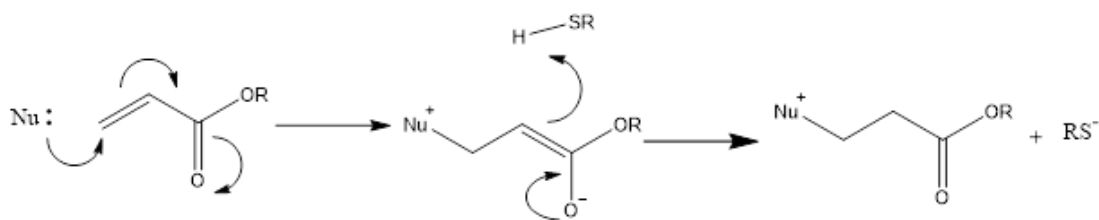
Thus upon UV irradiation, photo-initiator readily abstracts hydrogen from thiol monomer to form a thiyl radical, which is the initiation step. These thiyl radicals are the reactive sites which can add across a carbon-carbon double bond forming carbon centered radical (propagation step). This carbon centered radical subsequently abstracts a hydrogen from a second thiol generating thiyl radicals again which is similar to step growth polymerization lending the reaction mechanism a step-growth chain mechanism resulting in anti Markovnikov addition of thiol across an unsaturated group yielding thioethers.

Much of the fundamental research for thiol-ene polymerization was pioneered by Hoyle et al.<sup>54-57</sup> Most common thiol reactions are thiol radical mediated and base/nucleophilic catalyzed thio-Michael addition reactions, which depends on the electron density of the carbon double bonds.<sup>54</sup> In addition to thiol reacting with electron rich carbon double bond, several other reaction not limited to isocyanate, yne, epoxide are also possible.<sup>53</sup>

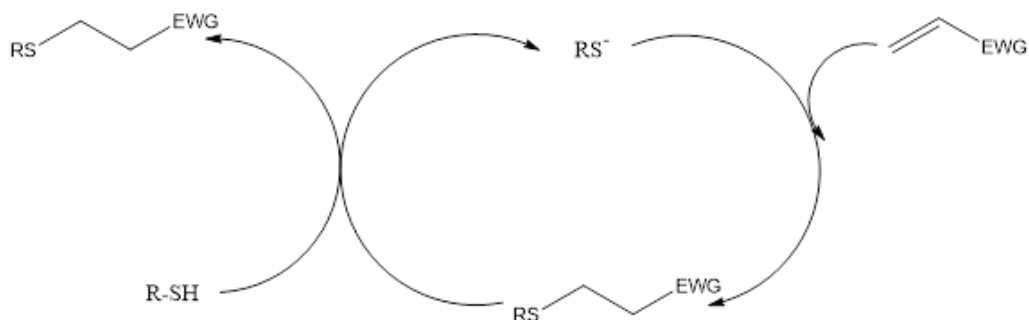
### **1.5.2 Thio-Micheal addition reactions**

The thio-Michael addition reaction was employed for the addition of PEG units as dangling chain ends on to thiol monomers. Essentially thiol-ene reaction is an addition reaction of thiol to a double bond (ene). Depending on the electronic character of the ene, the reaction may proceed either via radical mechanism or nucleophilic catalyzed anionic mechanism. The thio-Michael addition reaction refers to the addition of a nucleophile (Michael donor) across an electron deficient C=C (Michael acceptor). An electron deficient carbon-carbon double bond can be added to a thiol in presence of nucleophilic catalyst.<sup>54</sup> The thio-Michael addition reaction has been well investigated and the reaction mechanism is illustrated in Scheme 1.2.

Nucleophilic activation



Micheal-addition reaction mechanism



Scheme 1.2 Schematic of typical radical mediated thiol-ene photoinitiated reaction.

As shown in Scheme 2, a strong nucleophile such as primary amine reacts with an electron rich  $\text{C}=\text{C}$  double bond to form an enolate base. Subsequently, this enolate base deprotonates a thiol monomer forming a thiolate anion which further reacts with the  $\text{C}=\text{C}$  center. The amount of amine catalyst used in this reaction is very low. Thio-Michael addition reaction exhibits the qualities of a typical radical-mediated thiol-ene click reaction in which modular, orthogonal addition of thiol happens to an electron poor alkene. Most reactions can be carried out in the absence of catalyst, heat or light, and the addition reactions happens within few minutes of the reaction.

Thiol-ene click reaction has been of particular interest due its advantages over other acrylate based photo-curable systems. When compared to acrylate systems, atmospheric

oxygen does not inhibit the formation of thiyl radical nearly unaffected the kinetics of thiol related polymerization.<sup>58-60</sup> Also, several reports in literature points at the low stress build up due to the unique kinetics of thio-ene reactions.<sup>57,61</sup> Due to the step-growth radical reaction mechanism, they produce a dense uniform network leading to the narrow glass transition temperatures. Other advantages include the low viscosity of thiol-monomers allowing for a solvent less reaction.<sup>61</sup> The wide library of thiol and ene monomers commercially available coupled with the simple modification to attach functional groups via thio-Michael addition reaction allows them to tune for the required network properties.

## **1.6 Fire retardant polymers**

Fire is a destructive force which leads to loss of life and property. Global fire losses are estimated to be \$ 500 million a year.<sup>62</sup> For instance, the homes in the United states suffer unwanted fire every 10 seconds and every 2 hours there is a loss of life in a home fire.<sup>63</sup> Use of polymers, which accounts of 80% of the organic chemical industry, has increased over the past decade. Polymers are known for their high flammability and thus the risk associated with fire is still raising.<sup>64</sup> For instance, the fire risk associated in modern cars is not only the fuel tank rupturing but also the polymers used in the automotive parts.<sup>65</sup> The moment polymers are ignited, a sequence of exothermic oxidation reactions happens with release of heat, which causes degradation of chemical bonds which releases corrosive toxic gasses and smoke.<sup>66-69</sup> Thus, improving the fire retardancy is at most importance and since these are organic molecules, it also becomes a major challenge. Flame retardancy doesn't essentially mean the polymeric materials won't burn but rather slow down the fire spread, energy release and in some instances

self-extinguishing after being ignited.<sup>70</sup> National Institute of Standard and Technology (NIST) mentions a fire resistant material should increase the allowable escape time by minimizing the heat release and evolving less smoke and toxic gases.<sup>71</sup> In this introductory part, polymer combustion mechanisms will be discussed followed by some meaningful strategies to reduce the or decrease the heat release. This will be followed by the existing methods to determine the flame retardancy of polymers.

### **1.6.1 Combustion mechanism**

Combustion, defines as the reaction of oxygen and fuel accompanied by the release of heat, can occur when three essential elements coexists: fuel (combustible), oxygen (combustible) and heat (as energy) as shown in the fire triangle.<sup>72</sup> Polymeric materials combustion process is a highly complex process involving a series of related and /or independent steps that occur in condensed or gas phase, and in the interphase between these two phases.<sup>73</sup> Polymers are long chain macromolecules consisting of carbon and hydrogen. The most important step during the polymer combustion is the fuel production. When exposed to enough temperature above the thermal decomposition temperature, the polymers can irreversibility change the chemical structure. Thermal decomposition, initiated by main-chain or side chain scission, can lead to formation of small volatile fragments which acts a fuel for the flame. These volatiles are generally flammable and can be ignited when the auto-ignition temperature is attained in the presence of oxygen gas.<sup>63</sup> Not to mention, the products from pyrolytic decomposition includes, not limited to, combustible gases, non-combustible gases and carbonaceous char. Ignition can also be triggered at a lower temperature by an external source such as flame or spark. Once the volatiles are ignited, combustion is self-sustained either by the

act of an external source of irradiation or by substantial heat release due to exothermic chain reactions occurring in the gas phase which facilitate the decomposition of polymer thereby maintaining the critical concentration of evolved volatiles in the gas phase.<sup>71</sup>



Figure 1.8 Fire triangle emphasizing the importance of three components required for a sustainable fire.

### 1.6.2 Concepts of flame retardancy

Flame retardants are compounds intended to suppress or delays combustion under specific conditions. They interrupt the fire by physical (cooling, fuel dilution, formation of charring layer) or chemical action (reaction in solid or gas phase) thus reducing the release of heat, decomposition or spread of fire.<sup>71</sup> Figure 10 represents a fire cycle which consists of polymer pyrolysis leading to a combination of flammable and non-flammable gases along with other combustion products. A flame-retardant material breaks the cycle thus preventing or reducing fire. There are different strategies used to improve the flame retardancy of polymers as listed below (shown in Figure 10).<sup>74</sup>

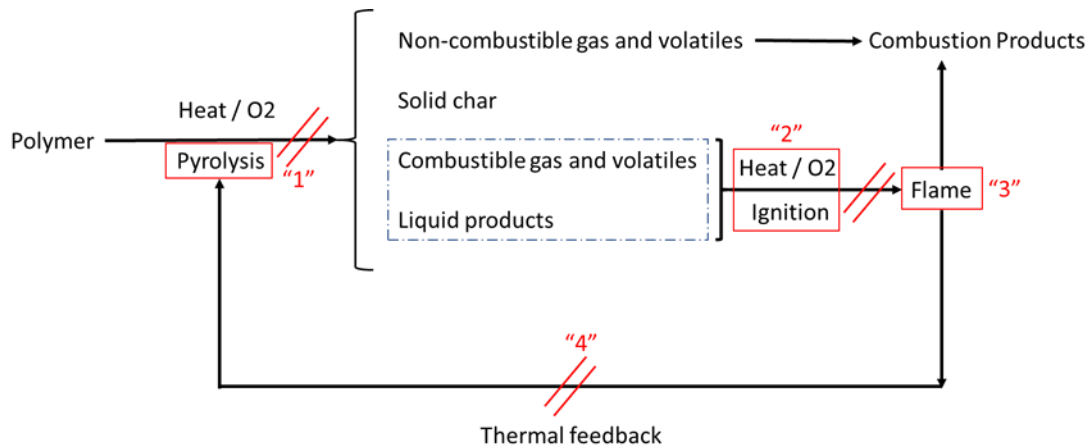


Figure 1.9 Potential mode of action of Flame retardants (1 to 4) in the combustion cycle.

The strategies that can be used to suppress fire is shown in Figure 2 is listed below.

“1”- The pyrolysis of a polymer can be modified to reduce the flammable volatiles or liquid products. This can be achieved by formation of non-flammable gases, diluting the fuel (H<sub>2</sub>O release while combustion) or of char which can act as a barrier between the flame and the polymer.

“2”- The heat and air can be isolated from fire to stop the combustion process

“3”- Flame inhibiting compounds which can quench the fire (through radical or via dilution of the flame)

“4”- reduce / block the thermal feedback from the existing fire either by a thermal insulation of char layer or intumescent coating formed when the polymer is exposed to fire conditions.



Current strategies include the use of flame retardants either in the form of reactive type (incorporated into polymer during synthesis or post grafting technique) or as additive to polymeric systems aiming in improving the char forming capabilities, radical quenching or diluting the flame by release of water.

Halogen-containing flame retardants act in general by interfering in the radical chain reaction that takes place in the gas phase.<sup>75</sup> The halogen radical reacts with the polymeric chain to form the hydrogen halide that is used to trap the high energy radicals ( $H^{\bullet}$  and  $OH^{\bullet}$ ) present in the flame. Iodine and fluorine containing FR additives are not used because these compounds are not stable. Chlorine and bromine based are the most effective FR additives.<sup>76</sup>

The other gas phase FR additive is the phosphorous containing flame retardants which is an alternate for Halogen based.<sup>77</sup> Phosphine, phosphates, phosphate esters, ammonium phosphate and red phosphate was known FR additives in this category. Phosphorous containing compounds (P-H or P-CH<sub>3</sub>) decompose due to weak bond to the P atoms generating small phosphorous species which act in gas phase to quench fire. Since the phosphorous compound is loosely bonded, they impose an environmental impact. Phosphorous based additives with nitrogen containing compounds like melamine cyanurate (melamine polyphosphate) exhibits high performance because of synergistic effect of hetero-nitrogen compounds.<sup>78</sup>

The other common FR additive is mineral fillers such as aluminum hydroxide or magnesium hydroxide. They decompose endothermally absorbing heat, release inert gases during the combustion process (water or carbon dioxide) and forming a protective inert char layer. The main disadvantage associated with this approach is the high loading

(typically about 50 wt%) levels used to achieve the flame retardancy. At such high loadings, these FR additives can hamper the mechanical properties of the polymer.<sup>79,80</sup>

### **1.6.3 Methods to determine the flame retardancy**

Flammability of polymers can be characterized by their time to ignition, heat release rate, total heat released, and flame spread rate. General flame test includes, limiting oxygen index (LOI), underwriters laboratory (UL-94) and cone calorimeter. LOI is a test method which indicate the materials flammability. LOI values defines the minimum oxygen concentration in a mixture of O<sub>2</sub>/N<sub>2</sub> gas that either maintains the flame combustion for 3 minutes or consumes a length of 5 cm of a vertical sample. Higher the LOI index the better the polymer flame retardancy.<sup>81,82</sup> The flame spread, and the ignitability is measured using a set of standard UL94 test for the flammability. The samples can either be vertical or horizontal and the rate at which the fire propagates through a certain distance is measured. Typically a blue flame with a power of 50 W and 20 mm height is applied to the edge of the sample for 10 seconds and then removed before the spread rate is determined.<sup>83,84</sup> Cone calorimeter is the most efficient polymer fire behavior tests which brings quantitative analysis to materials flammability research. A sample of specific surface area (typically 100 x 100 x 3mm) is placed on a load equipped to measure the real time weight loss. The sample is irradiated uniformly using a cone shaped heater as low as 10 – 100 kW/m<sup>2</sup>. Generally the heat of combustion of any organic materials is directly related to the amount of oxygen required for combustion in which 13.1 kJ g<sup>-1</sup> of heat is released per kg of oxygen consumed.<sup>85</sup> The measurements of oxygen concentration in the combustion gases are monitored to calculate the heat release per unit area and time.<sup>85,85-90</sup> The calibration of the heat release rate (HRR) is performed

with methane at a flow of  $5 \text{ mLmin}^{-1}$ . This is a powerful tool which is capable of simulating scenarios ranging from mild to large fires through the applied flux. The most important parameters that can be obtained via cone calorimeter are peak heat release rate (PHRR), average heat release rate (AHRR), Total heat evolved (THE), time to ignition ( $t_{ig}$ ), total mass loss (TML) as shown in Figure 11. The fire growth index can also be calculated by the ratio of PHRR to  $t_{ig}$  which is an accurate way of describing flame spread rate. In addition to the above mentioned parameters, cone calorimeter can detect the CO, CO<sub>2</sub> concentration in the combustion along with the amount of smoke released.<sup>89</sup>

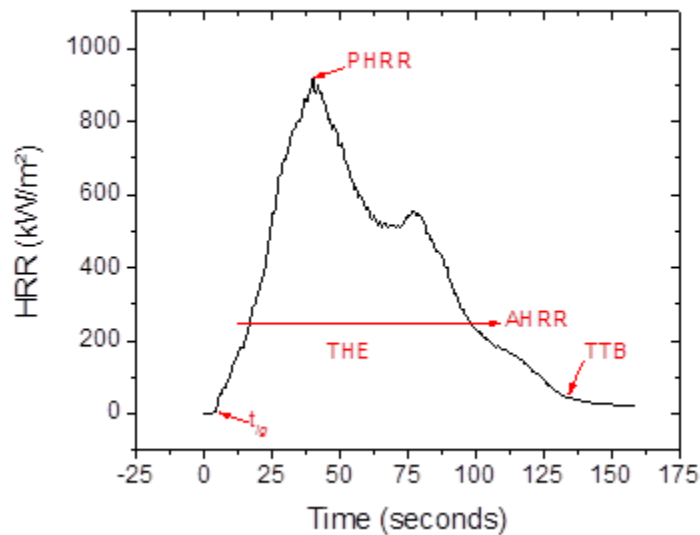


Figure 1.10 Typical cone calorimeter curve showing the obtained values.

Since cone calorimeter measures flammability in different way compared to LOI and UL-94 fire tests, these have a poor correlation among the tests. Morgan and Bundy points out the differences among LOI, UL94 and Cone calorimeter.<sup>62</sup> LOI is a small-

scale test that uses a controlled amount of oxygen atmosphere to maintain the flame, and UL94 applies a small calibrated flame at the edge for 10 s in atmospheric conditions followed by measuring time for the flame to spread a definite area. Cone calorimeter, on the other hand, uses a forced combustion in which radiant heat is projected onto a sample before ignition and during burning of the sample. The sample is usually in a horizontal configuration enclosed in an aluminum sheet at the bottom, thus eliminating any effects such as dripping or flowing. Also, the samples in cone which is exposed to continuous heat during the test is ventilated, which indicated the material response when exposed to continuous heat and fire, while in UL-94 is carried out in atmospheric conditions (without forced air) after the flame is removed. Thus the correlation between the tests cannot be established for unknown materials.

## **1.7 Epoxy resins**

Epoxy resins are a class of crosslinked polymers which have been widely used in reinforced composites, laminates, moldings, high performance coatings and adhesives.<sup>91</sup> Through the choice of monomer structure, excellent properties such as high tensile strength, high modulus and dimensional stability along with good electrical insulation capabilities can be achieved.<sup>92</sup> In uncured state epoxy resins are available in variety of forms ranging from low molecular weight liquids to high molecular weight solids. The versatility of these resins arise from the choice of monomer structure and the ability to be formulated as one pack, two-pack and co-cure systems.<sup>93</sup> Epoxy resins are monomers containing three membered oxirane ring in their structure (Figure 12). Epoxide ring is highly reactive which is associated with release of high ring

strain making it thermodynamically favorable.<sup>94</sup> Oxirane rings are generally present as a terminal group in the molecule.

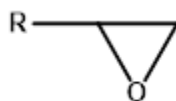
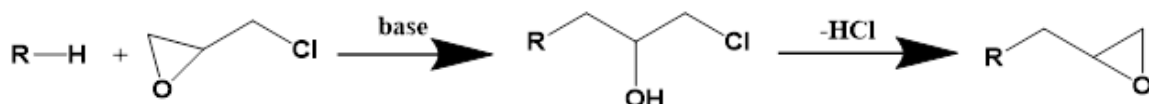


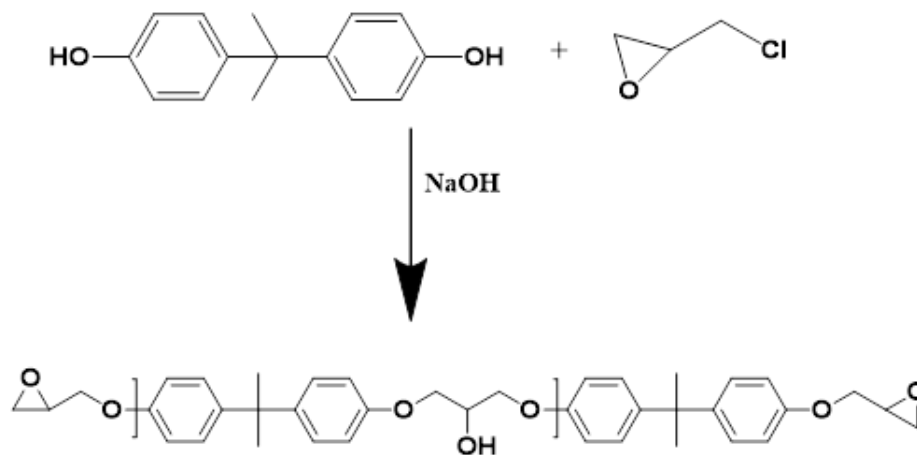
Figure 1.11 Three membered epoxide group.

The common route to synthesis epoxy resin is to react epichlorohydrin with compounds containing active hydrogen. A general synthetic route is shown in Scheme 1.3.<sup>95</sup>



Scheme 1.3 Generalized reaction for epoxy monomer synthesis

The most important class of commercial epoxy is the reaction product of bisphenol A and epichlorohydrin in the presence of base (sodium hydroxide) with the release of sodium chloride as byproduct as shown in scheme 1.4.<sup>95</sup>

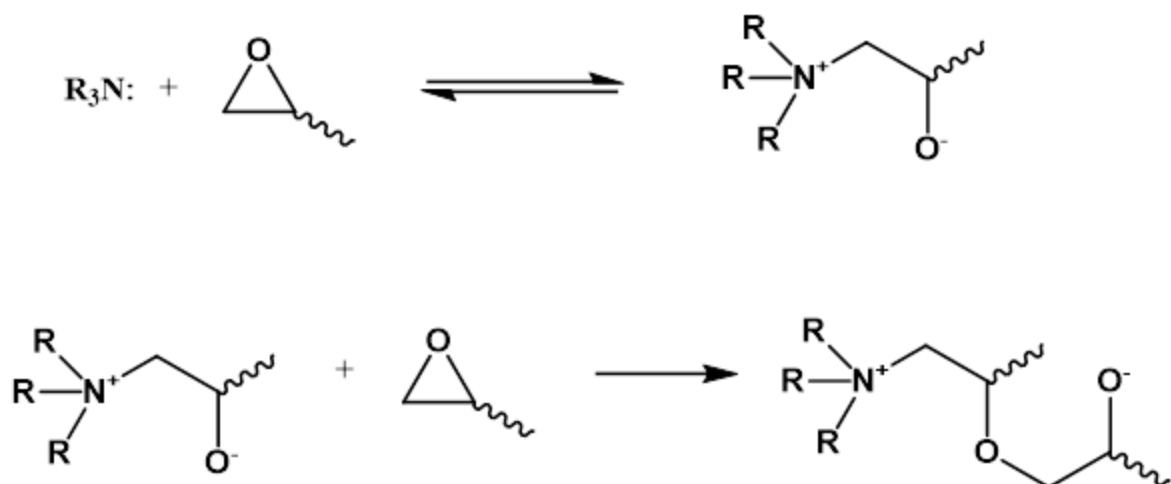


Scheme 1.4 Synthesis of DGEBA based epoxy from bisphenol A and epichlorohydrin.

There can be several structural variants not limited to long chain, multifunctional, aliphatic, alicyclic type and low molecular weight oligomeric epoxy resin which can be used to tune desired properties.

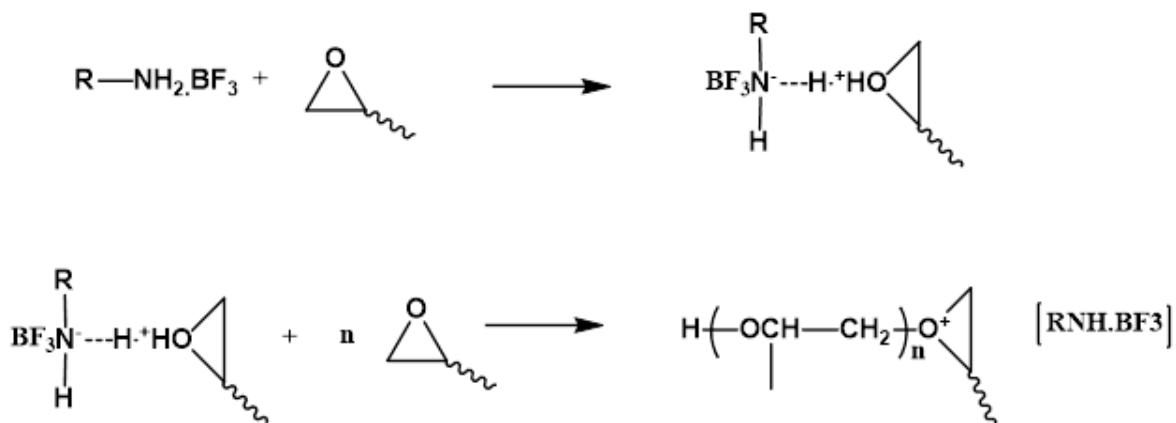
Broadly, there are two methods of crosslinking associated with the epoxy systems:<sup>96-98</sup> One catalytic cure, where a catalyst acts as an initiator which leads to homopolymers<sup>98</sup> and second is the stoichiometric curing agents where a comonomers reacts to form crosslinked network.<sup>96,97</sup> The functionality of epoxy resin depends on the type of curing path used. For homo-polymerization, the functionality of each epoxide group is considered as two, whereas in stoichiometric curing, the functionality of each epoxide group is one. This is will illustrated with the reaction scheme in the following sessions.

*Catalytic cure:* Lewis acid or bases can act as a catalyst to initiate the ring opening mechanism leading to homo-polymerization. Lewis bases contains unshared pair of electrons which acts as a nucleophilic sites of low electron density.<sup>99</sup> Tertiary amines are widely used for anionic homo-polymerization as depicted in Scheme 5. The reaction involves zwitterion which consists an ammonium and an alkoxide group.<sup>98</sup>



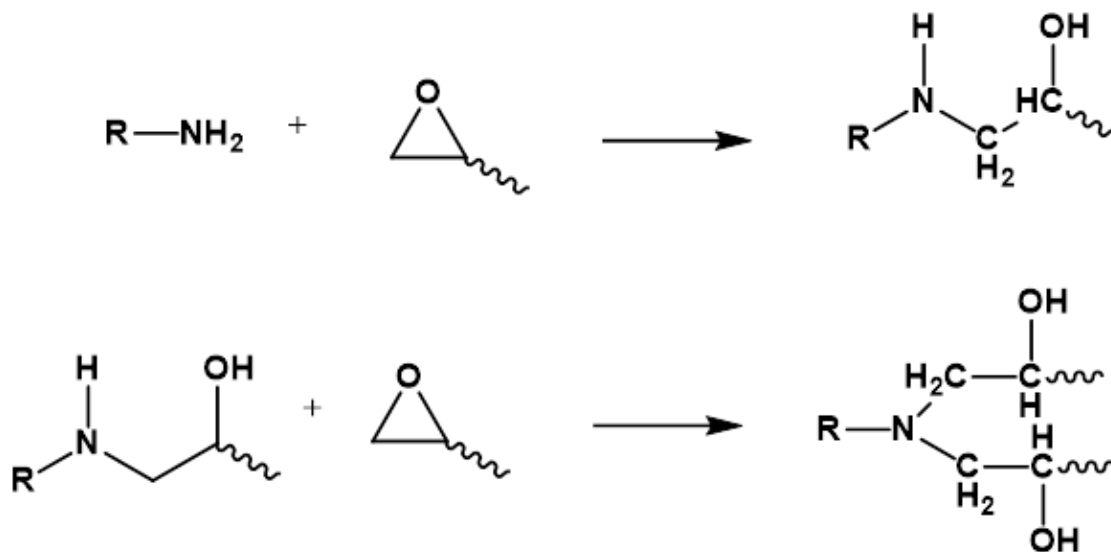
Scheme 1.5 Reaction mechanism of Lewis based catalyzed homo-polymerization of epoxy resins

Electron deficient Lewis acids such as boron trihalides can attack high electron density bearing oxygen atom in oxirane ring causing the rings to open to initiate the reaction. Several researchers studied the effect of halides on the kinetics of the reaction.<sup>100</sup> Complexing  $\text{BF}_3$  with amine is well reported since it yields good shelf life which is beyond the scope of this work. The generalized homo-polymerization scheme of Lewis acid catalyzed reaction is shown in scheme 1.6.



Scheme 1.6 Reaction mechanism of Lewis acid catalyzed homo-polymerization of epoxy resin

Second way to form a crosslinked network is using a co-cure agent to form covalent bonds across the monomers. Terminal epoxide groups and secondary hydroxyl groups spaced along the polymer chains are the potential sites for epoxy resin curing. Three dimensional infusible structure is formed when epoxy resin is reacted with a curing agent. Epoxide resin can react with monomers with containing active hydrogen. Certain monomers such as polyesters and acrylics are used as a modifying agents whereas amine, amides, polysulphides, anhydrides, isocyanates<sup>101,102</sup>, cyanate esters, phenolics, amino resins are used as crosslinking agents. In this work, we intended to study the effect of epoxy structure in fire properties. Hence to minimize the variation in curing agent, only amine-based monomers were selected as crosslinkers. A typical epoxy amine curing reaction is show in Scheme 1.7.<sup>19,20,102</sup>



Scheme 1.7 Reaction mechanism of Epoxy resin crosslinked with primary and secondary amine.



Both catalyst aided homo-polymerization and co-cure crosslinking reactions involves addition polymerization: there is no loss of small molecules like water, CO<sub>2</sub> thus leading epoxy systems with low shrinkage during curing.<sup>97</sup>

A versatile molecular structure can be achieved via choice of monomer, their stoichiometry and curing schedule which will affect the characteristics of the crosslinked network. Usually the stoichiometry is calculated based on the reaction between active hydrogen in amine group (2 hydrogens in primary and 1 hydrogen in secondary amines) with an epoxy group. Not to mention, certain reactions are carried out with lesser amount of amines to enhance the shelf life and shower the reactivity along with achieving desired properties.<sup>92</sup> For these reasons, epoxy networks are extremely versatile thermosets.

The ratio of resin to hardener has a strong effect on the structure of the cured systems and its physical characteristics. The extent of cross-linking is a measure of the degree of cure. The most important properties are obtained at maximum crosslinking.<sup>92</sup> Along with stoichiometry, the curing temperature largely influences the crosslink density achieved. Heating increases the molecular mobility resulting in higher crosslink density along with condensation reactions happening with the hydroxyl groups present in the backbone of the polymer. In the context of the work in this chapter, only epoxy- amine networks crosslinked in stoichiometric quantities will be discussed. The curing temperature was chosen according to the suppliers recommendation along with examining the crosslinked networks for free epoxide groups in FTIR.

Epoxy resins are well known for its high chemical resistance, mechanical and thermal properties. The degree of crosslinking affects the properties. Heat resistance of epoxy networks are directly related to the chemical structure, molecular weight between

crosslinks, stoichiometry and degree of crosslinking. The crosslinked nature enhances the resistance to softening at elevated temperatures. The crosslinked nature enhances the resistance to softening and deformation at elevated temperatures.

## CHAPTER II – PEG MODIFIED THIOL-ENE NETWORKS FOR ADVANCED CONTROL OF CO<sub>2</sub> GAS SEPARATION FROM OTHER LIGHT GASES

### Abstract

Polyethylene glycol (PEG) based membranes have been studied and employed for separation of CO<sub>2</sub> from the light gases such as N<sub>2</sub>, O<sub>2</sub>, CH<sub>4</sub>, H<sub>2</sub> etc. In addition to its high critical temperature, CO<sub>2</sub> can weakly interact with polar PEG moieties and these two factors result in far greater solubility and permeability of this ‘acidic’ gas as compared to other light gases. Previously we demonstrated the use of UV-curable thiol-ene click chemistry to prepare highly gas permeable, elastomeric network membranes which, however, contained rather large loadings of PEG varying from 38 wt% to 67 wt%. Interestingly, CO<sub>2</sub> gas solubility/selectivity of these membranes were comparable regardless of the PEG content used. So, we hypothesized that CO<sub>2</sub>-philic effect of these membranes leveled off at high PEG content.

In this study, we aimed to determine the minimum amount of PEG which has to be incorporated to achieve the maximum CO<sub>2</sub> gas solubility/selectivity effect. Four types of networks were designed such that two of the network series contained PEG units along the backbone, while the PEG moieties were placed as dangling chain for other two network series. In order to fabricate networks containing PEG in the backbone, the ene monomer was crosslinked with a PEG containing dithiol whose concentration was gradually increased replacing the non-PEG based thiol while maintaining 1:1 thiol-ene stoichiometry. Networks containing PEG in the dangling chains were fabricated via twostep process. In the first step, PEG containing thiol monomer was synthesized by addition of monofunctional PEG acrylate to a multifunctional thiol monomer via thio-

Michael addition reaction. A 1:1 stoichiometry of acrylate to thiol monomers enabled single thiol site to be modified allowing the other thiol functional groups to take part in the network formation reaction with ene monomer. These designs enabled to explore the concentration of PEG from 0 to 25 wt% of PEG with networks with varying architectures. All these crosslinked networks were fabricated via UV initiated photo polymerization of thiol and ene monomers.

All the four types of network designs exhibited different network properties arising from the structural difference. All these networks differed in properties such as glass transition temperature, and free-volume. One of the network containing PEG in the backbone showed a crystallization tendency while other networks were amorphous in nature. Despite of these differences in network characteristics, gas permeation measurements demonstrated that CO<sub>2</sub> gas solubility/selectivity increased with PEG weight content reaching the maximum effect at about 10 wt%. Increasing PEG content in beyond 10 wt%, however, produced no further changes in CO<sub>2</sub> gas solubility/selectivity in accord with our hypothesis. Eventhough there were differences in gas transport values, the CO<sub>2</sub>/light gas selectivity followed a master trend for all the networks explored in this study.

## **2.1 Background**

The weak acid-base interaction between polar ether groups and the acidic CO<sub>2</sub> gas has been utilized to enhance the permeability selectivity via tuning the solubility selectivity. Unfortunately, the flexibility and polar groups in PEO allow it to pack efficiently which leads to chain crystallization. Any crystalline region is effectively inaccessible volume for the permeating gas. As mentioned previously, the economic

viability of a membrane can be quantified using a selectivity plot where the membrane should possess high permeability along with high selectivity. Since pure PEO materials are crystalline, despite of having high selectivity for CO<sub>2</sub> gas, the permeability is lower making it unsuitable for separation processes by itself.

Thus, several polymer structural design strategies have been investigated including the use of low molecular weight poly(ethylene glycol), blending,<sup>46,103–109</sup> copolymerizing<sup>110–122</sup> and crosslinking<sup>46,49,55,123–129</sup> to suppress crystallization.

In the cross-linking strategy, typically a mixture of difunctional and monofunctional PEG acrylates are UV cured together. However, it has been shown that thiol-ene networks are superior due to low oxygen inhibition during polymerization, low shrinkage upon curing, and network homogeneity. These properties can be taken advantage of to produce amorphous PEG based UV curable thiol-ene elastomeric network membranes. In this method, PEG based dienes, were cross-linked with trifunctional thiols. To decrease the cross-link density of the membranes, the ratio of trifunctional thiol to PEG based bifunctional thiol was decreased, while maintaining 1:1 thiol: ene stoichiometry. This also led to simultaneous increases in PEG content. The cross-link junctions in PEG based membranes restrict the mobility of the chains, thereby preventing the crystallization of PEG. In the absence of crystallinity, these cross-linked PEG networks are elastomeric in nature because of the highly flexible nature of PEG moieties. Typically, decreasing the cross-link density is the strategy used to increase gas permeability of these PEG based network membranes. It is well known that, for elastomers, as cross-link density is decreased, free volume increases, which then results in gas diffusivity increase and thereby gas permeability increase. Considering that

changes in cross-link density also lead to simultaneous changes in PEG content within the membranes, it was possible to study the gas transport parameters as a function of PEG content. The thiol-ene membrane control which contained no PEG moieties had much lower CO<sub>2</sub> solubility (and selectivity) value in comparison to the PEG based thiol-ene membranes, but to our surprise changing PEG content between 38 wt% and 67 wt% had no effect on CO<sub>2</sub> solubility, and therefore we hypothesized that the solubility of CO<sub>2</sub> levels off at some value below 38%.

Thus the goal of this work was to identify minimum amount of PEG required to achieve the maximum value of CO<sub>2</sub> solubility. Obviously, the amount of PEG required for maximizing CO<sub>2</sub> solubility would also depend on the CO<sub>2</sub> pressure (or partial pressure) in the feed. Once the minimum PEG required for maximum CO<sub>2</sub> solubility (and selectivity) is identified, the future research can focus on developing hybrid membranes, where a portion of the membrane will be the necessary PEG content required to impart the CO<sub>2</sub> selectivity feature to the membranes, and the remaining portion of the membranes can be made of moieties which can produce highly permeable membranes.

## **2.2 Experimental**

### **2.2.1 Materials**

Aliphatic, 1,9-decadiene (DDE) was obtained from TCI America. Trifunctional thiol cross-linker, trimethylolpropanetri (3-mercaptopropionate) (3T) was provided by Bruno Bock. PEG containing dithiol, 2,2'-(Ethylenedioxy) diethanethiol (EDDT) and photo-initiator, 2,2-Dimethoxy-2-phenylacetophenone were obtained from sigma Aldrich. The structures of all chemicals are shown in Figure 1. The gases used in this study, CO<sub>2</sub>, H<sub>2</sub>, CH<sub>4</sub>, O<sub>2</sub> and N<sub>2</sub>, were obtained from Airgas. The purity of all gases was

higher than 97.5%. The monomers, gases and the photo-initiator were used as received without any further purification.

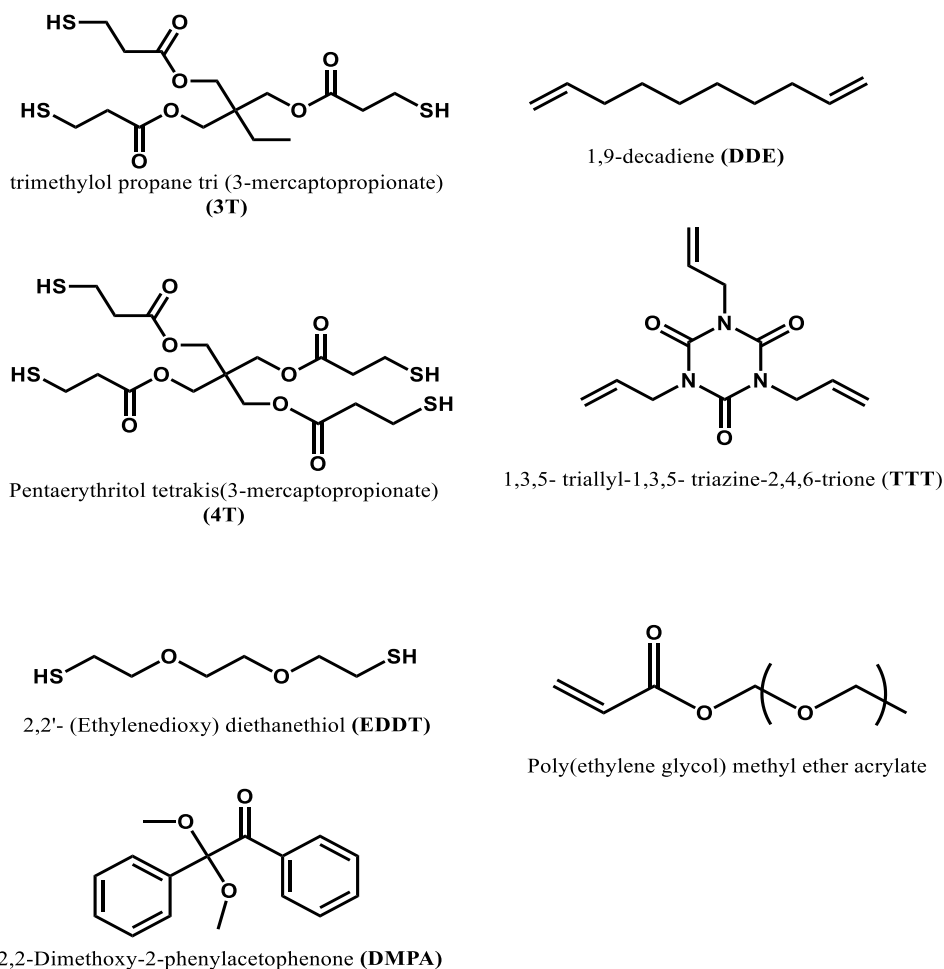
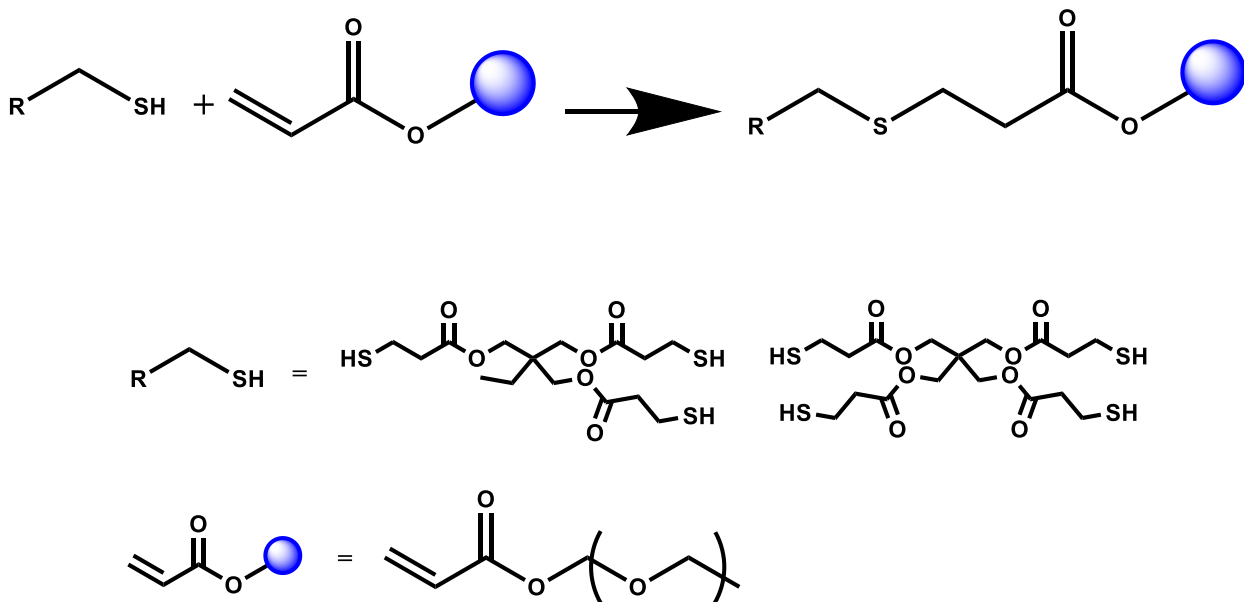


Figure 2.1 Dependence of solubility on critical temperature. Shown here is the solubility values for UV-curable thiol-ene flouro-polymeric networks

### 2.2.2 Synthesis of PEG modified thiol monomers

Tri and di functional thiol monomers with ethylene glycol (PEG) moiety dangling chain end were synthesized subsequently from 4T and 3T thiol monomers via thio-Micheal addition reaction in presence of a nucleophilic catalyst as in Scheme 2.1.



Scheme 2.1 Thio-Michael addition reaction used to attach PEG containing monofunctional acrylate.

Required quantities of tetrafunctional and trifunctional thiol monomers were placed in a flask. Approximately 1 wt% of dibutyl amine (nucleophilic catalyst) was added into the flask and mixed thoroughly with a magnetic stirrer. Calculated quantities of the monofunctional PEG containing acrylate was then added to the flask at 0.1 mL/min and the reaction mixture was allowed to stir overnight to ensure complete conversion of the acrylates. Solvents such as acetone was added in excess to ensure sufficient mixing of the monomers which was then removed under high vacuum after the course of the reaction. Monofunctional acrylate quantities were calculated such that only one of the thiol monomer functionalities was modified while leaving the other functionalities available for further crosslinking with alkene.

Formation of modified monomer was confirmed using  $^1\text{H}$  NMR technique through the disappearance of acrylate peaks at 6 ppm. 0.1 ml of the synthesized monomer



was dissolved in chloroform-d and exposed to a Varian Mercury 300 MHz. Shown below is the NMR spectrum for the unmodified and modified monomer, where the disappearance of acrylate peaks (at 6ppm) confirms the completion of the monomer synthesis. In addition to one functional modified thiol monomer, the existence of di, tri and tetra modified thiol monomer is equally probable. Statistical distribution was quantified through MALDI-TOF and the concentration of mono-modified thiol monomer is high about 84% through some scouting work done earlier in our group (results not shown here). Thus, we assume that the majority of the modified monomer contains mono-modified thiol monomer.

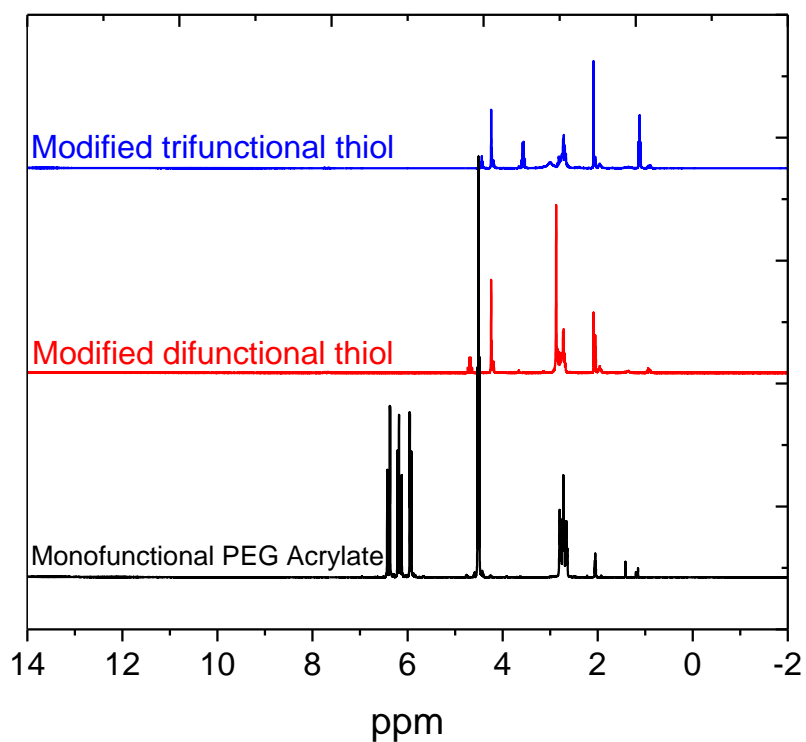


Figure 2.2  $^1\text{H}$  NMR spectra of unmodified (bottom) and modified (red and blue) thiol monomer

### 2.2.3 Membrane fabrication and network formation

Rational for the design: To the best of our knowledge, most literature focuses strategies on preventing crystallization while incorporating maximum PEG units. Earlier work in our group, Kweisnek et al.,<sup>130</sup> (BPEG-TEGDVE in Figure 4) studied the effect of increasing PEG units in the backbone along with decreasing the crosslink density. In the work, PEG content within the membranes was varied between 38 wt% to 67 wt%, and the solubility of CO<sub>2</sub> gas leveled off at that low concentration. We hypothesized that the solubility of the membranes levels off at some values below 38 wt% and thus the goal of this work was to identify the minimum amount of PEG required for achieving maximum CO<sub>2</sub> solubility. We intended to study if that minimum concentration is altered if the PEG is present in the backbone versus dangling chain end, with and without altering the crosslink density and with increasing chain rigidity of the networks.

Four design strategies were utilized, where in the first design followed a similar strategy as reported in Kweisnek work, but instead of a PEG based diene an aliphatic diene was used. This allowed to explore the amount of PEG to be varied from 0 to 25 wt% along with changing the crosslink density. The second strategy was to explore the lower PEG content with more rigid networks without changing the crosslink density. This was achieved using a trifunctional ene and a PEG containing dithiol as crosslinker. In third and fourth design the effect of PEG when present as dangling chain end was explored. Thiol monomers were modified with PEG units, as described earlier, and this was used as crosslinker. For more rubbery networks containing PEG as dangling chain, a difunctional ene was utilized, whereas for a rigid network, a trifunctional ene was utilized.

The naming scheme was adopted such that each network can be identified with the monomers used along with the placement of PEG either in backbone or as dangling chain. The prefix B or D in the naming scheme represents the location of PEG units if present in backbone or as dangling chain respectively. This is followed by the thiol crosslinker used which has the downward arrow indicating that this monomer is partially replaced by a PEG containing thiol crosslinker indicated in the successive with an upward arrow. The type of ene used in the networks follows the forward slash after the PEG containing thiol crosslinker. The suffix numbers indicate the amount of PEG weight percentage used in that particular type of network. For instance, B-3T↓EDDT↑/DDE-15 indicates a network fabricated using DDE monomer crosslinked with 3T thiol crosslinker partially replaced with PEG containing thiol, EDDT such that the PEG content of 15 wt% is present in the backbone. The calculated weight percentage exhibited linear relationship with molar content of PEG as shown in the Figure 2.3. To mention, all DDE containing networks are more rubbery compared to the TTT containing rigid networks (still in rubbery regime). Within the series of designs, the effect of varying the junction points is also explored. For instance, B-3T↓EDDT↑/DDE systems which has PEG in the backbone explores the effect of crosslink density whereas systems with B-HDT↓EDDT↑/TTT, the crosslink density remains constant within the series of networks. The monomers used for all the designs are shown in Figure 2.4 along with network naming schemes. The quantity of thiol crosslinker (with upward arrow in the figure 4) was altered such that the PEG concentration increased without alerting thiol-ene 1:1 stoichiometry.

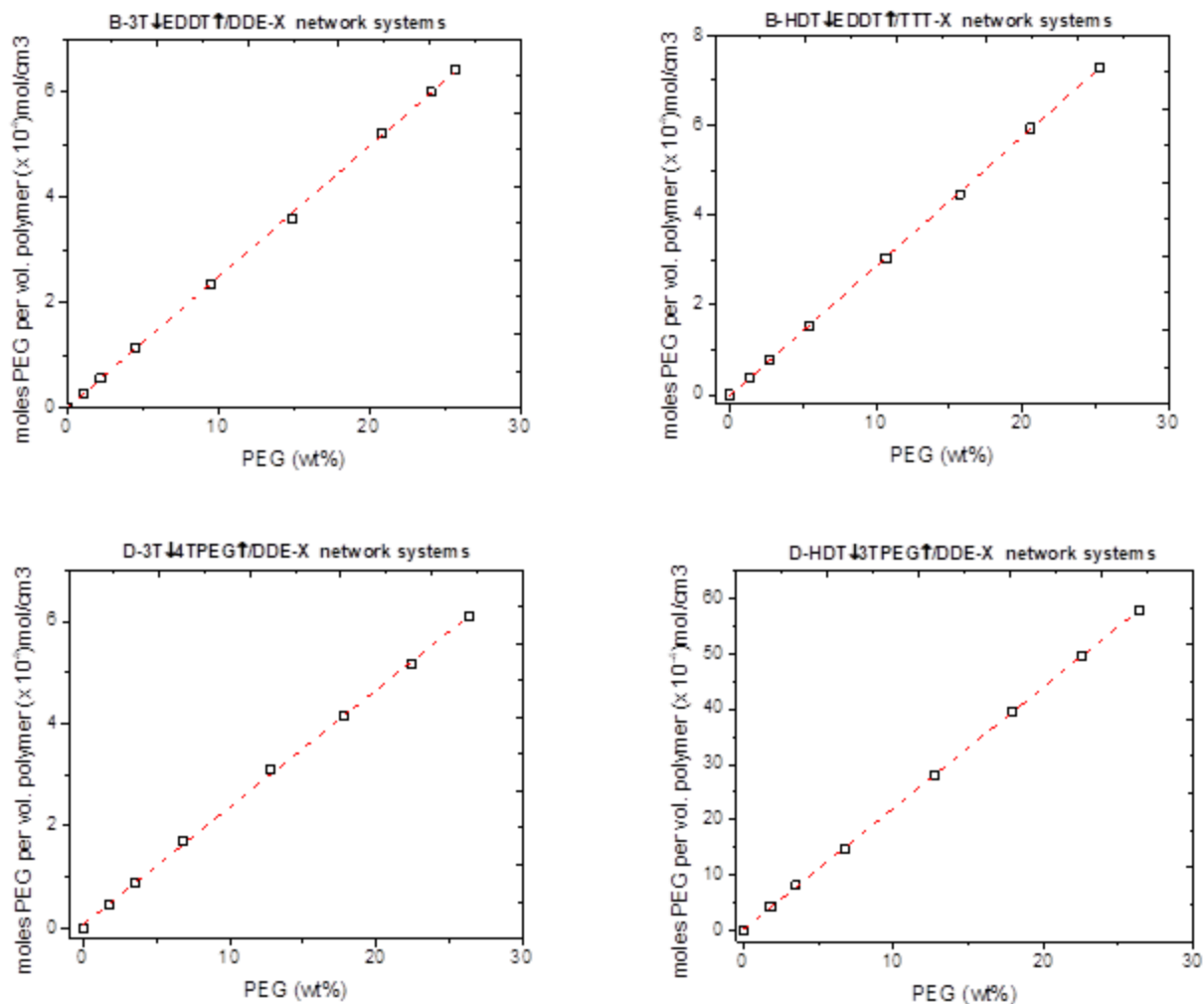


Figure 2.3 Linear dependence on PEG weight % and PEG molar content

All membranes were prepared in a similar fashion demonstrated by Kweisnek et al.<sup>131</sup> where thiol and ene monomers were added in stoichiometric quantities along with 1 wt% DMPA photo-initiator in a vial relative to the total amount of thiol and ene, which was mixed in vortexer followed by sonication (using a general purpose, cleaning type sonicator) for about 10 minutes to ensure that photo-initiator was dissolved and to remove any air bubbles trapped in the mixture. This homogeneous, bubble free mixture

was poured onto a glass plate. Another glass plate was then placed on top of the mixture. Spacers were placed between the glass plates to control the thickness of the membranes to be around 0.5 mm. The films were polymerized by exposure to 365 nm UV light (UVA400 UV, Cure-Tek curing systems with intensity 76 mW/cm<sup>2</sup>) for 1 minute, followed by flipping of glass plates and curing for additional 3 minutes to ensure that monomer conversion reaches near 100%. The curing reaction was very rapid such that the liquid mixture of monomers typically turned into a solid polymeric network within 1 minute of UV exposure. Glass plates were coated with a hydrophobic surfactant (Rain-X) to allow for easy removal of cured polymer after UV exposure. All prepared membranes were saturated at room temperature and humidity for at least 12 hours before performing any test.

Table 2.1 Critical temperature and kinetic diameter of various gases of interest

Sample Identity	Formulation (wt%)			PEG content (wt%)	PEG content (mol/cc)x 10 <sup>-4</sup>	Theoretical Mc (g/mol)
	TEGDVE	3T	EDDT			
B-3T↓EDDT↑/TEGDVE-38	43.23	56.77	0.00	38	103.0	467
B-3T↓EDDT↑/TEGDVE-39	43.61	54.42	1.97	39	n/d	488
B-3T↓EDDT↑/TEGDVE -40	44.01	52.02	3.97	40	n/d	511
B-3T↓EDDT↑/TEGDVE -43	44.82	47.10	8.08	43	117.5	564
B-3T↓EDDT↑/TEGDVE -49	46.54	36.68	16.78	49	131.4	724
B-3T↓EDDT↑/TEGDVE 55	48.40	25.43	26.17	55	144.1	1040
B-3T↓EDDT↑/TEGDVE 62	50.41	13.24	36.34	62	163.7	2010
B-3T↓EDDT↑/TEGDVE 63	50.94	10.04	39.02	63	167.9	2650
B-3T↓EDDT↑/TEGDVE 65	51.48	6.76	41.75	65	172.0	3930
B-3T↓EDDT↑/TEGDVE 66	51.76	5.10	43.14	66	174.5	5210
B-3T↓EDDT↑/TEGDVE 67	52.04	3.42	44.55	67	176.2	7770

Table 2.2 Formulation details for set B-3T↓EDDT↑/DDE-X

Sample Identity	Formulation (wt%)			PEG content (wt%)	PEG content (mol/cc)x 10 <sup>-4</sup>	Theoretical Mc (g/mol)
	1,9-DDE	3T	EDDT			
B-3T↓EDDT↑/DDE -0	34.2	65.8	0.0	0.0	0.0	404.0
B-3T↓EDDT↑/DDE -1	34.6	63.1	2.3	1.1	2.8	426.6
B-3T↓EDDT↑/DDE -2	34.9	60.4	4.6	2.2	5.6	451.2
B-3T↓EDDT↑/DDE -5	35.7	54.9	9.4	4.5	11.4	484.0
B-3T↓EDDT↑/DDE -10	37.3	43.0	19.7	9.5	23.5	617.7
B-3T↓EDDT↑/DDE -15	39.1	30.0	30.9	14.9	35.8	884.8
B-3T↓EDDT↑/DDE -21	41.0	15.8	43.2	20.9	52.2	1686.9
B-3T↓EDDT↑/DDE -24	42.0	8.1	49.9	24.1	60.0	3288.9
B-3T↓EDDT↑/DDE -26	42.6	4.1	53.3	25.7	64.1	6494.4
B-3T↓EDDT↑/DDE -28	43.1	0.0	56.9	27.5	68.4	Linear

Table 2.3 Formulation details for set B-HDT↓EDDT↑/TTT- X

Sample Identity	Formulation (wt%)			PEG content (wt%)	PEG content (mol/cc)x 10 <sup>-4</sup>	Theoretical Mc (g/mol)
	TTT	HDT	EDDT			
B-HDT↓EDDT↑/TTT -0	52.5	47.5	0.0	0.0	0.0	316.0
B-HDT↓EDDT↑/TTT -1	52.2	44.9	2.9	1.3	3.8	318.3
B-HDT↓EDDT↑/TTT -3	52.0	42.3	5.7	2.7	7.7	320.6
B-HDT↓EDDT↑/TTT -5	51.5	37.2	11.3	5.4	15.2	322.9
B-HDT↓EDDT↑/TTT -11	50.5	27.4	22.1	10.6	30.3	329.3
B-HDT↓EDDT↑/TTT -16	49.5	17.9	32.6	15.7	44.6	335.7
B-HDT↓EDDT↑/TTT -21	48.6	8.8	42.6	20.6	59.3	342.1
B-HDT↓EDDT↑/TTT -25	47.7	0.0	52.3	25.3	72.9	348.5

Table 2.4 Formulation details for set D-3T↓4TPEG↑/DDE-X

Sample Identity	Formulation (wt%)			PEG content (wt%)	PEG content (mol/cc)x 10-4	Theoretical Mc (g/mol)
	1,9-DDE	3T	4T-PEG			
D-3T↓4TPEG↑/DDE -0	34.2	65.8	0.0	0.0	0.0	404.0
D-3T↓4TPEG↑/DDE -2	33.6	61.3	5.2	1.8	4.5	404.0
D-3T↓4TPEG↑/DDE -4	32.9	57.0	10.1	3.5	8.9	404.0
D-3T↓4TPEG↑/DDE -7	31.7	48.8	19.5	6.8	17.1	404.0
D-3T↓4TPEG↑/DDE -13	29.6	34.1	36.3	12.7	31.1	404.0
D-3T↓4TPEG↑/DDE -18	27.7	21.3	51.0	17.9	41.6	404.0
D-3T↓4TPEG↑/DDE -22	26.0	10.0	64.0	22.4	51.7	404.0
D-3T↓4TPEG↑/DDE -26	24.6	0.0	75.4	26.4	60.9	404.0

Table 2.5 Formulation details for set D-3T↓4TPEG↑/DDE-X

Sample Identity	Formulation (wt%)			PEG content (wt%)	PEG content (mol/cc)x 10-4	Theoretical Mc (g/mol)
	TTT	HDT	3T-PEG			
D-HDT↓3TPEG↑/TTT -0	52.51	47.49	0.00	0.0	0.0	316.0
D-HDT↓3TPEG↑/TTT -2	48.50	41.67	9.83	1.8	4.3	342.0
D-HDT↓3TPEG↑/TTT -4	45.06	36.68	18.27	3.5	8.2	368.0
D-HDT↓3TPEG↑/TTT -7	39.46	28.55	31.99	6.8	16.1	421.1
D-HDT↓3TPEG↑/TTT -13	31.60	17.15	51.25	12.7	30.1	525.8
D-HDT↓3TPEG↑/TTT -18	26.36	9.54	64.11	17.9	37.6	630.5
D-HDT↓3TPEG↑/TTT -22	22.60	4.09	73.31	22.4	54.7	735.1
D-HDT↓3TPEG↑/TTT -26	19.79	0.00	80.21	26.4	57.9	839.8

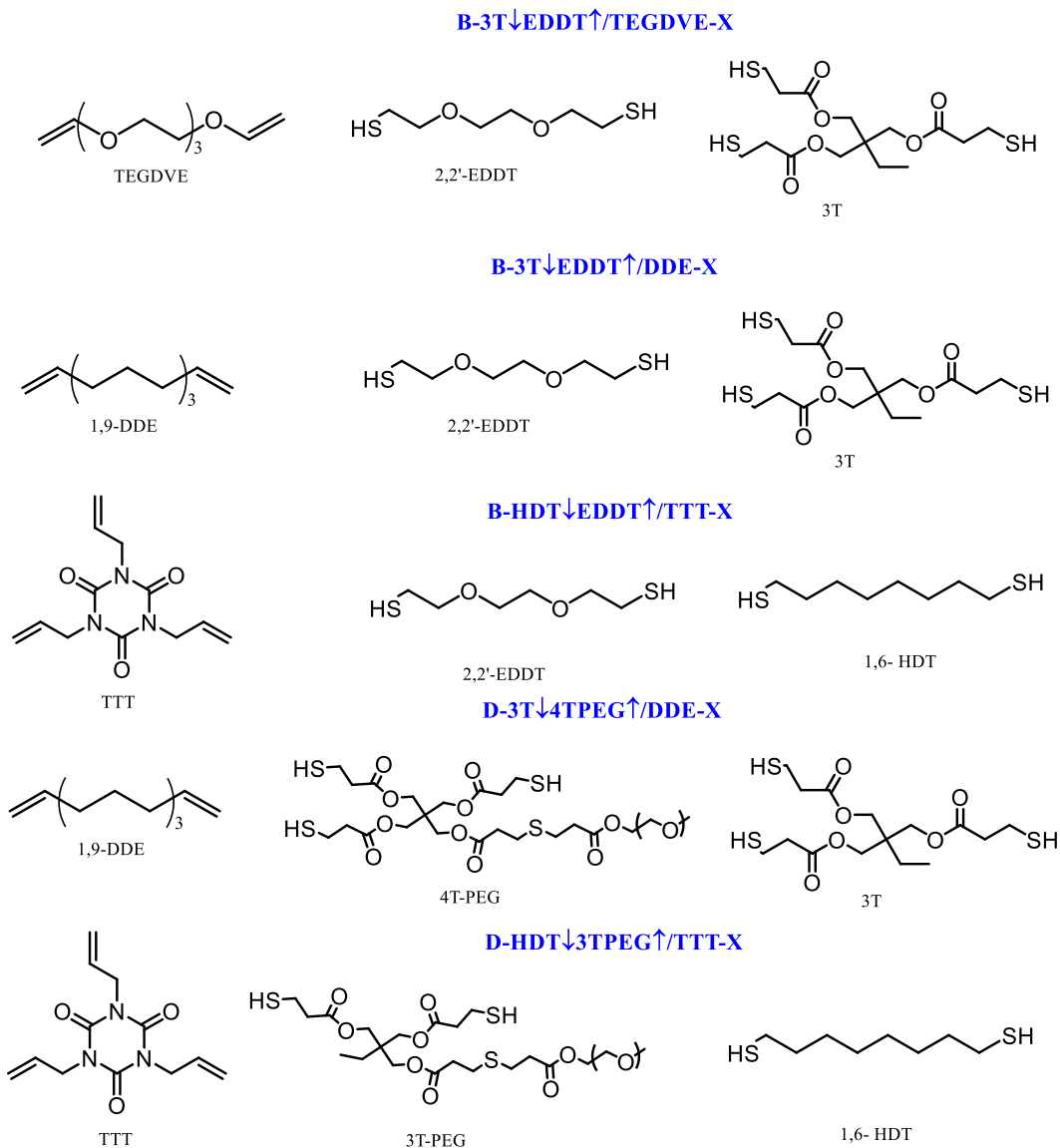


Figure 2.4 Corresponding network monomers and naming scheme used in chapter 2

### 2.2.4 Characterization

The cure kinetics were measured by monitoring thiol and ene functional group conversions using a Thermo Fisher Scientific Nicolet 8700 real-time FTIR spectrometer modified with a custom-made setup of a fiber-optic cable, with light intensity of 20 mW/cm<sup>2</sup> at 365 nm irradiance. A drop containing stoichiometric quantities of monomers along with photo-initiator was sandwiched between KBr salt plates and was subjected to



FTIR analysis. Baseline spectra with neat KBr plates were taken prior to sample runs to minimize the error through salt plate contamination if any. The change in area under the peak as a function of irradiation time was used to monitor the disappearance of thiol (-SH) groups (peak at 2570 cm<sup>-1</sup>) and ene (C=C) groups (peak at 3080 cm<sup>-1</sup>).

The density of the crosslinked polymer samples was measured by hydrostatic weighing using a Mettler Toledo Balance (Model XS-104) equipped with density kit which uses Archimedes principle. The film density was calculated automatically by the balance through the following equation.

$$\rho_P = \frac{W_A}{W_A - W_L} \cdot \rho_0$$

Where,  $W_A$  is the polymer weight in air,  $W_L$  is the samples weight in the auxiliary liquid, and  $\rho_0$  is the density of the auxiliary liquid. Deionized water was used as the auxiliary liquid with  $\rho_0$  of 0.997 g/mL.

Determination of average thickness of the membrane to was crucial to calculate reliable values of permeability (P) and diffusivity (D). Earlier work in our group, Sekelik et al.,<sup>132</sup> modeled the diffusion flux of a membrane by varying the periodic thickness of the membrane. The results reveal that the effect of thickness variation on diffusion flux become perceptible when the thickness variation is 30% and higher. Thus, thickness of the membrane becomes the key parameter in dictating the accuracy of P and D calculation. Since the network in our study is rubbery, using a caliper would be inappropriate which would lead to greater error and special care was taken to measure the average bulk thickness as described below. The bulk thickness ( $l$ ) of the membrane was measured by estimating the density of the membrane with specific surface area. Circular

disks of about 5.0715 cm<sup>2</sup> were carefully cut from the crosslinked polymer and weighed using a balance with accuracy of three decimal points. Bulk thickness was estimated through the simple relationship shown below.

$$\rho_P = \frac{W}{V}$$
$$V = A \cdot l$$
$$l = \frac{W}{\rho_P \cdot A}$$

Where,  $\rho_P$  is the measured density of the polymer, W is the mass of sample of known area, V is the volume which can be expressed as product of area (A) times thickness(l). This method was chosen to eliminate the manual error caused while using a caliper.

Thermal transitions were determined using a TA instruments Q200 differential scanning calorimeter (DSC). About 5 to 8mg of the crosslinked polymer was subjected to DSC analysis. Thermal history was erased by heating the sample up to 90°C at a rate of 10°C/min followed by quenching to -80°C at a rate of 5°C/min. The samples were then heated from -80°C to 90°C at the rate of 5°C/min and second heating scans were used to calculate the glass transition temperature of all the samples.

Dynamic mechanical thermal analysis (DMTA) was performed using Rheometric scientific DMTA V instrument equipped with a film fixture for tensile mode testing and a gas cooling accessory. Rectangular segments of 100 mm x 2 mm in dimensions were carefully cut and subjected to DMTA analysis. Temperature was lowered to -80°C and isothermally held for a period of 5 min before the temperature was increased to 90°C at a ramp rate of 5°C / min. Test was performed in a controlled strain (0.01%) with a

frequency of 1.0 Hz. Storage ( $E'$ ) and loss ( $E''$ ) moduli and loss factor,  $\tan \delta (=E''/E')$ , were recorded as a function of temperature. The glass transition temperature ( $T_g$ ) was determined as the peak maximum of  $\tan \delta$  versus temperature curve.

X-Ray Scattering analysis was performed using Xeuss 2.0 system (Xenocs, France) ( $\lambda = 0.152$  nm). The instrument uses a Pilatus 100K detector to detect the transmitted scattered radiation. The scattering experiments were conducted in room temperature, under vacuum, and the sample to detector distance was 158 mm, which was obtained by analyzing a Silver behenate calibration sample. X-Ray exposure time was 120 seconds for each sample.

Permeability of several pure gas through membranes were determined using a custom-built constant volume variable pressure (CVVP) apparatus described elsewhere<sup>127</sup> and a detailed description of the facility used in this study is available in chapter 7 of this thesis. The permeation cell is a stainless-steel filter holder from Millipore Corporation with an area of 13.8 cm<sup>2</sup>. The polymer membranes were cut out in circular shape of about an area of 15 cm<sup>2</sup> and the O-ring in the permeation cell was in direct contact with the polymer films to make sure the testing gas passes only through the membrane. After the membranes were mounted in the permeation cell, both upstream and downstream volumes were evacuated to vacuum using a vacuum pump overnight to degas the film. Permeation experiments were carryout out at an upstream pressure of around 3.47 atm and the temperature of the permeation cell was maintained at 23°C using a recirculating water as a chiller. The permeation cell was equipped with a slot for thermocouple to monitor the temperature of the cell and this was considered to be the temperature of the membrane. Five different gases, (CO<sub>2</sub>, O<sub>2</sub>, CH<sub>4</sub>, N<sub>2</sub> and H<sub>2</sub>) were tested individually and

the purity of the gases were reported above 99.8%. The pure gas was purged and held at a constant pressure, and the increase in pressure in the known downstream volume was recorded as a function of time. The leak rate in the system was always measured before starting to record the downstream volume increase.

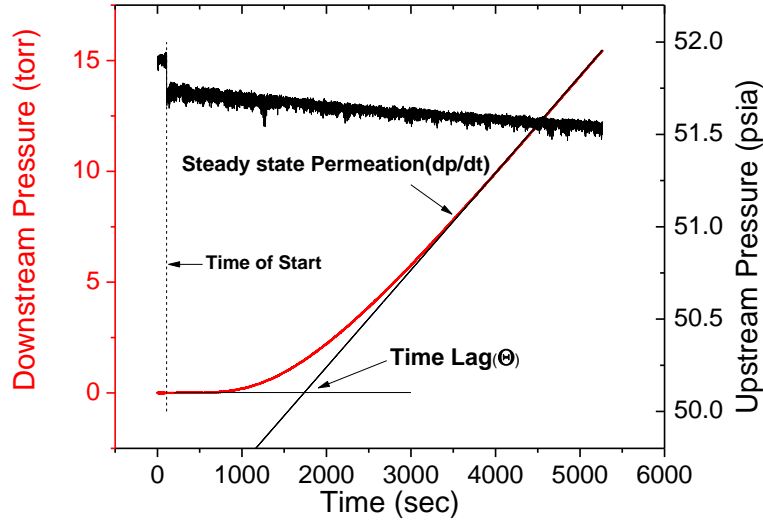


Figure 2.5 Representative plot of standard upstream and downstream pressure versus time collected during CVVP test

All membranes showed a typical Fickian behavior with well-defined steady state slopes as shown in Figure 4. Gas permeability was calculated from the steady state pressure increase in the fixed downstream volume as shown in the equation below.

$$P = \frac{V_D l}{p_2 A R T} \left[ \left( \frac{dp_1}{dt} \right)_{ss} - \left( \frac{dp_1}{dt} \right)_{leak} \right]$$

Where  $V_D$  is the known downstream volume,  $l$  is the film thickness,  $p_2$  is the upstream pressure,  $A$  is the area of gas exposure,  $R$  is the gas constant,  $T$  is the temperature of the membrane while testing.  $\left( \frac{dp_1}{dt} \right)_{ss}$  and  $\left( \frac{dp_1}{dt} \right)_{leak}$  are the steady state rates of pressure in the downstream volume at a fixed upstream pressure and in vacuum

respectively.  $\left(\frac{dp_1}{dt}\right)_{leak}$  was not more than 5 % than  $\left(\frac{dp_1}{dt}\right)_{ss}$  and was usually neglected in our calculations. The downstream pressure was measured in torr, which was very low compared to the upstream which was usually measured in atmospheres. (1 torr=  $1.3 \times 10^{-3}$  atm).

Diffusivity ( $D$ ) was calculated from time lag values,  $t_L$ , using the equation shown below.

$$D = \frac{l^2}{6t_L}$$

Since non-porous membranes follows solution-diffusion mechanism, solubility ( $S$ ) was calculated from the measured permeability ( $P$ ) and diffusivity ( $D$ ) values using the equation below.

$$S = \frac{P}{D}$$

Gas solubility was determined using a dual-volume apparatus based on the barometric pressure decay method. The description of the facility used in this work is detailed in chapter 7 in this thesis. The apparatus consists of two cell chambers of known volume isolated by a valve, a sample chamber containing polymer films and a charge chamber which is connected to the gas cylinder. Both cells along with polymer sample were degassed at least 12 hours prior to test. The whole setup was immersed in a water bath to maintain constant testing temperature.

The sample chamber is evacuated and then isolated from the charge chamber, which is subsequently charged with a target gas at known pressure. The valve between

the charge and sample chamber is opened briefly to introduce the gas to the sample chamber. The decrease in pressure in both chambers is monitored as a function of time after isolation of chambers. The difference between the initial pressure and the final pressure in the charge chamber can be used to calculate the number of moles of gas admitted into the sample chamber. As the polymer sample sorbs as, the pressure in the gas phase of the sample chamber decreases. When the pressure in the sample chamber reaches state, the polymer has sorbed all of the gas molecules that it can at that particular pressure. Through the equilibrium pressure in the sample chamber, the number of moles of gases in the gas phase can be calculated. The above protocol is followed to obtain the moles of sorbed gas at higher pressure.

Positron Annihilation Lifetime Spectroscopy (PALS) was used to quantify the average free volume hole size of the membranes. In this technique, a positron source, a Na<sup>22</sup> salt, is sandwiched between 2 polymer discs having dimensions, 1 cm diameter and 1 mm thickness. Positron gets thermalized with an electron from polymer to form positronium. A positronium species in which both electron and positron have spins in the same direction is called ortho-positronium (o-Ps). o-Ps localizes in the less electron dense regions i.e. free volume holes. o-Ps gets annihilated when it comes in contact with an electron from the wall of the free volume hole. Therefore, the lifetime of o-Ps will be proportional to the physical size of the free volume hole. Using the semi-empirical equation shown in eq. 1, the average radius of the free volume holes R can be obtained from the lifetime of o-Ps  $\tau_3$ .<sup>133</sup>

$$\tau_3 = 0.5 \left[ 1 - \frac{R}{R_0 + R} + \frac{1}{2\pi} \sin \left( \frac{2\pi R}{R_0 + R} \right) \right]^{-1} \text{ ns}$$

Where  $R_0 = 0.1656$  nm is the empirically derived electron layer thickness.

Assuming the free volume holes are spherical, the average volume of free volume holes was calculated as

$$\langle v_h \rangle = \frac{4}{3}\pi R^3$$

PALS measurements were carried out under vacuum over a temperature range of -40° C to 40° C with 5° C intervals. PALS spectrum was collected for 3600 seconds at each temperature to get at least 1 million incidences. Three temperature sweeps were performed to obtain average and standard deviation values of  $\langle v_h \rangle$  at each temperature. Each PALS spectrum was fit and deconvoluted to obtain o-Ps lifetime  $\tau_3$  values using PATFIT-88 software.<sup>134</sup>

An average of at least 3 runs was reported as final values for gas transport and free volume data. The error was calculated from the standard deviation for those parameters which was measured. For calculated parameters such as selectivity, standard propagation of error was calculated, where uncertainties of all relevant measured parameters propagate and contribute to the uncertainty of the parameters of interest.<sup>135</sup>

## **2.3 Results and discussion**

### **2.3.1 Fourier Transform Infrared Spectroscopy (FTIR)**

Real time FTIR was used to probe the conversion of thiol and ene monomers. Monomer conversions were calculated through the determination of the decrease of peak area of monomers upon time. Figure 2.6 shows the Real time FTIR spectrum of a representative network from which the thiol stretching at  $2570\text{ cm}^{-1}$  and ene stretching at  $3080\text{ cm}^{-1}$  was monitored over time after exposing to UV light. The differences in area

between the initial and the final peaks gave the extent of conversions of the monomer. The peak area decreased very rapidly upon UV light exposure for less than 3 min for all networks, which indicates the fast cure kinetics of thiol-ene networks.<sup>1</sup>

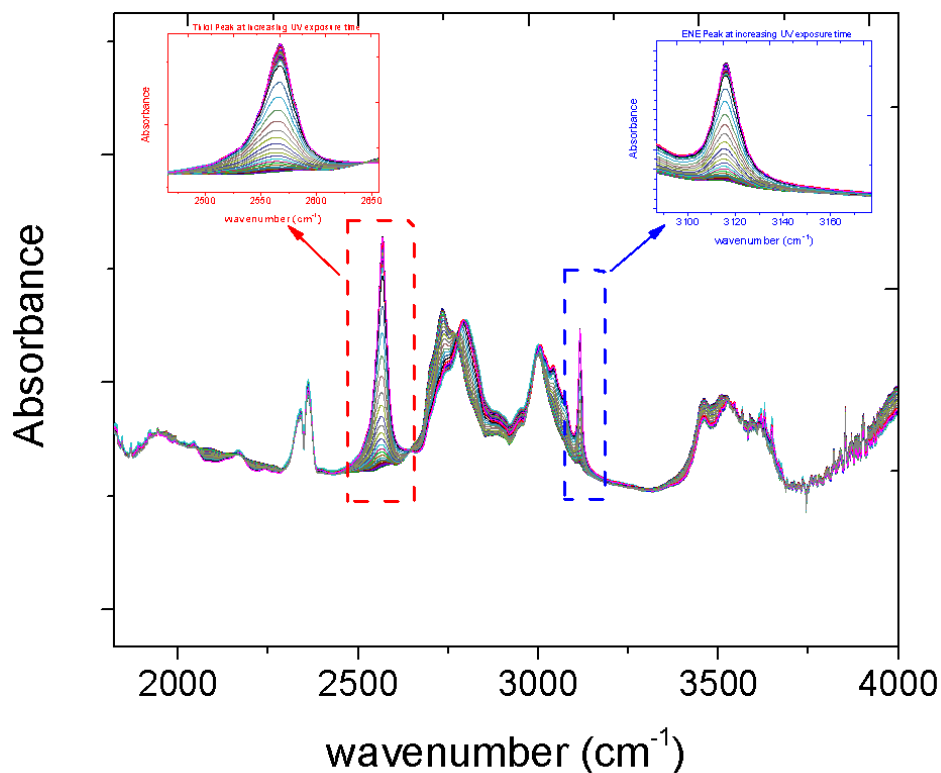


Figure 2.6 Representative Realtime FTIR plot to calculate the monomer conversion.

Figure 2.7 shows within few seconds at least 95% of thiol and ene functional groups reacted in all the formulations. Inset in the figures shows the decrease in peak area of monomers upon UV irradiation time which was used to calculate the percentage conversions. The conversion results indicated that the network membranes are formed within few seconds of UV exposure. Within DDE containing networks (B-3T↓EDDT↑/DDE and D-3T↓4TPEG↑/DDE), as the PEG containing thiol content



increased, the conversions were more rapid which is attributed to the increased chain mobility (decreased crosslink density). Systems containing tri-functional ene (B-HDT↓EDDT↑/TTT and D-HDT↓3TPEG↑/TTT) reached rapid conversions upto 90% and upon further exposure to UV light, the conversion gradually reached above 95% over time, but the difference is in minus scale. This is attributed to the chain vitrification caused by the aromaticity in the ene. Though network membranes containing higher bifunctional thiol monomers in B-3T↓EDDT↑/DDE systems (i.e. samples 20.9%, 24.1%, 25.75%) showed the presence of crystalline domains at room temperature, the presence/formation of crystalline domains did not seem to have any effect on network formation/functional group conversion.

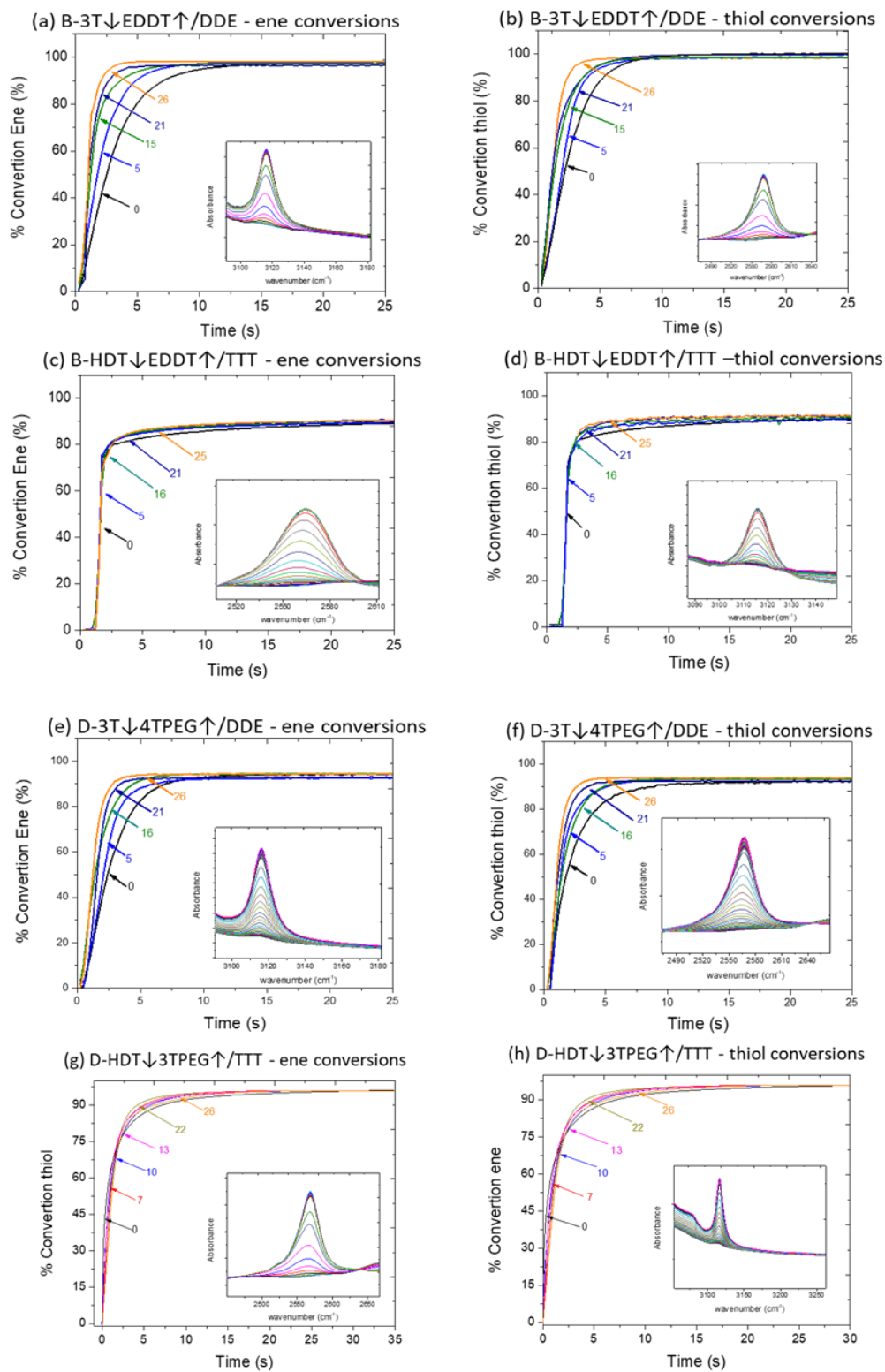


Figure 2.7 Real time FTIR of thiol and Ene monomers. Inset shows the decrease in peak area of monomers upon UV exposure.

### 2.3.2 Investigation of Thermal transitions

Figure 2.8 presents differential scanning calorimetry (DSC) thermograms (2<sup>nd</sup> scan) for various network designs (B-3T↓EDDT↑/DDE, B-HDT↓EDDT↑/TTT, D-3T↓4TPEG↑/DDE and D-HDT↓3TPEG↑/TTT). Glass transition temperatures ( $T_g$ ) reported in Table 2.6 represents the midpoint of the transitions in Figure 2.8. The first heating and the second heating scans were consistent reflecting a lack of thermal history effects on  $T_g$  for these rubbery polymers. Except for the network B-3T↓EDDT↑/DDE, all the other systems didn't show any crystalline transitions at room temperature (23 °C). Earlier in our groups, we were able to demonstrate that by using thiol-ene chemistry even at very low cross-linking density, stretchable (mechanically robust) and completely amorphous PEG based membranes can be prepared.<sup>3</sup> In general, a unit cell of PEO crystals in the unit cell contains 7 PEO repeating units which undergoes 2 turns (7/2 helix structure).<sup>4</sup> With the crosslinked thiol-ene systems in this study, regularly spaced bulky thioethers which behaves as defects, and along with the fast kinetics of this thiol-ene chemistry disrupts the packing of 7 consecutive ethylene oxide units as needed to form a crystal unit cell. Additionally, crosslinking may reduce conformational freedom of PEO chains to perfectly arrange into a unit cell thus suppressing the formation of PEO crystals. However, every compositions of B-3T↓EDDT↑/DDE systems showed crystallinity (Figure 8a), and the crystalline melting peaks were above testing temperature for those systems containing low crosslink densities. A brief discussion on the crystallinity of these networks is presented in section 4.1.4. All other systems (except for B-3T↓EDDT↑/DDE) did not crystallize in the temperature range between -90°C and 90°C.

Figure 2.8 (a) and Table 2.6 (a) shows that the B-3T↓EDDT↑/DDE network membranes had  $T_g$  lower than  $-37\text{ }^\circ\text{C}$ . With increasing concentration of bifunctional monomer (or PEG content), the glass transition temperatures of the membranes shifted to lower temperatures (Figure 2.8(a) and Table 2.6). As the PEG content increased, the degree of cross-linking of the membranes decreased (or  $M_C$  increased) in this system which coupled with the flexibility associated with the ether linkages, causing the lowering of  $T_g$ .

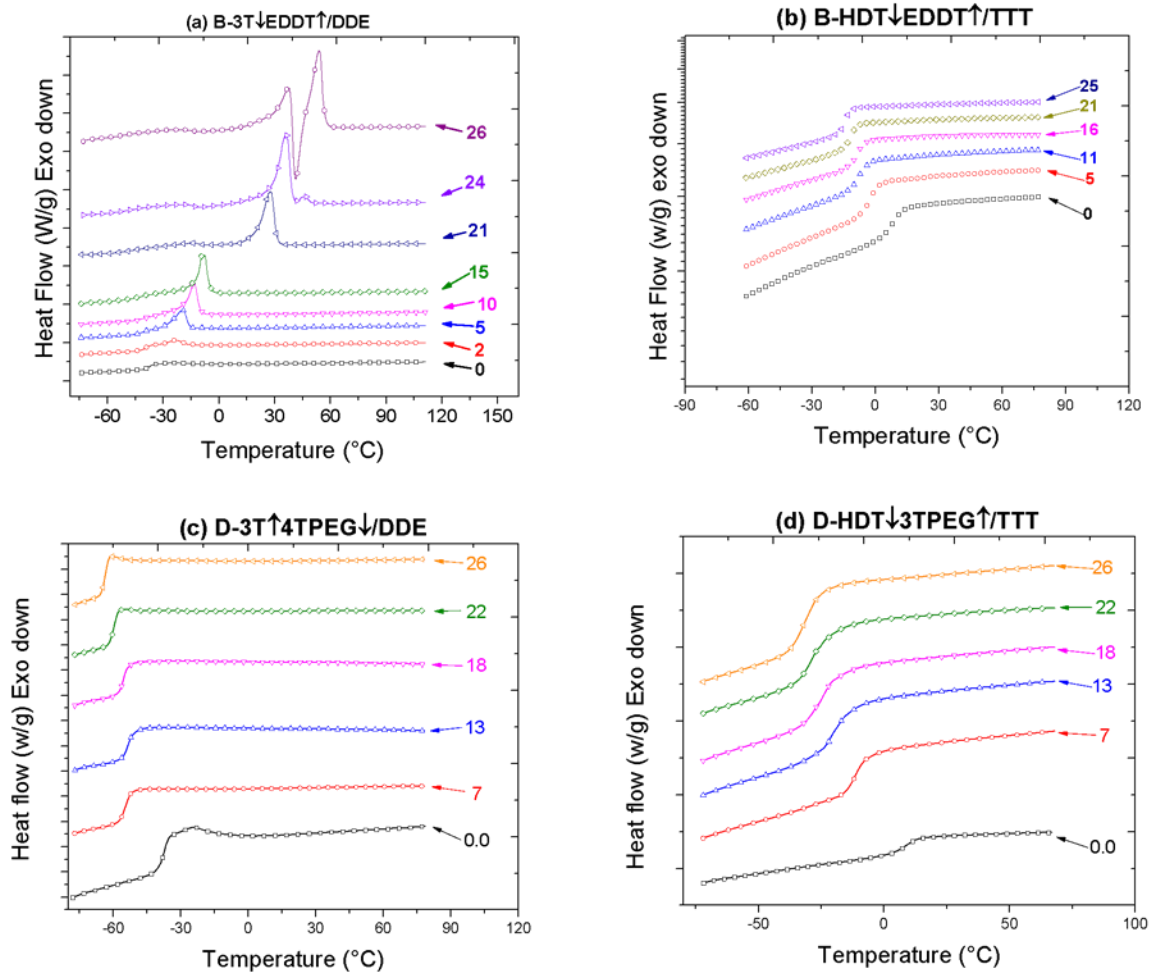


Figure 2.8 DSC thermograms of all networks(2nd heat). Curves are offset vertically for clarity.

Figure 2.8 (b) and Table 2.6(b) presents DSC thermograms of B-HDT↓EDDT↑/TTT systems, where the  $T_g$  values are higher than the B-3T↓EDDT↑/DDE (backbone PEG with difunctional ene), but still in the rubbery regimes. B-HDT↓EDDT↑/TTT were more rigid as compared to B-3T↓EDDT↑/DDE mainly due to the trifunctional ene present in the backbone. These networks show a decrease in  $T_g$  despite of having a similar crosslink density. This is associated with the incorporation of ether linkages which imparts the flexibility to the chains thus decreasing the  $T_g$  of these materials.

Figure 2.8 (c) and table 2.6 (c) represents the  $T_g$  of the most rubbery networks where PEG is present in the dangling chain. D-3T↓4TPEG↑/DDE networks contain difunctional ene and modified PEG containing thiol monomers which make it possible to locate the PEG as free dangling chain ends. Within this system, the crosslink density is maintained constant (as described in experimental) while the incorporation of dangling chain increases the network's chain spacing causing a reduction of  $T_g$ . as reported previously in our group.<sup>5</sup> The  $T_g$  values decreases from  $-37^\circ\text{C}$  to  $-53.5^\circ\text{C}$  with increasing dangling chain content despite of similar number of crosslink junction points.

Table 2.6 Glass Transition, melting temperature and enthalpy of fusion of the membranes obtained from second heat cycle of DSC analysis

(a) B-3T↓EDDT↑/DDE	
<i>Sample Identity</i>	$T_g$ (°C)
B-3T↓EDDT↑/DDE -0	-37.2
B-3T↓EDDT↑/DDE -1	n/d
B-3T↓EDDT↑/DDE -2	-39.1
B-3T↓EDDT↑/DDE -5	-40.4
B-3T↓EDDT↑/DDE -10	-41.7
B-3T↓EDDT↑/DDE -15	-43.2
B-3T↓EDDT↑/DDE -21	-45.5
B-3T↓EDDT↑/DDE -24	-52.4
B-3T↓EDDT↑/DDE -26	-53.1

(b) B-HDT↓EDDT↑/TTT	
<i>Sample Identity</i>	$T_g$ (°C)
B-HDT↓EDDT↑/TTT -0	9
B-HDT↓EDDT↑/TTT -1	n/d
B-HDT↓EDDT↑/TTT -3	n/d
B-HDT↓EDDT↑/TTT -5	-1
B-HDT↓EDDT↑/TTT -11	-7
B-HDT↓EDDT↑/TTT -16	-8
B-HDT↓EDDT↑/TTT -21	-12
B-HDT↓EDDT↑/TTT -25	-14

(c) D-3T↓4TPEG↑/DDE	
<i>Sample Identity</i>	$T_g$ (°C)
D-3T↓4TPEG↑/DDE -0	-37.2
D-3T↓4TPEG↑/DDE -2	-40.1
D-3T↓4TPEG↑/DDE -4	-44.3
D-3T↓4TPEG↑/DDE -7	-46.1
D-3T↓4TPEG↑/DDE -13	-50.3
D-3T↓4TPEG↑/DDE -18	-53.6
D-3T↓4TPEG↑/DDE -22	-54.1
D-3T↓4TPEG↑/DDE -26	-53.5

(d) D-HDT↓3TPEG↑/TTT	
<i>Sample Identity</i>	$T_g$ (°C)
D-HDT↓3TPEG↑/TTT -0	9
D-HDT↓3TPEG↑/TTT -2	n/d
D-HDT↓3TPEG↑/TTT -4	n/d
D-HDT↓3TPEG↑/TTT -7	-10.1
D-HDT↓3TPEG↑/TTT -13	-15.3
D-HDT↓3TPEG↑/TTT -18	-22.5
D-HDT↓3TPEG↑/TTT -22	-24.6
D-HDT↓3TPEG↑/TTT -26	-28.1

Figure 2.8(d) and Table 2.6(d) represents the thermograms for D-HDT↓3TPEG↑/TTT networks. The decrease in  $T_g$  is mainly attributed to two factors: the nature of difunctional thiol containing ester groups along the backbone, 3TPEG which partially replaced aliphatic dithiol, EDDT and secondly, the presence of PEG dangling chains which increased the chain packing. The synthesized PEG containing difunctional thiol has higher molecular chain length as compared to the aliphatic dithiol which

increases the molecular weight between crosslinks upon addition of PEG. This along with PEG as dangling chain, as mentioned earlier, increases the spacing between the chains leads to a greater decrease in  $T_g$  with addition of PEG containing dithiol.

### 2.3.3 Dynamic-mechanical thermal properties

DMA results provide complementary analysis to DSC results and allows evaluating the thermal and viscoelastic properties of the crosslinked networks. The crosslink density is normally determined by the storage modulus at the rubbery plateau: higher the level of this plateau relative to other curves, higher the number of crosslinks per unit volume. Thus, with increase in PEG containing dithiol the rubbery modulus decreases which indicates the reduction in crosslink density. The degree of homogeneity is usually quantified by the shape of the  $\tan \delta$  curve vs temperature. A narrow and symmetrical curve characterizes a very homogeneous material with equal distribution of crosslinks whereas a broad and asymmetrical curve describes a material with uneven distribution of crosslinks, and residual crystallinity. The intensity of maximal  $\tan \delta$  value at  $T_g$  is related to the degree of mobility of the chain segments between crosslinks at that temperature. Higher peak intensities reflect greater energy loss and therefore more viscous behavior, whereas lower intensities characterize more elastic behavior (more energy is stored within the material)<sup>6</sup>

Figure 2.9 represents the DMA results of B-3T↓EDDT↑/DDE networks. Glass transition occurred at 21°C where a steep decrease can be observed in storage modulus. This transition can also be presented in the form of a peak in the  $\tan \delta$  vs. temperature plot shown in Figure 2.9 (B). Similar to the DSC results,  $T_g$  determined by  $\tan \delta$  peak decreases with the increase if PEG content, which is coupled with a simultaneous

decrease in crosslink density. Also, as  $M_c$  (or PEG content) was increased, an additional plateau region was observed between glassy and rubbery plateaus, i.e. the crystalline plateau. The temperature range and the modulus of this crystalline plateau increased as  $M_c$  was increased, which indicates the increase in size of crystals and increase in percentage crystallinity, respectively, as a function of  $M_c$ . This agrees well with the DSC results.

Figure 2.9(b) shows that the  $\tan \delta$  peak reduces in height and broadens with increasing difunctional thiol content (or  $M_c$ ). As mentioned earlier this section, this is due to the restricted molecular motions with increasing crystallinity.<sup>6</sup> This has been reported that the peak width of  $\tan \delta$  at half height broadens with crystallinity and for thermoplastic polymers like nylon 6, it broadens by 1°C for 1% increase in crystallinity.<sup>6</sup>

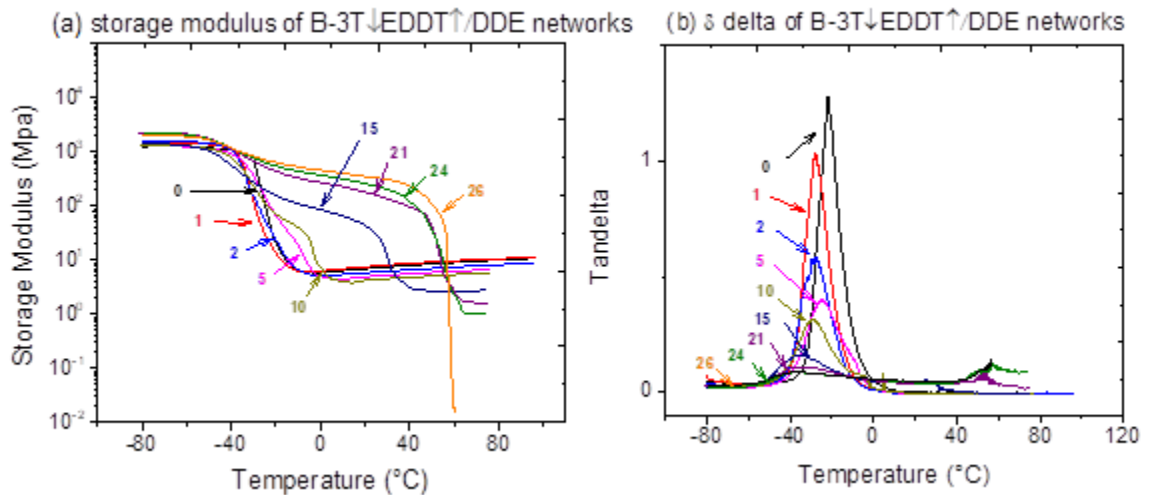


Figure 2.9 DMA curves for B-3T↓EDDT↑/DDE systems.

All the other networks, B-HDT↓EDDT↑/TTT, D-3T↓4TPEG↑/DDE and D-HDT↓3TPEG↑/TTT, showed a unimodal  $\tan \delta$  curve and no secondary storage modulus transition indicating the network homogeneity and absence of crystalline regimes (Figure



2.10). Even though the crosslink junction points were identical in B-HDT↓EDDT↑/TTT systems (aliphatic dithiol was replaced with PEG containing dithiol), with increase in PEG content, the  $\tan \delta$  peak shifts to the left and the rubbery plateau decreases because of the flexible ether linkages. In D-3T↓4TPEG↑/DDE and D-HDT↓3TPEG↑/TTT systems, the dangling PEG chains decreased the rubbery modulus and shifted the  $\tan \delta$  peak to the left indicating an increased chain spacing with increasing PEG content. Networks containing DDE at high concentrations had a hump in  $\tan \delta$  after the maximal peak which we hypothesize that it was due to the presence of impurities associated with DDE monomer which was used without purification.

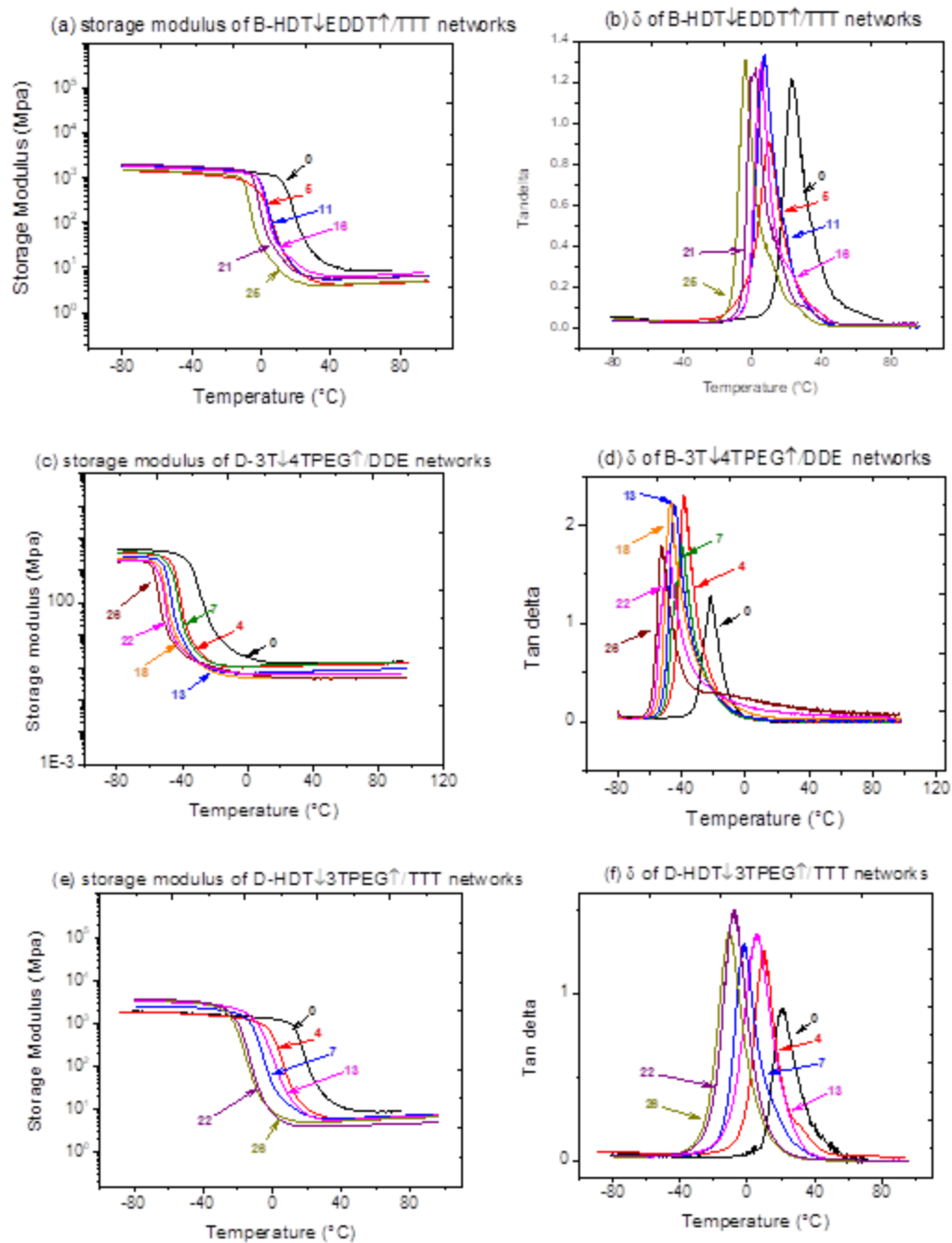


Figure 2.10 Storage modules (on left) and tan  $\delta$  (on right) for (a)B-HDT $\downarrow$ EDDT $\uparrow$ / TTT, (b)D-3T $\downarrow$ 4TPEG $\uparrow$ /DDE & (c) D-HDT $\downarrow$ 3TPEG $\uparrow$ /TTT.

### 2.3.4 Investigation of crystallinity of B-3T↓EDDT↑/DDE networks

Typically, cross-linking is used as one of the effective strategies to prevent crystallization of PEG segments, and thereby increase permeability.<sup>25-34</sup> All B-3T↓EDDT↑/DDE networks (including the systems without PEG) showed a tendency to crystallize which is evident from the DSC thermograms in Figure 2.8a. Systems without PEG (B-3T↓EDDT↑/DDE-0), showed a low endothermic melting peak which is due to the high crosslink density along with smaller aliphatic chain fragments. As the PEG containing dithiol is introduced in the network, along with reducing the crosslink density, higher flexibility is introduced which allows the aliphatic chains to fold and stack-up which leads to crystal domains.

Membranes containing up to 15 wt% PEG, showed a melting peak below room temperature. Membranes with high PEG content (high molecular weight between crosslinks,  $M_c$ ), B-3T↓EDDT↑/DDE-24, B-3T↓EDDT↑/DDE-26 and B-3T↓EDDT↑/DDE-28 showed melting peak above room temperature making it translucent as shown in Figure 2.11. The temperature of melting endotherms (i.e. melting temperature  $T_m$  of the membranes) increased as the  $M_c$  was increased (Figure 2.8a and Table 2.6). This shows that lowering of cross-link junctions led to increase in the size of crystals formed in the membranes. Also, the enthalpy of fusion increased as the  $M_c$  was increased, i.e. the percentage of crystalline phases (degree of crystallinity) increased as  $M_c$  in the membranes was increased. When compared to the work reported by Kweisnek et al.,<sup>3</sup> this series of network membranes, contains aliphatic segments (DDE) in addition to the PEG and thioether segments. We hypothesize that the effect of bulky thioethers is

partially negated by the higher flexibility imparted by aliphatic decadiene segments which likely facilitated the chain folding leading to the formation of crystalline domains.

To understand the crystallization behavior, the first DSC scans were compared with the second heat cycle. Interestingly, there is a second phase, as seen in the second DSC heat scans for samples with high PEG content (B-3T↓EDDT↑/DDE-26 and B-3T↓EDDT↑/DDE-28). We hypothesize that this is mainly related to the slow cooling (3°C/min) which facilitates the formation of both thermodynamic and kinetically favorable phases. When the sample is heated again (2<sup>nd</sup> heat), the thermodynamic favorable phase melts, starts recrystallizing to a kinetically favorable state which again melts at higher temperature (Figure 2.11).

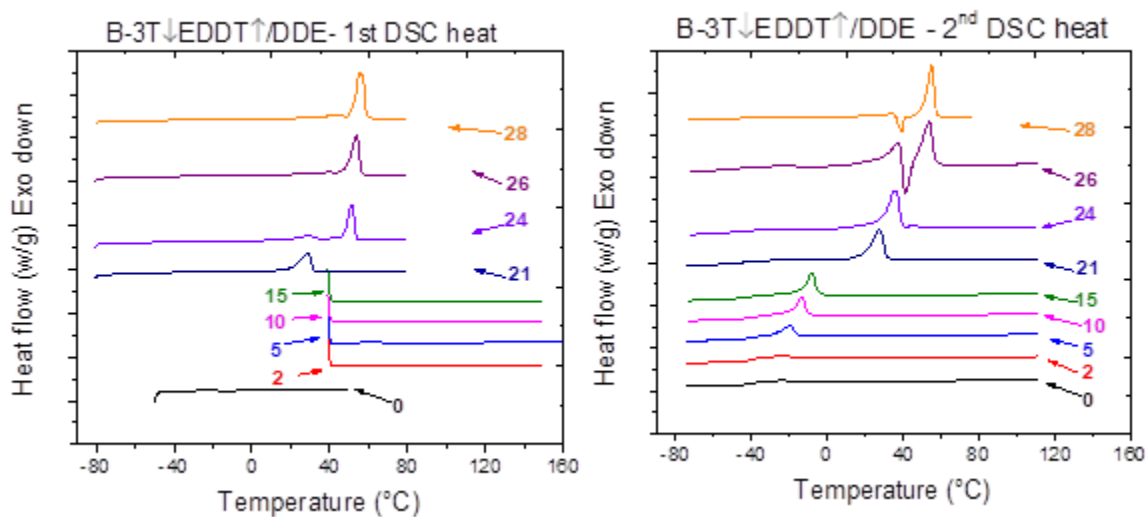


Figure 2.11 DSC first heat(on left) and DSC second heat (on the right). Curves are offset vertically for clarity.

Wide angle X-ray analysis was performed for these samples which is shown in Figure 2.12. The percent crystallinity of every samples where estimated by calculating the area under the peak. Since the samples which was exposed to X-ray analysis was not

thermally treated, the crystalline values correspond to the kinetically favorable crystalline phase of the membranes. This is important because, all the membranes which were exposed to gas transport and free-volume analysis were not thermally treated and corresponds to the effective crystallinity as determined via X-ray analysis.

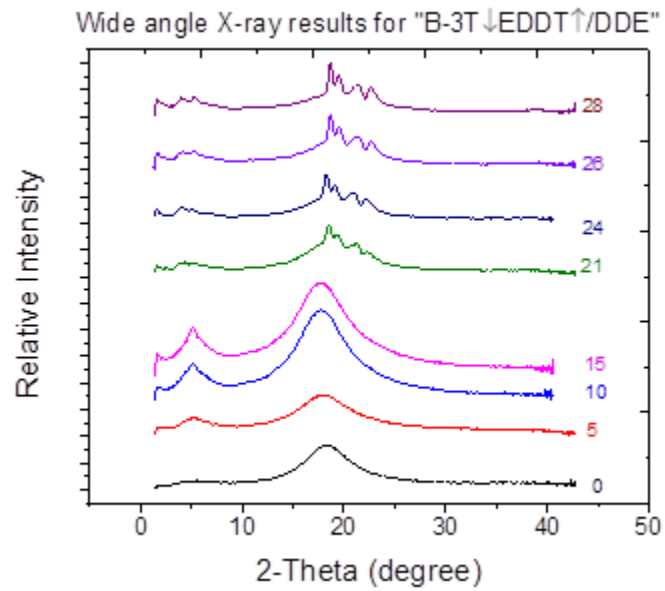


Figure 2.12 Wide angle X-ray of B-3T↓EDDT↑/DDE membranes. Curves vertically stacked for comparison.

Table 2.7 Melting temperature and enthalpy of fusion of the membranes obtained from second heat cycle of DSC analysis. The column on the right indicates the calculated % crystallinity using X-ray

<i>sample Identity</i>	<i>T<sub>m</sub> (°C)</i>	<i>enthalpy of fusion (J/g)</i>	<i>% crystallinity using X-ray (area under the curve)</i>
B-3T↓EDDT↑/DDE-0	-23.95	0.57	0.00
B-3T↓EDDT↑/DDE -2	-22.43	2.98	0.00
B-3T↓EDDT↑/DDE -5	-19.57	12.46	0.00
B-3T↓EDDT↑/DDE -10	-13.59	19.76	0.00
B-3T↓EDDT↑/DDE -15	-9.02	20.86	0.00
B-3T↓EDDT↑/DDE -21	27.35	34.66	25.28
B-3T↓EDDT↑/DDE -24	36.00	44.25	37.32
B-3T↓EDDT↑/DDE -26	53.76	44.25	35.79
B-3T↓EDDT↑/DDE -28	53.96	46.13	43.46

As discussed earlier, DSC heat cycle indicates there exists two phases, a thermodynamic favorable phase which is denoted as  $\alpha$ , and a kinetically favorable phase which is denoted as  $\beta$ . To further shed lights on the crystal phases, model network (B-3T↓EDDT↑/DDE -25.75) was annealed at 45°C for 10 min (to melt  $\alpha$  phase), rapidly cooled (10°C/min) to -40°C (to restrict the formation of  $\alpha$  phase) and subsequently heated to 90°C. In this first heat, we observe only the endothermic melting peaks (associated with the kinetically favorable phase) which confirms that annealing prevents the formation of two crystal phases. The same sample was further cooled to -60°C at a much slower rate (5°C/min) and subsequently heated to 90°C. This heat cycle contained both crystallizing and melting peaks as shown in Figure 2.13. This implies that, the slower cooling rate facilitates the formation of two crystal phases ( $\alpha$  and  $\beta$ ) where the

thermodynamic favorable phase melts and recrystallizes to a kinetically favorable phase which melts at higher temperatures.

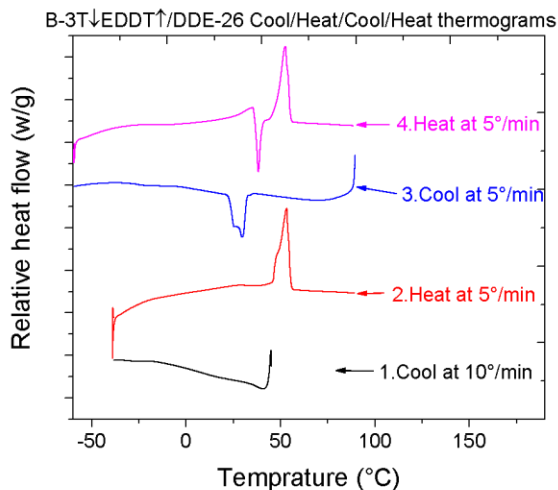


Figure 2.13 Wide angle X-ray of B-3T↓EDDT↑/DDE membranes. Curves vertically stacked for comparison.

The optical microscopic images are shown in Figure 2.14. As seen with increasing PEG content (higher  $M_c$ ) the size of the crystal increases which is confirmed through the increased melting temperature ( $T_m$ ) via DSC. The digital pictures are shown in Figure 2.15. As seen, the membranes with high PEG content turns opaque at room temperature. Even though all membranes does poses some crystallinity, only membranes with high PEG content (B-3T↓EDDT↑/DDE-21, B-3T↓EDDT↑/DDE24, B-3T↓EDDT↑/DDE-26 and B-3T↓EDDT↑/DDE-28) showed crystallinity at room temperature. For membranes with lower PEG, the crystalline melting temperature was below room temperature thus remained amorphous at room temperature (testing temperature). Further investigation of crystallinity is beyond the scope of this work

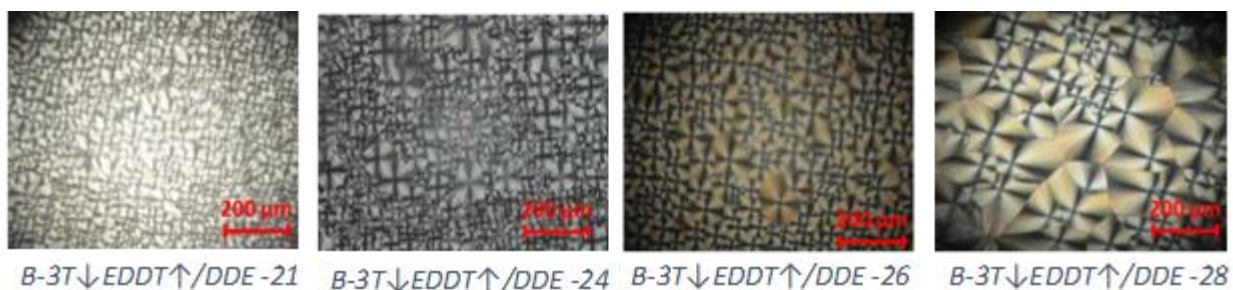


Figure 2.14 Optical Microscopic images at room temperature. With increasing PEG content (increasing  $M_c$ ) the crystal size grows..

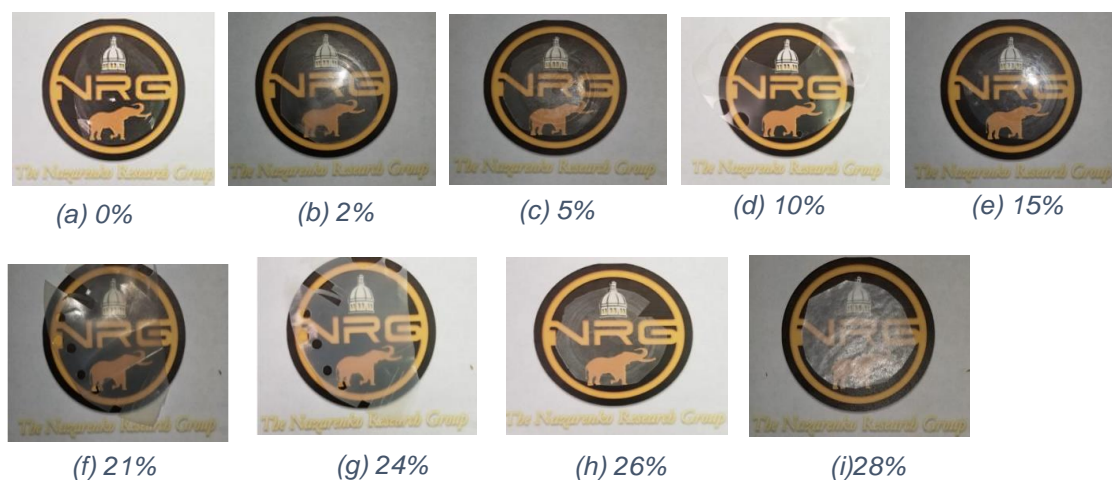


Figure 2.15 Digital images of B-3T↓EDDT↑/DDE at room temperature. (a) through (e) (top row) amorphous at room temperature. (f) through (i) opaque at room temperature.

### 2.3.5 Free-volume analysis and dependencies of all networks

Figure 2.16 shows the free-volume dependencies on glass transition temperature for all synthesized networks. It is very clear that the low  $T_g$  networks (DDE containing systems) had a very high free-volume as compared to the high  $T_g$  networks (TTT containing systems).



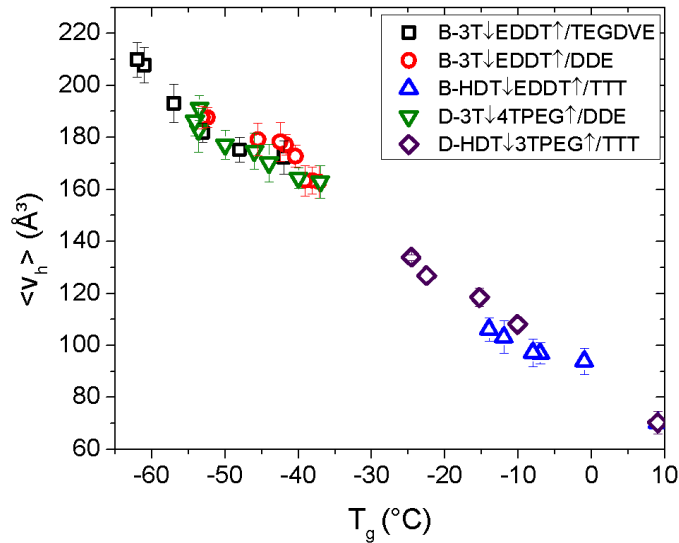


Figure 2.16 Free-volume plotted as a function of glass transition temperature.

Within a particular networks, the increase in free-volume is associated for various reasons. In B-3T<math>\downarrow</math>EDDT<math>\uparrow</math>/DDE systems, with increasing PEG content  $\langle v_h \rangle$  values increased mainly due to the decreasing cross-link density. With further increase in PEG content, the membranes were semi-crystalline at room temperature (from DSC results). We expect the presence of crystalline domains will led to decrease in free-volume. However, o-Ps can form only in amorphous regions within the sample, therefore the presence of crystalline domains in samples did not influence o-Ps lifetimes. Therefore, crystallinity showed no effect on free volume quantity  $\langle v_h \rangle$  measured using PALS.  $\langle v_h \rangle$  trend was just a reflection of how decreasing cross-link density resulted in free volume increase in the amorphous regions of the membranes.

In B-HDT↓EDDT↑/TTT systems, the addition of PEG units causes increases in flexibility with negligible increase in molecular weight between crosslinks. With increase in PEG content, the free-volume increases.

In systems with PEG in dangling chains (D-HDT↓3TPEG↑/TTT and D-3T↓4TPEG↑/DDE), even though the crosslink density is theoretically unaltered, the increase in free-volume with increase in dangling chain content is mainly due to the distortion of chain packing caused by the free moving chain ends. Thus, the glass transition temperature decreases with increasing dangling chain content. To note, the synthesized modified monomer might contain some impurities (more than one modification) which again alters the junction points affecting the T<sub>g</sub>. Since, this is beyond the scope of this project, the synthesized monomers were utilized without any purification and might contain a mixture of monomers (single modified to four modified).

### **2.3.6 Gas transport analysis**

The main objective of this work is to determine the minimum amount of PEG required to achieve maximum CO<sub>2</sub> gas solubility and selectivity over other light gases. The transport phenomena of gas through the membranes were determined via a constant volume variable pressure apparatus as described in the experimental session. In our previous work on PEG based thiol-ene membranes (B-3T↓EDDT↑/TEGDVE systems), both bifunctional thiol and bifunctional ene monomers were PEG based. In that series, PEG wt% within network systems varied between 38% and 67%. Increase in gas permeability in those networks was achieved by increasing gas diffusivity. That is, the cross-link density of the membranes was decreased, which increased the free volume within the membranes, and thereby resulted in increasing gas diffusivity (and

permeability). The change in PEG wt% between 38% and 67% did not have any effect on solubility of the membranes for CO<sub>2</sub> (or any other gas). But the aliphatic control membrane which did not contain any PEG groups showed significantly lower CO<sub>2</sub> solubility value.<sup>3</sup> Therefore, we hypothesized that the solubility of PEG based membranes for CO<sub>2</sub> levels off at some value below 38%, and thus goal of this work was to identify minimum amount of PEG required for maximum CO<sub>2</sub> solubility. Thus, all the gas transport parameters in the present study are plotted as a function of PEG wt% in the membranes. Figure 18 represents the B-3T↓EDDT↑/TEGDVE transport curves from Kweisnek et al., work replotted against PEG content.<sup>3</sup>

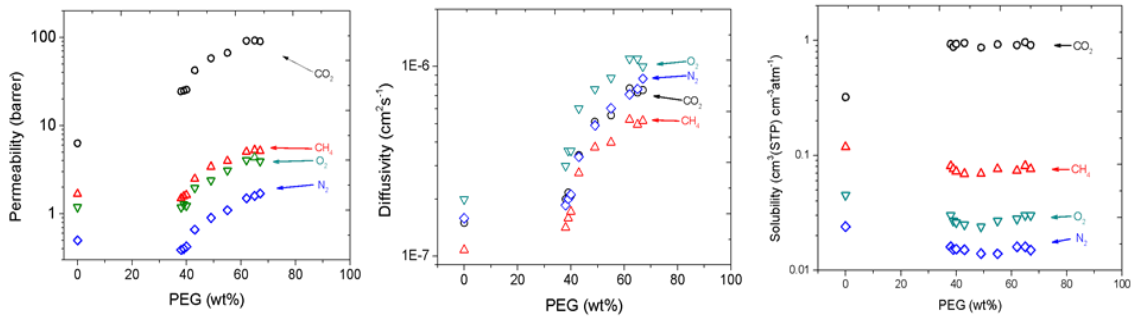


Figure 2.17 Permeability (P), Diffusivity (D) and Solubility (S) of B-3T↓EDDT↑TEGDVE systems plotted against PEG wt%. Data obtained from Kweisnek work<sup>3</sup>.

The permeability(P) was calculated from the steady state slope and for convenience, P is expressed in Barrer (1 Barrer = cc(STP)cm m<sup>-2</sup>day<sup>-1</sup>atm<sup>-1</sup>). Since all the networks (B-3T↓EDDT↑/DDE, B-HDT↓EDDT↑/TTT, D-3T↓4TPEG↑/DDE & D-HDT↓3TPEG↑/TTT) has different glass transition temperature ( $T_g$ ) and free volume (shown later), the permeability values were different for all systems. Figure 2.18 shows the permeability of all networks plotted against PEG weight % for four different gases

(CO<sub>2</sub>, N<sub>2</sub>, CH<sub>4</sub> and O<sub>2</sub>). B-3T↓EDDT↑/TEGDVE (Kweisnek et al., work) is also plotted for comparison.

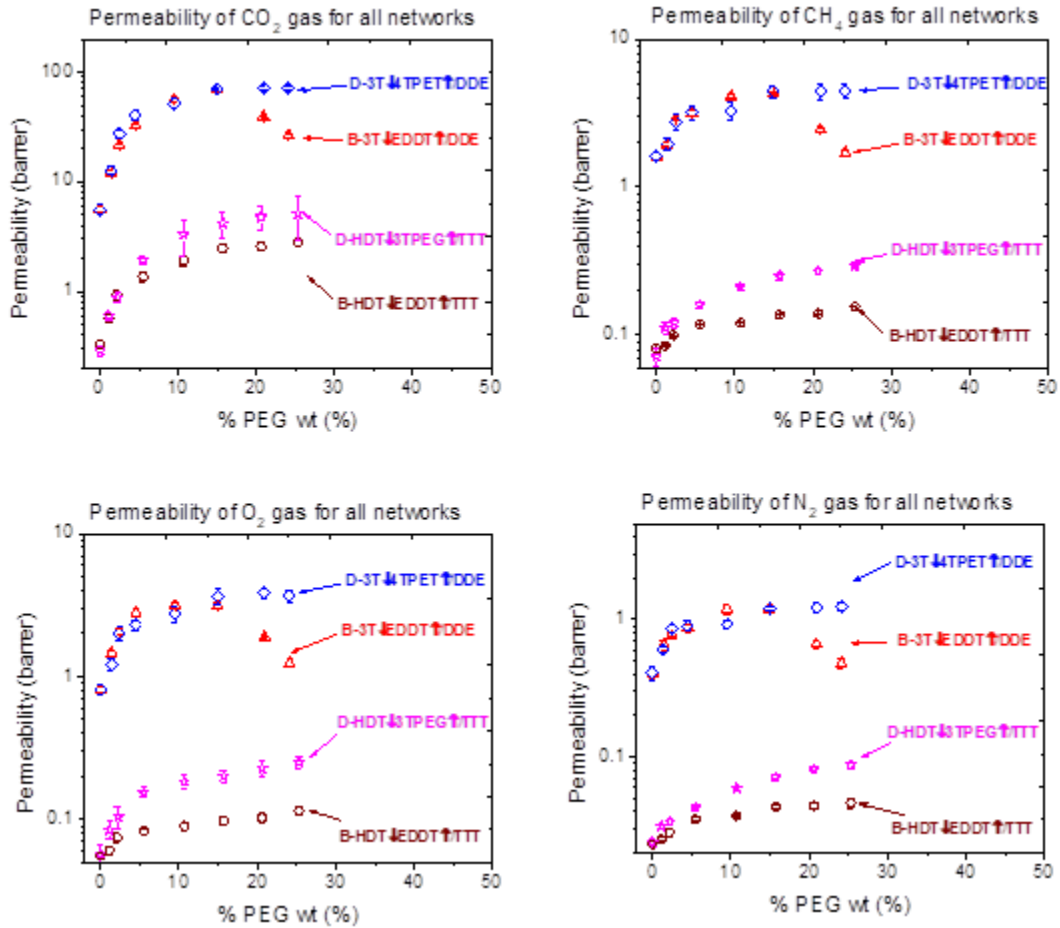


Figure 2.18 Permeability (P) of CO<sub>2</sub>, CH<sub>4</sub>, O<sub>2</sub> and N<sub>2</sub> gas of all networks (B-3T↓EDDT↑/DDE, B-HDT↓EDDT↑/TTT, D-3T↓4TPEG↓/DDE and D-HDT↓3TPEG↑/TTT) plotted against PEG wt%..

Earlier in our group, it was demonstrated that the permeability exhibits V-shaped trend when plotted against glass transition temperature, where the networks with  $T_g$  closer to testing temperature had the lowest permeability values.<sup>7</sup> As seen, all networks exhibits different permeability values because of the difference in  $T_g$  and free-volume. Networks containing DDE as the backbone had higher permeabilities (for all gases) mainly because these networks had  $T_g$  much lower compared to that of networks with

TTT in backbone. Permeability of 3T↓EDDT↑/DDE with higher PEG content (beyond 21 PEG wt%) decreased mainly because of the crystalline domains, (as discussed earlier) which reduced the flux through the membrane. D-HDT↓3TPEG↑/TTT exhibits higher permeability values than the B-HDT↓EDDT↑/TTT, which is because of the higher free-volume created by the free dangling chain ends. Permeability within the networks followed a trend where the permeability co-efficient of  $\text{CO}_2 > \text{CH}_4 > \text{O}_2 > \text{N}_2$  (plot not shown). This trend is mainly because of the combined effect of kinetic diameter along with the solubility of these gases

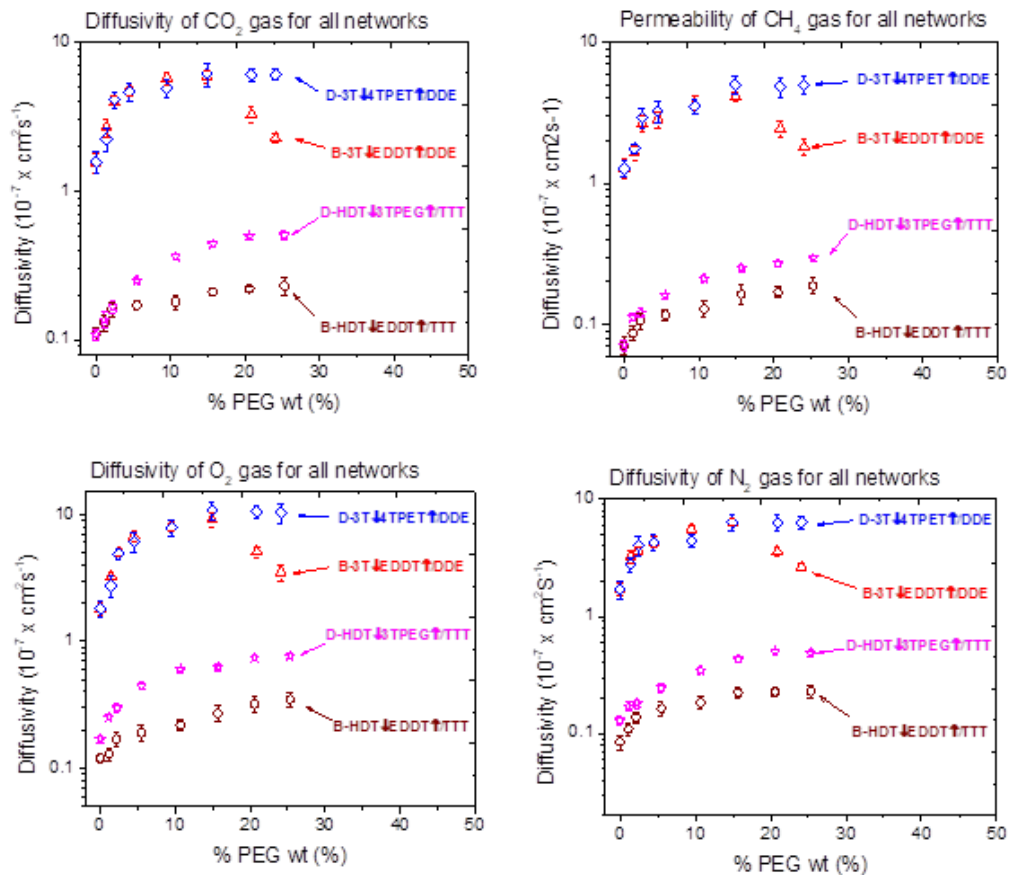


Figure 2.19 Diffusivity (D) of  $\text{CO}_2$ ,  $\text{CH}_4$ ,  $\text{O}_2$  and  $\text{N}_2$  gas of all networks (B-3T↓EDDT↑/DDE, B-HDT↓EDDT↑/TTT, D-3T↓4TPET↑/DDE and D-HDT↓3TPEG↑/TTT) plotted against PEG wt%.

Permeability values were deconvoluted to obtain diffusivity and solubility as described in the experimental session. The gas diffusivity of all the networks for different light gas plotted against PEG wt% is shown in Figure 2.19.

Diffusivity of all amorphous membrane systems increased with increasing PEG content except for the BPEG/DDE for the reasons stated above i.e., crystallinity. As diffusivity is a kinetic parameter, the extent of increase in diffusivity co-efficient depends on the functionality of the ene used, concentration of dangling chains, and molecular weight between crosslinks ( $M_c$ ). Diffusivity co-efficient for networks with trifunctional ene (TTT) was lower than the networks containing difunctional ene (DDE). For 3T↓EDDT↑/DDE networks, the increase in diffusivity was due to the combined effect of flexible ether groups and increase in  $M_c$ . At higher  $M_c$ , the decrease in the diffusivity was apparently due to the formation of crystal domains. For D-3T↓4TPEG↑/DDE & D-HDT↓3TPEG↑/TTT systems, even though the  $M_c$  was theoretically maintained constant, introduction of dangling chains created more free volume which increased the diffusivity upon increase in dangling PEG content. For B-HDT↓EDDT↑/TTT networks, while maintaining  $M_c$ , the increase in diffusivity was mainly due to the introduction of flexible polar groups (PEG containing dithiol) which replaced the aliphatic dithiol. With all systems, diffusion of  $O_2 > N_2 > CO_2 > CH_4$  is mainly due to the difference in kinetic diameter of the gases (plot not shown).

The solubility of  $CO_2$  gas increased as a function of PEG wt% due to the thermodynamic drive for  $CO_2$  to solubilize within the membranes (because of Lewis acid-base interaction between  $CO_2$  and PEG moieties). The  $CO_2$  solubility co-efficient for all networks (3T↓EDDT↑/DDE, D-HDT↓3TPEG↑/TTT, B-HDT↓EDDT↑/TTT and D-

HDT↓3TPEG↑/TTT), irrespective of the network architecture and PEG placements, followed a master trend and levelled off beyond 15 PEG wt%. For B-3T↓EDDT↑/DDE networks, beyond PEG content of 14.9 wt% there were crystalline domains present in the membranes at experimental conditions. Like gas diffusivity, gas solubility would also decrease as a function of percentage crystallinity of the membrane. But the leveling off behavior of CO<sub>2</sub> gas solubility values beyond 14.9 wt% was not due to the presence of crystalline domains, because at a PEG concentration of 14.9 wt%, the values for CO<sub>2</sub> solubility already matched the values that were achieved by the family of PEG based amorphous thiol-ene membranes that we previously reported and in that series PEG content was between 38% and 67%. Therefore, the minimum PEG concentration required for achieving maximum CO<sub>2</sub> solubility is 14.9 wt% and the crystallinity in the network didn't have any effect on CO<sub>2</sub> solubility. With all systems, solubility of CO<sub>2</sub>> CH<sub>4</sub>> O<sub>2</sub>> N<sub>2</sub> (plot not shown).

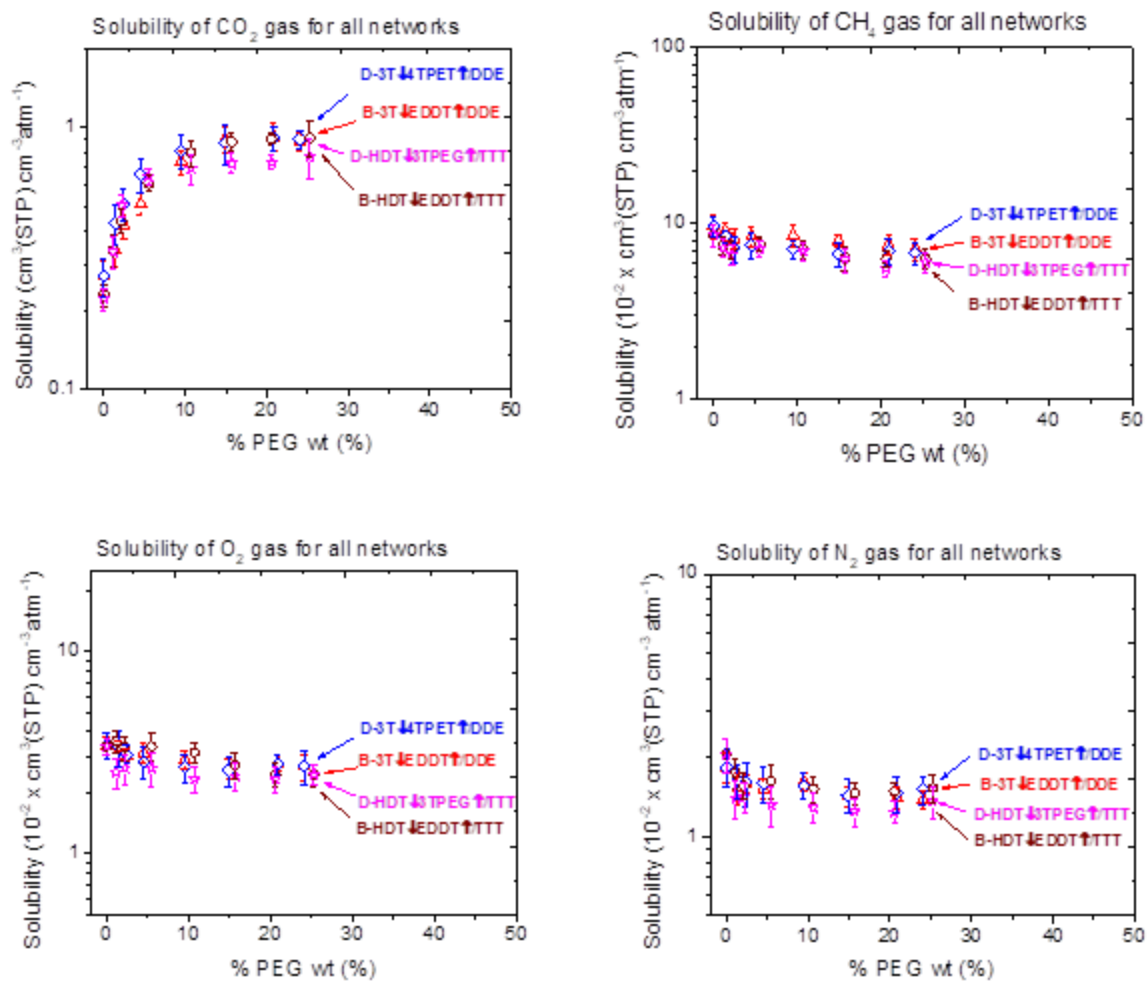


Figure 2.20 Solubility ( $S$ ) of  $\text{CO}_2$ ,  $\text{CH}_4$ ,  $\text{O}_2$  and  $\text{N}_2$  gas of all networks (B-3T↓EDDT↑/DDE, B-HDT↓EDDT↑/TTT, D-3T↓4TPET↑/DDE and D-HDT↓3TPEG↑/TTT) plotted against PEG wt%.

Solubility of  $\text{N}_2$  and  $\text{O}_2$  for all the networks marginally decreased with increasing PEG content. A representative graph showing the decrease in solubility of  $\text{N}_2$  gas (for B-HDT↓EDDT↑/TTT networks) is shown in Figure 2.20. This is probably because as the PEG content was increased, the polarity of the membranes increased which reduced the interaction of non-polar gases like  $\text{N}_2$  and  $\text{O}_2$ . This effect has been reported as shown in Table X that as the polarity of the membranes increases the solubility of the membranes for non-polar gases such as  $\text{O}_2$ ,  $\text{N}_2$  gets reduced slightly upon addition of polar moieties.



As shown in the table X, as the polar acrylonitrile groups are increased in the network, solubility of N<sub>2</sub> and O<sub>2</sub> gas decreases which confirms our hypothesis. On the other hand, with increase in polar moieties, the solubility of CO<sub>2</sub> gas increases as expected.

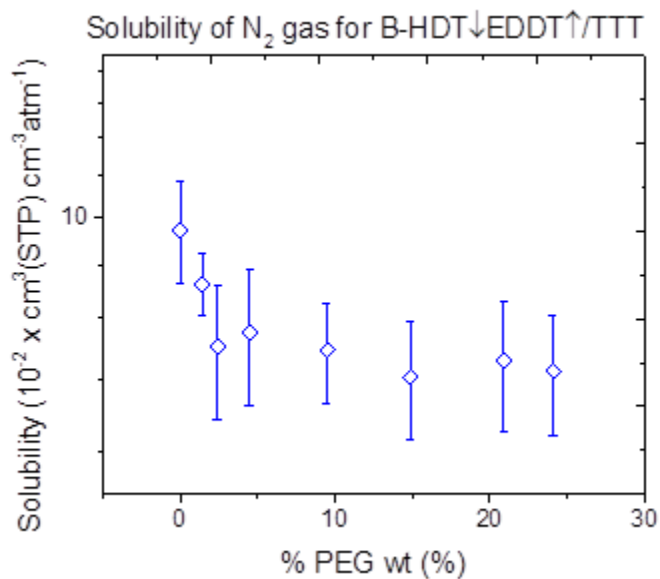
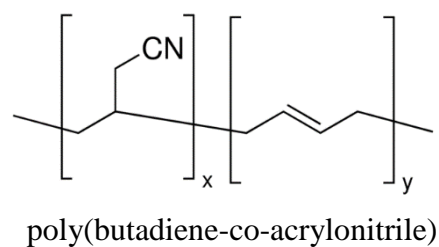
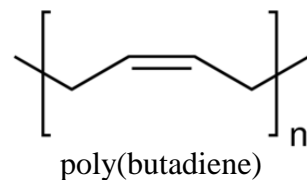


Figure 2.21 Representative plot showing reduced interaction of non-polar N<sub>2</sub> gas with increasing polar PEG content

Table 2.8 Literature values of solubility of N<sub>2</sub>, O<sub>2</sub>, CO<sub>2</sub> in polymers with and without polar group<sup>4</sup>

Gas	Polymer	S (x10 <sup>06</sup> )
N <sub>2</sub>	Poly (butadiene)	0.444
	Poly( butadiene-Co- Acrylonitrile) (80/20)	0.375
	Poly( butadiene-Co- Acrylonitrile) (73/27)	0.316
	Poly( butadiene-Co- Acrylonitrile) (68/32)	0.296
	Poly( butadiene-Co- Acrylonitrile) (61/39)	0.276
	Poly (butadiene) 29% crystallinity	0.405
O <sub>2</sub>	Poly (butadiene)	0.957
	Poly( butadiene-Co- Acrylonitrile) (80/20)	0.77
	Poly( butadiene-Co- Acrylonitrile) (73/27)	0.671
	Poly( butadiene-Co- Acrylonitrile) (68/32)	0.632
	Poly( butadiene-Co- Acrylonitrile) (61/39)	0.533
	Poly (butadiene) 29% crystallinity	0.708
CO <sub>2</sub>	Poly (butadiene)	9.87
	Poly( butadiene-Co- Acrylonitrile) (80/20)	11.2
	Poly( butadiene-Co- Acrylonitrile) (73/27)	12.2
	Poly( butadiene-Co- Acrylonitrile) (68/32)	13
	Poly( butadiene-Co- Acrylonitrile) (61/39)	14.7
	Poly (butadiene) 29% crystallinity	3.99



*Chemical structures of the reported polymers*

Table 2.9 Gas transport (P,D & S) values of all networks with standard error. Reported values are average of 3 individual runs

Sample Identity	Free Volume (Å <sup>3</sup> )	CO <sub>2</sub>			CH <sub>4</sub>			O <sub>2</sub>			N <sub>2</sub>		
		P	D x 10 <sup>-7</sup>	S	P	D x 10 <sup>-7</sup>	S x 10 <sup>-2</sup>	P	D x 10 <sup>-7</sup>	S x 10 <sup>-2</sup>	P	D x 10 <sup>-7</sup>	S x 10 <sup>-2</sup>
B-3T↓EDDT↑/DDE-0	163 ± 6	5.56 ± 0.39	1.56 ± 0.23	0.27 ± 0.04	1.62 ± 0.11	1.27 ± 0.2	9.7 ± 1.51	0.81 ± 0.05	1.8 ± 0.19	3.43 ± 0.36	0.41 ± 0.043	1.69 ± 0.21	1.84 ± 0.23
B-3T↓EDDT↑/DDE-1	n/d	11.97 ± 0.79	2.67 ± 0.35	0.34 ± 0.045	1.95 ± 0.06	1.64 ± 0.21	9.05 ± 1.13	1.46 ± 0.06	3.27 ± 0.18	3.39 ± 0.19	0.65 ± 0.048	3.25 ± 0.45	1.53 ± 0.21
B-3T↓EDDT↑/DDE-2	163 ± 6	21.54 ± 0.94	3.94 ± 0.4	0.42 ± 0.042	2.87 ± 0.06	2.66 ± 0.34	8.2 ± 1.04	2.05 ± 0.11	5.07 ± 0.35	3.07 ± 0.21	0.77 ± 0.031	3.63 ± 0.28	1.6 ± 0.13
B-3T↓EDDT↑/DDE-5	173 ± 4	32.56 ± 1.13	4.83 ± 0.44	0.51 ± 0.047	3.17 ± 0.13	2.85 ± 0.37	8.45 ± 1.08	2.79 ± 0.15	6.73 ± 0.73	3.16 ± 0.34	0.87 ± 0.059	4.35 ± 0.39	1.52 ± 0.14
B-3T↓EDDT↑/DDE-10	177 ± 4	55.6 ± 2.04	5.72 ± 0.6	0.74 ± 0.078	4.11 ± 0.16	3.64 ± 0.49	8.59 ± 1.16	3.13 ± 0.12	8.14 ± 0.83	2.92 ± 0.3	1.19 ± 0.089	5.58 ± 0.46	1.62 ± 0.14
B-3T↓EDDT↑/DDE-15	178 ± 6	69.79 ± 2.96	5.88 ± 0.62	0.9 ± 0.096	4.31 ± 0.11	4.1 ± 0.34	7.98 ± 0.67	3.14 ± 0.18	9.05 ± 1.07	2.64 ± 0.31	1.2 ± 0.066	6.42 ± 0.55	1.42 ± 0.12
B-3T↓EDDT↑/DDE-21	179 ± 4	39.01 ± 1.51	3.24 ± 0.4	0.92 ± 0.114	2.44 ± 0.06	2.45 ± 0.3	7.58 ± 0.92	1.89 ± 0.04	5.09 ± 0.5	2.81 ± 0.27	0.66 ± 0.052	3.59 ± 0.33	1.41 ± 0.13
B-3T↓EDDT↑/DDE-24	188 ± 4	26.24 ± 0.93	2.26 ± 0.18	0.88 ± 0.071	1.71 ± 0.08	1.82 ± 0.25	7.17 ± 1	1.24 ± 0.08	3.5 ± 0.52	2.7 ± 0.41	0.48 ± 0.042	2.64 ± 0.2	1.38 ± 0.1

84

Sample Identity	Free Volume (Å <sup>3</sup> )	CO <sub>2</sub>			CH <sub>4</sub>			O <sub>2</sub>			N <sub>2</sub>		
		P	D x 10 <sup>-7</sup>	S	P	D x 10 <sup>-7</sup>	S x 10 <sup>-2</sup>	P	D x 10 <sup>-7</sup>	S x 10 <sup>-2</sup>	P	D x 10 <sup>-7</sup>	S x 10 <sup>-2</sup>
D-3T↓4TPEG↑/DDE-0	163 ± 6	5.56 ± 0.6	1.56 ± 0.26	0.27 ± 0.045	1.62 ± 0.11	1.27 ± 0.16	9.7 ± 1.23	0.81 ± 0.07	1.8 ± 0.27	3.43 ± 0.51	0.41 ± 0.048	1.69 ± 0.27	1.84 ± 0.3
D-3T↓4TPEG↑/DDE-2	164 ± 4	12.56 ± 1.03	2.2256 ± 0.39	0.43 ± 0.076	1.96 ± 0.17	1.76 ± 0.14	8.47 ± 0.66	1.22 ± 0.12	2.74 ± 0.55	3.38 ± 0.68	0.6 ± 0.034	2.8 ± 0.41	1.64 ± 0.24
D-3T↓4TPEG↑/DDE-4	170 ± 7	27.41 ± 2.25	4.1004 ± 0.55	0.51 ± 0.07	2.76 ± 0.31	2.91 ± 0.48	7.23 ± 1.2	2 ± 0.21	4.88 ± 0.51	3.11 ± 0.33	0.86 ± 0.067	4.06 ± 0.78	1.61 ± 0.31
D-3T↓4TPEG↑/DDE-7	175 ± 7	40.48 ± 3.56	4.6369 ± 0.68	0.66 ± 0.101	3.2 ± 0.38	3.25 ± 0.54	7.5 ± 1.26	2.28 ± 0.19	6.06 ± 1.07	2.86 ± 0.51	0.9 ± 0.082	4.3 ± 0.66	1.59 ± 0.25
D-3T↓4TPEG↑/DDE-13	177 ± 6	51.78 ± 5.5	4.8865 ± 0.68	0.81 ± 0.12	3.3 ± 0.48	3.51 ± 0.43	7.17 ± 0.89	2.76 ± 0.35	7.85 ± 1.22	2.68 ± 0.42	0.92 ± 0.06	4.44 ± 0.49	1.57 ± 0.17
D-3T↓4TPEG↑/DDE-18	183 ± 9	70.64 ± 1.92	6.1525 ± 1.1	0.87 ± 0.156	4.43 ± 0.41	5.03 ± 0.74	6.71 ± 0.99	3.64 ± 0.42	10.7 ± 1.83	2.59 ± 0.44	1.2 ± 0.057	6.34 ± 0.97	1.44 ± 0.22
D-3T↓4TPEG↑/DDE-22	187 ± 6	72.03 ± 2.54	6.0161 ± 0.66	0.91 ± 0.1	4.47 ± 0.54	4.86 ± 0.78	6.99 ± 1.13	3.85 ± 0.3	10.54 ± 1.22	2.78 ± 0.32	1.22 ± 0.113	6.31 ± 1.01	1.46 ± 0.23
D-3T↓4TPEG↑/DDE-26	191 ± 5	71.62 ± 2.64	6.0248 ± 0.48	0.9 ± 0.073	4.46 ± 0.51	4.98 ± 0.73	6.81 ± 1.01	3.67 ± 0.34	10.34 ± 1.89	2.7 ± 0.49	1.25 ± 0.086	6.33 ± 0.8	1.51 ± 0.19

Sample Identity	Free Volume (Å <sup>3</sup> )	CO <sub>2</sub>			CH <sub>4</sub>			O <sub>2</sub>			N <sub>2</sub>		
		P	D x 10 <sup>-7</sup>	S	P	D x 10 <sup>-7</sup>	S x 10 <sup>-2</sup>	P	D x 10 <sup>-7</sup>	S x 10 <sup>-2</sup>	P	D x 10 <sup>-7</sup>	S x 10 <sup>-2</sup>
B-HDT↓EDDT↑TTT-0	70 ± 6	0.33 ± 0.03	0.11 ± 0.01	0.23 ± 0.022	0.081 ± 0.006	0.071 ± 0.01	8.63 ± 1.26	0.056 ± 0.003	0.12 ± 0.011	3.4 ± 0.32	0.023 ± 0.001	0.085 ± 0.012	2.06 ± 0.3
B-HDT↓EDDT↑TTT-1	n/d	0.57 ± 0.05	0.13 ± 0.017	0.34 ± 0.046	0.085 ± 0.006	0.087 ± 0.01	7.48 ± 0.85	0.061 ± 0.004	0.13 ± 0.015	3.6 ± 0.43	0.025 ± 0.001	0.109 ± 0.014	1.75 ± 0.23
B-HDT↓EDDT↑TTT-3	n/d	0.92 ± 0.09	0.16 ± 0.016	0.44 ± 0.047	0.1 ± 0.009	0.106 ± 0.013	7.17 ± 0.88	0.075 ± 0.006	0.17 ± 0.023	3.35 ± 0.45	0.028 ± 0.002	0.137 ± 0.016	1.56 ± 0.18
B-HDT↓EDDT↑TTT-5	94 ± 5	1.36 ± 0.14	0.17 ± 0.011	0.61 ± 0.043	0.118 ± 0.007	0.117 ± 0.011	7.67 ± 0.7	0.083 ± 0.004	0.19 ± 0.029	3.4 ± 0.52	0.035 ± 0.001	0.164 ± 0.023	1.63 ± 0.23
B-HDT↓EDDT↑TTT-11	97 ± 6	1.91 ± 0.22	0.18 ± 0.019	0.8 ± 0.093	0.121 ± 0.011	0.129 ± 0.016	7.16 ± 0.89	0.09 ± 0.006	0.22 ± 0.023	3.17 ± 0.33	0.037 ± 0.001	0.183 ± 0.021	1.52 ± 0.17
B-HDT↓EDDT↑TTT-16	97 ± 5	2.48 ± 0.18	0.21 ± 0.014	0.88 ± 0.064	0.137 ± 0.013	0.163 ± 0.026	6.38 ± 1	0.098 ± 0.006	0.27 ± 0.039	2.75 ± 0.4	0.043 ± 0.002	0.224 ± 0.022	1.46 ± 0.15
B-HDT↓EDDT↑TTT-21	103 ± 6	2.57 ± 0.21	0.22 ± 0.01	0.9 ± 0.045	0.14 ± 0.012	0.169 ± 0.015	6.31 ± 0.58	0.103 ± 0.009	0.32 ± 0.043	2.45 ± 0.33	0.044 ± 0.002	0.227 ± 0.019	1.49 ± 0.12
B-HDT↓EDDT↑TTT-25	106 ± 5	2.8 ± 0.23	0.23 ± 0.034	0.91 ± 0.138	0.156 ± 0.014	0.188 ± 0.025	6.29 ± 0.83	0.114 ± 0.007	0.35 ± 0.043	2.45 ± 0.3	0.046 ± 0.004	0.229 ± 0.028	1.53 ± 0.19

Sample Identity	Free Volume (Å <sup>3</sup> )	CO <sub>2</sub>			CH <sub>4</sub>			O <sub>2</sub>			N <sub>2</sub>		
		P	D x 10 <sup>-7</sup>	S	P x 10 <sup>-2</sup>	D x 10 <sup>-7</sup>	S x 10 <sup>-2</sup>	P x 10 <sup>-2</sup>	D x 10 <sup>-7</sup>	S x 10 <sup>-2</sup>	P x 10 <sup>-2</sup>	D x 10 <sup>-7</sup>	S x 10 <sup>-2</sup>
D-HDT↓3TPEG↑/TTT-0	70 ± 4	0.32 ± 0.03	0.11 ± 0	0.22 ± 0.022	7.133 ± 0.6	0.08 ± 0.01	8.63 ± 1.26	5.75 ± 0.3	0.17 ± 0.011	3.4 ± 0.32	2.38 ± 0.1	0.13 ± 0.012	2.06 ± 0.3
D-HDT↓3TPEG↑/TTT-2	n/d	0.6 ± 0.04	0.14 ± 0	0.34 ± 0.046	11.188 ± 0.6	0.12 ± 0.01	7.276 ± 0.85	8.45 ± 0.4	0.25 ± 0.015	2.54 ± 0.43	3.11 ± 0.1	0.17 ± 0.014	1.39 ± 0.2
D-HDT↓3TPEG↑/TTT-4	n/d	1.1 ± 0.07	0.17 ± 0	0.51 ± 0.047	12.129 ± 0.9	0.14 ± 0.01	6.655 ± 0.88	10.48 ± 0.6	0.3 ± 0.023	2.654 ± 0.45	3.36 ± 0.2	0.18 ± 0.016	1.417 ± 0.2
D-HDT↓3TPEG↑/TTT-7	108 ± 2	2.14 ± 0.09	0.25 ± 0	0.65 ± 0.043	16.035 ± 0.7	0.17 ± 0.01	7.159 ± 0.7	15.47 ± 0.4	0.44 ± 0.029	2.656 ± 0.52	4.26 ± 0.1	0.25 ± 0.023	1.321 ± 0.2
D-HDT↓3TPEG↑/TTT-13	118 ± 3	3.31 ± 0.31	0.36 ± 0	0.7 ± 0.093	21.26 ± 1.1	0.23 ± 0.02	6.962 ± 0.89	18.43 ± 0.6	0.6 ± 0.023	2.336 ± 0.33	5.9 ± 0.1	0.35 ± 0.021	1.29 ± 0.2
D-HDT↓3TPEG↑/TTT-18	127 ± 3	4.2 ± 0.18	0.44 ± 0	0.73 ± 0.064	25.079 ± 1.3	0.31 ± 0.03	6.224 ± 1	20.06 ± 0.6	0.63 ± 0.039	2.424 ± 0.4	7.09 ± 0.2	0.43 ± 0.022	1.247 ± 0.2
D-HDT↓3TPEG↑/TTT-22	134 ± 1	4.8 ± 0.23	0.5 ± 0	0.73 ± 0.045	27.047 ± 1.2	0.37 ± 0.02	5.562 ± 0.58	22.75 ± 0.9	0.74 ± 0.043	2.333 ± 0.33	8.11 ± 0.2	0.5 ± 0.019	1.24 ± 0.1
D-HDT↓3TPEG↑/TTT-26	n/d	5.11 ± 0.19	0.51 ± 0	0.77 ± 0.138	29.532 ± 1.4	0.37 ± 0.03	6.021 ± 0.83	24.97 ± 0.7	0.77 ± 0.043	2.473 ± 0.3	8.69 ± 0.4	0.48 ± 0.028	1.363 ± 0.2

P in barrer

D in cm<sup>2</sup> s<sup>-1</sup>

S in cm<sup>3</sup> (STP) cm<sup>-3</sup> atm<sup>-1</sup>

### 2.3.7 Selectivity analysis of CO<sub>2</sub>/ light gases

Previous work on PEG thiol-ene network membranes (3T↓EDDT↑/TEGDVE), except for the membrane containing no PEG, the CO<sub>2</sub>/ light gas selectivity ( Permeability selectivity, diffusivity selectivity and solubility selectivity) values didn't have an effect with increasing PEG and remained constant.<sup>3</sup> This was because at PEG concentration of 37 wt%, the membrane was already at its maximum CO<sub>2</sub> solubility. Further increase in PEG concentration did not change CO<sub>2</sub> solubility (or any other gas solubility), therefore solubility selectivity remained constant as a function of PEG content. Though gas diffusivity changed as a function of PEG content, gas diffusivity trends were similar for all the gases, and hence diffusivity selectivity also remained constant as a function of PEG content. Thus, CO<sub>2</sub> selectivity of those PEG based membranes had already leveled off when the PEG concentration was between 39 wt% and 67 wt%. Whereas, the networks (3T↓EDDT↑/DDE, D-3T↓4TPEG↑/DDE, B-HDT↓EDDT↑/TTT and D-HDT↓3TPEG↑/TTT) unraveled the effect of lower concentrations of PEG along with the network rigidity and PE placements on CO<sub>2</sub> selectivity values. Figure 2.22 shows the representative plots of CO<sub>2</sub>/CH<sub>4</sub>, CO<sub>2</sub>/O<sub>2</sub> and CO<sub>2</sub>/N<sub>2</sub> selectivities for BPEG/DDE network. All the networks followed a similar behavior in line with BPEG/DDE, thus one such network is shown here. For all networks, the permeability selectivity followed the trend as follows: CO<sub>2</sub>/N<sub>2</sub> > CO<sub>2</sub>/O<sub>2</sub> > CO<sub>2</sub>/CH<sub>4</sub>. The high CO<sub>2</sub>/N<sub>2</sub> is mainly due to the lowest N<sub>2</sub> solubility (making N<sub>2</sub> less permeable). As described in experimental, in solution-diffusion model, permeability can be defined as the product of diffusivity and solubility. Thus, permeability selectivity can be defined as the product of diffusivity selectivity and solubility selectivity.

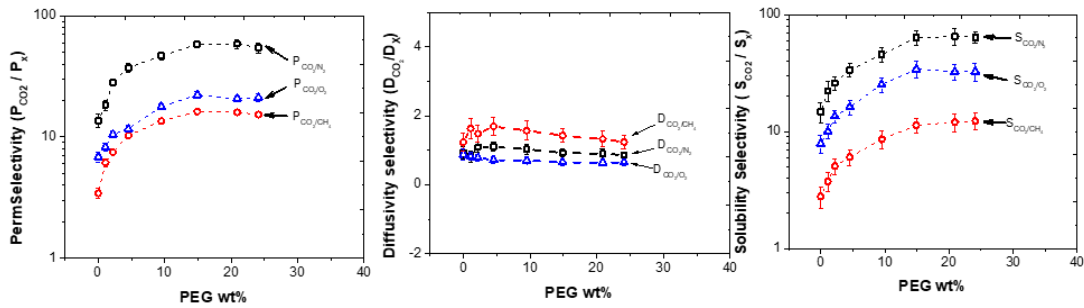


Figure 2.22 (a) Permeability selectivity, (b) Diffusivity selectivity and (c) Solubility selectivity of  $CO_2$  / light gas plotted against PEG wt%.

To explain the selectivity trends better, decoupled selectivity values i.e., diffusivity selectivity and solubility selectivity values were calculated. The diffusivity selectivity for  $CO_2$  remained constant as a function of PEG concentration (Figure 2.22 (b)). Though PEG concentration ( $M_C$ , and flexible polar groups) had a strong influence on gas diffusivity as discussed earlier, the trends were consistent across all gases (the ratio remained the same). Thus,  $CO_2$  gas diffusivity selectivity of the membranes over other gases remained constant. The solubility selectivity of the membranes showed same trends as that of the permeability selectivity curves i.e. the values increased up till 14.9 wt% of PEG, and beyond that the solubility selectivity values showed a plateau as a function of PEG concentration. From 0 wt% to 14.9 wt%, changing PEG concentration increased the solubility of the membranes for  $CO_2$ , and further increase in PEG concentration led to leveling off behavior of  $CO_2$  solubility values. Whereas PEG concentration had minimal influence on solubility of the membranes for other gases such as  $O_2$ ,  $N_2$ ,  $CH_4$  etc. Therefore,  $CO_2$  solubility selectivity of the membranes over other gases increased up till 14.9 wt%, and further increase in PEG concentration had no effect on  $CO_2$  solubility selectivity, simply mimicking the trend shown by  $CO_2$  solubility values. Since the

diffusivity selectivity for CO<sub>2</sub> remained constant and solubility selectivity for CO<sub>2</sub> changed as a function of PEG concentration, the product of these two factors i.e. the trend for overall selectivity for CO<sub>2</sub> as a function of PEG concentration took the same form as that of solubility selectivity for CO<sub>2</sub>. At PEG concentration of 14.9 wt%, the CO<sub>2</sub> selectivity values obtained were comparable to the values that were reported for the membranes in the previous paper (B-3T↓EDDT↑/TEGDVE membranes having PEG concentration 38 wt% to 67 wt%) as shown in Figure 2.22.<sup>3</sup> As mentioned earlier, the permeability selectivity trend was dictated by solubility selectivity, whereas the diffusivity selectivity remained constant closer to unity (shown in Table 2.9).

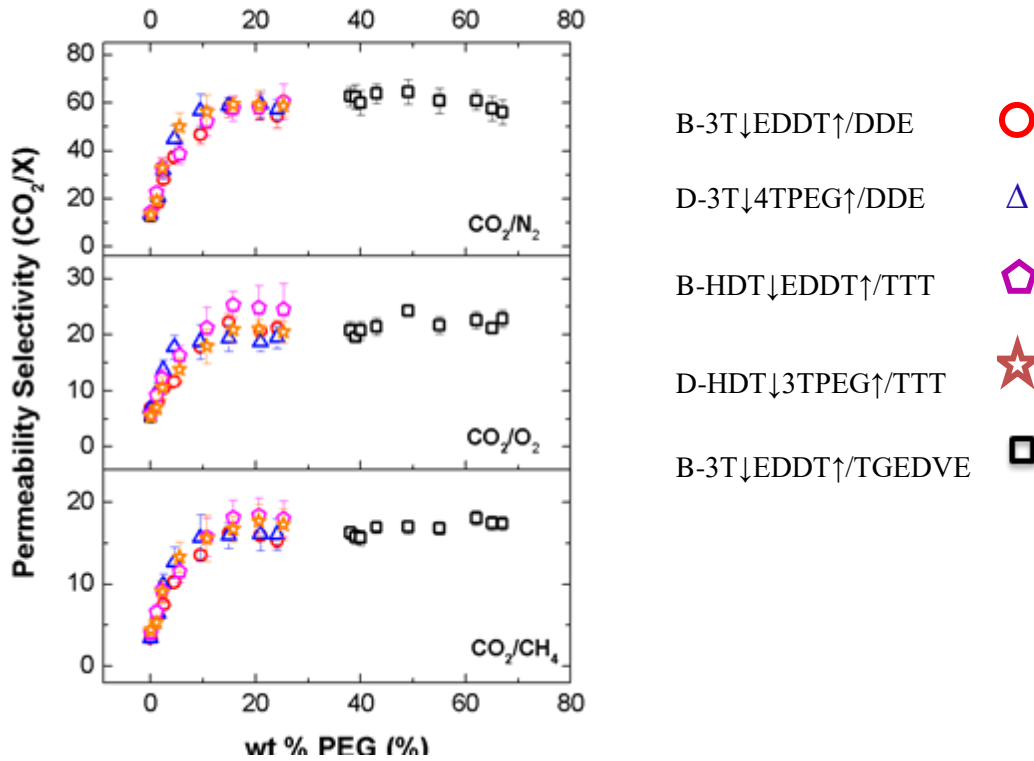


Figure 2.23 Selectivity of CO<sub>2</sub>/N<sub>2</sub>, CO<sub>2</sub>/O<sub>2</sub> and CO<sub>2</sub>/CH<sub>4</sub> for B-3T↓EDDT↑/DDE, D-3T↓4TPEG↑/DDE, B-HDT↓EDDT↑/TTT and D-HDT↓3TPEG↑/TTT following a master trend. Data from previous work B-3T↓EDDT↑/TGEDVE is presented for comparison.

Table 2.10 CO<sub>2</sub>/CH<sub>4</sub>, CO<sub>2</sub>/O<sub>2</sub> and CO<sub>2</sub>/N<sub>2</sub> selectivity values of all networks with calculated propagation of error. Reported values are average of 3 individual runs

Sample Identity	CO <sub>2</sub> /CH <sub>4</sub>						CO <sub>2</sub> /O <sub>2</sub>						CO <sub>2</sub> /N <sub>2</sub>					
	P		D		S		P		D		S		P		D		S	
B-3T↓EDDT↑/DDE-0	3.42 ± 0.327	1.23 ± 0.26	2.79 ± 0.6	6.84 ± 0.61	0.87 ± 0.16	7.899 ± 1.43	13.65 ± 1.72	0.93 ± 0.18	14.76 ± 2.83									
B-3T↓EDDT↑/DDE-1	6.14 ± 0.451	1.63 ± 0.3	3.77 ± 0.69	8.22 ± 0.64	0.82 ± 0.12	10.06 ± 1.44	18.36 ± 1.8	0.82 ± 0.16	22.34 ± 4.28									
B-3T↓EDDT↑/DDE-2	7.51 ± 0.36	1.48 ± 0.24	5.07 ± 0.82	10.52 ± 0.71	0.78 ± 0.09	13.53 ± 1.66	28.12 ± 1.68	1.09 ± 0.14	25.91 ± 3.32									
B-3T↓EDDT↑/DDE-5	10.27 ± 0.555	1.69 ± 0.27	6.06 ± 0.96	11.67 ± 0.74	0.72 ± 0.1	16.25 ± 2.31	37.32 ± 2.82	1.11 ± 0.14	33.64 ± 4.31									
B-3T↓EDDT↑/DDE-10	13.54 ± 0.732	1.57 ± 0.27	8.6 ± 1.47	17.78 ± 0.95	0.7 ± 0.1	25.31 ± 3.71	46.76 ± 3.88	1.03 ± 0.14	45.6 ± 6.13									
B-3T↓EDDT↑/DDE-15	16.2 ± 0.805	1.43 ± 0.19	11.3 ± 1.53	22.22 ± 1.56	0.65 ± 0.1	34.19 ± 5.44	58.16 ± 4.05	0.92 ± 0.12	63.54 ± 8.65									
B-3T↓EDDT↑/DDE-21	15.96 ± 0.73	1.32 ± 0.23	12.08 ± 2.1	20.69 ± 0.89	0.64 ± 0.1	32.54 ± 5.15	58.8 ± 5.13	0.9 ± 0.14	65.12 ± 10.06									
B-3T↓EDDT↑/DDE-24	15.32 ± 0.874	1.24 ± 0.2	12.32 ± 1.98	21.11 ± 1.55	0.65 ± 0.11	32.67 ± 5.56	54.66 ± 5.17	0.86 ± 0.09	63.89 ± 7.02									

Sample Identity	CO <sub>2</sub> /CH <sub>4</sub>						CO <sub>2</sub> /O <sub>2</sub>						CO <sub>2</sub> /N <sub>2</sub>					
	P		D		S		P		D		S		P		D		S	
D-3T↓4TPEG↑/DDE-0	3.42 ± 0.51	1.23 ± 0.25	2.79 ± 0.59	6.84 ± 0.94	0.87 ± 0.19	7.9 ± 1.77	13.65 ± 2.19	0.93 ± 0.21	14.76 ± 3.42									
D-3T↓4TPEG↑/DDE-2	6.41 ± 0.77	1.26 ± 0.24	5.07 ± 0.98	10.29 ± 1.31	0.81 ± 0.22	12.68 ± 3.41	20.87 ± 2.08	0.8 ± 0.18	26.24 ± 6.03									
D-3T↓4TPEG↑/DDE-4	9.92 ± 1.39	1.41 ± 0.3	7.03 ± 1.52	13.71 ± 1.83	0.84 ± 0.14	16.32 ± 2.82	31.96 ± 3.63	1.01 ± 0.24	31.62 ± 7.45									
D-3T↓4TPEG↑/DDE-7	12.65 ± 1.86	1.43 ± 0.32	8.85 ± 2.01	17.78 ± 2.15	0.77 ± 0.18	23.22 ± 5.43	44.99 ± 5.7	1.08 ± 0.23	41.75 ± 9.07									
D-3T↓4TPEG↑/DDE-13	15.67 ± 2.81	1.39 ± 0.26	11.24 ± 2.17	18.76 ± 3.09	0.62 ± 0.13	30.12 ± 6.48	56.59 ± 7.05	1.1 ± 0.2	51.46 ± 9.53									
D-3T↓4TPEG↑/DDE-18	15.93 ± 1.55	1.22 ± 0.28	13.02 ± 3.02	19.41 ± 2.31	0.57 ± 0.14	33.76 ± 8.35	58.85 ± 3.22	0.97 ± 0.23	60.61 ± 14.27									
D-3T↓4TPEG↑/DDE-22	16.11 ± 2.02	1.24 ± 0.24	13.02 ± 2.55	18.7 ± 1.62	0.57 ± 0.09	32.77 ± 5.24	59.26 ± 5.89	0.95 ± 0.18	62.19 ± 12.08									
D-3T↓4TPEG↑/DDE-26	16.06 ± 1.93	1.21 ± 0.2	13.28 ± 2.24	19.53 ± 1.93	0.58 ± 0.12	33.5 ± 6.7	57.17 ± 4.46	0.95 ± 0.14	60.06 ± 9.01									



Sample Identity	CO <sub>2</sub> / CH <sub>4</sub>						CO <sub>2</sub> / O <sub>2</sub>						CO <sub>2</sub> / N <sub>2</sub>														
	P		D		S		P		D		S		P		D		S										
B-HDT↓EDDT↑TTT-0	4.06	±	0.46	1.52	±	0.26	2.67	±	0.47	5.9	±	0.61	0.87	±	0.12	6.77	±	0.91	14.3	±	1.41	1.27	±	0.22	11.21	±	1.95
B-HDT↓EDDT↑TTT-1	6.64	±	0.81	1.47	±	0.26	4.53	±	0.8	9.22	±	1.04	0.98	±	0.17	9.43	±	1.7	22.5	±	2.39	1.16	±	0.22	19.4	±	3.66
B-HDT↓EDDT↑TTT-3	9.29	±	1.22	1.51	±	0.24	6.13	±	0.99	12.25	±	1.56	0.93	±	0.16	13.12	±	2.26	32.92	±	4.16	1.17	±	0.18	28.16	±	4.46
B-HDT↓EDDT↑TTT-5	11.53	±	1.35	1.45	±	0.16	7.95	±	0.91	16.31	±	1.83	0.91	±	0.15	17.97	±	3.03	38.61	±	4.08	1.03	±	0.16	37.37	±	5.79
B-HDT↓EDDT↑TTT-11	15.75	±	2.34	1.41	±	0.23	11.17	±	1.91	21.2	±	3.75	0.84	±	0.13	25.19	±	3.95	52.28	±	6.14	0.99	±	0.15	52.68	±	8.53
B-HDT↓EDDT↑TTT-16	18.11	±	2.19	1.31	±	0.22	13.81	±	2.38	25.31	±	2.46	0.79	±	0.13	32	±	5.15	57.68	±	5.13	0.96	±	0.12	60.35	±	7.44
B-HDT↓EDDT↑TTT-21	18.37	±	2.14	1.28	±	0.13	14.34	±	1.49	24.84	±	4.01	0.67	±	0.09	36.85	±	5.25	57.97	±	5.09	0.95	±	0.09	60.88	±	5.85
B-HDT↓EDDT↑TTT-25	17.95	±	2.21	1.24	±	0.24	14.45	±	2.9	24.57	±	4.56	0.66	±	0.13	37.15	±	7.21	60.51	±	7.34	1.02	±	0.19	59.24	±	11.57

Sample Identity	CO <sub>2</sub> / CH <sub>4</sub>						CO <sub>2</sub> / O <sub>2</sub>						CO <sub>2</sub> / N <sub>2</sub>														
	P		D		S		P		D		S		P		D		S										
D-HDT↓3TPEG↑/TTT-0	4.43	±	0.66	1.3	±	0.26	2.57	±	0.54	5.49	±	0.75	0.64	±	0.14	6.52	±	1.46	13.3	±	2.13	0.84	±	0.19	10.76	±	2.49
D-HDT↓3TPEG↑/TTT-2	5.35	±	0.64	1.16	±	0.22	4.61	±	0.89	7.08	±	0.9	0.54	±	0.15	13.21	±	3.55	19.26	±	1.92	0.8	±	0.18	24.13	±	5.55
D-HDT↓3TPEG↑/TTT-4	9.11	±	1.28	1.2	±	0.26	7.59	±	1.64	10.54	±	1.41	0.55	±	0.09	19.04	±	3.29	32.92	±	3.74	0.92	±	0.22	35.67	±	8.4
D-HDT↓3TPEG↑/TTT-7	13.32	±	1.96	1.47	±	0.33	9.07	±	2.06	13.81	±	1.67	0.56	±	0.13	24.44	±	5.72	50.09	±	6.35	1.02	±	0.22	49.14	±	10.68
D-HDT↓3TPEG↑/TTT-3	15.61	±	2.8	1.56	±	0.29	10.01	±	1.93	18	±	2.97	0.6	±	0.13	29.84	±	6.42	56.29	±	7.01	1.04	±	0.19	54.04	±	10.01
D-HDT↓3TPEG↑/TTT-8	16.74	±	1.63	1.43	±	0.33	11.69	±	2.71	20.94	±	2.49	0.7	±	0.17	30.01	±	7.42	59.26	±	3.24	1.02	±	0.24	58.34	±	13.73
D-HDT↓3TPEG↑/TTT-22	17.73	±	2.22	1.35	±	0.26	13.17	±	2.58	21.09	±	1.83	0.67	±	0.11	31.4	±	5.02	59.15	±	5.88	1	±	0.19	59.07	±	11.47
D-HDT↓3TPEG↑/TTT-26	17.3	±	2.08	1.36	±	0.22	12.77	±	2.15	20.46	±	2.02	0.66	±	0.14	31.09	±	6.22	58.8	±	4.59	1.04	±	0.15	56.4	±	8.46

### 2.3.8 Literature values comparison

As mentioned in the background section, for a polymer to be used as a separation membrane, it should possess high selectivity along with high permeability. To enhance the selectivity, the use of polar PEG moieties has been identified and blending,<sup>8-15</sup> copolymerizing<sup>16-28</sup> and crosslinking<sup>8,29-36</sup> strategies are being used to suppress the crystallinity thus enhancing the permeability.

To the best of our knowledge, there exists no systematic study where the PEG concentration has been varied to determine the effect on selectivity. All the reported studies aim to fabricate an amorphous membrane while containing maximum PEG content. This is because, with addition of PEG, along with specific polar interaction, the flexible ether link can enhance the permeability. But the focus of this study is to determine the minimum amount of PEG to achieve maximum selectivity, there by the permeability can be enhanced with the use of other flexible moieties such as siloxane.

Table 2.11 shows several strategies (copolymerizing, blending and crosslinking) reported in literature to prevent poly(ethylene oxide) (PEO) from crystalizing. Semi-crystalline PEO is also reported for comparison.

Table 2.11 Reported literature values for amorphous PEO membranes on CO<sub>2</sub> permeability and CO<sub>2</sub>/N<sub>2</sub> selectivity

	Polymer	PEO Cont ent Wt%	T <sub>g</sub>	Δp (atm)	Testing Temperature (°C)	P <sub>CO<sub>2</sub></sub> (barrer)	Selectivity (CO <sub>2</sub> /N <sub>2</sub> )	Ref
	Semi-Crystalline PEO	100	-52			12	48	16
<b>Block-Copolymers</b>	P10: PMDA-pDDS/PEO4(80)	68.6	-62.0	2.0	35	238.0	49.0	22
	B1: BPDA-ODA/DABA/PEO1(75)	41.2	-36.0	2.0	35	2.7	56.0	
	M1: MDI-BPA/PEG(75)	53.6	-42.0	2.0	35	31.0	44.0	
	M2: MDI-BPA/PEG(80)	60.5	-41.0	2.0	35	48.0	47.0	
	M3: MDI-BPA/PEG(85)	66.0	-41.0	2.0	35	59.0	49.0	
	L3: L/TDI(20)-BPA/PEG(90)	64.5	-43.0	2.0	35	47.0	51.0	
	I4: IPA-ODA/PEO3(80)	68.3	-45.0	2.0	35	58.0	53.0	
	B5: BPDA-ODA/DABA/PEO2(70)	43.3	-42.0	2.0	35	14.0	57.0	
	B6: BPDA-ODA/DABA/PEO2(80)	53.4	-44.0	2.0	35	36.0	56.0	
	B7: BPDA-ODA/PEO3(75)	52.3	-56.0	2.0	35	75.0	52.0	
	B13: BPDA-mPD/PEO4(80)	53.1	-61.0	2.0	35	81.0	54.0	
	P5: PMDA-mPD/PEO3(80)	55.9	-62.0	2.0	35	99.0	50.0	
	P6: PMDA-APPS/PEO3(80)	68.3	-55.0	2.0	35	159.0	51.0	
	P7: PMDA-APPS/PEO4(70)	61.2	-66.0	2.0	35	136.0	53.0	
	P8: PMDA-mPD/PEO(80)	58.9	-61.0	2.0	35	151.0	52.0	
	P9: PMDA-ODA/PEO4(80)	66.6	-62.0	2.0	35	167.0	52.0	
	PEO-ran-PPO <sub>5000</sub> -T6T6T- 0	64.3	-58.0	1.0	35	447.0	42.5	
	PEO-ran-PPO <sub>5000</sub> -T6T6T-10	65.9	-61.0	1.0	35	583.0	39.9	
PEO-ran-PPO <sub>5000</sub> -T6T6T-30	69.0	-64.0	1.0	35	731.0	36.7		

	PEO-ran-PPO <sub>5000</sub> -T6T6T-50	72.2	-67.0	1.0	35	896.0	36.0	
	PEO <sub>1000</sub> -T6T6T	61.6	-45.0	3.9	35	75.0	41.0	23
	PEO <sub>2000</sub> -T6T6T	76.2	-48.0	3.9	35	180.0	49.0	
	PEO <sub>2000</sub> /T <sub>2500</sub> -T6T6T	69.0	-44.0	3.9	35	121.0	49.0	
	PEO <sub>2000</sub> /T <sub>5000</sub> -T6T6T	74.8	-43.0	3.9	35	176.0	53.0	
	Pebax <sup>®</sup> 1074 (55PEO/PA12)	55.0	-55.0	10.0	35	120.0	51.4	24
	Pebax <sup>®</sup> 4011 (57PEO/PA12)	57.0	-55.0	10.0	35	66.0	56.4	
	Polyimide (PMDA-pDDS)	68.6	n/d	2.0	35	238.0	49.0	16
	Polyimide (BPDA-ODA)	62.3	n/d	2.0	35	117.0	51.0	
	Polyamide (IPA-ODA)	68.3	n/d	2.0	35	58.0	53.0	
	Polyamide (PA 12)	55.0	n/d	10.0	35	120.0	51.0	
	Polyamide (PA 6)	57.0	n/d	10.0	35	66.0	56.0	
	Polyurethane (MDI-BA)	60.5	n/d	2.0	35	48.0	47.0	

<b>PEO blends</b>	Poly(amide-b-ethylene oxide)	50.0	n/d	0.0	30	151.0	47.0	10
	Poly(ethylene oxide)- poly(butylenes terephthalate)	40.0	n/d	0.3	30	750.0	40.0	11
	Poly(styrene-b-ethylene oxide-b-styrene)	45.0	n/d	0.0	35	86.0	36.0	8

<b>Crosslinked PEO</b>	DM14/MM9(0)	80.0	-42.0	0.97	25	65.0	53.0	32
	DM14/MM9(10)	80.0	-44.0	0.97	25	85.0	54.0	
	DM14/MM9(30)	80.0	-51.0	0.97	25	129.0	51.0	
	DM14/MM9(50)	79.9	-56.0	0.97	25	185.0	50.0	

	DM14/MM9(70)	79.9	-62.0	0.97	25	260.0	48.0	
	DB30/MM9(0)	78.4	-47.0	0.97	25	128.0	49.0	
	DB30/MM9(10)	78.5	-49.0	0.97	25	140.0	50.0	
	DB30/MM9(30)	78.8	-54.0	0.97	25	185.0	51.0	
	DB30/MM9(50)	79.1	-58.0	0.97	25	231.0	48.0	
	DB30/MM9(70)	79.4	-62.0	0.97	25	308.0	47.0	
	DM9/MM9(10)	72.8	-34.0	0.97	25	28.0	53.0	
	DM23/MM9(10)	86.1	-57.0	0.97	25	194.0	52.0	
	DB10/MM9(10)	57.2	-14.0	0.97	25	12.0	48.0	
<b>UV- Crosslink ing</b>	XLPEGDA (100 wt.%)	83.0	-40	ID	35	110.0	50.0	31
	XLPEGDA (80 wt.%)	83.0	-42	ID	35	110.0	52.0	
	XLBPAEDA4 (100 wt.%)	51.2	11	ID	35	12.0	55.0	
	BPAEDA4 (85 wt.%) /PEGMEA	55.5	-	ID	35	23.0	50.0	
	BPAEDA4 (70 wt.%) /PEGMEA	59.9	-	ID	35	54.0	45.0	
	BPAEDA4 (50 wt.%) /PEGMEA	65.8	-	ID	35	132.0	44.0	
	BPAEDA4 (25 wt.%) /PEGMEA	73.1	-	ID	35	288.0	52.0	
	XLBPAEDA15 (100 wt.%)	79.7	-34	ID	35	152.0	54.0	
	BPAEDA15 (80 wt%)/PEGMEA	79.8	-39	ID	35	198.0	57.0	
	BPAEDA15 (70 wt%)/PEGMEA	79.9	-41	ID	35	221.0	53.0	
	BPAEDA15 (60 wt%)/PEGMEA	80.0	-44	ID	35	261.0	56.0	
	BPAEDA15 (50 wt%)/PEGMEA	80.0	-	ID	35	300.0	51.0	
	BPAEDA15 (80 wt%)/DEGEEA	73.2	-38	ID	35	197.0	49.0	
	BPAEDA15 (70 wt%)/DEGEEA	70.0	-38	ID	35	205.0	43.0	
	BPAEDA15 (60 wt%)/DEGEEA	66.8	-38	ID	35	252.0	43.0	
BPAEDA15 (50 wt%)/DEGEEA	63.5	-	ID	35	270.0	46.0	37	

Figure 2.24 represents a comparison of reported values in the literature with the values obtained in this work. As seen, selectivity of all literature reported values (for copolymers, blends and crosslinked networks) are in the range between 30 to 55 units while the PEG loading was no less than 40 wt %. Whereas in this work the CO<sub>2</sub>/N<sub>2</sub> selectivity reaches around 60 with just 15 wt% PEG for all networks in this study irrespective of the network rigidity and placement of PEG. Thus, with much less addition of PEG, the desired selectivity can be achieved, while the permeability can be increased via adding more flexible moieties such as siloxane in the network. Also, interestingly, the selectivity values for all thiol-based networks showed an increased selectivity values as compared to the reported literature values probably attributed to the uniform distribution of PEG in thiol-ene based networks.

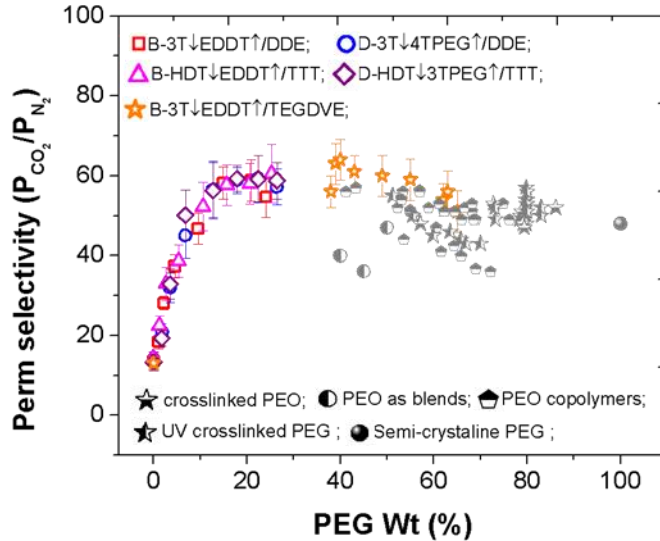


Figure 2.24 Permeability selectivity of CO<sub>2</sub>/N<sub>2</sub> plotted against PEG wt%. Half-filled indicates the reported literature values ( Table 2.11)

### 2.3.9 Pressure dependencies

In the previous sections, we determined the selectivity of all the network (with varied architecture) followed a master curve which leveled off at around 15 PEG wt% at an applied feed pressure for 3 atm. The leveling off depends on the ratio of molar concentration of CO<sub>2</sub> to the available to interact with PEG units. Thus, obviously the minimum amount PEG concentration required for achieving maximum CO<sub>2</sub> solubility would depend on the CO<sub>2</sub> concentration in the feed (i.e CO<sub>2</sub> partial pressure in the feed). In the following section, we aim in determining if the selectivity master curve is affected by the applied feed pressure i.e., the concentration of CO<sub>2</sub> gas.

D-3T↓4TPEG↑/DDE networks were considered for pressure dependent studies because the *Mc* is maintained constant while increasing the PEG content as dangling chains. This design gave the exclusive effect on PEG concentration while the number of junction points remained the same. The upstream pressure was varied from 2 tm to 12.45 atm with increments of 2 atm while maintaining the experimental temperature as 23°C to probe the concentration effect on gas transport properties. For simplicity, only three gases (CO<sub>2</sub>, N<sub>2</sub> and CH<sub>4</sub>) was studied and selectivities of CO<sub>2</sub>/ N<sub>2</sub> and CO<sub>2</sub>/O<sub>2</sub> were estimated.

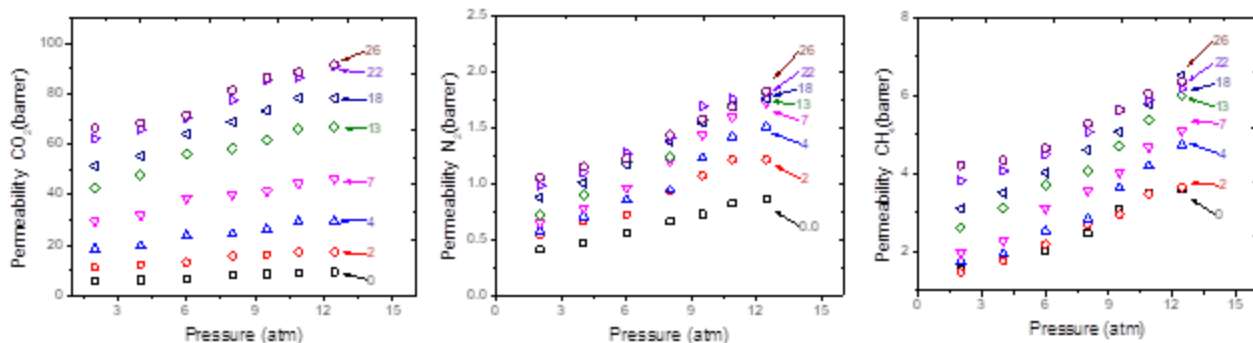


Figure 2.25 Permeability of (a)CO<sub>2</sub>, (b)N<sub>2</sub> and (c) CH<sub>4</sub> of D-3T↓4TPEG↑/DDE networks plotted against applied pressure feed pressure.

As seen in Figure 2.25, with increase in applied pressure the permeabilities of all gasses increased. The rate of increase (slope) of permeability of CO<sub>2</sub> gas with applied feed pressure in a non-polar membrane is much lower than the rate of increase in a polar PEG based membrane. This might be due to the combined effect of increased diffusivity which happens due to increased flexibility imparted by polar ether groups and increased solubility because of increasing polarity arising from PEG units with CO<sub>2</sub> gas. However, the rate of increase in permeability for N<sub>2</sub> and CH<sub>4</sub> gas remains constant with applied feed pressure i.e., the rate of increase is same irrespective of the nature of the membranes (polar or non-polar). This increase in permeability is exclusively due to the increased diffusivity of gases through the membrane.

The permeability values obtained from the steady state slope (from CVVP) were deconvoluted to diffusivity and solubility as explained in experimental session. But, it has been reported that the Fickian diffusion deviates when the permeation coefficient varies with applied feed pressure. Thus solubility co-efficient for all DPEG/DDE networks were calculated via direct sorption measurements using dual chamber pressure decay method



explained in experimental section. This method typically determines the number of moles of gas sorbed in the given volume of polymer at a given partial pressure (concentration).

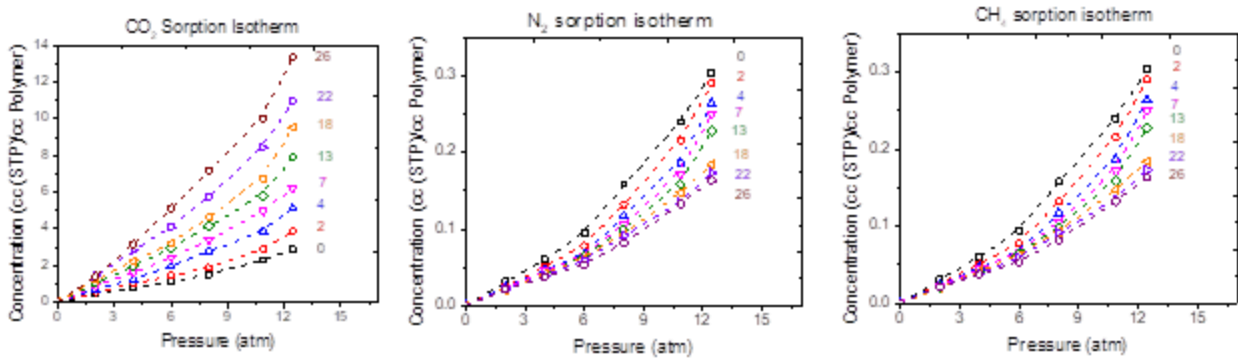


Figure 2.26 Sorption isotherm of D-3T↓4TPEG↑/DDE demonstrating the Henry mode of sorption at lower feed pressure. Each curve represents the network exposed at varied feed pressure. The lines shown is to guide the eyes

Figure 2.26 represents the sorption isotherms of CO<sub>2</sub>, N<sub>2</sub> and CH<sub>4</sub> gases at increasing applied pressure. For polar CO<sub>2</sub> gas, the slope of the isotherm increases with increasing PEG content and the concentration at a given feed pressure increases with PEG content in the membrane. This is mainly because of the increased interaction of CO<sub>2</sub> gas with polar PEG moieties causing an increasing sorption sites. On the other hand, the concentration of non-polar gases such as N<sub>2</sub> and CH<sub>4</sub> decreases with increasing polar PEG content. This is in agreement with the observed results explained in section 4.1.5, where the solubility of N<sub>2</sub> gas decreases with increasing PEG content. All three gases follows Henry mode of sorption at low feed pressure (upto 8 atm) beyond which it deviates. For the networks with high PEG content, the deviation from the Henry mode of sorption was lesser for N<sub>2</sub> and CH<sub>4</sub> gas. The extraction of solubility coefficient in Henry mode regime was taken in to account, while at higher feed pressure, the calculations considers the Flory-Huggins interaction parameter which is beyond the scope

of this work. Hence the obtained concentration values were used to calculate solubility at 3.6 atm which was only used as a complementary method to confirm the values obtained through CVVP.

The solubility co-efficient obtained from dual mode sorption at 3.6 atm was compared with the solubility values calculated from CVVP and presented in Figure 2.27 for all three gases (CO<sub>2</sub>, N<sub>2</sub> and CH<sub>4</sub>). As seen, the solubility values obtained through both the methods were in good agreement and the values dictates that the calculated solubility values through CVVP for all previous studies represents the true solubility co-efficient of that particular network.

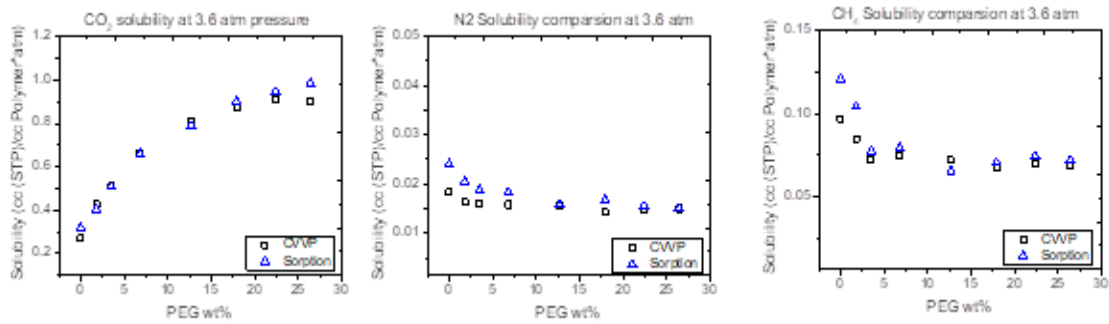


Figure 2.27 Comparison of solubility co-efficient of D-3T↓4TPEG↑/DDE (a) CO<sub>2</sub> (b) N<sub>2</sub> and (c) CH<sub>4</sub> determined via CVVP and sorption technique.

The other interesting factor observed with applied feed pressure is that for a given pair of gas (CO<sub>2</sub>/N<sub>2</sub> and CO<sub>2</sub>/CH<sub>4</sub>) the permeability selectivity deviates from the master curve (trend seen at an applied feed pressure of 3.4 atm). With increasing feed pressure, the permeability selectivity decreases and at highest applied feed pressure (12.45 atm in this study) the selectivity didn't level off. This is mainly due to the increased concentration of the gas molecules which probably required a greater number of moles of PEG to saturate to reach the levelling off. Probably with high PEG content membranes,

the selectivity could level off at the high applied feed pressure considering the increase in molar CO<sub>2</sub> gas concentration.

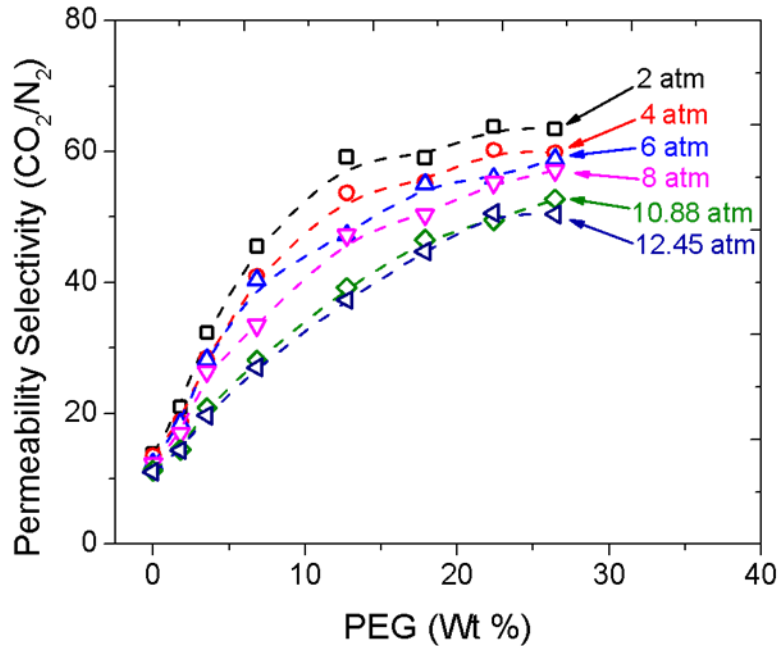


Figure 2.28 Permeability selectivity of D-3T↓4tPEG↑/DDE networks, at different feed pressures, plotted against PEG wt%. At 2 atm feed pressure, permeability selectivity levels off at around 12 wt%, whereas with 12.45 atm applied feed pressure, the permeability. Lines shown here is only to guide eyes.

The ratio of concentration of PEG to the concentration of CO<sub>2</sub> gas was theoretically calculated to be 23.9 (PEG to CO<sub>2</sub> gas ratio) which corresponded to about 0.0017 mol of PEG/ volume of polymer. Thus at higher feed pressure, the CO<sub>2</sub> gas concentration becomes very high that the ratio is altered which makes the selectivity to level off at higher PEG content.

## 2.4 Conclusions

Series of crosslinked thiol-ene networks with varying PEG content, from 0 to 25 wt%, was prepared. All the network series varied in glass transition, crosslink density and the placement of PEG units within the network series. Permeability was determined via steady-state permeation apparatus and diffusivity was determined via time lag method. Solubility co-efficient were calculated and confirmed with direct sorption measurements. The selectivity values were calculated for gas pairs, (CO<sub>2</sub>/N<sub>2</sub>, CO<sub>2</sub>/CH<sub>4</sub> and CO<sub>2</sub>/O<sub>2</sub>). The flux through the membrane increases with increase in PEG content for all the networks primarily due to increase in diffusivity in combination with solubility. The increase in diffusivity within BPEG/DDE networks is attributed to the increase in molecular weight between crosslinks (Mc) and the decrease at high Mc is due to crystallization. In BPEG/TTT, with the Mc unaltered, the diffusivity increase is associated with the flexible ether linkage with increasing PEG units. In networks DPEG/TTT and DPEG/DDE (PEG in the dangling chains), the increase in diffusivity is mainly attributed to the increase in free-volume cause by the free moving dangling chain ends. The solubility of polar CO<sub>2</sub> gas increased with increasing PEG content and the solubility decreased with increasing PEG content for non-polar gases such as O<sub>2</sub>, N<sub>2</sub> and CH<sub>4</sub>.

Interestingly the selectivity values obtained were independent of the glass transition temperature, cross-link density and the placement of PEG units (backbone or dangling chain) which followed a master trend and the selectivity leveled off for all the gas pairs at around 15 wt% of PEG. As mentioned earlier, a membrane should possess high selectivity along with high permeability to be used in separation process. To the best of our knowledge, all reported studies utilizes PEG units for two reasons: to increase selectivity (caused via increased acid-base interaction) and to achieve increased

permeability (through the flexible ether groups). With the findings that the selectivity can be achieved by utilizing much low content of PEG, a high permeability co-efficient without compromising the selectivity can be achieved by utilizing more flexible and high free volume moieties such as siloxane and fluorinated compounds in combination with the PEG moieties at a minimum concentration.

It was also determined that the applied feed pressure affects the minimum PEG required for the maximum selectivity. Model network, DPEG/DDE, was exposed at varied feed pressure and permeability values were determined via steady-state permeation apparatus. With increasing feed pressure, the permeability coefficient for all gases increased. Interestingly, the feed pressure decreased CO<sub>2</sub>/ light gas selectivity. For reduced feed pressure (2atm), the CO<sub>2</sub>/ light gas selectivity reached maximum at around 14 wt% while for high feed pressure (12.45 atm), the selectivity doesn't level off for the quantity of PEG used in this study. This is attributed to the ratio of number of PEG units to saturate the CO<sub>2</sub> molar volume of the gas is altered with increased concentration We hypothesize that at high feed pressure, the selectivity would reach maximum at much high PEG weight loadings (when the ratio is achieved).

Knowing these details, one could tune the membranes performance by selecting the appropriate content of PEG in combination with other high free volume materials to achieve high permeability and selectivity which can be used for CO<sub>2</sub>/ light gas separations.

CHAPTER III – FUNDAMENTAL INVESTIGATION OF FLAMMABILITY OF  
THIOL-ENE NETWORKS: EFFECT OF NETWORK STRUCTURE AND  
ARCHITECTURE

**Abstract**

Thermal and fire behavior properties of UV-cured thiol-ene networks are reported. A family of photocured thiol-ene networks are fabricated by reacting thiol and ene monomers of various functionality (2-4) and structural rigidity. The glass transition temperatures ( $T_g$ ) of the cross-linked networks are studied using a DSC.  $T_g$  values range from  $-33$  to  $54$  °C and are dependent on both, network composition and degree of cross-linking. TGA experiments reveal that the onset as well as the mid-point temperatures of degradation occur at lower temperatures for the networks fabricated using the di functional thiol monomer as compared to tri or tetra functional thiol based networks. Reaction-to-fire properties are investigated using a cone calorimeter. The peak heat release rate (PHRR) values span between  $700$ - $1800$  kW/m<sup>2</sup> and 4T-TTT, the network fabricated using a tetra functional thiol (4T) and an allyl isocyanurate ene monomer (TTT) shows the lowest PHRR, at about  $700$  kW/m<sup>2</sup>, and the longest time to sustained ignition at about  $54$  s in this series of thiol-ene networks. The burning specimens were extinguished and quenched in liquid nitrogen and the morphology of incompletely burned specimen with progressing time is analyzed. A correlation between the morphology of burning specimen and cone parameters like PHRR, AMLR and smoke is presented and related to thiol-ene chemical group rigidity and network linking density. Finally, scanning electron microscopy (SEM) of partially burnt specimen revealed that the networks fabricated with structurally similar monomers shows distinct pyrolysis

behavior. Networks containing allyl triazine (TOT) showed bulk pyrolysis behavior due to the early degradation happening at the C-O bond along the backbone of the network. Networks with allyl isocyanurate (TTT) showed a surface pyrolysis due to its aliphatic linking chain along the backbone. The chemical composition of partially burnt networks, examined via SEM equipped with energy dispersive X-ray analysis (EDAX) served as a means of quantitative analysis for pyrolysis zone. EDAX analysis of TOT containing networks quenched at 20 s in liquid nitrogen revealed that the bulk zone of the network contained higher concentrations of carbon and oxygen compared to the neat unburnt systems indicating the start of bulk degradation. Whereas the networks containing TTT, the bulk zone had carbon, oxygen and sulfur closer to the neat network indicating that the bulk was still intact.

### **3.1 Background**

UV-cured polymeric materials have the capability of responding to this intensive demand of new polymers with advanced properties because of the several types of polymers that can be produced in a matter of minutes.<sup>136</sup> The success of UV-curing is largely due to its inherent advantages such as high energy efficiency compared with other processing methods, eco-friendly 100% reactive component formulations that do not emit VOCs, as well as the flexibility of spraying, dipping, or rolling on a reactive mixture and then curing in seconds with UV light.<sup>137,138</sup>

The majority of UV-cured materials used commercially are acrylates which undergo a UV-initiated, free-radical, chain-growth polymerization mechanism to form crosslinked network materials, finding application in many areas including the fabrication of adhesives, inks, protective films on floors and wood products, coatings on compact

discs, and optical fibers.<sup>76,139</sup> This field is developing fast and being widely used in many fields.

Thiol-enes are a class of UV-cured networks where thiols add to double bonds (enes). Like acrylates, thiol-enes also undergo a UV-initiated, free-radical mechanism. However, the UV-photoinitiated thiol-ene reaction, recognized as a “click” reaction,<sup>140–142</sup> is a unique step-growth reaction<sup>53,143</sup> with a chain transfer step: carbon-centered radicals, instead of propagating to each other via chain-growth, abstract hydrogen from thiols, regenerating thiyl radicals which continue the polymerization process. Because of this hydrogen-abstraction step, thiol-ene are almost completely insensitive to oxygen.<sup>144</sup> Peroxy radicals formed during polymerization in air are generally unreactive toward double bonds, but readily abstract hydrogen from thiols. Indeed it has been shown that polymerization rates of thiol-ene in air and in inert nitrogen are nearly comparable. Thiol-ene networks are also generally optically clear, flexible, and robust. In addition to the above merits, thiol-ene provide an excellent platform for studying structure property relationships in networks due to the uniformity, low shrinkage, lack of crystallinity, and the ability to tune properties like  $T_g$ , modulus, hardness, and gas barrier over enormous ranges simply by mixing and matching commercial thiols and enes.<sup>145,146</sup>

As far as we are aware, there are no reports on the inherent flammability of commercially-available UV-cured thiol-ene networks and also very little work has been done on the flammability of commercial UV-cured acrylates<sup>147</sup> or urethanes.<sup>101,148</sup> Several research groups have focused on fire retardant additives like phosphorous compounds in UV-cured coatings.<sup>149,150</sup> However there is a lack of fundamental, starting-point analysis of the reaction-to-fire properties of commercial UV-cured polymeric



materials. We feel that this information could allow UV-curing to expand into even more fields, perhaps as UV-cured flame-retardant coatings for flammable polymers or as stand-alone bulk flame-resistant materials. Thus, the purpose of this work is to study the flammability of thiol-ene networks fabricated using common and commercially available thiol and ene monomers. Next, this work aims to identify fundamental structure-flammability relationships and set a baseline for further development in this field.

In this study, a series of thiol-ene networks are prepared from three chemically similar di, tri, and tetra functional thiol propionate ester monomers and three tri-functional ene monomers, i.e., an allyl ether, an allyl triazine, and an allyl isocyanurate. The thermal and fire behavior properties of thiol-ene networks are investigated with an emphasis to reveal the effect of thiol functionality and ene rigidity on  $T_g$ , thermal stability (gravimetric analysis) and reaction-to-fire properties in cone tests. To rationalize the data, thermal behavior trends and fire retardant properties are organized in groups. Within the group, the ene monomer is kept the same while the thiol functionality varies from 2-4. The morphology of incompletely combusted films is analyzed and used to gain additional insight into the burning behaviors of the networks. Finally, using two structural isomeric ene monomers, TTT and TOT, the relationships between the morphology of final char residues and fire performance is further investigated.

## **3.2 Experimental**

### **3.2.1 Materials**

Ethylene bis(3-mercaptopropionate) [2T], trimethylolpropane tris(3-mercaptopropionate) [3T] and pentaerythritol tetrakis (3-mercaptopropionate) [4T] were obtained from Bruno Bock Thiol-Chemical-S. Pentaerythritol allyl ether [TAE], 2,4,6-

triallyloxy-1,3,5-triazine [TOT], Triallyl-1,3,5-triazine-2,4,6 (1H,3H,5H)-trione [TTT] and photo initiator 2,2-Dimethoxy-2-phenylacetophenone (DMPA) were purchased from Sigma Aldrich chemical company. All materials were used as received. The chemical structures of various monomers used in this study are shown in Figure 3.1

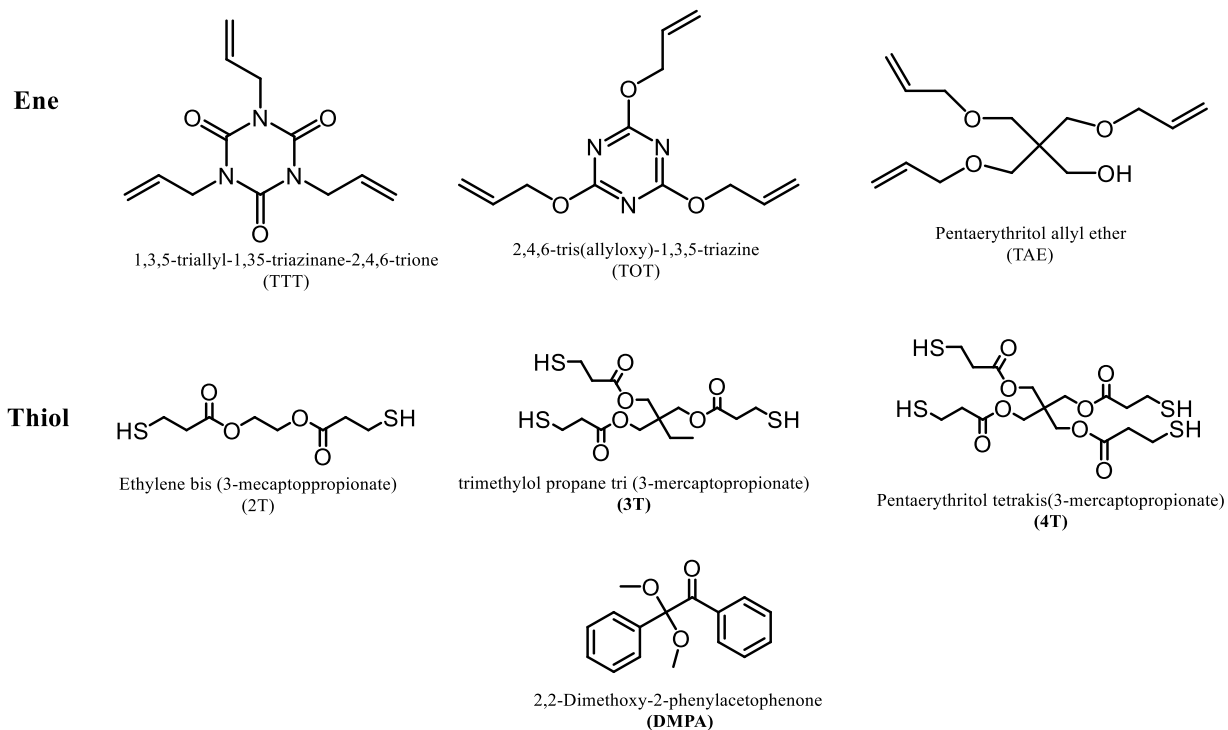


Figure 3.1 Chemical structures of monomers used in investigate FR properties of thiol-ene networks

### 3.2.2 Membrane fabrication and rational for the design

Several thiol-ene model networks were prepared from three chemically similar di, tri and tetra functional thiol propionate ester monomers and three tri-functional ene monomers. This study is intended to investigate the effect of thiol functionality and ene rigidity on glass transition temperature ( $T_g$ ), thermal stability and fire-resistant behavior. To rationalize the data, thermal behavior trends and fire-resistant properties are organized in groups as shown in Table 1. Within the group, the ene monomer is kept the same while

the thiol functionality varies from 2-4. The morphology of incompletely combusted films is analyzed and used to gain additional insight into the burning behaviors of the networks. Finally, using two structural isomeric ene monomers, TTT and TOT, the relationships between the morphology of final char residues and fire performance is further investigated. Each network is identified by its unique name to differentiate and the naming scheme is adopted with a prefix being thiol monomer and a suffix with the respective ene monomer used in the network.

Table 3.1 Network Description

Thiol		Ene		Network name
Monomer	functionality	Monomer	functionality	
2T	2	TAE	3	2T-TAE
3T	3	TAE	3	3T-TAE
4T	4	TAE	3	4T-TAE
2T	2	TTT	3	2T-TTT
3T	3	TTT	3	3T-TTT
4T	4	TTT	3	4T-TTT
2T	2	TOT	3	2T-TOT
3T	3	TOT	3	3T-TOT
4T	4	TOT	3	4T-TOT

All networks were prepared in a similar fashion demonstrated by our group elsewhere,<sup>151</sup> where thiol and ene monomers were added in stoichiometric quantities along with 1 wt% DMPA photo- initiator in a vial relative to the total amount of thiol and ene, which was mixed in vortexer followed by sonication (using a general purpose, cleaning type sonicator) for about 10 minutes to ensure that photo-initiator was dissolved and to remove any air bubbles trapped in the mixture. This homogeneous, bubble free mixture was poured into a preformed glass mold (100 x 100 x 3 mm<sup>3</sup>) and UV-cured for 3 minutes in the air using a low-pressure mercury lamp (wavelength 305 nm and light

intensity  $\sim 0.1 \text{ mW/cm}^2$ ). The films were post-cured for 1 day at 80°C to ensure maximum conversion of the functional groups.

### 3.2.3 Characterization

TGA was performed on a Q500 thermogravimetric analyzer (TA Instruments Inc.) at the 10 mg scale under a flowing nitrogen atmosphere at a scan rate of 10 °C/min. Temperature is reproducible to  $\pm 1$  °C and mass to  $\pm 0.2\%$ . TGA experiments were done in duplicate and the averages are reported.

The glass transition temperatures ( $T_g$ )s of the networks were obtained using a differential scanning calorimeter, a DSC Q100 (TA DSC). All samples (specimen mass of approximately 10 mg) were subjected to the following heating/cooling profile: the sample was cooled from 25 to -70 °C at 10 °C/min. Next, the sample was maintained for 1 minute at -70 °C, and then heated from -70 to 150 °C to obtain the first heat-flow result. The sample was subsequently cooled at 10 °C/min from 150 back to -70 °C. For the second time, the sample was maintained for 1 minute at -70 °C, and then reheated from -70 to 150 °C to obtain the second heat-flow result. The second heating scans are reported and the inflection point of the heat flow at the glass transition was conventionally assigned to  $T_g$ .

A Govmark cone calorimeter was used to investigate the reaction-to-fire properties of the networks in compliance with ASTM E 1354-90. A detailed description of Cone calorimeter is given in Chapter 7 of this thesis. The standard heat flux for this investigation was 50 kW/m<sup>2</sup> and the exhaust flow was set at 24L/sec. All cone specimens (sample size: 100 mm x 100 mm x 3 mm) were tested in a horizontal position. Typical

results from cone calorimetry are reproducible to within about  $\pm 10\%$ ; these uncertainties are based on many runs in which thousands of samples have been combusted.

To investigate the fire propagation through the bulk of polymer, the combustion was freeze quenched by immersing the burning polymer specimen in to liquid nitrogen at various time intervals, say 5, 10, 15 and 20 seconds. The resulting specimen with partial char on the surface was cryo-fractured and cut to a small size of dimension approximately 1 mm x 1 mm x 2 mm, to examine the cross-section in order to understand the fire propagation using scanning electron microscope. To get better imaging, all samples were subjected to cryo-microtome using a Leica EM FC6 Ultramicrotome equipped with a Cryo-ultra-microtomy chamber. Glass knife was used to smoothen the specimens cross section with a speed of 60 mm/s and a feed rate of 2000 nm.

The pyrolysis behavior of specimens which are freeze quenched at various timing was examined through imaging technique using scanning electron microscopy (SEM). The cryo-microtome samples were coated with silver using a Quorum Emitech K550X sputter coater to avoid charge build up on the specimen while imaging. Samples were charged under Argon gas and 25 mAmps for three minutes resulting in a coating thickness of approximately 10 nm. SEM images of the cross section were taken using Quanta FEI 200. The operating conditions including the high voltage, width, spot size, magnification varied with sample and it can be found in bottom of the individual image.

To investigate the elemental composition across the cross-section, energy-dispersive X-ray spectroscopy (EDX) having a Thermo Scientific UltraDry EDX detector with NSS3® micro-analysis software was used. SEM images provided an qualitative

information of the char thickness with increasing burning times whereas the EDX analysis provided a quantitative degree of char formation.

### 3.3 Results and discussion

In this chapter, our emphasis is to reveal the effect of thiol-ene chemical group rigidity and network crosslinking density on  $T_g$ , thermal stability (gravimetric analysis) and reaction-to-fire properties. Multifunctional thiols used in this investigation are thiol propionate esters with variation in functionality (2, 3 and 4 respectively for 2T, 3T and 4T). Ene monomers used comprised an ally ether (TAE), an allyl triazine (TOT) and an allyl isocyanurate (TTT). To rationalize the data, thermal behavior trends and fire retardant properties presented in the chapter is organized in groups. Within each group, the ene monomer is kept the same while the thiol functionality is varied from 2-4. A comparison within a group reveals the effect of thiol functionality while a comparison between various groups exposes the effect of thiol ene structure (rigidity) on properties. A study on fire performance between two structural isomers, TTT and TOT, were also compared. Networks fabricated using these two rather similar ene monomers were used as model compounds to further elucidate the influence of network composition on fire performance.

It should be noted here that the synthesis of all these networks has been reported in the past and it has been shown that changing thiol and ene monomers affects the glass transition temperature.<sup>145</sup> As compared to  $T_g$ , less is known about thiol-ene networks thermal stability. Furthermore, the fire behavior properties of these materials, to our best knowledge, have not been reported, as yet. This report is part of our ongoing efforts to

probe the fire risks associated with the potential use of thiol-ene networks in the fabrication of next generation of flame-resistant UV-cured polymers.

### 3.3.1 Differential Scanning Calorimetry (DSC)

The glass transitions of thiol-ene networks were determined by DSC. The DSC thermograms for thiol-ene networks are shown in Figure 3.2 while the determined  $T_g$  and  $\Delta C_p$  values are provided in Table 3.2. The networks exhibited a broad range of  $T_g$  values, the lowest at about -33 °C for the 2T-TAE and the highest at about 53 °C for 4T-TTT system. For a given series of thiol-ene networks (films fabricated using TAE-, TOT- or TTT- ene monomers), networks fabricated using 2T thiol monomers showed lowest  $T_g$  values;  $T_g$  values increased gradually when 3T and 4T thiol monomers were used. Interestingly, the difference between the glass transition temperatures of the di thiol and tri thiol-based networks which is 20-30°C, was consistently larger than the difference between the glass transition temperatures of the tri and tetra based ones, which is 10-20°C. On the other hand, when the same thiol functionality was selected for comparison between the groups, the TTT monomer-based network always exhibited the largest  $T_g$  while its TAE based analog showed the lowest  $T_g$ .

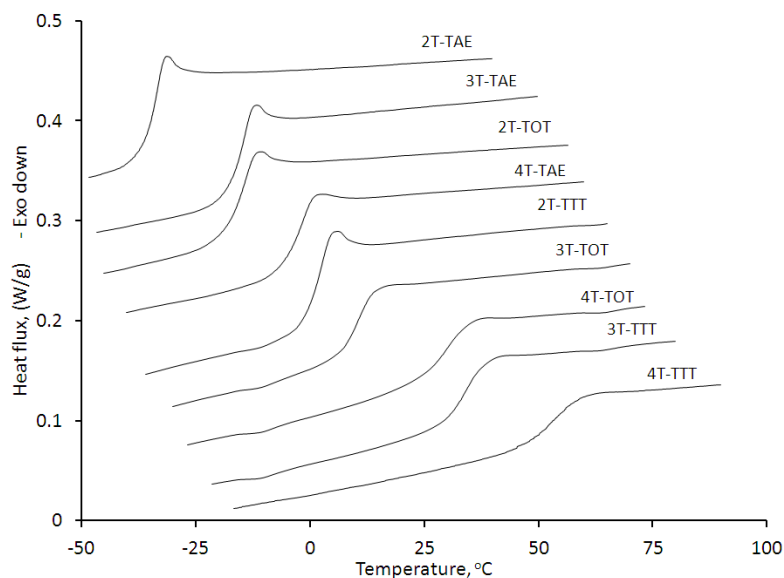


Figure 3.2 2<sup>nd</sup> heating scan DSC thermograms of photopolymerized thiol-ene networks. Curves are stacked vertically for clarity.

Variations in  $T_g$  values for analogous networks can be attributed mainly to an increase in cross-linking density for networks (generalized trends:  $2T < 3T < 4T$ ): polymer networks become more rigid and therefore a higher energy is required to facilitate the movements of molecular segments.<sup>152,153</sup> The effect of crosslinking on glass transition temperature has been accurately explained in the past using the free volume concept.<sup>154</sup> The literature shows that crosslinks reduce the free volume of a polymer in the rubbery state. Thus, the polymer vitrifies at higher temperature as presumably less cooling is required to reach the critical amount of free volume increasing the network crosslinking density (the crosslink density in a polymer is increased with an increase number of junction point functionality). This qualitatively justifies why an increase of thiol monomer functionality leads to higher  $T_g$  within the group. However, it is not quite apparent why this effect is somewhat diminished with a further increase of the thiol



functionality (comparing tri and tetra functional based thiol-ene networks within a group). One hypothesis is that an increase of junction point functionality to some extent may lead to a structurally more heterogeneous network. Network heterogeneity results in noticeable broadening of the  $T_g$  range with the increase of thiol functionality (see Figure 3.2). Broadening of the glass transition range may serve as an indirect proof that a network becomes less structurally homogeneous.<sup>53</sup> The glass transition temperature of any network structure in addition to crosslink concentration also depends on rigidity of its structural components. This fact explains why incorporation of more rigid ene monomers such as TOT and TTT, containing triazine and isocyanurate ring structures, led to higher  $T_g$  as compared to more flexible system TAE made of linear segments

Table 3.2 Glass transition temperature values for all the networks in this study. Reported values are the midpoints of inflection from the 2<sup>nd</sup> heat cycle

Materials	<i>Glass transition</i>	<i>Specific heat capacity</i>
	$T_g$ (°C)	$\Delta C_p$ ( $J g^{-1} °C^{-1}$ )
2T-TAE	-33.3	0.525
3T-TAE	-13.2	0.517
4T-TAE	-1.7	0.472
2T-TTT	2.6	0.527
3T-TTT	34.2	0.404
4T-TTT	52.8	0.336
2T-TOT	-14.2	0.470
3T-TOT	10.5	0.406
4T-TOT	30.3	0.376

The increase in degree of cross-linking also explains the gradual decrease in  $\Delta C_p$  in series fabricated using a same ene parent monomer since the heat capacity of the material increases with the number of active modes of movements and decreases with the rigidity of the material.<sup>155</sup>

### 3.3.2 Thermal Stability

The thermal stability of thiol-ene networks was evaluated in TGA experiments under a nitrogen environment; the TGA traces are shown in Figure 3.3 and the data are presented in Table 3.3. The influence of thiol-ene network composition on thermal stability was studied for (I) TAE-containing networks, (II) TTT-containing networks, and (III) TOT-containing networks. Each thermogram was characterized by measuring several parameters including onset temperature of degradation ( $T_{10\%}$ ), mid- point temperature of degradation ( $T_{50\%}$ ) and residual mass. Within each group, the onset temperature of decomposition as well as the mid- point temperature of degradation occurred at lower temperatures for the networks fabricated using the difunctional thiol monomer (2T) as compared to its 3T or 4T based analog. The difference between 3T and 4T based networks, in this regard, was rather insignificant. On the other hand, the relative amount of decomposition residues were somewhat similar for 2T and 3T based networks while the amount of char residues were about twice as much for 4T-based networks relative to the previous two.

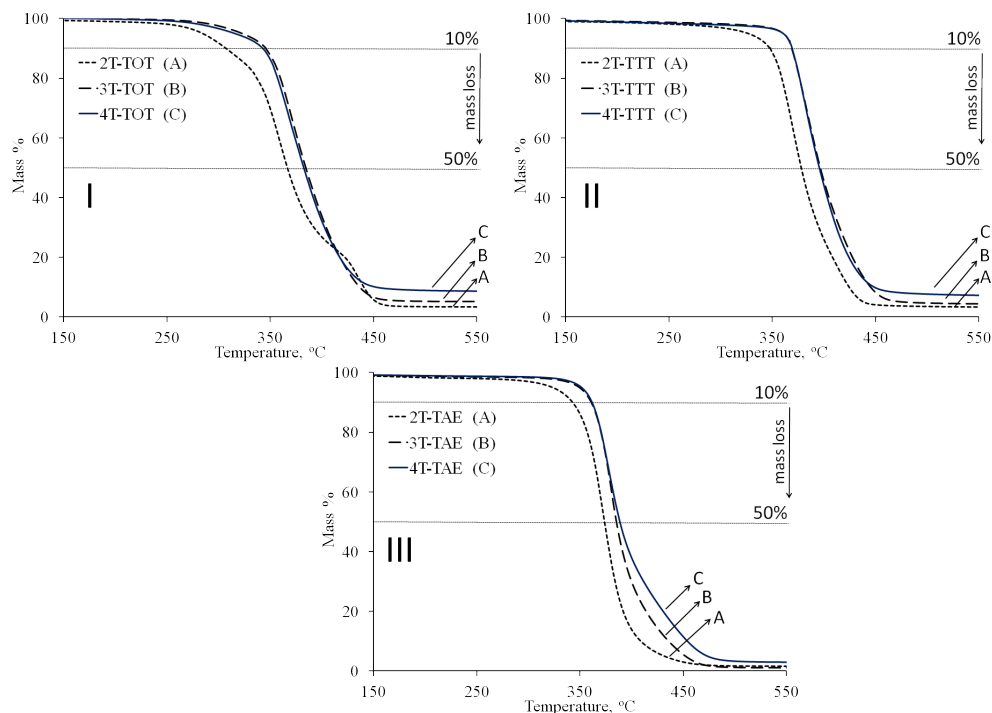


Figure 3.3 TGA curves of (I) TOT-, (II) TTT- and (III) TAE-containing thiol-ene networks. Note: heating ramp rate is 10 °C/min; experiments run in a nitrogen environment from 30-800 °C.

As thermal decomposition is a process which involves breaking of chemical bonds, it was anticipated that the crosslink density, defined within the group by the thiol monomer functionality, would strongly affect the thermal stability. Indeed, for a more cross-linked network, a larger amount of thermal energy must be absorbed to volatilize the polymer leading to an increase of the onset or mid- point of degradation temperatures (in a non-isothermal experiment such as TGA).<sup>155–157</sup> Accordingly, Brauman<sup>158</sup>, Rabek and Lucki<sup>159</sup>, and Wilkie and co-workers<sup>160,161</sup> have all shown that cross-linking does increase thermal stability. Additionally, various researchers have been documented that crosslinking usually promotes the char formation. To this end, for example, Brauman reports that cross-linking enhances char formation because it causes otherwise volatile

fragments to remain in the polymer for a longer time.<sup>162</sup> Looking at the available literature and analyzing the data in Table 3.3, two questions though must be posed. First, why, in regard to the onset or mid- point of degradation temperatures, did the 3T and 4T based networks show a smaller difference than the 2T and 3T based systems? Second, why, in terms of the residue char, did the 3T and 4T based networks show larger difference as compared to the 2T and 3T pair? We don't know the answer to this question as yet.

The thermal stability of networks fabricated using same parent thiol compound (4T) but different ene monomers (TAE, TOT and TTT) was studied and is shown in Figure 3.4. The effect of ene structure on thiol-ene network thermal stability is interesting as it contradicts our anticipation that the thermal stability of TTT and TOT based matrices would be superior over their TAE-based analogs, which is based on the typical observation that linear monomers or polymers are less thermally stable relative to monomers or polymers containing several ring structures. Indeed, we found that the TTT based networks were the most thermally stable networks in the series. However, the thermal stability of the TOT based networks was found to be lower than expected. The mid- point temperatures of degradation for the TOT based networks were comparable with those for the TAE based systems assuming the same thiol functionality, and the onset of degradation temperatures were noticeably lower by 20-30 °C.

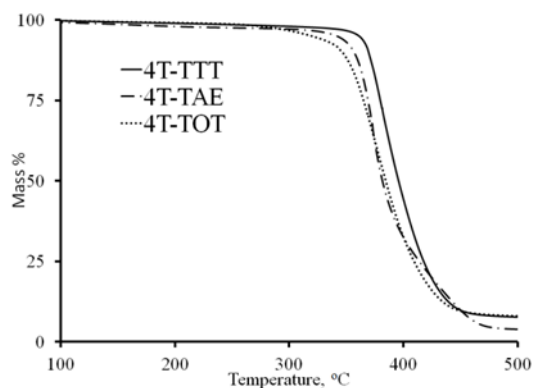


Figure 3.4 Thermal Stability of networks fabricated using same thiol compound but with different ene.

Naturally, a question was posed: why TTT and TOT, two structural isomers (i.e. TTT and TOT have different chemical structures but their chemical composition is the same) led to noticeable differences in the network thermal stabilities? To address the above question, beside structural rigidity, another thermodynamic argument was then considered based on the available literature on similar materials. A study conducted elsewhere using low molecular compounds structurally similar to TOT revealed a spontaneous thermal transformation of the cyanurate ring into the isocyanurate ring in the melt and no intermediates could be isolated at temperatures above 473 K.<sup>163</sup> The observed lower onset temperature of decomposition for TOT-containing networks relative to their TTT analogs evokes the existing literature on the rearrangement of cyanurate into isocyanurate ring structures when heated to higher temperatures.<sup>163</sup> For small TTT- and TOT-like monomers, Intermolecular O $\rightarrow$ N methyl rearrangement in the liquid state occurs at high temperatures (above 473K) converting TOT-like into TTT-like structures. The above reported information could then be correlated with the differences in thermal stability observed for TOT-based networks relative to their TTT-analogs. Side

group rearrangements in a network are achieved through the breaking covalent bonds and destroying network connectivity. However, the current results raise an important question of whether TTT- and TOT-based networks decompose following the trends predicted by their parent monomers. Later in this chapter, a clear understanding of the differences in thermal degradation is investigated through analyzing the pyrolysis behavior of the two isomers. But, the nature and type of the degradation products released when both 4T-TTT and 4T-TOT networks are heated to higher temperatures are beyond the scope of this study and are the subject of other ongoing studies.

Table 3.3 Temperatures for the mass loss of 10 and 50 wt.% ( $T_{10\%}$ ,  $T_{50\%}$ )

Material	$T_{10\%}$ (°C)	$T_{50\%}$ (°C)	Char yield (wt.%) (600 °C)
2T-TAE	343	374	1.5
3T-TAE	361	385	1.1
4T-TAE	362	389	2.9
2T-TOT	312	376	4.0
3T-TOT	349	391	4.7
4T-TOT	346	384	7.4
2T-TTT	348	379	3.3
3T-TTT	369	397	4.3
4T-TTT	369	396	7.1

### 3.3.3 Fire resistant properties

The fire behavior of basic thiol-ene networks has been investigated via cone calorimetry; the parameters obtained include the time to sustained ignition ( $t_{ign}$ ), the peak heat release rate (PHRR), the total heat release (THR), the average mass loss rate (AMLR), the average specific extinction area or smoke (ASEA), the effective heat of combustion (EHC) and the residue amount. PHRR is an important fire parameter measured by cone. It indicates the size of a fire or the likelihood of a fire to ignite

adjacent objects.<sup>164,165</sup> In this paper, to simplify the interpretation of the flammability data, a general discussion of various trends observed in cone parameters is provided first. A detailed analysis of time-dependent responses of specimens with respect to heat release, mass loss and smoke production is provided next. Furthermore, changes in the morphology for burning networks, the cross section analysis through SEM-EDAX to understand the pyrolysis behavior at incremental fire exposure timings are discussed last to allow a complete picture of the fire behavior properties of the networks.

Table 3.4 Cone calorimeter data for TAE, TOT & TTT networks at an external irradiation of 50 kW/m<sup>2</sup>

Network	$t_{\text{ign}}$ (s)	PHRR (kW/m <sup>2</sup> )	AMRL (g/m <sup>2</sup> .s)	THR (MJ/m <sup>2</sup> )	Residue (wt.%)
2T-TAE	34	1792	49.8	94.2	0.0
3T-TAE	38	1696	41.7	98.8	0.0
4T-TAE	39	1035	30.0	97.7	0.0
2T-TTT	38	1174	31.4	90.4	0.7
3T-TTT	48	929	27.8	92.3	1.0
4T-TTT	54	674	23.2	86.1	2.6
2T-TOT	26	1643	38.1	94.6	0.5
3T-TOT	38	1426	36.0	93.5	1.6
4T-TOT	36	1322	31.7	89.3	3.1

**Note:** Data provided is averages of 2 runs:  $t_{\text{ign}}$ , time to sustained ignition; PHRR, peak heat release rate; AMLR, average mass loss rate; THR, total heat release; Residue = (final mass/initial mass) x 100.

Table 3.4 summarizes the cone data, including  $t_{\text{ign}}$ , PHRR, AMLR, THR and collected residues (wt.%). 2T-TAE shows the highest PHRR at 1792 kW/m<sup>2</sup> while 4T-TTT has the lowest value, at 674 kW/m<sup>2</sup>. The general trend is that, within a group, the 2T based network has the highest PHRR value, followed by the 3T-containing network and the 4T-containing network shows the lowest PHRR in the group. The times to sustained ignition seemed to follow similar trends: the 2T based network shows the lowest time to ignition, and the 4T based network the largest. This data is somehow not surprising as

the resistance to combustion of a polymer is in some way connected to both the number of crosslinks and the strength of the bonds that make up the cross-linked structure.<sup>166</sup> Indeed, Lyon reported that excluding the halogenated polymers, high thermal stability roughly correlates with flame resistance.<sup>167</sup> High thermal stability results from strong primary and secondary bond and low hydrogen content, all of which favor recombination/cross-linking (charring) reactions during thermal degradation rather than the hydrogen transfer/termination reactions which lead to mass loss.<sup>160</sup>

Interestingly however, while a gradual and pronounced decrease in PHRR with an increase in thiol-ene network cross-link density is clearly visible for TTT- and TAE-containing networks, this difference is rather modest between TOT based thiol-ene networks. For example, the difference between the PHRR of the di thiol and tetra thiol based networks at 500-800 kW/m<sup>2</sup>, was consistently larger for TTT and TAE based networks than the difference between the PHRR values of the TOT ones, which was 321 kW/m<sup>2</sup>.

Table 3.4 also reveals a correlation between the % reductions in PHRR (using the 2T based network as the baseline) and the average mass loss rate (AMLR) values. This information is consistent with the existing literature that shows that for materials with a constant effective heat of combustion, the mass loss rate controls the HRR.<sup>168</sup> Accordingly, the average effective heat of combustion is approximately the same for all networks (Effective heat of combustion values for various networks are tabulated in Table 3.5: TAE-containing networks, 30.3 ±1.7 kJ/g; TTT-containing networks, 28.4 ±1.3 kJ/g; TOT-containing networks, 29.0 ±1.2 kJ/g).



The cone data also allowed the determination of some fire safety engineering parameters like FIGRA (fire growth rate, determined by dividing the peak HRR by the time to ignition values). Increasing FIGRA values for materials tested in cone experiments have been correlated with faster flame spread and higher likelihood of igniting nearby objects by the burning polymer.<sup>85,169</sup> FIGRA values were determined to be 22.7, 18.9 and 9.4 respectively for 2T-TAE, 3T-TAE and 4T-TAE. The above data points to 4T-TAE as the better network in the series. For TOT-containing networks, FIGRA values were calculated to be 24.2, 21.0 and 20.3 respectively for 2T-TOT, 3T-TOT and 4T-TOT. FIGRA values were determined to be 17.6, 8.6 and 5.4 respectively for 2T-TTT, 3T-TTT and 4T-TTT. FIGRA values identify the networks prepared using the tetrafunctional thiol monomer as the best systems for each series of TTT- or TOT-containing networks. It should be pointed out that these engineering indices (e.i. FIGRA) concentrate important information into a single number and interpretation of the cone data using only these indices is not sufficient and can be misleading in some cases. The uncertainty around the times to peak HRR for example will be addressed later in the section where the shapes of representative HRR curves for these networks are discussed. The analyses of shapes of HRR curves along with physical observations provide additional key information about the fire performance of materials in cone tests.<sup>85</sup>

### **3.3.4 Shapes of heat release rate curves for various thiol-ene networks at 50 kW/m<sup>2</sup>.**

A further assessment of the burning behavior of thiol-ene networks is gained by observing the shapes of the heat release curves. To simplify the interpretation of the data, the networks are also studied in groups. Figure 3.5 presents the HRR and MLR curves of TAE-based networks. A good correlation between HRR and MLR curves is exposed.

With 2T-TAE and 3T-TAE, a quick rise in HRR after ignition is observed and continues until a maximum is reached (PHRR), followed by a sharp decrease. In contrast, the HRR pattern of 4T-TAE is broader relative to the previous two systems. It starts with a rapid rise in HRR for about 20 seconds, followed by a modest increase in the rate of HRR up to a maximum is noted. The intensity of the maximum peak is decreased and the duration of the cone fire experiment is increased as compared to the first two systems.

All thiol-ene networks evaluated for fire behavior properties in this investigation can be classified as thermally thin materials using the available literature on cone testing. Additionally, the networks yielded very little to no char residue (3 wt.%  $\leq$ ) at an external irradiation of 50 kW/m<sup>2</sup>. A non-charring thermally thin polymer typically shows a sharp and intense HRR curve in a cone test because the material is pyrolyzed in a very short period of time.<sup>170</sup> Thus, the sharp HRR curves observed for 2T-TAE and 3T-TAE networks were somehow to be expected. In contrast, the HRR curve of the 4T-TAE network is an interesting one and seems to suggest that the rate of pyrolysis was relatively slower relative to the previous two, which resulted in longer burning times for the latter network.

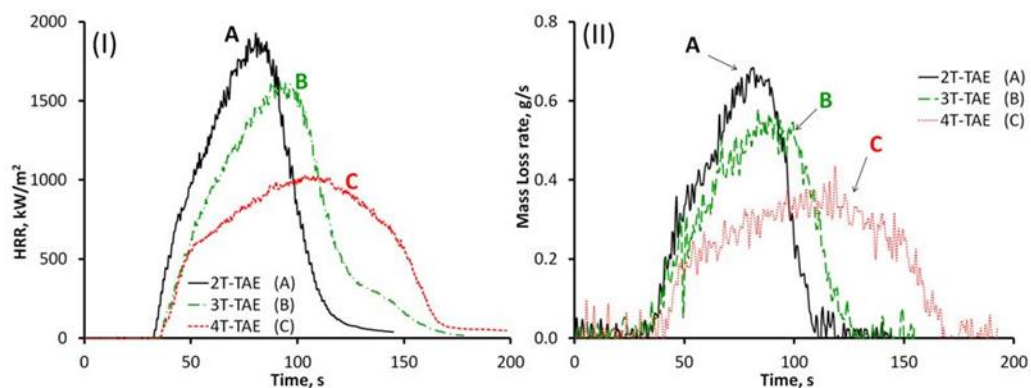


Figure 3.5 Cone calorimeter representative time dependent curves of [TAE]-containing thiol-ene networks at an external irradiation of 50 kW/m<sup>2</sup>: (I) heat release (HRR) and (II) mass loss (MLR) curves

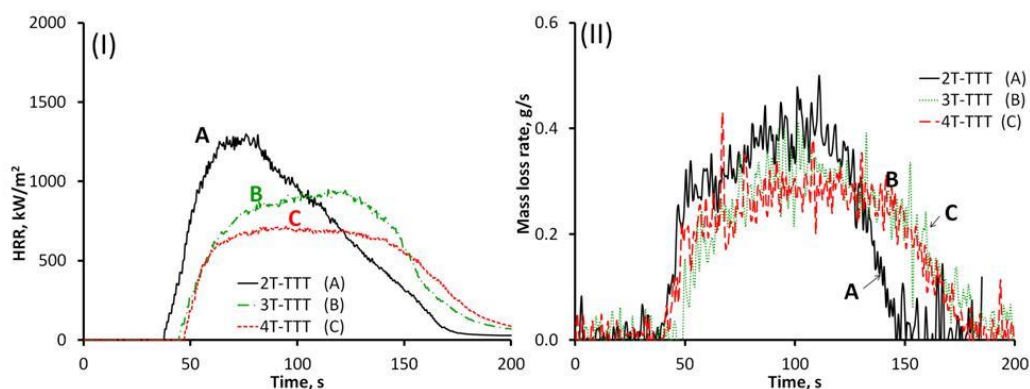


Figure 3.6 Cone calorimeter representative time dependent curves of [TTT]-containing thiol-ene networks at an external irradiation of 50 kW/m<sup>2</sup>: (I) heat release (HRR) and (II) mass loss (MLR) curves

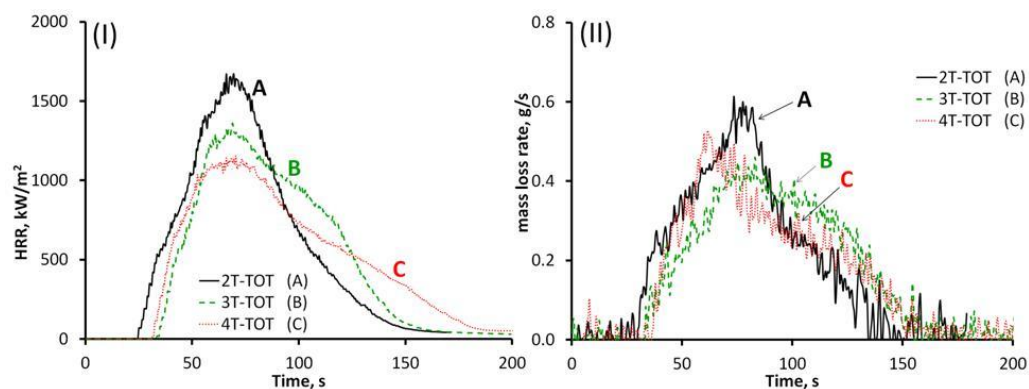


Figure 3.7 Cone calorimeter representative time dependent curves of [TOT]-containing thiol-ene networks at an external irradiation of 50 kW/m<sup>2</sup>: (I) heat release (HRR) and (II) mass loss (MLR) curves

The HRR and MLR curves of TTT-containing networks are provided in Figure 3.6. 2T-TTT shows an asymmetric HRR curve, characterized by a very quick rise in HRR after ignition to reach the maximum HRR, followed by a rather slow decrease in HRR. With 3T-TTT and 4T-TTT networks, the sharp rise in HRR levels off at about 20 seconds in the test, and a plateau is observed, followed by a rather sharp fall in HRR. While the 3T-TTT and the 4T-TTT networks show similar HRR behaviors, the maximum HRR is much lower for 4T-TTT compared with 3T-TTT. The HRR of 4T-TTT shows a shape that is typically observed for polymer filled with nanoparticles.<sup>170</sup> The steady state or plateau results from the formation of a barrier layer composed of nanoparticles over the surface of the burning polymer. In later section, we will show that this polymer, surprisingly, decomposes under fire condition forming a carbonaceous char layer that may work well as a barrier to heat or slow down the release of the flammable volatile, and thus, results in the lower HRR and longer burning times.

In Figure 3.7, the HRR patterns of TOT-containing thiol-ene networks are presented. Similarities in the shapes of the HRR curves for the three networks are easily noted. All networks show a rapid rise in HRR after ignition, leading to maximum HRR, or PHRR. Interestingly, the PHRR is reached approximately at the same time for all networks, at around  $69 \pm 2$  seconds. Overall, a modest but gradual decrease in PHRR is observed in the sequence, 2T-TOT > 3T-TOT > 4T-TOT, with 4T-TOT showing the lowest PHRR value in the series. The time to burn out follows a reverse trend and 4T-TOT burn for a longer time relative to the first two. Obviously, an important question is raised: what is indeed controlling the burning behaviors of these networks? Specifically,

TTT and TOT, two structural isomers, led to the fabrication of a series of networks that show totally different fire behavior properties as measured by cone.

As a summary, in Figure 3.8, the heat release rate curve for the network with lowest peak HRR value and highest time to ignition values (e.i. 4T-TTT) is provided along with the curves of thiol-ene networks fabricated using same thiol (e.i. 4T) but different ene monomers. The differences in shapes of HRR curves for the three networks highlight different burning behaviors for this set of thiol-ene networks. In particular, the burning behaviors of two rather similar networks, 4T-TTT and 4T-TOT, is highlighted. As indicated in introduction section, TOT and TTT ene monomers are structural isomers, but clearly, they perform very differently in cone tests under similar fire conditions. In next sections, 4T-TTT and 4T-TOT networks are used as model compounds to investigate factors that control the fire behavior properties in thiol-ene systems.

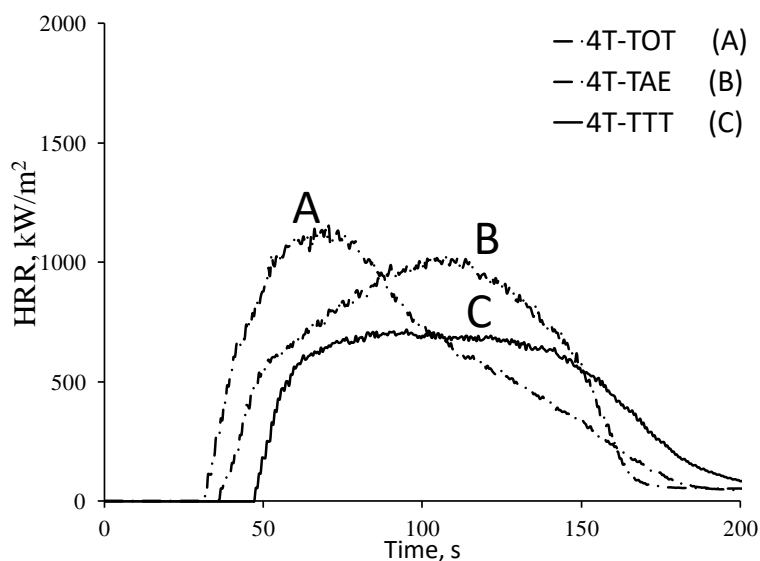


Figure 3.8 Representative HRR plots for HRR curves for networks fabricated using the tetrafunctional thiol (4T) monomer. All networks were tested at an external heat flux of  $50 \text{ kW/m}^2$

In our investigation, we also compared the PHRR values of thiol-ene networks with the reported values for other relevant commodity polymers. Our findings highlight the broad range of fire properties covered by thiol-ene networks. Accordingly, the thiol-ene material with the highest PHRR value in this work, 2T-TAE at 1792 kW/m<sup>2</sup>, is comparable to what has typically been reported for fuel rich polymeric materials such as polyethylene and poly(propylene) under similar experimental conditions (heat flux of 50 kW/m<sup>2</sup>, specimen thickness of about 3 mm).<sup>171,172</sup> The PHRR values observed for 4T-TAE or 2T-TTT (the average materials in this work using PHRR as indicator; PHRR is 1000 ± 100 kW/m<sup>2</sup>) are comparable to the reported values for PMMA. In contrast, 4T-TTT, the best material in our work (PHRR of about 650-700 kW/m<sup>2</sup>) is in the range of what has typically been observed for a flame retarded PMMA composite.<sup>173</sup>

### **3.3.5 Changes in surface morphology and composition in cone experiments**

An analysis of the changes in specimens' morphology during the combustion test was performed. A very interesting finding was made by visually analyzing the changes in morphology of the burning network: formation of a short lived black layer over the specimen was observed. The morphology and life time of this temporary morphology were found to depend on network identity. To achieve a qualitative analysis of this surface layer, and hopefully, gain brief insights into burning behavior characteristics of the networks, a novel experimental protocol was adopted. A burning sample (specimen 3 x 50 x 50 mm<sup>3</sup>) was combusted for about 60 seconds (just enough for the fire to propagate down the specimen) in cone at an external irradiation of 50 kW/m<sup>2</sup> and subsequently extinguished and quenched in liquid nitrogen. Digital images of incompletely burned specimens are provided in Figure 3.8.

With 2T-TAE and 3T-TAE, a significant portion of these two networks volatilizes in the first 60 seconds of the combustion test. In contrast, with 4T-TAE, at about one minute into the test, the network is still somehow intact, but covered with residues forming a black layer. The latter coverage is hypothesized to hinder the release of flammable volatile and is correlated with the earlier observed reduced rate of HRR for 4T-TAE relative to its TAE-containing analogs. This assumption is somehow consistent with the reduced mass loss rate also observed for the latter network in comparison with the previous two networks (Figure 3.5). It should be pointed out that at an external irradiation of  $50 \text{ kW/m}^2$ , the standard heat flux for this study, TAE-containing networks are consumed in the cone fire test. This observation is consistent with relatively similar total heat release rate values observed for all networks.

The images of incompletely burned TTT based networks are also provided in Figure 3.8. With 2T-TTT network (Figure 3.9, C1), chunk of residues are observed and they form a continuous layer, but a few large hole are also visible. With 3T-TTT and 4T-TTT networks (Figure 3.9, C2 and C3), the holes in residues of incompletely burned specimens are no longer visible. Instead, large cracks that seem to form some kind of valleys are observed. The residues of incompletely burned TOT-containing systems very much resemble those of TTT-containing systems at time 60 seconds.

The above experimental protocol established to study char yield and morphology in incompletely burned thiol-ene network was particularly revealing because at the external irradiation of  $50 \text{ kW/m}^2$  (the standard heat flux of this investigation), thiol-ene network yield very little to no-residue at the end of the cone experiment. The above observation is supported by the rather similar THR values ( $93.0 \pm 4.0 \text{ MJ/m}^2$ ) as

tabulated in Table 3.4. THR values reflect the similarities in initial specimen sizes prior to the fire tests ( $33 \pm 1$ g) and the low yields of residues ( $\leq 3$  wt.%) observed at end of the combustion tests. TAE based networks did not leave any residue or char while smaller quantities of unburned materials are observed for TOT- and TTT- monomer based networks.

Table 3.5 Cone calorimeter smoke and gas related test results

Network	EHC (kJ/g)	ASEA (m <sup>2</sup> /kg)	CO yield (kg/kg)	CO <sub>2</sub> yield (kg/kg)
2T-TAE	29.9	124	0.085	3.40
3T-TAE	32.1	219	0.065	3.65
4T-TAE	29.0	260	0.066	3.40
2T-TTT	28.2	139	0.051	2.87
3T-TTT	28.0	219	0.077	2.83
4T-TTT	25.9	269	0.111	2.36
2T-TOT	29.4	141.2	0.072	2.76
3T-TOT	30.0	229.6	0.086	2.55
4T-TOT	27.7	245.2	0.121	2.55

**Note:** EHC, average effective heat of combustion; ASEA, average specific extinction area or smoke.



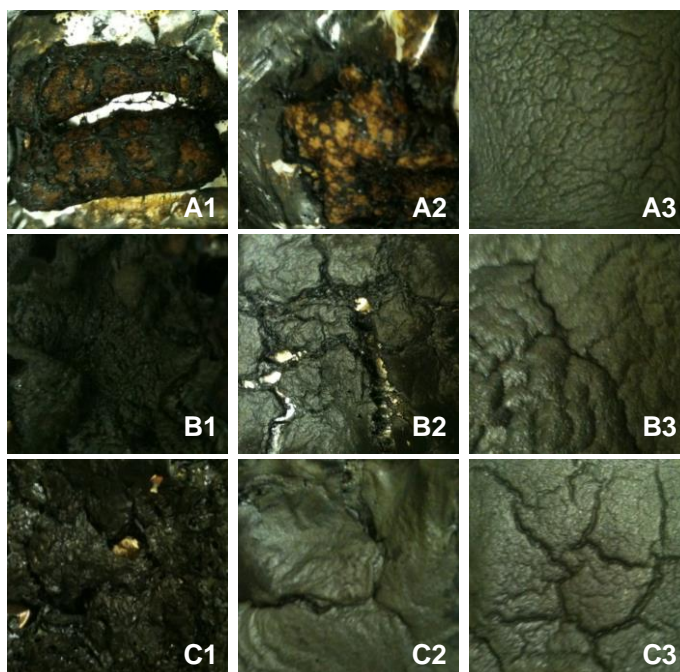


Figure 3.9 Optical photographs of incompletely burned thiol-ene networks in cone at an external irradiation of 50 kW/m<sup>2</sup>. (A1) 2T-TAE; (A2) 3T-TAE; (A3) 4T-TAE; (B1) 2T-TOT; (B2) 3T-TOT; (B3) 4T-TAE; (C1) 2T-TTT; (C2) 3T-TTT; and (C3) 4T-TTT. The specimens were combusted for about 60 seconds, and then subsequently extinguished and quenched using liquid nitrogen

### 3.3.6 Effective heat of combustion and smoke

The effective heats of combustion (EHC) of thiol-ene networks are presented in Table 3.5 and the measured values ranged between 26 - 32 kJ/g. In a group, there is very little variation in the measured value. A close analysis of the data may suggest that the network fabricated using 4T thiol monomer slightly shows the lowest value within each series. Also, comparing the groups, TTT and TOT based networks show relatively smaller values of EHC relative to their TAE based analogs. The later observation was somehow expected as the heat of combustion of a polymer is related to the heat of combustion of the volatile and char; thus, the observed residue yields (~ 3wt.%) for 4T-

TTT and 4T-TOT networks may be correlated with the relatively lower EHC values observed for this set of networks taking into account that other networks did not yield any char.

The average effective heat of combustion of thiol-ene, at  $29.2 \pm 1.5$  kJ/g, is well in the range of the average polymer heat of combustion. Lyon tabulated a broad range of polymers and determined the average heat of combustion of polymers to be  $29 \pm 6$  kJ/g.<sup>168</sup> The polymers listed in his work include the following: polytetrafluoroethylene at 8.38 kJ/g, polyoxymethylene at 15.44 kJ/g, poly(methyl methacrylate) at 23.2 kJ/g, polysulfone at 30.02 kJ/g, bisphenol-A-epoxy at 31.10 kJ/g, polystyrene at 42.00 kJ/g and polyethylene at 48.05 kJ/g.

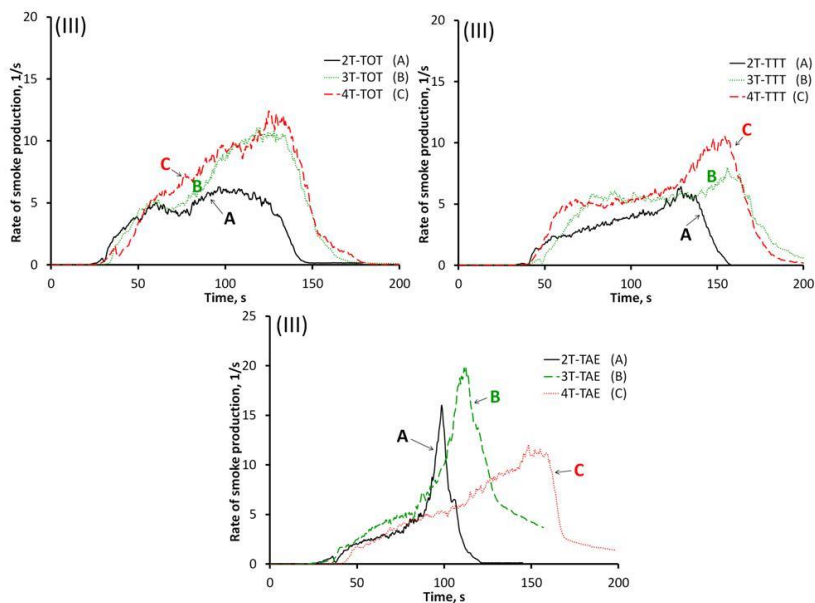


Figure 3.10 Smoke production rates of thiol-ene networks for (I) [TAE], (II) [TTT] and (III) [TOT] containing thiol-ene networks.

In addition to the effective heat of combustion, other gas related measurements obtained from cone data are: carbon monoxide yields, rates of smoke production and average specific extension area values. Carbon monoxide typically originates from the incomplete combustion of the organic fuel. The ratio of CO/CO<sub>2</sub> can also be used to characterize the efficiency of the oxidation reactions in cone fires. The smoke determined via cone as specific extension area (ASEA) represents the concentration of soot particulates generated by the combustion of the sample. ASEA is calculated from the extinction measurement of a He-Ne laser beam passing through the exhaust duct of the Cone Calorimeter divided by the volume flow rate in the duct and the transient mass loss rate.

The smoke evolved from the combustion of these networks is made up primarily of carbon dioxide, and to a smaller extent, carbon monoxide and other unburned higher molecular weight hydrocarbons including some sulfur-containing compounds. The gas related results for thiol-ene networks are presented in Table 3.5. The data shows that, within a group, there is an increase in smoke (ASEA) of 3T or 4T-containing thiol-ene networks relative to their 2T-based analogs. The above increase in smoke is tentatively correlated with the formation of larger number of longer hydrocarbons during the combustion of 4T-based networks relative to their 3T or 2T-based analogs. The short lived barrier layer observed in the highly cross-linked 4T-based networks can increase the residence time of the primary pyrolysis gases, giving them an opportunity to react with each other via recombination reactions, thus increasing the degree of secondary pyrolysis reactions that may occur. This proposition is supported by studies conducted by Straka *et al* who found that during slow pyrolysis, the output gases consisted of a substantial

amount of CO<sub>2</sub> with the balance being primarily C2 and C3 hydrocarbons.<sup>174</sup> Similarly, Marney and co-workers suggested that the formation of a barrier layer of HNT over the surface of a burning PA6/HNT nanocomposite facilitate pyrolysis gas recombination and hence increasing the release of more smoke for the nanocomposites.<sup>175</sup> Within a group, the ratio CO<sub>2</sub>/CO is higher for 2T-containing networks relative to their 3T or 4T analogs indicates that 2T-based networks are burning rather more efficiently since carbon monoxide is a measure of incomplete combustion.

Interestingly, the rates of smoke production curves reveal a fascinating difference between linear monomer -based network versus the triazine or isocyanurate -based networks (Figure 3.10). With TTT- and TOT-containing systems, the increase in thiol monomer functionality appears to accelerate the rate of smoke production at any stage of the burning process. With TAE-containing networks, the rate of smoke production shows a distinctive peak maximum and this peak occurs at 98 s, 112 s and 152 s, respectively for 2T-TAE, 3T-TAE and 4T-TAE. This difference is correlated with the observation that TAE-based networks volatilize during combustion (at a rate that depends on thiol monomer used in the fabrication of the network) while TTT and TOT based networks form a residue layer that cover the underlying polymer during combustion. Future work, which is beyond the scope of this study, would analyze the degradation products and establish the composition of the observed smoke.

### **3.3.7 Comparative studies: 4T-TTT and 4T-TOT networks**

TOT and TTT, a triazine- and an isocyanurate-ring containing ene monomers, are structural isomers. Interestingly, TTT-containing networks outperformed their TOT-analogs with respect to PHRR and time to ignition values (see Table 3.4). In particular,

4T-TTT was the best material of this work while 4T-TOT, the analogous network fabricated using the structural isomer of TTT (TOT), performed poorly. The two systems were then selected for additional studies to gain further insights into burning mechanisms of thiol-ene networks.

### **3.3.7.1 Fire behavior properties of 4T-TTT and 4T-TOT under different fire scenarios.**

Firstly, to establish the superiority of 4T-TTT network over its analogous network, 4T-TOT, were tested under three different external irradiation. Figure 3.11 provides the HRR patterns of the two networks at an external irradiation of 25, 50, and 75 kW/m<sup>2</sup>. The results were consistent and indicate that the 4T-TOT burns for a shorter time and shows a higher PHRR relative to its analog, 4T-TTT. As expected, lowering the external heat flux (from 75 to 25 kW/m<sup>2</sup>) results in a gradual decrease in PHRR values and an increase in time to ignition for either material. These experiments clearly demonstrate that 4T-TTT outperforms 4T-TOT. In terms of the residues collected at end of cone experiments, quantitatively, comparable amounts of char residues were obtained for both systems: 4T-TTT gave 5.1 ± 0.3, 2.9 ± 1.2 and 2.2 ± 0.7 wt.% while 4T-TOT gave 4.2 ± 0.2, 3.0 ± 0.3 and 2.4 ± 0.3 wt.% respectively at 25, 50 and 75 kW/m<sup>2</sup>. Interestingly, for both networks, the residue collected at 25 kW/m<sup>2</sup> cover the specimen holder and the residue retains the original shape of the sample (Figure 3.12). Thus, it was then anticipated that the morphology of this residue may shine the light on the difference in the fire performance of the two materials established in previous sections.

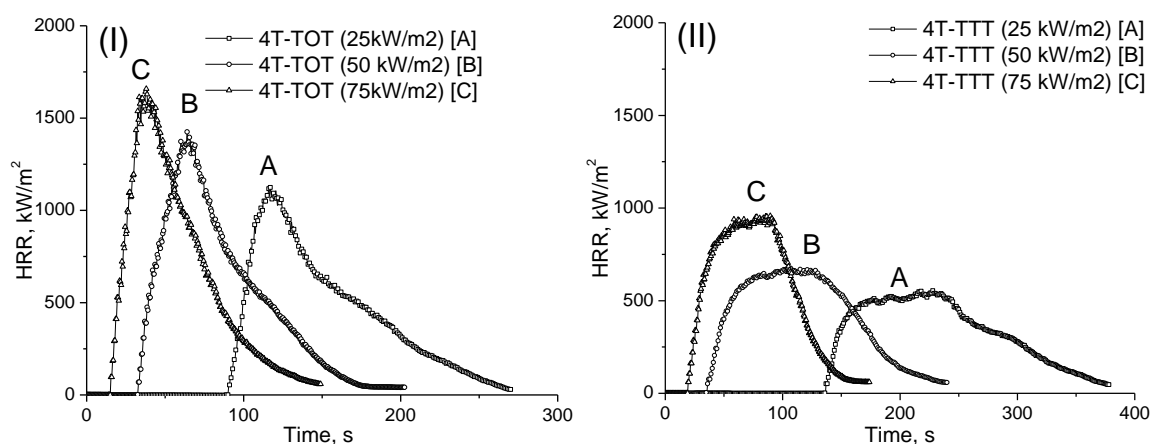


Figure 3.11 Cone calorimeter HRR of (I) 4T-TOT and (II) 4T-TTT, for 25, 50, and 75 kW/m<sup>2</sup> irradiation.

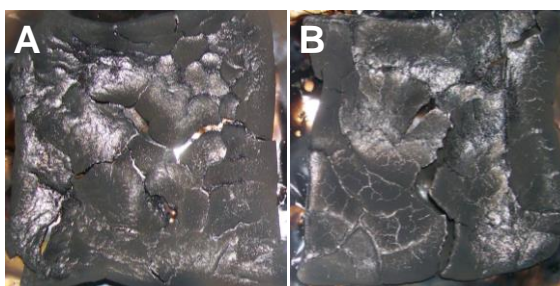


Figure 3.12 Pictures showing the residues remaining after combusting (A) 4T-TOT and (B) 4T-TTT at an external irradiation of 25 kW/m<sup>2</sup>

For both systems, 4T-TTT and 4T-TOT, lowering external irradiances in a cone resulted in a gradual decrease in the peak HRR values (Figure 3.13). These experiments clearly show that 4T-TTT network outperforms 4T-TOT per the following parameters: PHRR, time to PHRR and time to ignition. In terms of residues collected at end of cone experiments, quantitatively, comparable amounts of char residues were obtained for both model thiol-ene networks: 4T-TTT gave  $5.1 \pm 0.3$ ,  $2.9 \pm 1.2$  and  $2.2 \pm 0.7$  wt.% while

4T-TOT gave  $4.2 \pm 0.2$ ,  $3.0 \pm 0.3$  and  $2.4 \pm 0.3$  wt.% respectively at 25, 50 and 75 kW/m<sup>2</sup>. However, as pointed out in earlier discussion, thiol-ene networks showed a light-black solid layer that formed shortly after ignition, whose rate of formation and morphology seemed to depend on network composition and test condition with 4T-TTT showing this black layer prevailing for a relatively longer time relative to other systems.

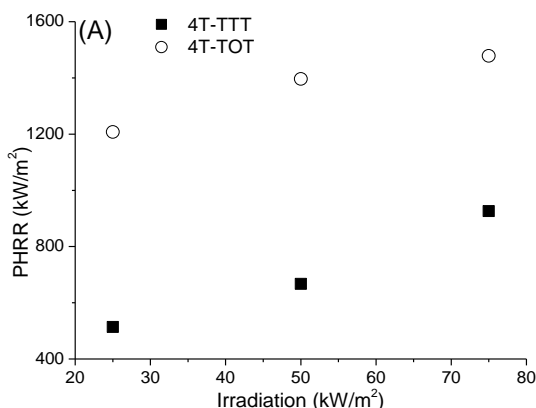


Figure 3.13 Cone calorimeter peak HRR values for 4T-TTT and 4T-TOT at external irradiances of 25, 50 and 75 kW/m<sup>2</sup>

Thermal analysis of the residue was also conducted to investigate the role, if any, of the thermal stability of residue collected after combusting 4T-TTT and the results are compared with that of the 4T-TOT network. In preparing the sample for the TGA experiments, the residue of either network was crushed using a mottle/pestle and the collected powder is then collected. The entrapped air or moisture in the residues is removed using the following experimental protocol: the sample was quickly heated to 100 °C and maintained at this temperature for 60 minutes. As anticipated, both materials lost 8-10 wt.% (moisture or entrapped air) as they were being quickly heated to 100 °C or being held at this temperature for 60 minutes. The TGA curves (dynamic heating

experiment, 20 °C/min, 100-900 °C) of the cone residues for both, 4T-TTT and 4T-TOT are provided in Figure 3.14. The results indicate similar decomposition patterns for both materials in either, air or nitrogen environment.

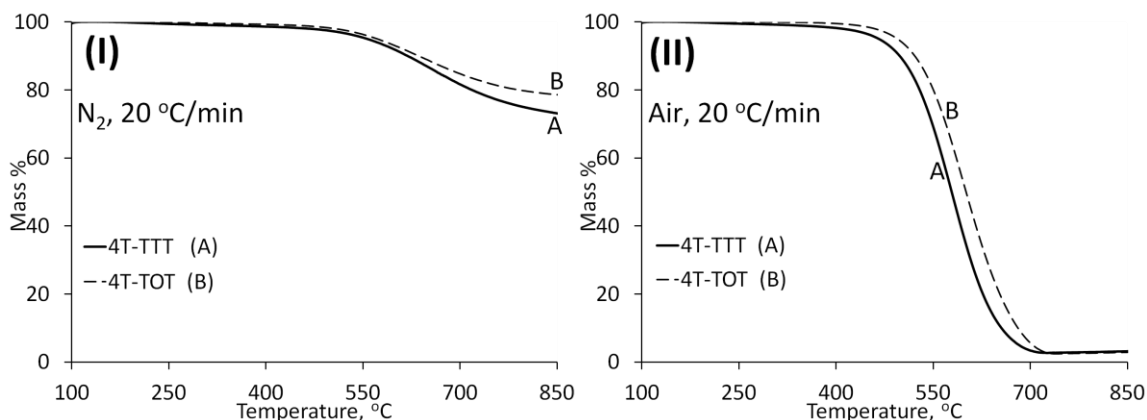


Figure 3.14 TGA curves of cone residues (external heat flux 25 kW/m<sup>2</sup>) for 4T-TTT and 4T-TOT networks performed in a nitrogen environment (I) or in Air (II) at a heating ramp rate of 20 °C/min. The cone residue and the residues collected after burning the two networks in cone calorimeter at an external irradiation of 25 kW/m<sup>2</sup>

With a naked eye, the images of the residues of 4T-TTT and 4T-TOT, at 25 kW/m<sup>2</sup>, are rather similar and do not help in explaining the cause of differences in fire behavior properties. In the next section, higher magnification images of the residues, SEM images, are then obtained to allow further characterization of the residues on micro level. The top layer of the residues (the area that was directly exposed to the fire) is analyzed and the results are compared with that of the bottom layer of the residue (the area facing away from heat source and in direct contact with aluminum foil sample holder). Figure 3.15 provides the SEM images of the residues. With 4T-TTT, the residue of the top surface layer (Figure 10 A<sub>1</sub>) is made of small interconnected cells forming a continuous network structure. A few cracks are observed but they appear to not reach



deep inside the residue. Interestingly, the bottom surface area of this residue (4T-TTT sample, Figure 10 A<sub>2</sub>) shows minor deterioration. This image may indicate that, at time 60 seconds, the char and pyrolysis zones have not penetrated the whole polymer as yet. This result evokes the work reported by Schartel *et al*<sup>85</sup> who identified three zones in a burning polymer, i.e. a residue, a pyrolysis zone and an intact, pure polymer underneath. In contrast, with 4T-TOT, the top surface area of the residue shows significant deterioration. Both small and large openings are visible. It is postulated that these openings (vent holes) formed as the products of decomposition of 4T-TOT network escape from the superheated bulk polymer, enter the gas phase and burn. The authors of this study recognize that the fire scenario determined by a lower heat flux (25 kW/m<sup>2</sup>) in a cone calorimeter is not a translation of the events that take place at higher external irradiation (50 or 75 kW/m<sup>2</sup>). However, the results obtained at this lower external irradiation present a strong case in addressing the burning behavior mechanisms of the two networks. The results clearly show that the poorer fire stability of 4T-TOT network relative to its 4T-TTT analog may be originating from the ease of decomposition and possibly ease of release of flammable volatiles of 4T-TOT network relative to its 4T-TTT analog. This conclusion is supported by TGA results for the two networks as discussed in previous sections.

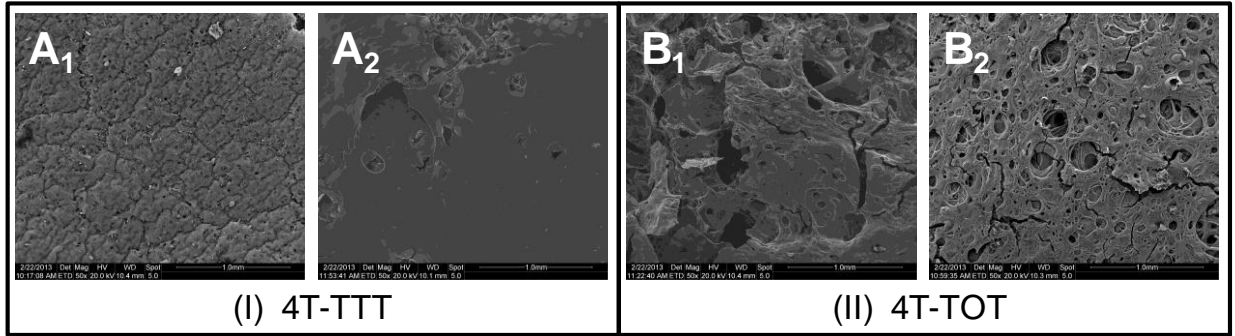


Figure 3.15 SEM images of the residues obtained after combusting 4T-TTT (A<sub>1</sub>, A<sub>2</sub>) and 4T-TOT (B<sub>1</sub>, B<sub>2</sub>) networks in cone at an external irradiation of 25 kW/m<sup>2</sup>. The subscript 1 is used to indicate the top surface layer of residue while the subscript 2 is used for the bottom area of sample, in direct contact with aluminum foil sample container.

### 3.3.8 Investigation of pyrolysis behavior through SEM/EDAX

Additionally, the pyrolysis behavior was investigated through the cross-section analysis of the samples which were partially burnt and force quenched using liquid nitrogen at shorter times, followed via examining through scanning electron microscope and elemental analysis and presented in Figure 13. Below is the protocol used for this analysis: all TTT and TOT contained networks ( combined with 2T, 3T and 4T) were exposed at a heat flux of 50 kW/m<sup>2</sup> for 5, 10, 15 & 20 seconds before quenching it to liquid nitrogen to interrupt the fire. The samples were then examined at the cross-section at 500 μm scale under scanning electron microscope.

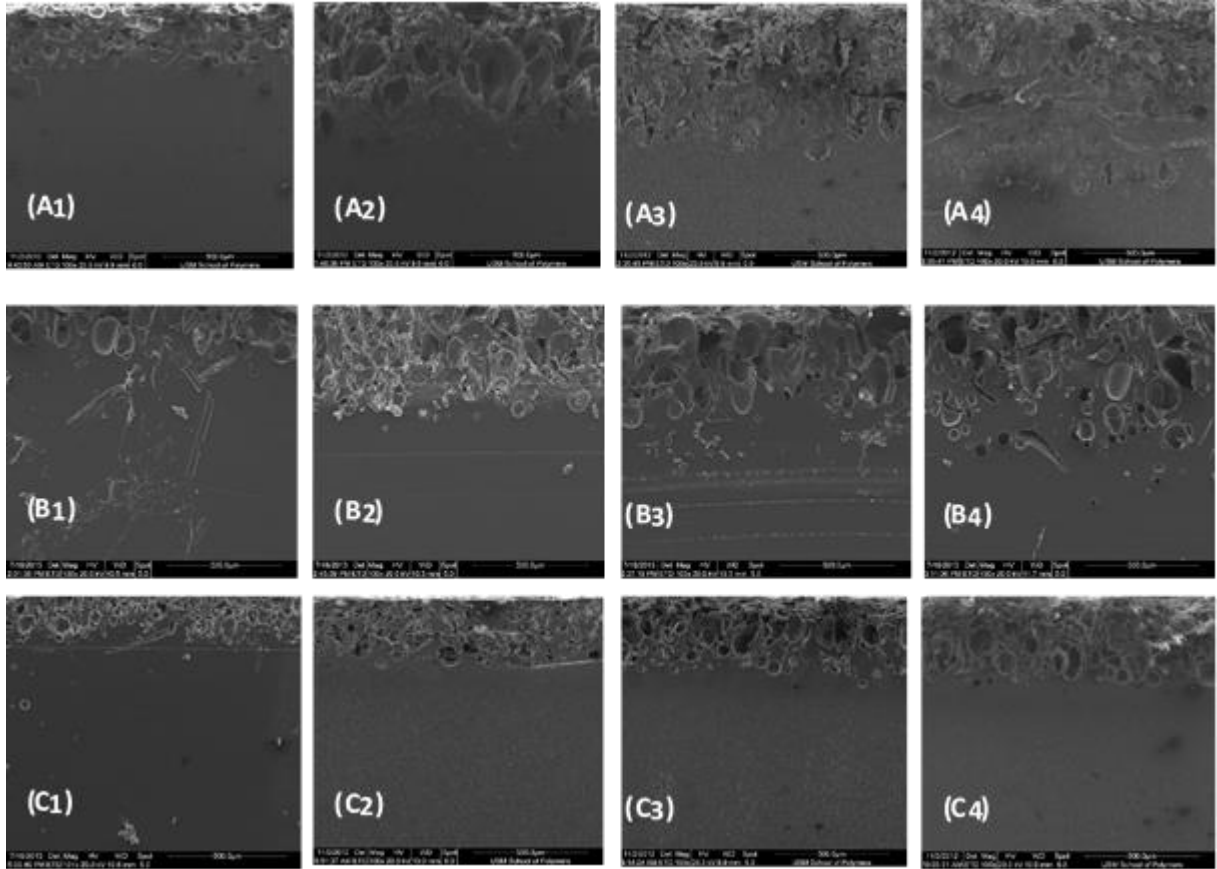


Figure 3.16 Cross-sectional image of partially burnt networks. (A) represents 2T-TTT,( B) – 3T-TTT and (C)- 4T-TTT networks. Subscripts indicates the combustion times. (1) – 5 sec, (2)-10 sec, (3)- 15 sec,(4)- 20 sec.

Figure 3.16 presented here shows the cross-sectional images obtained through scanning electron microscope for TTT based networks with varying crosslink density, while Figure 3.17 represents for TOT based systems. From left to right pictures indicate the cross-sectional image of a particular network, say 2T-TTT for Figure 3.16-A1 through Figure 3.17-A4, at increased combustion time, while comparing from top to bottom gives an insight on pyrolysis behavior of different networks at similar time. As seen there exists three layers: thin crust of residue on top, pyrolyzed layer and then an

intact polymer layer on the bottom. For all samples, the pyrolysis zone increased with increasing time because of the fire propagation. Since the time of combustion was small, there was only a thin crust of residue for all samples. The fire propagation was different for samples with different crosslink density. 2T being the least crosslinked (Figure 3.17-A4) showed a high degree of degradation in the early phase of the combustion (at 20 sec). With increasing crosslinked density ( $4T > 3T$ ) the effective depth of pyrolysis from the surface reduced., ie., at 20 sec the pyrolysis layer for 4T-TTT (Figure 3.17-C4) was lesser than the pyrolyzed layer obtained for 3T-TTT (Figure 3.17-B4).

The pyrolysis behavior of TOT networks (Figure 3.18), upon comparison with TTT networks, reveals the two isomers typically follows a different pyrolysis behavior: TOT burns faster. Even though TTT and TOT are structural isomers, the pyrolysis behavior is different due to the difference in backbone structure. The C-O bond dissociation energy in TOT containing networks are much lower (bond breaks at much lower temperature) as compared to C-C bonds available in TTT networks.<sup>176-178</sup> Not to mention, some reports point at the rearrangement of TOT monomers at higher temperature to TTT as discussed early in the TGA section.

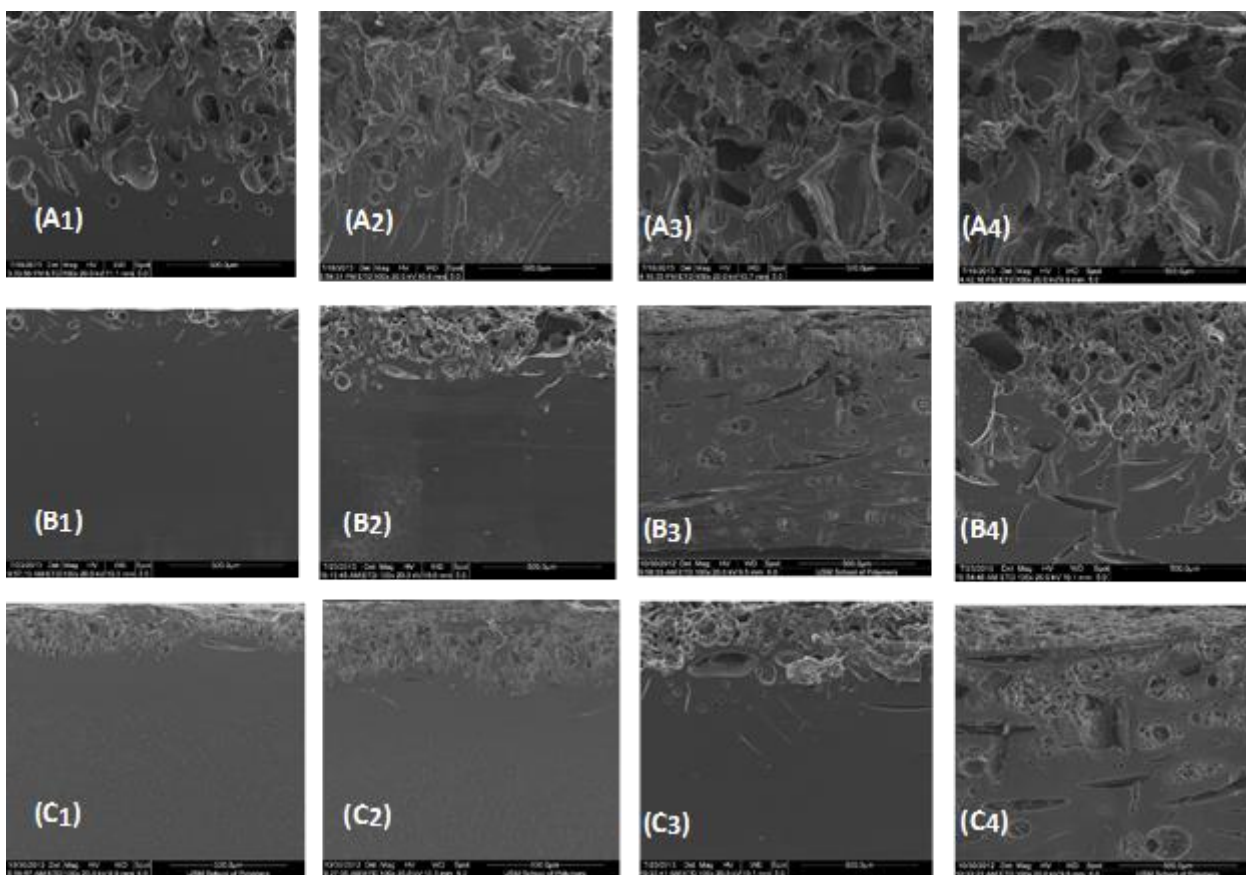


Figure 3.17 Cross-sectional image of partially burnt networks. (A) represents 2T-TOT, (B) – 3T-TOT and (C)- 4T-TOT networks. Subscripts indicates the combustion times. (1) – 5 sec, (2)-10 sec, (3)- 15 sec,(4)- 20 sec.

To quantify and confirm the pyrolysis behavior, elemental analysis was performed to detect the elemental composition at varying depth of the cross section. 4T-TTT and 4T-TOT systems whose combustion was force stopped at 20 sec was used as a model system in EDAX for elemental quantification. Since these are thiol networks, the unburnt polymer zone is expected to have sulfur along with carbon and oxygen (oxygen from the TTT and TOT molecule). Upon comparing the composition with unburnt neat polymer, we expect to have oxidized products in the combustion zone. Figure 3.18 shows

the SEM image of 4T-TTT systems and to the left indicates the composition of carbon, oxygen and sulfur at different zones. For comparison, neat unburnt 4T-TTT was examined to have 51.5 % of carbon, 18.3 % of oxygen and 30.2 % as sulfur. All concentrations reported here are an average of 3 measurements in that pyrolysis zone.

Zone	Carbon	Oxygen	Sulfur
<b>E</b>	66.7 ± 1.5	33.3 ± 1.5	0.0 ± 0.0
<b>D</b>	66.8 ± 1.2	27.2 ± 5.4	5.9 ± 4.5
<b>C</b>	61.9 ± 2.1	31.3 ± 0.07	6.8 ± 1.4
<b>B</b>	53.6 ± 4.8	17.3 ± 1.0	30.9 ± 5.6
<b>A</b>	51.8 ± 5.3	17.3 ± 1.9	30.9 ± 5.6
<b>Neat</b>	51.5 ± 9.5	18.3 ± 6.5	30.2 ± 15.5

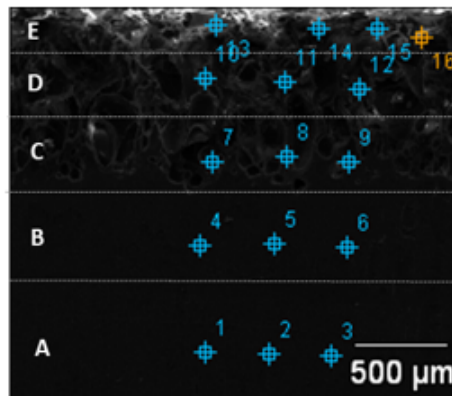


Figure 3.18 Elemental analysis of 4T-TTT networks exposed to combustion for 20 sec. A, B,C,D and E represents the imaginary pyrolysis zone. The composition indicated in the left is an average of 3 scans in that zone. Neat represents the unburnt pristine polymer samples.

Figure 3.19 represents 4T-TOT network exposed to combustion for 20 sec. When compared with 4T-TTT elemental scans, the composition of TTT containing systems over different zones vary to a greater extent as compared to TOT networks, ie., the increase in oxygen concentration over pyrolysis range (A to E) varies higher as compared to TOT networks. Also, zone A in TTT networks resembles the pristine polymer composition which is an indication of intact polymer zone at the bottom, whereas in TOT containing systems the zone A is already in oxidized state.

Zone	Carbon	Oxygen	Sulfur
E	63.6 ± 1.1	36.7 ± 0.8	0.0 ± 0.0
D	64.9 ± 0.9	33.3 ± 3.6	1.8 ± 2.7
C	63.1 ± 3.9	31.3 ± 0.7	6.8 ± 1.4
B	59.7 ± 1.9	25.4 ± 1.5	10.5 ± 3.4
A	64.3 ± 0.8	26.1 ± 1.2	9.5 ± 1.5
Neat	43.9 ± 2.8	18.1 ± 1.2	38.1 ± 2.4

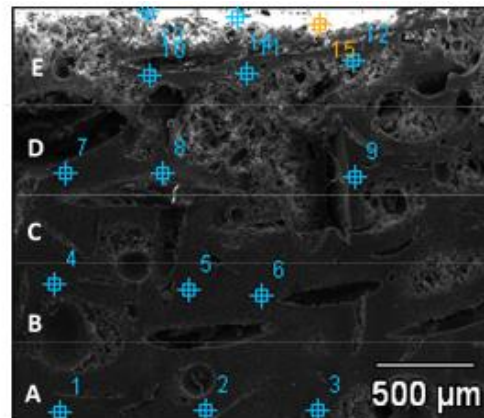


Figure 3.19 Elemental analysis of 4T-TOT networks exposed to combustion for 20 sec. A, B,C,D and E represents the imaginary pyrolysis zone. The composition indicated in the left is an average of 3 scans in that zone. Neat represents the unburnt pristine polymer samples.

The pyrolysis investigation lead to an interesting finding that the structural isomers follows two different burning mechanism: surface to bulk pyrolysis happens in TTT while bulk pyrolysis happens in TOT. This in in agreement with the morphological studies done on the direct and indirect surface of burnt samples. The indirect morphological pictures of TOT revealed the burnt pockets which is due to the bulk pyrolysis while the intact polymer found in TTT samples reveal the surface to bulk pyrolysis behaviors.

### 3.4 Conclusion

In this work, thiol and ene monomers of varying functionality and structural rigidity were used to fabricate a series of thiol-ene networks by UV light and the thermal stability, glass transition temperature and fire behavior properties were determined.  $T_g$  values spanned between -33 and 54 °C and were dependent on network parents' both monomer functionality and rigidity. In groups,  $T_g$  values increase with an increase of the crosslink density which in turn is increased with an increase of junction point

functionality. The thermal stability, shown by the onset and midpoint temperatures of degradation, showed similar trends and the 4T-based network is the most thermally stable network. However, the difference between tri or tetra functional thiol based networks was rather insignificant.

The morphology of partially burnt thiol-ene networks was evaluated. A short lived protective layer was observed to form over the surface of burning thiol-ene samples and was consumed as the fire was progressing to yield negligible or no residue at the end of the cone test (external irradiation of  $50 \text{ kW/m}^2$ ). The morphology of the short lived protective layer was conserved for further analysis by quenching a burning sample in liquid nitrogen. At time 60 seconds after ignition, a residue layer covers the entire sample surface of the tetra thiol-based thiol-ene networks while incomplete coverage or shrinkage of specimen is observed for di thiol-based networks. Comparing the three different groups, visually, TTT and TOT based materials show somehow similar specimen morphology while TAE exhibit shrinkage and evaporation of network at time 60 seconds.

The fire behavior properties of thiol-ene networks were also probed. The PHRR values of the networks covered a broad range and spanned between  $700 - 1800 \text{ kW/m}^2$ . In a group (material fabricated using a same 'ene' monomer but different 'thiol' monomer), a gradual increase in PHRR is observed in the following order:  $2T > 3T > 4T$ . The shapes of the HRR curve revealed different burning behavior characteristics for the various networks. Di thiol based monomers showed rather sharp HRR curves, indicating that the samples are pyrolyzed quickly. Deviation from this behavior is observed with increasing the network linking density. Tetra thiol based thiol-ene networks show rather



broad HRR curves. In particular, for 4T-TTT, the HRR curve shows a sharp increase in HRR after ignition, a steady state plateau for about 100 seconds followed by a sharp decrease at flame out. A correlation between HRR and MLR curves is demonstrated and this finding indicates that the rate of fuel generation and pyrolysis of burning network is controlling the fire performance for the network. Also, partial volatilization or aromatized polymer structures is responsible for smoke and CO increases during combustion of the tri or tetra based networks relative to their di based analogs.

We also compared the fire properties of two rather similar networks (4T-TTT and 4T-TOT) under different fire scenarios. TTT and TOT monomers are structural isomers. However, the networks fabricated using the two monomers performed so differently in cone. The samples under fire was quenched at time frames 5 s, 10 s, 15 s and 20 s using liquid nitrogen to understand the pyrolysis behavior. Both networks, being isomers, followed two different methods of burning profile: TTT burns from the surface propagating to bulk while TOT burns via bulk pyrolysis. This mechanism of burning was confirmed through elemental analysis by examining the cross-section of the burnt specimens. The 4T-TTT network is the best material in this study using PHRR and time to sustained ignition as indicator while its analog, 4T-TOT, performed poorly under similar conditions. SEM studies of the final residues collected after combusting the two networks at low external irradiation ( $25 \text{ kW/m}^2$ ) were obtained and the morphologies of both, top and bottom surface of residues, were compared. The results clearly indicate a more compact and less deteriorated residue for 4T-TTT relative to its 4T-TOT analog.

The results presented in this work show that the fire behavior and thermal properties of UV-cured thiol-ene networks can be fine-tuned by controlling the network

cross-linking density and chemical composition. The variation in property performance induced by the chemistry and structural change means that future UV curing technologies, currently dominated by acrylic-based materials, may take advantage of the broad range of properties attainable through the use of thiol-ene networks, and fabricate the next generation of fire resistant and thermally stable UV-cured networks.

### **3.5 Acknowledgements**

The author would like to thank Dr. Charles Manzi-Nshuti for his experimental work carried as a part of this work.

## CHAPTER IV – FUNDAMENTAL INVESTIGATION OF FLAMMABILITY OF EPOXY-AMINE NETWORKS: EFFECT OF VARIOUS EPOXY MONOMERS

### **Abstract**

Epoxy amine networks are the other class of polymers with very wide application range from dental fillings to rocket castings. Despite of its wide usage, they do suffer from relatively poor thermal stability and flame retardancy limiting their applications in more demanding areas such as aerospace and electronic industries. In this chapter, we aim to establish structure-fire retardant property of neat epoxy resins crosslinked with amine to form a crosslinked network. Key structural parameters such as network crosslink density, aromatic content, presence of hetero atoms such as nitrogen and oxygen were varied and examined for its influence in flame retardant properties. Thermal stability and activation energy was determined using thermogravimetric analysis and fitting to an Ozawa plot respectively. Differential scanning calorimetry was used to determine the glass transition temperatures which varied within the series of networks examined. Cone calorimeter was used to determine the fire retardant properties compliance with ASTM 1354-90. Several correlations between the structural parameters and flame-retardant properties were established. In this work, numerical group contribution method was employed for the first time for a crosslinked networks to predict the heat release and heat capacity of epoxy amine networks. Specific attention was paid to the influence of isomers on glass transition temperature, thermal stability, free-volume and flame retardancy and it was determined that the key structural changes can influence these properties without altering the key chemical nature.

## 4.1 Background

Epoxy resins are well known for its high chemical resistance, mechanical and thermal properties. The degree of crosslinking affects the properties. Heat resistance of epoxy networks are directly related to the chemical structure, molecular weight between crosslinks, stoichiometry and degree of crosslinking. The crosslinked nature enhances the resistance to softening at elevated temperatures. The crosslinked nature enhances the resistance to softening and deformation at elevated temperatures.

*Fire properties of epoxy-amine networks:* Despite of the advantages, like most polymers and other organic compounds, epoxy-amine systems when subjected to suitable ignition sources will undergo self-sustained combustion in presence of air. After ignition from external sources, polymers are most responsible for the flame spread and propagation.<sup>179</sup> During the polymer combustion processes, several chemical reactions occur: within the bulk of polymer phase, at the interface between the polymer and the gas phase and in the gas phase. Typically, several complex steps happen when the polymer is exposed to fire. In the first step, when the polymer gets heated up, it causes to degrade forming small combustible matter (volatile) which diffuse to the surface of the polymer. When a suitable spark or source of ignition is brought near, these volatiles migrate to the gas phase to start and sustain the combustion. Under steady-state burning, part of the heat is transferred back to polymer surface producing more volatile fragments which sustain the combustion. The combustion process stops only when there the production of small volatile mater stops, ie., when there is no more polymer to support the fire.<sup>180</sup>

During combustion process of a typical epoxy network based on bio based monomers, kuo etal demonstrated the thermal degradation mechanism using a TGA

equipped with FTIR to monitor the chain scission reactions.<sup>181</sup> The work modelled different chain rearrangement reactions, chain scission and possible small molecules released during combustion to feed the combustion is discussed. Figure 4.1 indicates a typical epoxy amine chain and associated bond dissociation energy.

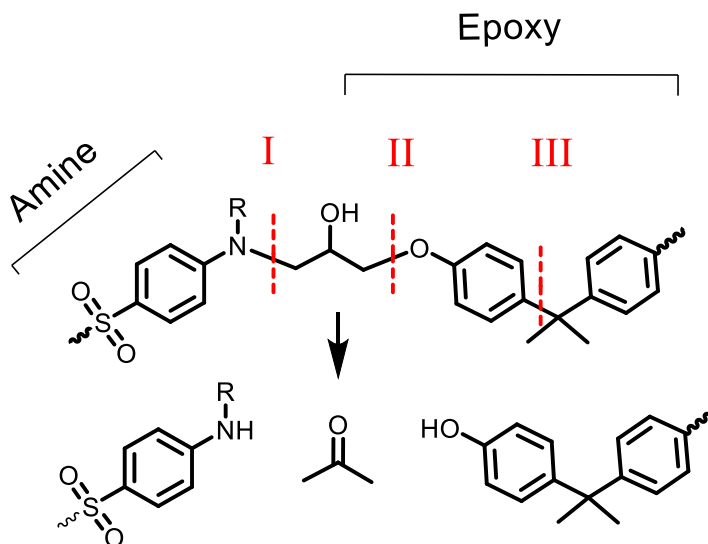


Figure 4.1 Typical epoxy amine chain indicating three possible chain scission sites (indicated in red dotted line), to release small molecule which sustains the combustion

In typical epoxy-amine molecular chain, there are three sites for dominant degradation as indicated through red dotted lines in Figure 4.1. The dissociation energy corresponding to I, I and II are 65kJ/mol, 70 KJ/mol and 347 kJ/mol respectively.<sup>181</sup> It is very clear from the bond dissociation energy that I and II are dominant sites for degradation reaction which will release acetone in addition to other small molecules. These small molecules are highly flammable contributing to a self-sustained fire.

During combustion process the associated fire hazard includes oxygen depletion, heat, smoke, toxic gases and structural failure which can threaten human life.<sup>182</sup> Thus a fire retardant polymer should not only have lower heat release but also slow release of energy along with reduced smoke and toxic gas released. Several research has been carried out in this regard and several commercial materials are in place targeting such slow release of energy and reduced smoke release. Generally, there are two mechanisms by which polymer combustion can be inhibited. One is solid-phase inhibition, where a thermally insulating char is formed at the interface between the fire and the polymer acting as a thermal barrier for the fire to degrade the polymer. This also includes an evolution of non-combustible substance (during the combustion process) such as water or non-flammable gasses which have large endothermic demands for thermal degradation, thus reducing the heat released. Use of flame retardant materials including, halogenated materials<sup>183–185</sup>, phosphates<sup>89,149,186,187</sup>, inorganic materials<sup>18,36–38</sup> and hydroxides<sup>74,188,189</sup> have been suggested to enhance the fire resistant properties of polymers. But, to the best of our knowledge, there exists no fundamental studies where the effect of polymer structure and chemical groups are examined for fire properties of polymer networks. It is important to understand the thermal decomposition and fire resistance mechanism on a molecular level in order to develop fire resistant polymers in a much same and economic way.

In this work we intend to establish the correlation between polymer structure, composition to their macroscopic flammability. The overall goal is accomplished by achieving the following goals listed below.

## 4.2 Experimental

### 4.2.1 Materials

The structures in Figure 4.2 and Figure 4.3 are chosen in order to study the effects of specific variables in molecular structure which influences the materials property including, crosslinking, aromatic content, naphthalene content and presence of hetero atoms such as nitrogen, and the effect of crosslinker's molecular structure, ie., the position of amine groups either on para or meta substitution. Several epoxide containing monomers and oligomers were obtained from sources mentioned below. Some chemicals are represented using their abbreviation and some others according to their industrial name. Naming scheme shown in this work is listed with their trade name and supplier along with chemical name in Table 4.1. Number in the parenthesis indicates the chemical structure shown in Figure 1. DGEBA (1), bisphenol-A based epoxy resin (JER 825, epoxy equivalent weight (EEW)= 175 g/eq) and longchain- DGEBA (4), long chain bisphenol-A based epoxy resin (JER 1001), EEW = 475 g/eq) was supplied by Mitsubishi Chemical Corporation. DGEBF (2), bisphenol-F based epoxy resin (Epiclon 830, EEW = 175 g/eq) was procured from DIC Corporation. Cycloaliphatic-DGEBA (3), alicyclic bisphenol-A based epoxy resin (Eponex 1510, EEW = 215 g/eq) was obtained from Hexion. Naphthalene (5), difunctional naphthalene containing epoxy resin (Araldite MY 0816, EEW = 148 g/eq) , DGA (6), aniline based epoxy resin (Technirez GAN, EEW = 125 g/eq), TGPAP (7), aminophenol based epoxy resin (Araldite MY0610, EEW = 100 g/eq) TPMTGE (8), trifunctional epoxy resin (Tactix 742, EEW = 160 g/eq), TGDDM (9), tetra-functional bis-benzenamine based epoxy resin (Araldite MY721, EEW = 120 g/eq), bisnaphthalene (10), tetra-functional naphthalene containing epoxy

resin (Araldite MY921, EEW = 163 g/eq), and oligomers EPN 1138 (11), phenol novolac based epoxy resin (Araldite EPN 1138, EEW = 178 g/eq), and Tactix 556 (12), phenol novolac with dicyclo-pentadiene based epoxy resin (Tactix 556, EEW = 225 g/eq), where supplied by Huntsman. All monomers and oligomers were used as received. The monomer structures are shown in Figure 4.2.

Curing agents used in this study includes 4,4'-Diaminodiphenyl sulfone (13), (Araldite 9719-1, AHEW = 62.075 g/eq) and 3,3'-Diaminodiphenyl sulfone (14), (Ardur 976-1, AHEW = 62.075 g/eq) are obtained from Huntsman and used without any purification as well. The curing agents structure is reported in Figure 4.3.



Table 4.1 List of monomers and oligomers used in this study. The names listed in industry/ product name is the trade names associated with the supplier

<b>Abbreviation</b>	<b>Chemical name</b>	<b>Industry<sup>®</sup> / product name</b>	<b>Supplier</b>
DGEBA	Diglycidyl ether bisphenol A	JER825	Mitsubishi Chemical
DGEBF	Diglycidyl ether bisphenol F	Epiclon 830	DIC Inc.
Cycloaliphatic-DGEBA	Cycloaliphatic diglycidyl ether bisphenol A	Eponex 1510	Hexion
Longchain-DGEBA	Long chain diglycidyl ether bisphenol A	JER 1001	Mitsubishi Chemical
Naphthalene	1,6-Bis (2,3-epoxypropoxy) naphthalene	Araldite MY 0816	Huntsman ACCI specialty
DGA	n,n-diglycidyl aniline	Technirez GAN	Materials
TGPAP	Triglycidyl- p -aminophenol	Araldite MY 0610	Huntsman
TPMTGE	Triphenylol methane triglycidyl ether	Tactix 742	Huntsman
TGDDM	n,n,n',n'-Tetraglycidyl-4,4'-methylenebisbenzenamine	Araldite MY 721	Huntsman
Bisnaphthalene	2,2'- bis(2,3-epoxypropoxy) bisnaphthalene	Araldite MY921	Huntsman
EPN 1138	Polyfunctional epoxidized phenol novolac resin	Araldite EPN 1138	Huntsman
Tactix 556	Low Moisture Polyfunctional epoxidized phenol novolac resin	Tactix 556	Huntsman
3,3'- DDS	3,3'-diamino diphenyl sulfone	Araldite 9719-1	Huntsman
4,4'- DDS	4,4'-diamino diphenyl sulfone	Aradur 976-1	Huntsman

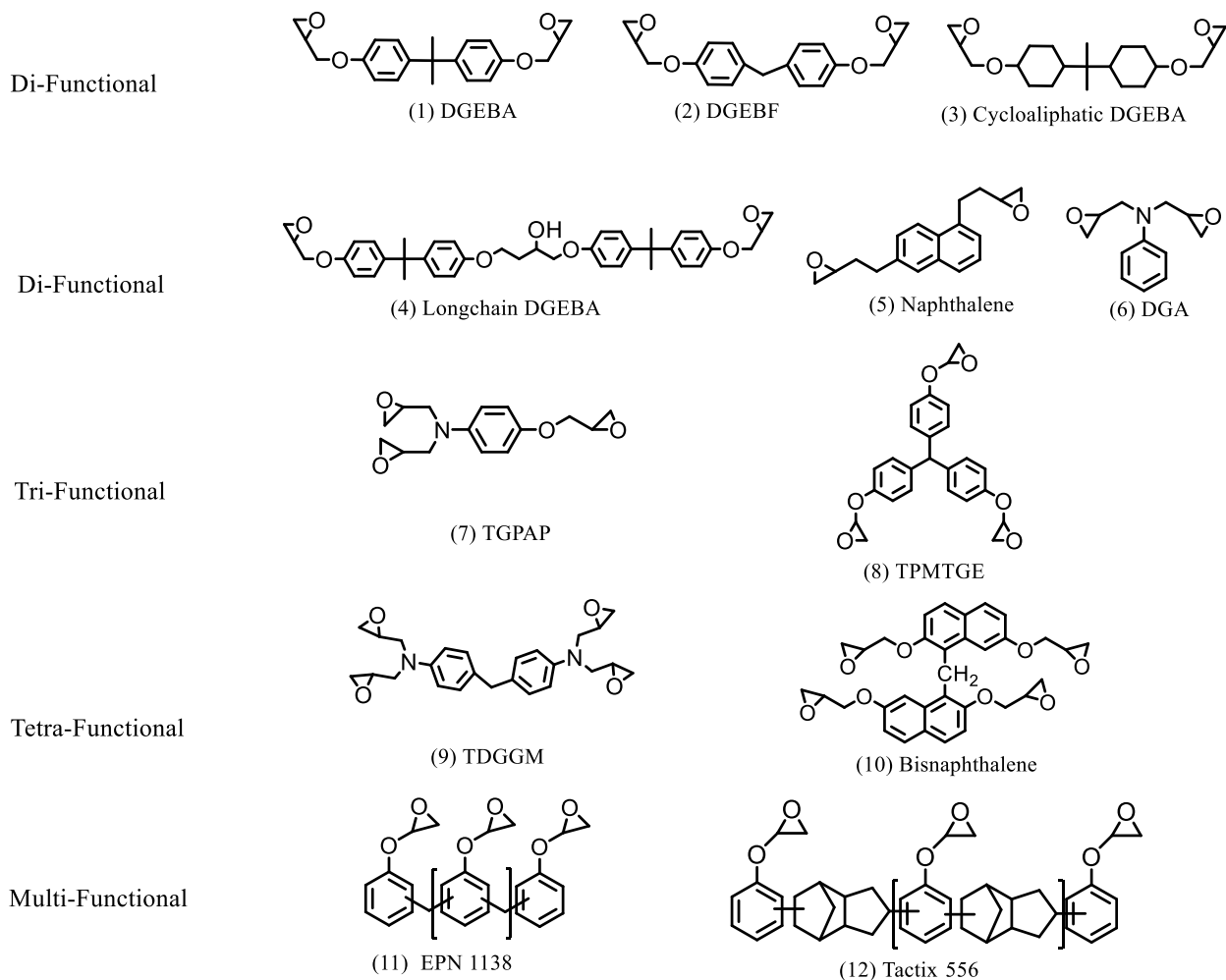


Figure 4.2 Chemical structures of epoxy monomers used in this work

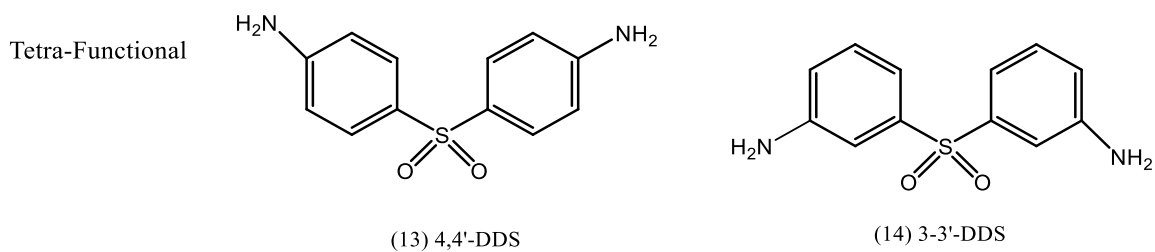


Figure 4.3 Chemical structures of amine curing agents used in this work

#### 4.2.2 Network formation and rational for the design

In this work we intend to study and establish a correlation of several factors such as glass transition temperature ( $T_g$ ), aromatic content and naphthalene content on flame retardancy of crosslinked polymer network. We also aim, for the first time for crosslinked networks, to estimate theoretical heat release using group contribution method and verify to the experimental values obtained via cone calorimeter.

For the purpose of ease of understanding, the monomers have been grouped as explained below and analyzed within the groups. Certain groups may have monomers repeated to establish a better understanding of various factors that contribute for flame retardancy of the crosslinked networks.

Glass transition temperature ( $T_g$ ): The effect of  $T_g$  on flame retardancy is examined via tuning the functional groups present in the monomers. For comparison, the amine (curing agent) used in this comparison is kept constant which is 4,4'-Diaminodiphenyl sulfone (4-4' DDS). Epoxy monomers are segregated as difunctional (monomers 1, 2, 3, 4, 5 and 6 in Figure 1), trifunctional (monomer 7 and 8), Tetrafunctional (monomer 9 and 10) and multifunctional (monomer 11 and 12) according to the epoxide functional groups in the molecule.

Aromatic and Naphthalene content: The aromatic content of the monomers is calculated theoretically for most of the monomers except no.5 and no.10, which were compared for its naphthalene content.

Aromatic group in pendent Vs backbone: While comparing GAN (monomer 6) and TGPAP (monomer 7) we can determine the effect of aromatic group when present in the backbone and as pendent moieties.

Epoxide containing monomers were blended with amine bearing monomers in 1:1 stoichiometric quantity to make sure no unreacted monomers are present in the compositions which were exposed to flame retardancy. In order to compare the effect of network structure, epoxy monomer/ oligomers structure was varied while the curing agent was 4,4'- DDS. To model the isomeric effect, the effect of 4,4'-DDS was compared to 3,3'- DDS in subsequent sessions using selected epoxy monomers.

#### **4.2.2.1 Specimen preparation.**

All the networks were formulated based on epoxide to amine hydrogen 1:1 stoichiometry. Two different protocols were used and the curing schedule along with the prototype is listed in Table 4.2. Two prototypes were followed because of the limited solubility of 4,4'-DDS due to its solid state at room temperature.

Certain liquid epoxy monomers were able to dissolve the solid amine crosslinker, DDS. For the systems which had difficulties in dissolution, 4,4'-DDS was melted at 150°C in oven until a homogeneous mixture was obtained (for about 30 minutes) prior mixing it with the epoxy monomer. Certain solid epoxy monomers were also preheated prior mixing in stoichiometric quantities. These different prototypes are numbered and listed in table 2 for the ease of understanding. In prototype 1, the monomers were mixed at room temperature followed by casting and curing. In prototype 2, 4,4'-DDS was preheated for 150°C in oven prior mixing it with epoxy monomer, whereas in prototype 3, epoxy resin and amine curative (4,4'-DDS) are preheated separately prior mixing in stoichiometric amounts.

After mixing epoxy and amine compounds, the homogenous mixture was degassed and then casted in a silicon mold of dimensions 100 mm x 100 mm x 3 mm. the

curing and post cure profiles are listed in Table 4.2 along with the prototype used. All the networks were post cured at elevated temperatures to make sure free epoxy and amine functional groups are not present and completely consumed.

Table 4.2 Curing profile used to prepare network. Calculated quantities of aromatic content for each network when cured with 3,3'-DDS. The aromatic contribution from each monomer is accounted to calculate the aromatic content

Chemical Composition	Cure Schedule	Post cure schedule	Prototype	% wt of Aromatic ring in networks
DGEBA	220 °C / 30 min	250°C / 4 hours	Prototype 1	45.85
DGEBF	220°C / 30 min	250°C / 4 hours	Prototype 1	49.24
Cycloaliphatic DGEBA	220°C / 30 min	250°C / 4 hours	Prototype 1	16.08
Longchain DGEBA	220°C / 30 min	250°C / 4 hours	Prototype 2	25.42
Naphthalene*	250°C / 30 min	280°C / 4 hours	Prototype 3	49.02
DGA	220°C / 30 min	250°C / 4 hour	Prototype 1	41.69
TGPAP	250°C / 30 min	280°C / 4 hours	Prototype 1	40.09
TPMTGE	250°C / 30 min	280°C / 4 hours	Prototype 1	52.69
TGDDM	250°C / 30 min	280°C / 4 hours	Prototype 2	43.25
Bisnaphthalene*	250°C / 30 min	280°C / 4 hours	Prototype 3	45.75
EPN 1138	250°C / 30 min	280°C / 4 hours	Prototype 2	59.56
Tactix 556	250°C / 30 min	280°C / 4 hours	Prototype 2	31.70

\* naphthalene rings are considered as 1 aromatic ring for the ease of comparison

### 4.2.3 Characterization

Densities of crosslinked samples were determined by hydrostatic weighing according to Archimedes principle. Mettler Toledo Balance (model XS-104) equipped with a density kit was used in this work. The specimens weight in air was recorded at a

controlled temperature followed by measuring the mass of the same specimen in an auxiliary liquid. The difference in mass along with the recorded temperature is used to calculate the density using the following equation.

$$\rho_P = \frac{W_A}{W_A - W_L} \cdot \rho_0$$

where,  $W_A$  is the polymer weight in air,  $W_L$  is the samples weight in the auxiliary liquid, and  $\rho_0$  is the density of the auxiliary liquid. Deionized water was used as the auxiliary liquid with  $\rho_0$  of 0.997 g/mL.

Thermogravimetric analysis is based on the weight loss of a sample when subjected to a heat treatment because of degradation processes that lead to the release of volatiles. Thermogravimetry is a technique widely used in the thermal characterization of polymer materials in dynamic conditions, which measures the weight loss experienced by a sample subjected to a controlled heating scan as well as in isothermal conditions in which the weight loss is measured versus time at a given temperature. With the later it is possible to calculate the activation energies of the degradation processes which is beyond the scope of this work. The TGA analysis can be performed under nitrogen or air atmosphere to give information on the thermal stability in inert or oxidizing media. TGA was performed on a Q500 thermogravimetric analyzer (TA Instruments Inc.) at the 10 mg scale under a flowing nitrogen atmosphere at a scan rate of 10 °C/min up to 600°C. Temperature is reproducible to  $\pm 1$  °C and mass to  $\pm 0.2\%$ . TGA experiments were done in duplicate and the averages are reported.

Heating the sample in an inert atmosphere first causes the loss of volatiles such as solvents and water absorbed, followed by the loss of low molecular weight components.

Thermogravimetric curve is analyzed for characteristic parameters are usually defined as  $T_{\text{onset}}$ ,  $T_d(x\%)$  and  $R_c$  (Figure 4.4):

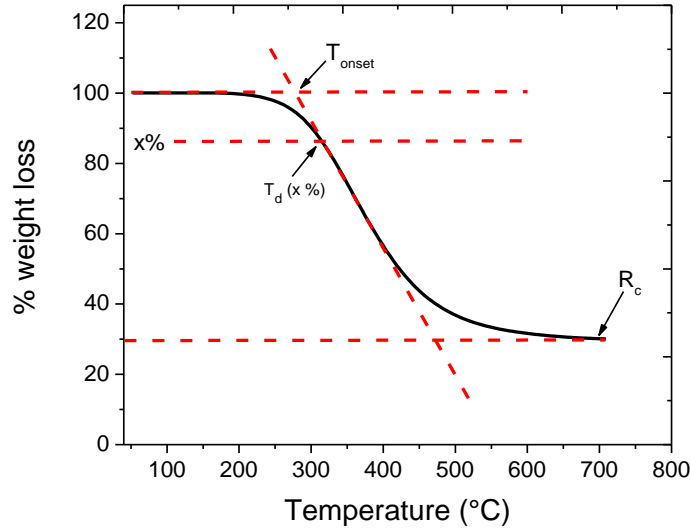


Figure 4.4 Representative thermogravimetric curve showing the analyzed parameters ( $T_{\text{onset}}$ ,  $T_d$  and  $R_c$ )

- $T_{\text{onset}}$ : temperature at which the process of weight loss ( $T_d$ ) begins, ie., the bonds just start to decompose. Usually this value is calculated by taking the tangent to the curve and determining the cross point with the prolongation of the flat line before decomposition begins.

- $T_d(x\%)$  The one other parameter often reported is the data for the temperatures at which partial decompositions have taken place represented as  $T_d(x\%)$  where  $x\%$  represents 5, 10, 50% weight loss.

- $R_c$ : carbonaceous residue is the weight (%) of the sample remaining after degradation.

Bond dissociation energy present in the chemical structure of the polymer is the parameter that determines the temperature of degradation of polymer (heat resistance). Table 1 shows the bond dissociation energy of certain common chemical bonds.<sup>190</sup> The presence of high-energy bonds provides high heat resistance to the polymer, as is the case of sp<sup>2</sup> bonds C = C in conjugated aromatic rings. By contrast, the presence of labile bonds may trigger the rapid decomposition of the polymer and reduce its thermal resistance. Not to confuse with the heat released which depends both on bond dissociation energy as well as the char forming capacity of the molecule. For instance, presence of aromatic ring in the molecule will promote char formation which will reduce the heat released by the polymer.

Table 4.3 Bond dissociation energy of several chemical bonds considered in this work

Bond Type	C-H	C-N	C-C	C=C	C-O	C=O	Benzene
Energy (KJ/mol)	413	305	347	614	358	799	518

There are other structural parameters that significantly influence the thermal stability of a polymer. Some of the most important are:<sup>191</sup>

- a) Structures that do not easily transpose.
- b) Structures stabilized by resonance (benzene).
- c) Bond angles not stressed in the ring structures.
- d) Intermolecular Interaction forces.
- e) High molecular symmetry (structural regularity).



The glass transition temperature,  $T_g$  is the temperature at which the transition of the onset long-range cooperative movements of the molecular chain in crosslinked amorphous polymers. At this temperature there is a significant increase in large scale movements of the macromolecular chains and as a consequence of this, the chain mobility is increased, making it rubbery above the  $T_g$ . Thermal transition, the glass transition temperatures ( $T_g$ )s of the networks were obtained using a differential scanning calorimeter, a DSC Q100 (TA DSC). Samples were accurately weighed (about 5 mg in a Mettler Toledo weighing balance) and were subjected to a heat/cool/heat scanning profile. In the first heat cycle, the sample was heated to 300°C at a ramp rate of 10°C, which was subsequently cooled down to room temperature at a rate of 5 °C/min. Next, the sample was again heated to 300°C at a ramp rate of 10°C/min and observed for any thermal transitions. The second heating scans are reported and the inflection point of the heat flow at the glass transition was conventionally assigned to  $T_g$ . The  $T_g$  was determined as the value of the temperature at the midpoint in the interval where heat capacity changes.

In this work, we tried to establish a relationship between  $T_g$  and heat release of crosslinked systems. Hence it is important to understand the factors affecting  $T_g$  described as follows.  $T_g$  is strongly influenced by the chemical structure of the polymer, molecular rigidity and the intensity of the intra-and intermolecular interactions and other factors:

- a) Crosslink density/ monomer functionality: A more flexible chain yields a lower  $T_g$ . The flexibility depends on the crosslink density which in turn depends on the functionality of the monomers used.

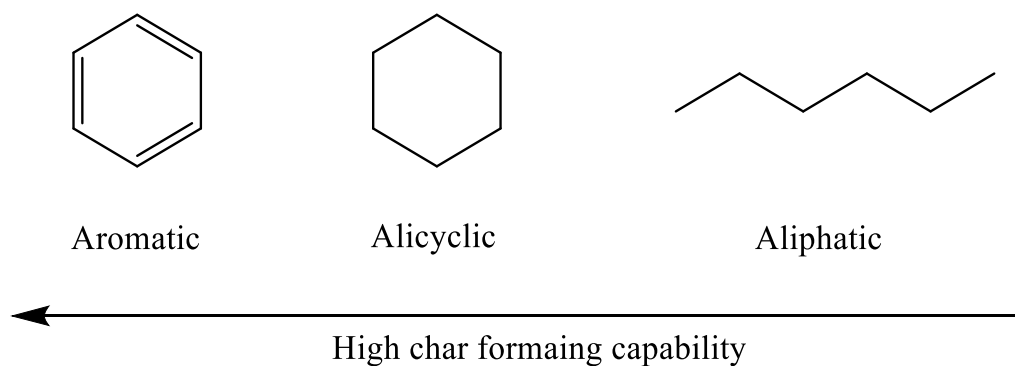
- b) Molecular weight between crosslinks: High molecular weight monomers/oligomers lead to increased molecular weight between crosslinks ( $M_c$ ). Networks with high  $M_c$  will have lower  $T_g$  due to the increased mobility of the chains.
- c) Structural rigidity/Bulky groups: The presence of bulky groups, such as aromatic ring, in the network can either increase or decrease the  $T_g$  depending on if it is present in the backbone or as pendent molecule. When the bulky group is present as pendent molecule, decrease in  $T_g$  is attributed to the separation of chains, caused by the volume of the groups, thereby hindering the formation of hydrogen bonds or other interactions between them; and, the presence of these groups in the backbone increases intramolecular interactions, resulting in increased structural rigidity and, therefore, an increase in  $T_g$ .
- d) Polar groups. The presence of polar groups such as ether linkage (C-O) even though it favors the interaction between chains due to dipole interactions, the C-O bonds are more flexible than the aliphatic chains which will reduce the network rigidity causing a decrease in  $T_g$ .
- e) Low molecular weight fragments: Unreacted low molecular weight compounds may act as plasticizers, lowering the thermal (and mechanical) properties of the material being evaluated.

As mentioned in the previous chapter, the cone calorimeter measures the rate of heat release via measuring the oxygen combustion during burning. Polymer specimen of dimensions 10 x 10 x 3mm with a known weight is continuously exposed to specific heat radiation (corresponding to a heat flux of 50 Kw/m<sup>2</sup>) while the fire is ignited forcefully

through igniting spark. The rate of loss of weight of the specimen is monitored while under fire along with measuring the released CO, CO<sub>2</sub> concentration through the sensors through analyzing the gas at the exhaust. Parameters such as time to ignition ( $T_{ig}$ ), heat release rate (HRR), peak heat release (PHR) total heat released (THR), mass loss rate (MLR) and smoke and toxic gas release rate can be quantified through this technique.

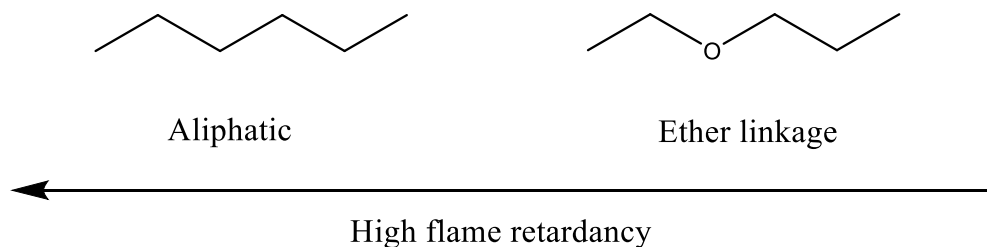
We aim in establishing a relationship between the structure- fire retardant properties of crosslinked networks. Certain factors affecting flame retardant properties which are reported in literature is described below.<sup>182,192,193</sup>

- a) Aromatic content: In general, aromatic compounds promote the char formation during combustion process. Char is a carbonized layer, which is composed of non-combustible compounds, reduces the thermal conductivity, slows or prevents the volatiles to escape to feed the fire, thus making it flame retardant materials. Presence of aromatic group in the polymer contributes for the formation of char thus making the polymer a flame-retardant material as compared to aliphatic and alicyclic compounds.



- b) Presence of week chemical bonds: Presence of week bonds in the polymer backbone creates thermally unstable compounds when exposed to heat. The

production of volatile compounds aid in feeding the fire. Thus presence of weak bonds which are prone of early degradation will lead to production of higher volatiles which reduces the flame retardancy of polymers.



c) Presence of heteroatoms: Presence of hetero atoms such as nitrogen is well reported to promote the char yield during the combustion process. Thus presence of high char yielding compounds will help retard the flammability of polymers. These parameters provides an insight of some factors affecting the flame-retardancy of polymers. But in reality the effects might be synergistic or deteriorating depending on the individual systems under investigation.<sup>194</sup>

Average heat release is a parameter which can be calculated from the total heat released over a specific time. This parameter, which is different from PHR, gives an in-depth knowledge of the flammability of the polymer, ie., a sample having a prolonged heat release but can having one high peak heat release (Figure 4a) is better than a curve having big area with a lower peak hear release point (Figure 4b).

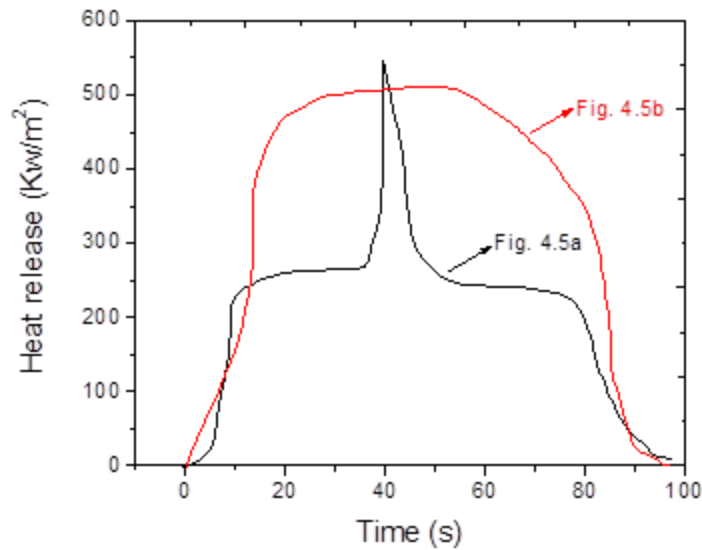


Figure 4.5 Representative plot showing the significance of average heat release. This plot doesn't show the real data from the instrument and this is hand drawn to show the difference in curve

In this work we aim to address the following research questions.

1. What is the most effective chemical structure to achieve inherent flame retardant polymer material?
2. What are the key variables influencing the flammability of neat polymer not limited to crosslink density, bulkiness and aromaticity etc.
3. What material property has effect on fire properties such as pHRR, time to ignition, average HRR and THR?
4. Can we predict the fire properties of a crosslinked networks via group contribution method?
5. What is the effect of isomers in fire behavior and how it relates to the free-volume in the networks?

## 4.3 Results and discussion

### 4.3.1 Thermogravimetric analysis (TGA):

Thermogravimetric analysis of the networks conducted in N<sub>2</sub> atmosphere (pyrolytic decomposition), is presented in Figure 4.6(A). All the network compositions differed in T<sub>onset</sub> temperature, and % char yield which is reported in Table 3. For all networks, degradation temperature falls between 330°C to 500°C resulted in loss of low molecular weight compounds. Thermograms revealed that the networks decompose in a single mass loss step except for cycloaliphatic DGEBA based networks. We anticipate the two-step degradation mechanism for cycloaliphatic based networks is the high strain associated with the ring structure caused it to decompose at an early stage, indicated as the first step in thermal degradation<sup>195,196</sup> with low onset degradation temperature around 329°C, followed by the chain scission of backbone at second thermal degradation step happening at around 370°C. However, this must be further analyzed, and it is beyond the scope of this investigation.

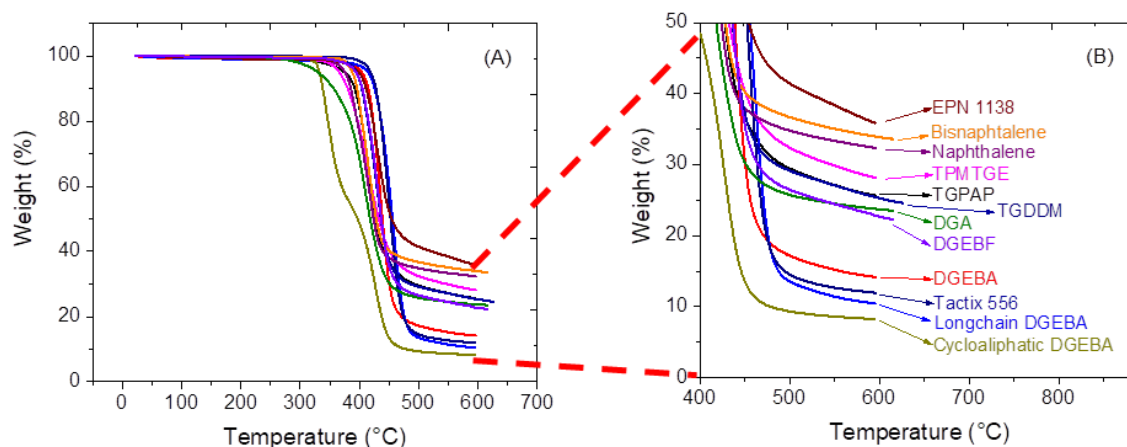


Figure 4.6 TGA curves for all networks heated up to 600°C in nitrogen. (B) Plot indicating different networks has different char yield

**$T_{onset}$ :** The onset degradation temperatures ( $T_{onset}$ ) indicates the temperature at which the degradation and chain scission starts. Table 4.4 list different parameters measured using TGA and  $T_{onset}$  varies broadly from 330 °C to 430 °C. This is dependent on several factors, not limited to crosslink density, bond dissociation energy of the backbone chemical structure, chain packing to name a few. Compounds, cycloaliphatic DGEBA, DGEBA and DGEBF, despite of structural similarities have different onset temperature. Cycloaliphatic DGEBA having lowest onset temperature mainly because of the low thermal stability associated with the ring strain of cycloaliphatic structure as compared to their analog compounds. Between DGEBA and DGEBF, the former has lower onset temperature due to the interrupted chain packing arising from the presence of methyl groups in the backbone structure.

The onset degradation temperature of the networks analyzed the following trend:

Cycloaliphatic DGEBA< DGA< TPMTGE< TGPAP< Bisnaphthalene<  
TGDDM< DGEBA< EPN 1138< DGEBF< Tactix 556< Longchain DGEBA.

Longchain DGEBA has higher onset degradation temperature compared to other networks under investigation. We hypothesize this is due to the chain flexibility and the ability to ring-flip at 1,4 substituted phenyl positions acting as a mechanism for energy dissipation associated with the long chain epoxy component which requires more energy for the chain cessions to occur. The networks based on Tactix 556 (epoxidized phenol novolac based polymer with cyclic rings) has the second highest onset degradation temperature.<sup>197</sup> Compared with EPN 1138, which is from the same family of polymers (epoxidized phenol novolac), the higher onset temperature of Tactix 556 is mainly observed due to the thermal rearrangements associated with the cyclic ring structures.<sup>198</sup>

**Char Yield-** The other important information via TGA is the % char yield. The amount of char yield depends on the several factors not limited to presence of electronegative elements such as nitrogen and charring moieties such as aromatic and naphthalene-based compounds. Table 3 is sorted in the order of increasing char. The data reveals that DGEBA based epoxy (cycloaliphatic DGEBA, Longchain DGEBA and DGEBA) has the lowest char yield, whereas naphthalene-based compounds possess highest char yield. It has been well reported in literature that the naphthalene has the highest char forming capabilities among the family of organic compounds.<sup>199,200</sup> Comparing EPN 1138 and Tactix 556, being same family of epoxy novolac resins, the former yields higher char than later. The reason behind this is unknown at the moment and needs further investigation. These compounds are obtained from industry and the exact chemical structures, impurity level etc., are unknown. A better understanding the



chemical structure is required to justify the properties associated with these compounds. DGEBF and DGEBA, though these are structural isomers, DGEBF yields higher char (22.69%) compared to DGEBA (14.15 %). This needs further investigation and to our best of our knowledge, no studies has been done.

Table 4.4 TGA data for all networks in studying structure- FR properties of epoxy amine

Material	T <sub>onset</sub> (°C)	T <sub>10%</sub> (°C)	T <sub>50%</sub> (°C)	Char	
				Yield(wt%)	DT <sub>max</sub> (°C)
Cycloaliphatic DGEBA	329.68	338.19	396.94	8.27	342.48 & 425.14
Longchain DGEBA	428.43	425.31	455.96	10.45	457.13
Tactix 556	423.34	429	441.49	12.01	453.91
DGEBA	402.04	416.23	438.65	14.15	437.08
DGEBF	411.97	406.29	436.95	22.69	433.23
DGA	369.41	356.92	416.52	23.73	410.78
TGDDM	398.35	405.45	436.09	25.61	414.31
TGPAP	386.15	391.83	428.72	25.64	429.54
TPMTGE	374.52	380.19	433.83	28.13	413.85
Naphthalene	378.49	385.58	423.33	32.37	416.95
Bisnaphthalene	387.57	396.37	427.58	33.88	421.52
EPN 1138	403.18	411.97	456.24	35.85	433.99

T<sub>onset</sub> – Onset temperature; T<sub>10%</sub> - Temperature at 10% degradation; T<sub>50%</sub> - Temperature at 50% degradation; DT<sub>max</sub> – Maxima of mass loss rate

The presence of oxygen atmosphere during combustion will certainly have some effect in degradation process. Lyon et al. demonstrated the difference in thermal degradation behavior and the characteristic temperatures when the degradation experiments are carried out at different atmosphere, ie., in N<sub>2</sub> or in air.<sup>201</sup> Thus the TGA

data reported in this work corresponds to the combustion carried out in N<sub>2</sub> atmospheres and potentially the results will vary if the experiments were carried out in air.

#### **4.3.2 Effect of Curing temperature on fire properties of crosslinked networks:**

There have been several reports on the network properties being dependent on the curing profile (temperature and time).<sup>202</sup> In this work, we aim to determine, if any, the effect of curing temperature on the fire properties of the network. TGDDM was taken as a model system to examine this effect because of its wide usage as matrix materials in composite applications. Calculating activation energy and relating that to cone calorimeter results were chosen as a reasonable way to determine the fire properties.

##### **4.3.2.1 Activation energy of decomposition via Ozawa Plots.**

To determine the activation energy of networks, constant heating rate TGA technique was used based on Flynn & wall method.<sup>203,204</sup> According to this method, each sample requires weight loss determination for three or more different linear heating rate, usually 0.5 to 50°C/ minute. The characteristic temperatures, T<sub>onset</sub>, T<sub>x%</sub> and D<sub>Tmax</sub>, are dependent on the heating rate applied. In general, as the heating rate increases, the characteristic temperatures shift to higher values.

This approach assumes basic Arrhenius equation as shown in Equation 1 below.

$$\frac{d\alpha}{dt} = Z \exp\left(-\frac{Ea}{RT}\right) (1 - \alpha)^n$$

where,  $\alpha$  – fraction of decomposition

t – time (sec)

Z – pre-exponential factor (1/sec)

E<sub>a</sub> – activation energy (J/mole)

R – gas constant (8.314 J/mole K)

N – reaction order (dimensionless)

This equation is rearranged to determine activation energy as shown below

$$Ea = \left(-\frac{R}{b}\right) \frac{d \ln \beta}{d \left(\frac{1}{T}\right)}$$

Where, b – constant (n=1)

B – heating rate (°C/min)

T – temperature of weight loss (°C)

In this study we intend to determine if there is any change in activation energy for similar network cured at different temperature. TGDDM, being commonly used in composites, we varied the curing temperature from 150°C, 180°C and 220°C for 30 min. TGA experiments were carried out at three different heating rate, 10°C/min, 20°C/min and 40°C/min for the samples cured at different temperatures mentioned above. Figure 4.7 is a representative plot of TGDDM- 3,3'-DDS based networks cured at 220°C for 30 min.

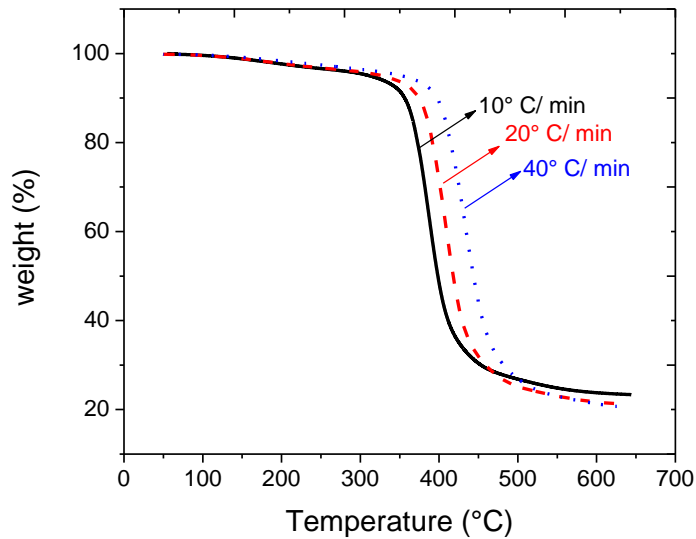


Figure 4.7 Representative plot of TGDDM exposed to TGA at different heating rate

The temperature of degradation,  $T_d$  (x%), at various weight percentage is extracted from the Figure 4.7, termed as  $\beta$  and plotted as a function of inverse ramp temperature (Figure 4.8). It follows a linear trend for the three observed points.

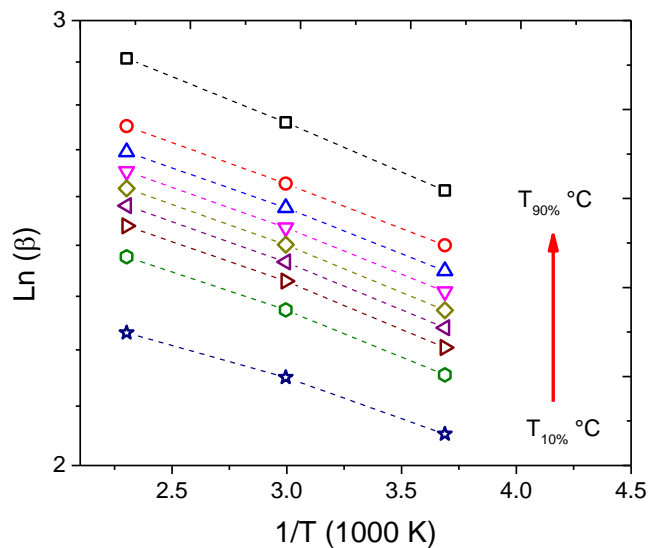


Figure 4.8 Flynn & wall method: Temperature of degradation at various heating rate plotted as a function of heating rate

The slopes of the lines were extracted to calculate the activation energies at various temperature of degradation  $T_d$  (x%) as shown in Figure 4.9. As seen the activation energy increases initially then plateaus off till 80 % degradation. Beyond 80% degradation, ie., after complete decomposition of the network, the activation energy is high because of low mass content and complete formation of char. Averaging the activation energies over the entire range of degradation extent gives the activation energy of TGDDM- 4,4'-DDS system cured at 220°C for 30 min as 94.4 KJ/mol.

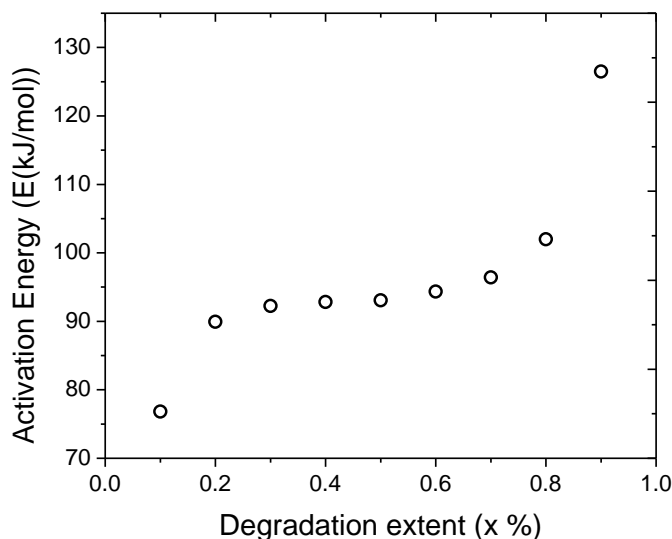


Figure 4.9 Activation energies at various partial degradation of TGDDM network

TGDDM network cured at various temperatures, 150°C and 180°C, also followed a similar trend and the calculated activation energies were 90.4 and 92.8 KJ/mol respectively. As seen, the activation energy of a system cured at higher temperature was found to be higher as compared to the systems cured at low temperatures. This is in agreement with the heat release rate determined via cone calorimeter explained below.

#### 4.3.2.2 Cone calorimeter results of TGDDM networks cured at varying temperatures

The heat release rate of TGDDM based epoxy resin cured with 4,4'-DDS crosslinker obtained via cone is shown in Figure 4.10. Networks cured at 150°C / 30 min had higher peak release rate whereas networks cured at 220°C / 30 min had the lowest. Even though the networks didn't have any free epoxide or amine functional groups (examined using FTIR, not shown) the differences could probably arise from the extent of condensation reactions occurring between the hydroxyl groups present in the network's backbone. This is not certain at this moment and this needs further investigation. This can be modelled or confirmed by analyzing for free hydroxyl groups using FTIR, while heating the networks to elevated temperatures.

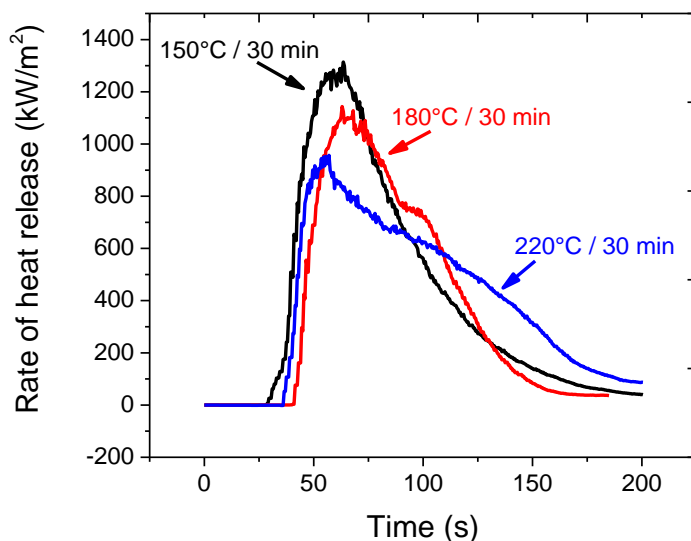


Figure 4.10 Heat release rate of TGDDM epoxy based networks crosslinked with 4,4'-DDS at different temperatures, 150°C, 180°C and 220°C for 30 min

Currently, 5°C/ min and 30°C/min ramp rate experiments are being carried out for all other networks to determine the activation energies of various networks.

### 4.3.3 Differential scanning calorimetry (DSC):

The DSC thermograms shown in Figure 4.11 indicates the absence of crystalline domains and a clear transition of heat flow at glass transition. As seen in Figure 4.11, the glass transition temperature of all the networks varied from 121°C to 291 °C with Longchain DGEBA being the lowest and TPMTGE highest.  $T_g$  of all networks is listed in Table 4.5.

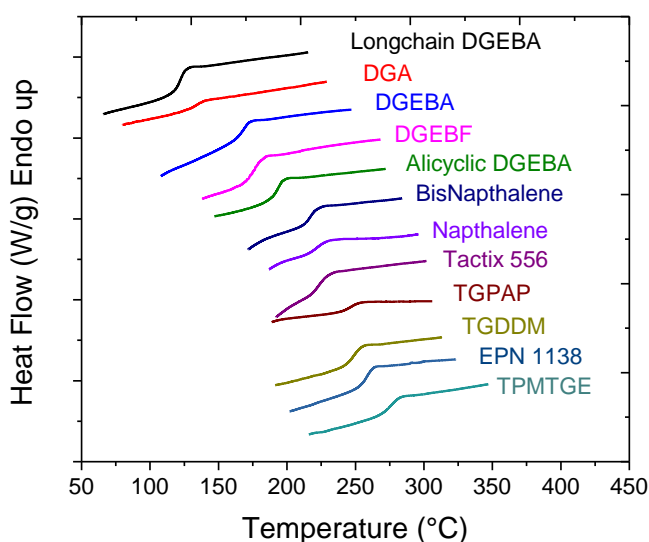


Figure 4.11 DSC thermograms of all networks. Second heat reported for  $T_g$  determinations. Curves vertically offset for clarity

Longchain DGEBA containing networks possess low  $T_g$  because of the high molecular weight between crosslinks. The  $T_g$  of DGA containing networks is low due to two hypothetical reasons: the first being a difunctional epoxy which leads to low crosslink junction points and the second being the structural complexity due to the aromatic ring which is attached to the backbone via nitrogen compounds causing the chains to rotate along the axis (see Figure 4.2 in experimental session). DGEBA, DGEBF

and alicyclic DGEBA being isomeric structures, DGEBA has the lowest  $T_g$ . The presence of methyl groups in the linkage interrupts the chain packing causing the molecular motions to reduce the  $T_g$  of these networks as compared to DGEBA based networks.

Table 4.5 Glass transition and density of networks crosslinked with 4,4'-DDS

Name	$T_g$ (°C)	Density (gm/cc)
Longchain DGEBA	121	1.192
DGA	135	n/d*
DGEBA	165	1.268
DGEBAF	175	1.248
Alicyclic DGEBA	190	1.184
Bisnaphthalene	215	1.262
Naphthalene	220	1.318
Tactix 556	221	1.227
TGPAP	241	1.325
TGDDM	245	1.273
EPN 1138	255	1.283
TPMTGE	291	1.272

Bisnaphthalene being a tetra functional monomer, the  $T_g$  is lower than the difunctional naphthalene monomer because of the methyl linkage present between the naphthalene units which promotes the cis-trans rotation.<sup>200</sup> Oligomers Tactix 556 and EPN 1138, which are both novolac based epoxy systems, differ in  $T_g$ . Tactix 556 has lower  $T_g$  because of the ring structure which connects the aromatic ring increasing the molecular weight between crosslinks. Polymers with high steric hinderance, which is associated with aromatic groups, will have high rigidity thus increasing the glass transition temperature. Since these are oligomers, the impurities should also be taken into considerations. TGPAP is a trifunctional monomer which contains an additional ether linkage making it flexible compared to the other trifunctional monomers used in this



study. TGDDM in addition to its four functionalities, the aromaticity in the backbone, due to steric hindrance, imparts rigidity to the network which leads to high  $T_g$  of these networks. TPMTGE based networks have high  $T_g$  when compared to the tetra-functional and other monomers mainly due to the tri benzene structure which leads to the most rigid networks.<sup>205</sup>

#### **4.3.4 Density:**

Densities of all networks, measured via Archimedes principle, are reported in Table 4.5. As seen the networks possess varying densities and this depends on both the chemical composition and the network crosslink density. Usually, density is a good measure of crosslink density of networks having identical chemical moieties: networks with high crosslink density will have high density and vice versa. As seen from the obtained data, density measured (1.192 g/cc) for longchain DGEBA containing networks is the lowest which indicates this has the lowest crosslink density, whereas networks with TGPAP (density = 1.325 g/cc) has the highest. As mentioned earlier, the density depends on the chemical composition as well. Despite naphthalene-based epoxy resins are difunctional, one would expect a low crosslink density, the density of naphthalene based compounds (1.318 g/cc) is higher than the tetra-functional bisnaphthalene based compounds (1.262 g/cc). This is mainly due to the conformational changes associated with the bisnaphthalene monomers making the chain be more flexible leading to a less dense crosslinked networks.

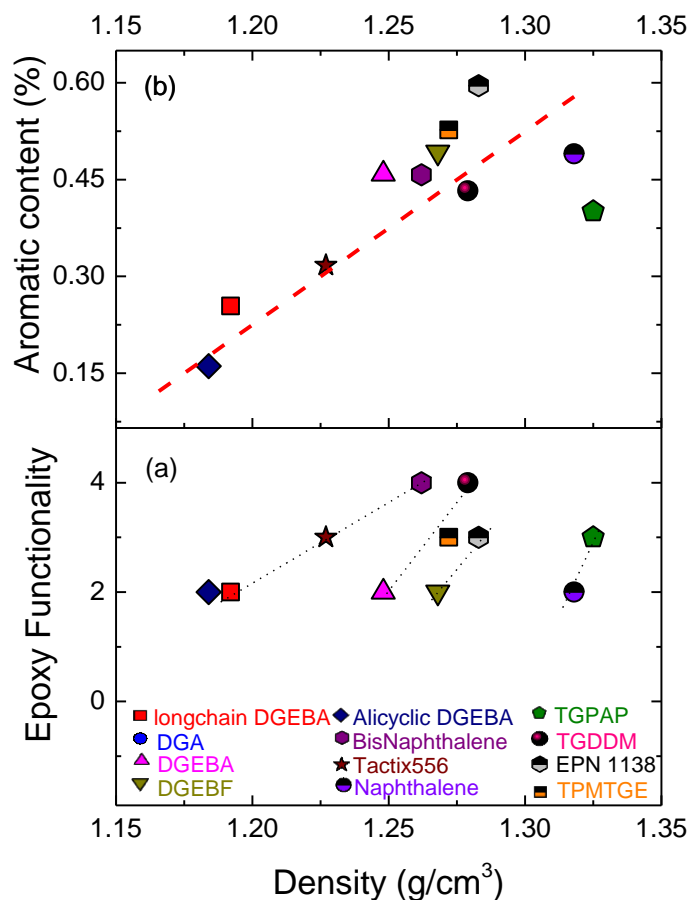


Figure 4.12 (a) Epoxy functionality and (b) aromatic content plotted as a function of density of the crosslinked networks.

Based on our previous work detailed in chapter 2, for a chemically identical networks, density decreases with decreasing crosslink density. The functional groups present in the monomers affected the crosslink density. Hence networks are grouped based on their epoxy functionality and plotted as a function of density of the network in Figure 11a. Unfortunately, in this study, the effect of change in crosslink density cannot be isolated from the effect of phenyl/ naphthalene content. Thus, the networks having similar functionality (difunctional group: alicyclic DGEBA, long chain DGEBA,

DGEBA, DGEBF and naphthalene) possess different densities. The density of these networks doesn't depend only on the degree of crosslinking but also the chemical compounds such as aromatic rings and hetero atoms present in the network. Figure 4.12b displays aromatic content plotted as a function of density. As seen with increasing aromatic content the density increases which indicated the density depended on the bulky aromatic content in the network. Despite having a trend with increasing density with aromatic ring, the values are not completely in agreement which indicated the density of the networks doesn't solely depend on the aromatic content, but also several factors such as crosslink density, presence of hetero atoms (nitrogen) in the network.

#### **4.3.5 Cone calorimeter:**

The fire assessment of the prepared networks were studied using a cone calorimeter, which is a standard technique compliance with ASTM E1354 as described in the previous chapter and elsewhere.<sup>62,85,206,207</sup> Networks were casted to standard dimensions ( 100 mm x 100 mm x 3 mm) and tested in a horizontal position at a heat flux of 50 Kw/m<sup>2</sup> at the surface with 24L/sec as exhaust flow. All specified epoxy monomers were cured with 4,4'-DDS to study the exclusive effect of epoxy structure on properties. Specimens were tested for parameters such as time to ignition (  $T_{ig}$ ), peak heat release rate (PHRR), time to peak heat release rate ( $T_{PHRR}$ ), total heat release ( THR), Average effective heat of combustion, mass loss rate, and char yield.

The results are presented in groups to simplify the data interpretation of the networks. Networks having difunctional epoxy monomers are placed in one group whereas networks containing multifunctional epoxide groups are in the other group. Not to mention, the segregation is just to display the heat release curves and later in this

section, we have compared several monomers to analyze and interpret various effect of flame retardancy of these networks. All networks followed a solid state pyrolysis (networks converted to a solid char during combustion without changing to liquid) which is a characteristics of crosslinked systems.

*Di-functional epoxide containing networks:* This group comprises of difunctional epoxies, DGEBA, DGEBF, Alicyclic DGEBA, Longchain DGEBA, Naphthalene and DGA containing networks. The heat release curves of all these networks are presented in Figure 4.13.

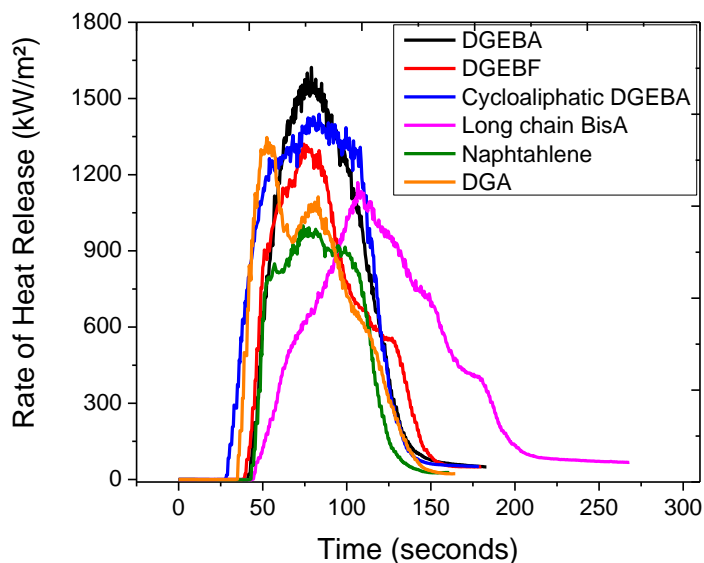


Figure 4.13 Heat release curves of difunctional epoxide containing monomers

As seen in Figure 4.13, the curves typically follow the burning behavior of reported in literature.<sup>73</sup> The sharp peak in HRR curve of DGEBA based networks indicates the entire sample is being pyrolyzed without or little char formation. Similar behavior is observed for structurally similar monomers, DGEBA, DGEBF, cycloaliphatic

DGEBA and longchain DGEBA. For DGA containing networks, there exists two peaks and the curve essentially indicates the char forming capability which may be due to the presence of high aromatic content as pendent molecule. The first HRR peak associated with DGA containing networks can be explained by the rapid decomposition of the aliphatic backbone nature of these networks which initiates the combustion and the reduction in HRR is because of the formation of char (thermal barrier). The second heat in HRR happens when the formed char breaks down to release the trapped volatiles underneath it. For naphthalene containing systems, there exists three integral peaks which is due to the high char forming capability of naphthalene rings.

Longchain DGEBA had a delayed  $t_{PHRR}$  and a lower HRR among the difunctional based epoxy resins. The delayed  $t_{PHRR}$  can be explained and related to the energy dissipation mechanism happening due to the rotation happening at 1,4 phenyl substitution along the backbone. This also lead to an increase in combustion time. Long chain DGEBA based networks, despite of low aromatic content(25.42%- Refer table 2 in experimental), the HRR is the lowest among the family of difunctional epoxy based networks. The reason for this is unknown at the moment and further investigation is carried out. DGEBA, DGEBF and Longchain DGEBA (structurally similar monomers) exhibits similar time to ignition (around 48 seconds), whereas cycloaliphatic DGEBA's time to ignition is much lower (37 seconds) which is in agreement with the onset temperatures recorded via TGA for the above said reasons.

The other interesting feature noted here is the total duration of the burns. DGA containing networks has lowest burn duration which is an indication of rapid release of energy during combustion process. This can be explained via the aliphatic bonds present

in the backbone which has low bond dissociation energy. Structurally similar monomers except longchain DGEBA has similar duration to burn. The reasons for longchain DGEBA to have higher duration of burn along with slower rate of heat release points to the chain rotation to dissipate the energy which requires high activation energy for the bonds to dissociate.

Peak heat release rate (PHRR) is a measure of the maximum heat released during combustion process. All the networks except naphthalene-based networks possess PHRR above  $1000 \text{ kW/m}^2$ . It is important to note that, PHRR alone as a parameter might mislead the interpretation of the fire characteristics of polymers. A combination of time PHRR along with average heat release, char yield and the nature of the curve is to be considered while investigation of flame characteristics of polymers.

Average heat release (AHR) is an important parameter which is calculated by integrating the area under the HRR curve over combustion time. AHR essentially indicates the heat release over the entire combustion time. It is a parameter that combines the total heat release with the peak heat release. As seen in Table 4.6, the AHR of naphthalene containing networks are the lowest mainly because of the low HRR along with high char yield of these systems. Cycloaliphatic DGEBA containing networks despite of having lower PHRR values compared to DGEBA, possess higher Average HRR which is mainly because of the faster combustion process happening at the early stages of fire. (From the HRR curves in Figure 4.13).

Table 4.6 Cone calorimeter data for Difunctional (top set) and multi-functional (bottom set) epoxide containing networks

Chemical Composition	T <sub>ig</sub> (sec)	PHRR (kW/m <sup>2</sup> )	T <sub>PHRR</sub> (sec)	Avg. HRR (kW/m <sup>2</sup> )	THR (MJ/m <sup>2</sup> )	Avg MLR (g/m <sup>2</sup> s)	Char yield [%]
DGEBA	45	1622	79.0	698	95.6	48.7	5.4
DGEBF	48	1409	79.8	589	85.2	47.5	9.7
Cycloaliphatic DGEBA	37	1438	83.5	737	108.4	51.6	5.6
Long chain DGEBA	51	1540	105.0	534	100.1	42.2	6.3
Naphthalene	46	999	74.0	469	62.4	34.9	25.4
DGA	39	1347	52.5	642	80.3	41.6	10.5
TGDDM	40	1009	63.5	491	78.5	37.4	17.9
TPMTGE	41	1448	88.0	573	72.8	47.7	22.6
Tactix 556	45	1461	86.5	622	103.9	48.3	4.7
EPN 1138	46	1214	97.5	465	72.1	41	24.4
TGPAP	49	1346	82.0	656	65.3	43.5	21.6
Bis Naphthalene	39	1438	61.5	615	55.7	36.8	24.6

**Note:** T<sub>ig</sub> – time to ignition; Duration – total time for combustion; PHRR – peak heat release rate; T<sub>PHRR</sub> – time to PHRR; Avg. HRR – average heat release rate; THR – total hear release; Avg. MLR – average mass loss rate; char yield – amount of residue after combustion

Total heat release (THR) is a measure of combustible substance within the network. It is directly related to the amount of char yield: higher the presence of char formation lowers the THR. The components in the network has to transform either to volatiles or into a char during combustion process. As seen in Table 4.6, naphthalene networks has the highest char forming capability and it posses lowest THR among difunctional epoxide containing networks. DGEBA and its structurally similar monomers (DGEBF, Cycloaliphatic DGEBA and long chain DGEBA) has the lowest char yield and higher total heat release.

Cone calorimeter measures the mass loss for the entire combustion period and this is termed as average mass loss rate (avg. MLR). This gives the measure of volatiles

released and it can be used in evaluating the char formation capabilities of the network. Naphthalene based systems which has high char yield has low average MLR which implies that, the amount of volatiles released is lower and naphthalene transforms to incombustible char during combustion process. The average MLR for cycloaliphatic DGEBA based networks are the highest which might be explained through the fast decomposition characteristics of cyclic rings. This can be further confirmed through the low char yield for cycloaliphatic containing networks.

*Multifunctional epoxide containing networks:*

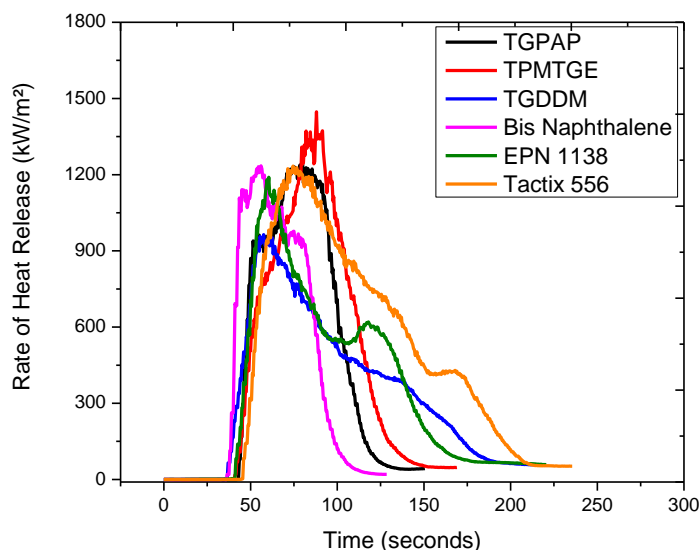


Figure 4.14 Heat release curves of multi-functional epoxide containing monomers

Figure 4.14 represents the raw heat release rates of networks containing multi-functional epoxide groups. This group includes TGDDM, TPMTGE, TGPAP, bis naphthalene and oligomers Tactix 556 and EPN 1138. most of the networks have similar time to ignition except for Tactix 556, EPN 1138 and TGPAP. Among the networks



containing multi-functional epoxide groups, bis naphthalene systems had shorter duration of combustion along with high char yield. This is primarily due to the presence of aliphatic linkages between naphthalene units which decomposes at a faster rate compared to aromatic groups and combustion of naphthalene units promote char formation as mentioned previously. When bis naphthalene and naphthalene containing networks are compared for PHRR, bis naphthalene exhibits higher value. When the curves are compared, the bis naphthalene networks when exposed to heat flux, there is a rapid release of energy primarily arising from the methylene linkages between the bis naphthalene units. This weak bond tends to dissociate at a faster rate which explains the reason of having high PHRR. TPMTGE containing networks despite of high char yields, the PHRR is the highest. We hypothesize this is due to the C-C linkages between the bulky aromatic group which tend to degrade but needs further investigation. The HRR curves of networks TGDDM and EPN 1138 indicates char forming behavior, i.e., the curve reaches its peak followed by a gradual decrease in HRR due to the formation of thermally insulating char. Tactix 556 networks has high PHRR and a prolonged period of combustion. The prolonged combustion period is due to the dimerization tendency of these oligomers at elevated temperatures.<sup>198</sup> The low char yield for Tactix 556 networks, which is explained by the low aromatic content in the network (Table 4.2 in experimental session), and high THR explains that the networks decompose to form more volatiles under combustion. One would expect to have high average HRR for bis naphthalene based systems. But our results indicated that the degradation rate was rapid and despite of higher functionality (4 functional) as compared to naphthalene (2 functional), the former exhibited higher average HRR.

It is important to note that, a single parameter might mislead the interpretation of the fire characteristics of polymers as seen in the case of TPMTGE where these networks has high PHRR values but have low average heat release and high char yield. A combination of time PHRR along with average heat release, total heat release, char yield, smoke production and the nature of the curve is to be considered while investigation of flame characteristics of polymers.

#### **4.4 Correlation analysis**

In the field of polymer flammability, to the best of our knowledge, no single material property by itself has been related with fire performance because the burning rate, ignition and heat release rate depends on the extrinsic quantities such as temperature, atmosphere of combustion and the reaction products released when polymer is exposed to heat and so on. In this work we aim to establish a relation between polymer properties to the fire properties. When such physical property is plotted as a function of fire property, the magnitude of  $R^2$  is considered to provide the regression accounts for dependence or not. When  $R^2$  equals 1, the regression accounts for all variations in the physical property accounts for change in fire properties thus the correlation is deterministic. On the other hand,  $R^2$  equal zero indicates the physical property accounted has no effect on the fire property of that networks.

As mentioned earlier, average HRR appears to provide insight about the fire properties of a polymer since it takes account the heat release, which is rooted to the chemical structure, over the entire combustion time. On the other hand, the most important parameter in studying the effect of polymer structure on its properties is the glass transition temperature ( $T_g$ ). One would expect that the rigid networks will require

high bond dissociation energy which will lower average HRR and vice versa. As seen in Figure 4.15, ( $R^2 = 0$ ) there is no correlation between the glass transition temperature of the networks and its corresponding average heat release rate. This is mainly because of the complex dependence of average HRR not only on the rigidity of the networks but also several other parameters not limited to the char forming ability, thermal stability etc. Hence, average HRR of a network cannot be predicted just by the knowledge of glass transition temperature. The average HRR obtained was also compared with the char yield of the networks (not shown). The apparent average HRR values didn't depend on the amount of char formed at the end of combustion.

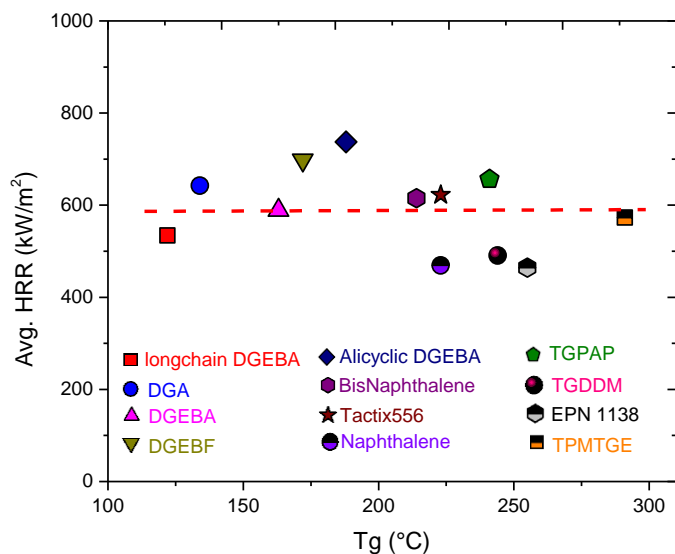


Figure 4.15 Average HRR plotted as a function of glass transition ( $T_g$ ) of networks. The graph indicates there is no relationship between the Avg. HRR and the  $T_g$ . The magnitude of  $R^2 = 0$  indicating the average HRR is independent of  $T_g$

The next essential parameter in fire property of a polymer network is its time to ignition ( $T_{ig}$ ). It is a measure of polymers stability to fire conditions and it is important for

the material development since flame spread could be seen as a succession of ignition.  $T_{ig}$  was compared to the thermal degradation of networks at 5% ( $T_{5\%}$ ) determined via TGA and shown in Figure 4.16. Overall, the time to ignition of networks with higher  $T_{5\%}$  is greater. The values doesn't absolutely match, but the relation between these two factors are quite satisfactory. The magnitude of  $R^2= 0.54$  which indicates the moderate dependence of time to ignition to the temperature of 5% degradation possibly because the values determined for  $T_{5\%}$  is via TGA in nitrogen atmosphere where as the  $t_{ig}$  is through cone calorimeter under atmospheric air conditions. However, this is a good indication that the networks which tend to degrade faster in TGA will have rapid time to ignition.

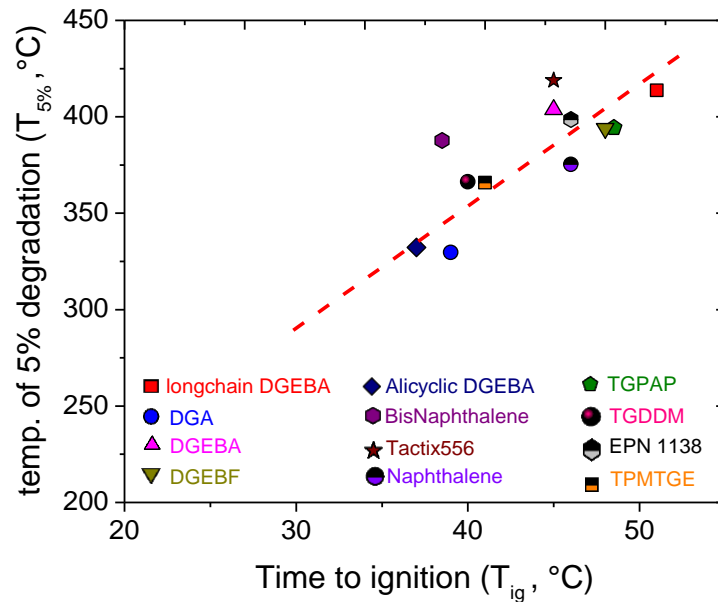


Figure 4.16 Temperature of 5% degradation (from TGA data) plotted as a function of time to ignition (from cone calorimeter)

Total heat release is one other parameter of interest where it estimates the amount of volatiles released during combustion process. As discussed earlier, during combustion

process, polymer either converts in to volatile compounds, to further feed the flame, or it turns into an insulating layer of char, to stop the combustion process. The char yield can serve as an indirect indication of flame retardancy. Thick char becomes a better thermal insulating layer, which undergoes slow oxidative degradation, isolates the released volatiles to reach the fire along with preventing heat reaching the unburnt layer of the polymer. Thus, in general, materials which tend to form char doesn't release volatile (combustible matter) which will have reduced total heat released. Thus, it is important to establish a relationship between char yield and THR. Figure 4.17b displays the THR plotted against char yield which indicates an inverse relationship. the magnitude of  $R^2$  (= 0.85) determines a strong relationship between THR and char yield. Networks which yielded high char such as naphthalene and bisnaphthalene had lowest THR, while networks with lowest char forming capability such as DGEBF and DGEBA based monomers (DGEBA, Alicyclic DGEBA and Long chain DGEBA) resulted in high THR. While investigating the reasons for char formation, we found the concentration of structural units which contribute to the formation of char played an important role in char yield which affected the THR of the networks. An increase in charring induces a decrease in the amount and rate of combustible volatile release, resulting in lower flammability which is evidenced by lower THR.

As seen in Figure 4.17a, networks with high aromatic content yielded high char. The magnitude of  $R^2$  (= 0.42) indicated a moderate dependence since other atoms including electronegative nitrogen, dense naphthalene also accounts for char formation which can't be neglected. The aromatic content is not only calculated based on the epoxy monomer but also the curing agent, 4,4'-DDS. Naphthalene based compounds yielded

highest char while the networks composed of alicyclic DGEBA possess lowest char. Our finding indicates that the amount of char formation follows the below order:

Naphthalene > aromatic > alicyclic ~ aliphatic

For the sake of comparison between naphthalene and aromatic compounds, one naphthalene unit is assumed to one aromatic ring structure in our calculations. With increasing aromatic content, the amount of char yield increases linearly. It is to be noted that the networks even with alicyclic rings (Cycloaliphatic DGEBA) had some aromatic content in the network which essentially arose from the curing agent, 4,4'-DDS.

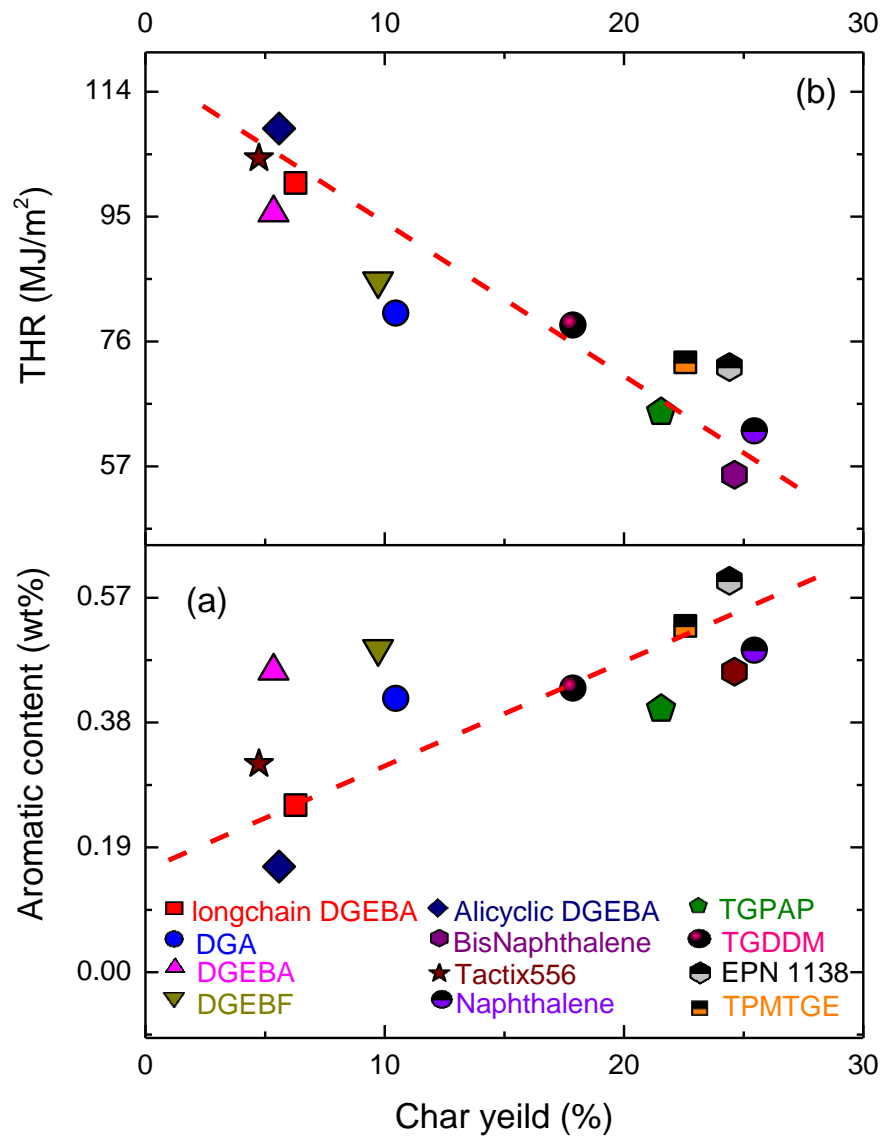


Figure 4.17 Plot signifying the relationship between THR, aromatic Content and Char yield. Char yield is linearly dependent on aromatic content (Plot 9a on bottom) and inversely proportional to THR (Plot 9b on top)

As mentioned earlier, the degradation depends on several factors including the rate of exposed heat, atmosphere of burn etc. The char formed remains more or less unchanged in nitrogen atmosphere, while the presence of an oxidant medium facilitates

its oxidation at high temperatures (in air), leading in most cases to a very small char yield. In our study, there is a fair relationship in char formation between TGA (nitrogen atmosphere) and cone (room atmosphere) though there is some level of discrepancy (DEGF and DGA based networks). We hypothesize that the agreement arises from the absence of flame retardant material, such as phosphorous or metal hydroxides, which exclusively promote char formation. The formed char is based on the amount of organics present in the networks. It will be a meaning full comparison if the TGA char yield was recorded in air atmosphere and was compared with cone char yield, which is being carried out.

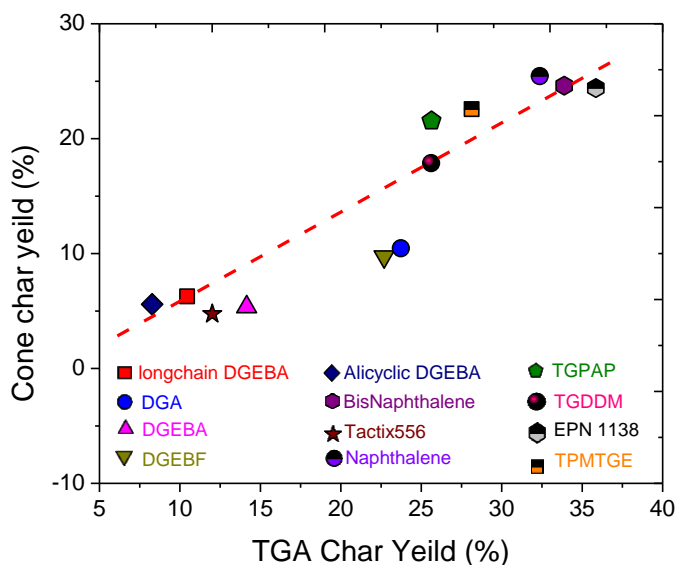


Figure 4.18 Display of char yield % from two different experiments: TGA on X-axis and Cone calorimeter on Y-axis



## **4.5 Molar group contribution method to determine polymer flammability**

Predicting the polymer property theoretically is of great interest because it helps developing polymers with desired flame retardancy with certain advantages not limited to the quick assessment and inexpensiveness. In this work, we aim to validate if the flame property of a crosslinked epoxy network estimated via group contribution method is in agreement with the experimental values determined via cone calorimeter. Heat release rate (HRR), heat release capacity ( $\eta_c$ ) and total heat release (THR) are three parameters which reflect the combustion properties of a material. Van Krevelen proposed an additive group contribution method based on the polymer repeat units to determine several properties of polymers.<sup>208</sup> Lyon et al., estimated the thermal combustion properties of several polymers of known chemical composition using group contribution method.<sup>192</sup>

### **4.5.1 Prediction of heat release capacity (HRC):**

Specific heat release capacity is defined as the amount of energy required to raise the temperature of one-gram sample by one degree kelvin. HRC combines the thermal stability with the combustion properties, thus can be a good predictor of fire properties of polymeric networks. Experimental HRC can be obtained by dividing the experimentally determined HRR by the rate of temperature rise during combustion process. Theoretically, since HRC is a material's property that depends on the chemical structure of the polymer, it can be calculated from the additive molar group contribution method. In the group contribution method established by Lyon and co-workers to calculate HRC is based on two criteria:<sup>208-212</sup>

- a) Polymers which thermally decompose in a single step

- b) Materials where there are no interactions or reactions between the chemical structural units, and
- c) The contribution from groups were determined using thermoplastics.

The calculated heat capacity of polymers in their studies were in agreement with experimental values within  $\pm 15\%$  obtained via microscale combustion calorimetry.<sup>208</sup>

In a group contribution method, the intrinsic property of a polymer is calculated from its chemical groups assuming that groups  $i$  and  $j$  contribute an amount  $P_{ij}$  to a property  $P$  by summing according to the mole fraction of each groups.

The heat release on mass basis in J/g-K, can be obtained using the equation below.

$$\eta_{cr} = \frac{\psi}{M} = \frac{\sum_i n_i \Psi_i}{\sum_l n_l M_l}$$

where,  $\eta_{cr}$  – Heat release capacity theoretical

$\psi$  – molar fraction of the repeat unit

$M$  – molar mass of the repeat unit

The experimental HRC in our work is calculated by dividing Heat release rate (HRR) by the rate of temperature rise as mentioned earlier. Since in cone calorimeter, the samples are exposed at a constant heat flux through out the combustion period, the rate was determined assuming the heat-flux over the entire combustion period.

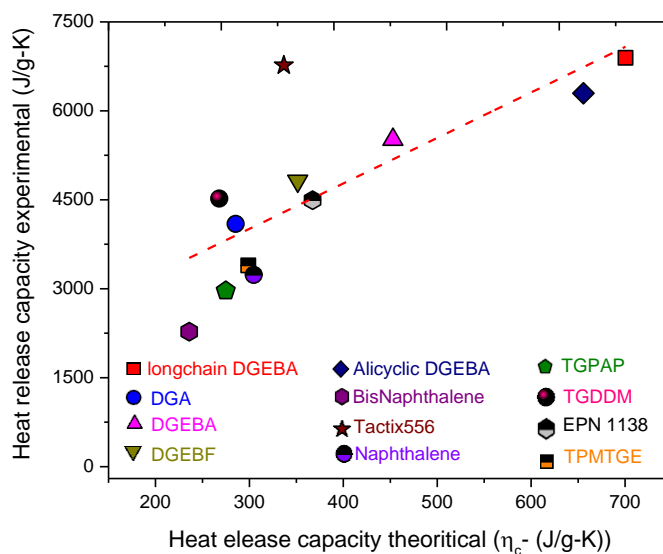


Figure 4.19 Experimental HRC determined via cone calorimeter plotted as a function of calculated HRC. Magnitude of  $R^2=0.54$  indicating a moderate decency of the experimental HRC and the theoretical HRC

As seen in Figure 4.19, the magnitude of  $R^2(=0.54)$  indicates a moderate dependency between the experimentally determined HRC via cone calorimeter and theoretically calculated HRC. The absence of strong dependency can be rationalized via two hypothesis:

1. Calculation of HRC of network is based on the HRC of repeat units which was experimentally determined via microscale combustion calorimeter (MCC)
2. Lyon's method did not account of the interactions which may take place within functional groups. As the temperature of sample was increased, as evidenced in the effect of curing temperature studies detailed before there could be some degree of condensation reaction happening prior to degradation to happen.

3. The networks studied in this work tend to form char which was not accounted in their work.

#### 4.5.2 Prediction of total heat release (THR):

Sonnier et al proposed an improved model to calculate the total heat release (THR) of polymers using Van Krevelen's additive group contribution method using a total of 31 groups and validated 107 polymers.<sup>211</sup>

This model essentially contained three rules: First, the contribution arising from a carbon atom depends on the covalent bonds associated with it. For instance, Carbon atom bonded with C, H, O/OH, N, F and Cl atoms possess different contribution. Secondly, contribution from aromatic groups, including pyridine and naphthalene atoms, depends on the atom to which it is associated with. Third is the placement of these aromatic groups if it is in backbone or as a pendent molecule. Essentially, once the individual group's contribution to total heat release (THR) is determined, the fire property of the polymer can be estimated through the following equation.

$$THR = \sum_i w_i \times THR_i$$

where,  $w_i$  – weight fraction of the group  $i$

$THR_i$  – THR contribution of the group  $i$

In this method, the THR of a the group is determined via experimentally exposing thermoplastic polymers in pyrolysis combustion flow calorimeter (PCFC) under standard conditions from 25 to 750°C at 1°C/s in nitrogen atmosphere.<sup>211</sup>In their work, thermoset polymers were studied in combination with flame retardant agents such as phosphorous

compounds to look in the effect of phosphate, causing a lack of information on the true thermoset effect.

Figure 4.20 illustrates the correlation between the measured THR via cone calorimeter and predicted THR via group contribution method. The values along with the error between the experimental and predicted THR is listed in Table 4.7. As seen the measured THR for all the samples are higher than the calculated values. These might deviate from the predicted values due to the following reasons.

1. The estimated value of THR which is derived from the THR contributions of several individual groups in the polymer is estimated via PCFC technique. As mentioned in chapter 3, the obsolete values of flame property of a material might vary depending the measurement technique used. It is to be noted that, in this study we were able to compare the experimental results while changing the chemical structure since all the networks were exposed to single technique under similar conditions.
2. The model systems used to determine the THR contributions of groups didn't consider the char formation capabilities. All the polymers were forced to complete combustion in excess of oxygen at 900°C to decompose the formed char. Also, the data accuracy for char inducing polymers is low due to the inadequate number of evaluated polymers in their study.<sup>211</sup>

Table 4.7 Experimentally determined and theoretically calculated fire properties of networks in this study

Network Identity	Heat Release capacity $\eta c$ (J/g-K)		Total heat release (THR)	
	Experimental	Theoretical	Experimental	Theoretical
Cycloaliphatic DGEBA	656	6297	19.40	10.9
DGA	285	4094	26.0	16.0
TPMTGE	299	3392	24.8	17.8
Naphthalene	305	3234	17.3	12.1
TGPAP	275	2966	29.4	25.8
Bisnaphthalene	236	2276	27.4	21.2
TGDDM	268	4521	15.5	11.2
DGEBF	351	4817	19.2	10.5
EPN 1138	367	4494	21.4	10.9
DGEBA	453	5517	17.2	10.5
Tactix 556	337	6769	15.1	11.8
Longchain DGEBA	701	6895	21.5	12.1

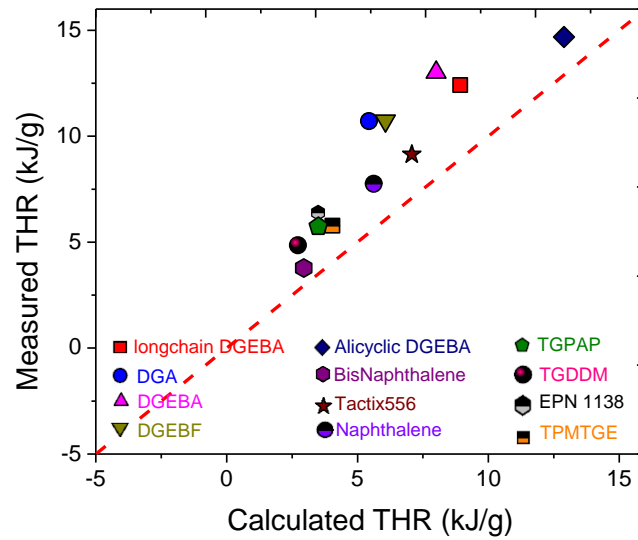


Figure 4.20 Plot of measured THR (Cone calorimeter) as a function of calculated THR via group contribution method. Shown in red is the imaginary line if the measured THR and calculated THR is in agreement. Magnitude of  $R^2 = 0.83$  indicates good agreement.

## 4.6 Isomeric effect.

The effect of structural isomers on fire properties was studied using structurally similar isomeric amine compounds. Epoxy resins used in this session include structurally similar DGEBA and DGEBA along with TGDDM to its wide usage in composites. The chemical structure is shown in Figure 4.21 and the network identification is indicated in Table 4.8.

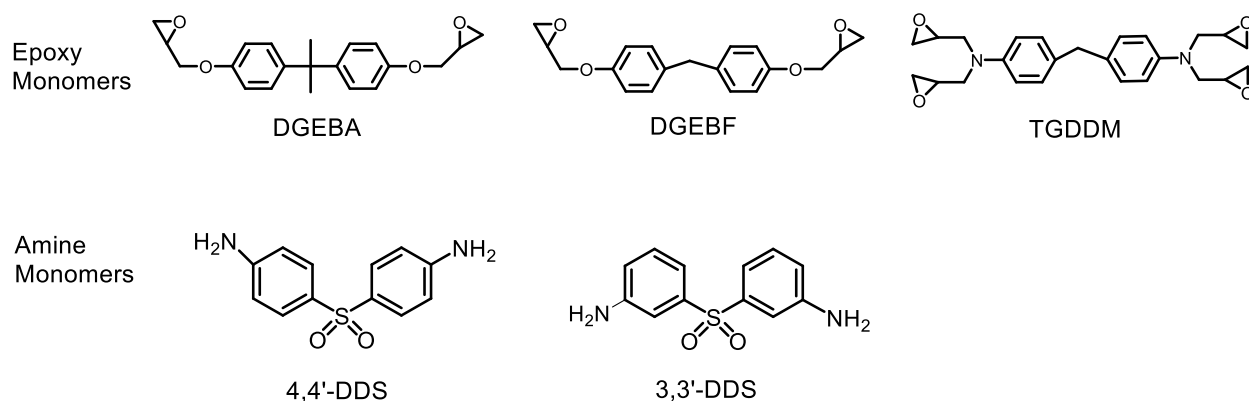


Figure 4.21 Chemical structures of epoxy and amine monomers used in analyzing the isomeric effect on flame retardant properties.

Table 4.8 Naming scheme used in this work to represent the networks formed using isomers

Epoxy		Amine		Network name
Monomer	functionality	Monomer	functionality	
DGEBA	2	4,4'-DDS	2	44DGEBA
DGEBF	2	4,4'-DDS	2	44DGEBF
TGDDM	4	4,4'-DDS	2	44TGDDM
DGEBA	2	3,3'-DDS	2	33DGEBA
DGEBF	2	3,3'-DDS	2	33DGEBF
TGDDM	4	3,3'-DDS	2	33TGDDM

To rationalize the data, the results are shown in groups: the first group consists of 4,4'-DDS as curing agent while the second group is cured with 3,3'-DDS. In each group, three epoxy monomers, DGEBA, DGEBF and TGDDM are used. The naming scheme used to compare the effect of isomers is shown in Table 4.9. The networks are named with numbers in the prefix indicating the type of amine groups followed by the type of epoxy resin used in the suffix. For the ease of understanding and comparison, the indicated names will be used in the remainder of this session.

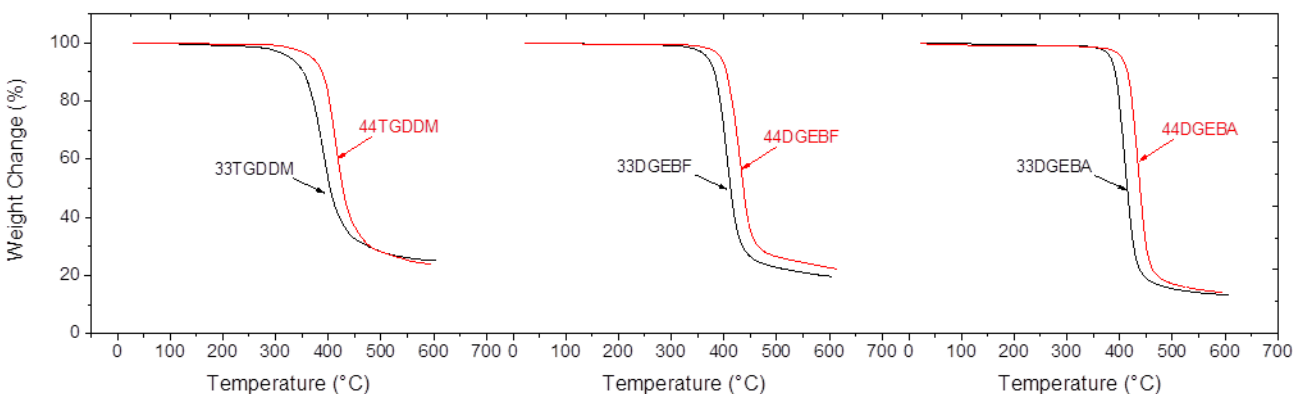


Figure 4.22 Chemical structures of epoxy and amine monomers used in analyzing the isomeric effect on flame retardant properties.

The thermal gravimetric results showed in Figure 4.22 indicated the networks containing 3,3'-DDS degraded faster as compared to similar networks cured with 4,4'-DDS. The onset temperature ( $T_{\text{onset}}$ ), temperature at 10% and 50% degradation ( $T_{10\%}$  &  $T_{50\%}$  respectively), % char yield and temperature of maximum degradation is listed in Table 4.6.



Table 4.9 TGA results listed for isomer networks

Material	Char				
	T <sub>onset</sub> (°C)	T <sub>10%</sub> (°C)	T <sub>50%</sub> (°C)	Yield(wt%)	DT <sub>max</sub> (°C)
44DGEBAs	413.22	414.75	438.67	14.15	436.16
44DGEBF	401.19	404.89	436.82	22.27	433.32
44TGDDM	386.74	388.22	427.49	23.89	412.31
33DGEBAs	387.85	390.15	412.74	13.29	408.57
33DGEBF	382.75	381.91	412.50	19.65	407.42
33TGDDM	351.82	352.25	403.67	25.09	389.25

T<sub>onset</sub> – Onset temperature; T<sub>10%</sub> - Temperature at 10% degradation; T<sub>50%</sub> - Temperature at 50% degradation; DT<sub>max</sub> – Maxima of mass loss rate

As seen in Table 4.9, T<sub>onset</sub> of 4,4'-DDS containing networks (for all three epoxy monomers) is higher than the isomeric 3,3'-DDS amine curing agent. It has been reported in literature that the difference in configurational entropy between 3,3'-DDS and 4,4'-DDS causing the difference in physical properties including the glass transition temperature, density and free-volume which essentially dictates other thermal and mechanical properties.<sup>213</sup> This is in agreement with the results obtained in our study which will be explained in the respective sessions.

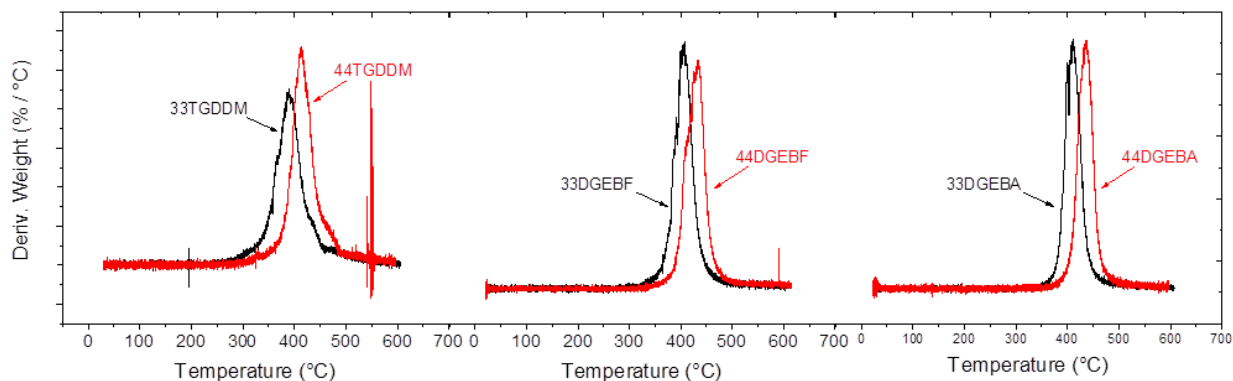


Figure 4.23 Derivative weight loss plotted as a function of temperature

Figure 4.22 indicates the weight loss mechanism for all the networks happens through single degradation step. It is clear that the curve for both 4,4'-DDS and 3,3'-DDS look identical except that the maxima of mass loss rate happens at low temperature for 3,3'-DDS containing systems which is consistent for all three epoxy monomers. This can be explained through the absence of “ring-flip” events along the axis of symmetry, as a way of energy dissipation, associated with the networks containing 3,3'-DDS curing systems. The orthogonal substitution in 4,4'-DDS can undergo ring flip along the 1,4 phenyl position (as shown in Figure 4.24) along the axis of symmetry. This acts as a method of energy dissipation., i.e., when 4,4'-DDS networks are subjected to an external energy such as thermal energy, certain amount of energy is dissipated which is associated with the ring-flipping, causing more energy requirements to break the bonds. Unlikely, the meta substitution in 3,3'-DDS doesn't possess an axis of symmetry. Thus when one of the bonds in 3,3'-DDS flips(Figure 4.24b), torsional strain is induced in the network which is compensated through the cooperative motions of the polymer backbone., This

makes it impossible to undergo ring-flip, which was a mechanism of energy dissipation in 4,4'-DDS. Due to the absence of energy dissipation mechanism the bonds degrade at much lower temperature as compared to 4,4'-DDS.

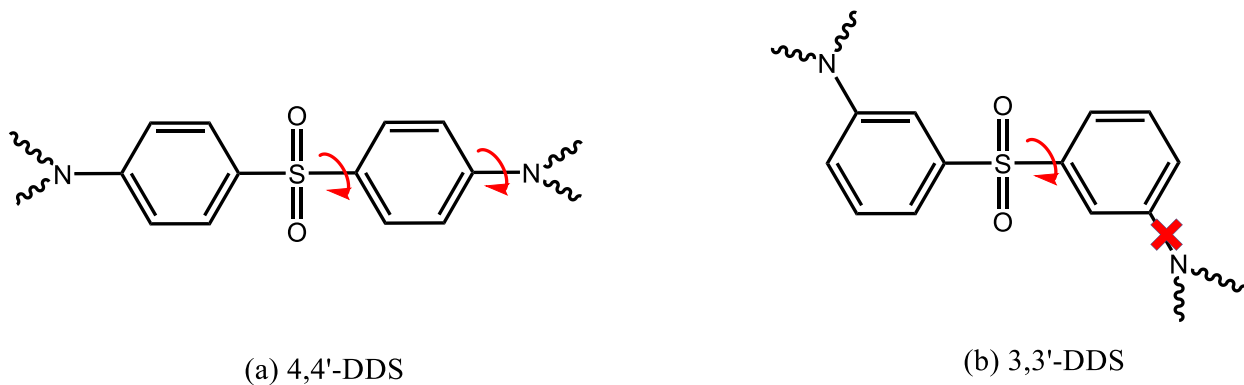


Figure 4.24 (a) para substituted 4,4'-DDS monomer showing the possible ring-flip mechanism along the axis of symmetry and (b) meta substituted 3,3'-DDS monomers in the network which can't undergo ring flip due to meta substituted positions

As seen in DSC thermograms in Figure 4.25, the networks cured with 3,3'-DDS possess lower  $T_g$  as compared to 4,4'-DDS network counterparts. The results of tan delta peak obtained from dynamic mechanical analysis (DMA) is also in agreement. The glass transition from both technique, DSC and DMA along with the free-volume is listed in Table 4.10 below.

The reason for the networks consisting 3,3'-DDS to have lower  $T_g$  as compared to 4,4'-DDS can be explained through the difference in configurational entropy associated with the difference in meta and para substitution of the amine groups in the monomers. 3,3'-DDS monomer possesses more configurations above the glass transition, due to meta substitutions, as compared to para substituted 4,4'-DDS. Due to higher configurations in rubbery state, larger amount of energy (cooling) is required to freeze or

eliminate the configurational entropy leading to lower glass transition temperatures for meta substituted 3,3'-DDS.<sup>214</sup>

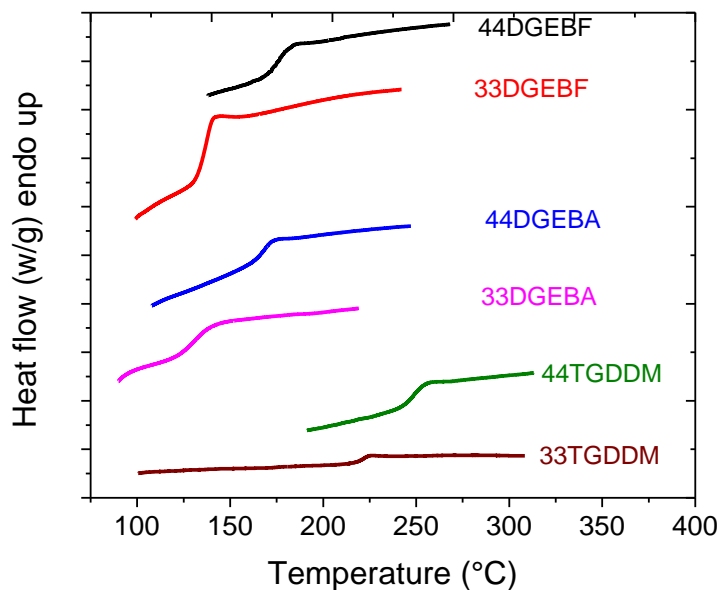


Figure 4.25 DSC thermograms of networks cured with isomers 3,3'-DDS & 4,4'-DDS

As seen in the table 4.10, there is a significant difference in glass transition temperature values obtained via two techniques, DSC and DMA for the same network. The reasons for the difference in  $T_g$  are beyond the scope of this work, however, this difference is in agreement with the reports available in literature due to the difference in method of determination.<sup>215,216</sup>

However, irrespective of the technique used, 4,4'-DDS based systems possess higher  $T_g$  as compared to 3,3'-DDS for the reasons mentioned before. Densities of these networks were also measured using Archimedes principle as explained in the experimental session. The densities of networks crosslinked with 3,3'-DDS is higher indicating the closely packed chains arising from higher configurational entropy

associated. The chains with more conformations can pack better which increases the density of the networks.<sup>214</sup>

Table 4.10 Physical characteristics of networks crosslinked with isomers 3,3'-DDS and 4,4'-DDS

Network	T <sub>g</sub> (°C)		Density (g/cc)	Free-Volume (Å)
	DSC	DMA		
33DGEBAs	130	174	1.273	77
44DGEBAs	166	213	1.248	82
33DGEBFs	136	140	1.293	67
44DGEBFs	177	150	1.268	76
33TGDDMs	216	233	1.320	52
44TGDDMs	244	255	1.279	59

The explanation for 3,3'-DDS possessing higher density (chain packing) also explains the decreased free-volume in these types of network. The free-volume was analyzed using positron annihilation lifetime spectroscopy (PALS) and indicated in Table 4.10. Networks cured with 3,3'-DDS possessed lower amount of free-volume arising from the higher conformational entropy leading to better chain packing.

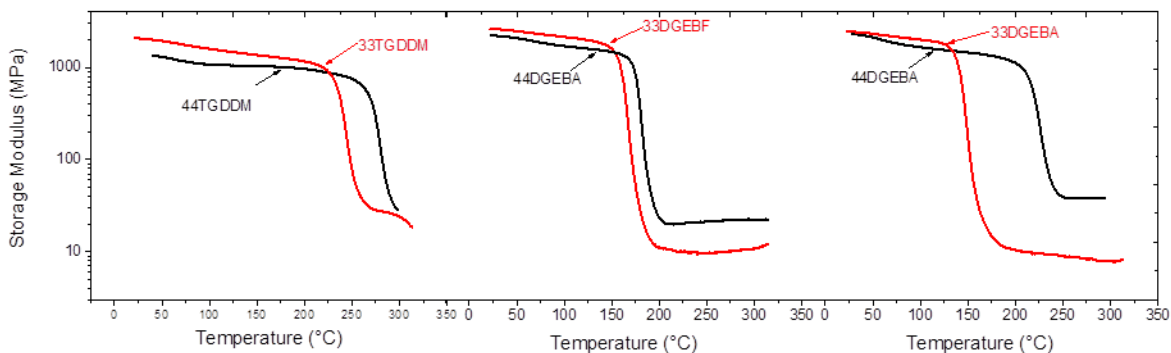


Figure 4.26 DMA curves showing storage modulus plotted as a function of temperature

The storage modulus for (a) TGDDM, (b) DGEBF and (c) DGEBA plotted vs temperature is shown in Figure 4.26. The curve indicates that the networks crosslinked with 3,3'-DDS has higher storage modulus before the glass transition temperature. Beyond the glass transition temperature, the rubbery plateau of these networks (3,3'-DDS containing networks) are lower as compared to networks crosslinked with 4,4'-DDS. This can be explained with the context of chain packing associated with the molecular mobility of meta substituted 3,3'-DDS. Due to the more conformational entropy associated with the meta substituted 3,3'-DDS, the molecular chains pack creating more toughness to the networks thus increasing the storage modulus. For the same reasons, due to higher conformations associated beyond glass transition temperature, the rubbery modulus of 3,3'-DDS networks is higher.

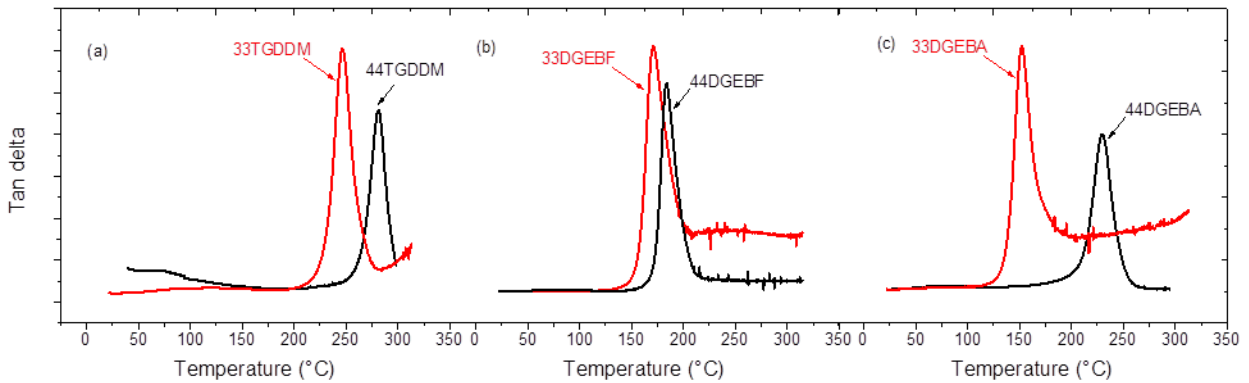


Figure 4.27 DMA curves showing the dynamic loss tangent plotted as a function of temperature

Figure 4.27 shows the dynamic loss tangent ( $\tan \delta$ ) of (a) TGDDM, (b) DGEBF and (c) DGEBA based networks cured with 3,3'-DDS and 4,4'-DDS networks. The molecular motions in the networks are shown by the distinct peak maxima ( $\tan \delta$ ), which

is higher for networks crosslinked with 4,4'-DDS monomers. This is in agreement with the results obtained through DSC (Figure 24).

Figure 4.28 displays the rate of heat of release of TGDDM, DGEBA and DGEBF based networks cured with 4,4'-DDS exposed to a cone calorimeter at a heat flux of 50Kw/m<sup>2</sup>. It is very evident that the networks crosslinked with 3,3'-DDS had slower time to ignition, lower peak heat release and a delayed peak heat release. These factors are inter related which can be explained via the better chain packing of 3,3'-DDS containing networks arising from the high configurational entropy associated with the meta substitution explained earlier. Several parameters obtained from cone calorimeter for networks crosslinked with isomeric networks is listed in Table 4.10.

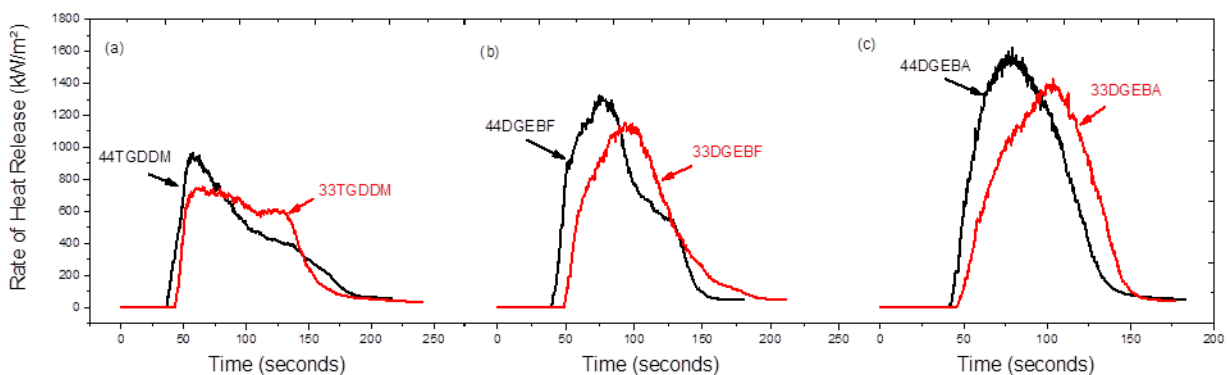


Figure 4.28 DSC thermograms of networks cured with isomers 3,3'-DDS & 4,4'-DDS

As seen in Table 4.11, the time to ignition ( $t_{ig}$ ) is higher of all three types of epoxy containing networks crosslinked with 3,3'-DDS which is due to intact networks caused by the meta substitution as compared to para substituted 4,4'-DDS containing systems. Although the difference is minuscule, the difference is consistent with all three type of epoxy systems. It might be an uncertainty in experimental error which needs further

investigation. 3,3'-DDS containing networks has lower peak heat release (PHRR) and a delayed time to PHRR.

Table 4.11 Cone calorimeter results of networks crosslinked with 3,3'-DDS and 4,4'-DDS isomeric amine

Network	tig sec	PHRR kW/m <sup>2</sup>	tPHRR sec	THR MJ/m <sup>2</sup>	AMLR g/m <sup>2</sup> s	Char yield %
33DGEB A	50.5	1138.2	114.3	88.4	25.9	7.9
44DGEB A	45.0	1622.3	79.0	95.6	49.7	5.4
33DGEB F	52.5	1163.5	88.8	80.4	22.6	9.6
44DGEB F	48.0	1409.2	79.8	85.2	43.5	9.7
33TGDDM	45.0	1033.3	83.0	72.4	11.4	15.6
44TGDDM	40.0	1008.5	63.5	78.5	37.4	17.9

tig – time to ignition; PHRR – peak heat release rate; tPHRR – time to PHRR; THR – total heat release; AMLR- average mass loss rate;

Surprisingly, the 3,3'-DDS cured systems yielded slightly higher char which is in contradictory with the results obtained through TGA (4,4'-DDS has higher char yield in TGA). The atmosphere of combustion process between these two experiments is different (nitrogen in TGA and atmosphere in cone calorimeter) which might influence the char forming tendency. But this needs further investigation. The other important observation is the average mass loss rate (AMLR) which is approximately 50% slower for 3,3'-DDS containing networks. This can be rationalized due to its char forming capability and the intact molecular chains which reduces the mass loss rate. The total heat released is different even though both the networks contains similar chemical groups mainly because the 3,3'-DDS networks tend to form higher char as compared to 4,4'-DDS containing systems.



In summary of isomeric studies, networks crosslinked with isomers possess different physical characteristics despite of having identical chemical moieties. This has been explained through the placement of amine groups in the monomer, either as meta substitution or para substitution for 3,3'-DDS and 4,4'-DDS respectively, affecting the network architecture. 3,3'-DDS has lower T<sub>g</sub>, lower free-volume, higher density and higher modulus compared to 4,4'-DDS containing systems. The fire property of two similar networks were different due to the difference in network architectures.

#### **4.7 Conclusion**

In summary, the intrinsic relationships between polymer structure, composition and fire behavior has been explored using epoxy-amine as model networks. The effect of curing schedule on activation energy and flame retardancy was modelled through TGDDM-4,4'-DDS based networks. The activation energy was calculated using Flynn and wall method using TGA technique. Thermal stability against ignition, heat release rate, total heat release rate and char yield were identified to be the most important parameters determining polymer flammability. Glass transition temperature, network composition of the networks were related to the polymer fire characteristics. For the first time, group contribution method was used to predict the flammability of polymers. This work demonstrated and validated the use of group contribution method in predicting the heat release and heat capacity of crosslinked networks.

Through this work, we determined the difference in activation energy and fire-resistant properties of similar networks cured at different temperatures. Higher the curing temperature, the network lead to higher activation energy and better fire resistant polymers. Our findings also indicate the presence of naphthalene, aromatic and hetero

atoms such as N, O are the basic structural units for fire retardant polymers. Average heat release rate showed no dependence on glass transition temperature of the networks. The heat release rate was dependent on the amount of presence of char forming chemical moieties within the network and the char yield increased with the increasing aromatic content. Thermal stability, free-volume, glass transition and fire properties of isomers, 3,3'-DDS and 4,4'-DDS were compared by curing with DGEBA, DEBF and TGDDM epoxy monomers. The results revealed that the para substituted 4,4'-DDS exhibits ring-flip mechanism along the axis of symmetry with less configurational entropy leading to higher glass transition temperature compared to 3,3'-DDS systems. Whereas, the meta substituted 3,3'-DDS possessed more configurational entropy which decreased the free volume, and most importantly improved the fire retardant properties as compared to 4,4'-DDS containing systems. This demonstrated the influence of network architecture on flame retardant properties of networks with similar chemical compositions.

#### **4.8 Acknowledgements**

The author would like to thank Mr. Ryohei Watari, (Toray composite materials, Japan) for his collaborative work in designing experiments. The author would like to also acknowledge Troy composite materials for generously providing needed samples.

CHAPTER V – DEVELOPMENT OF NOVEL GRAPHENE OXIDE GRAFTED  
SILOXANE AND PHOSPHORUS CONTAINING ADDITIVES AS FLAME  
RETARDANTS FOR EPOXY-AMINE NETWORKS.

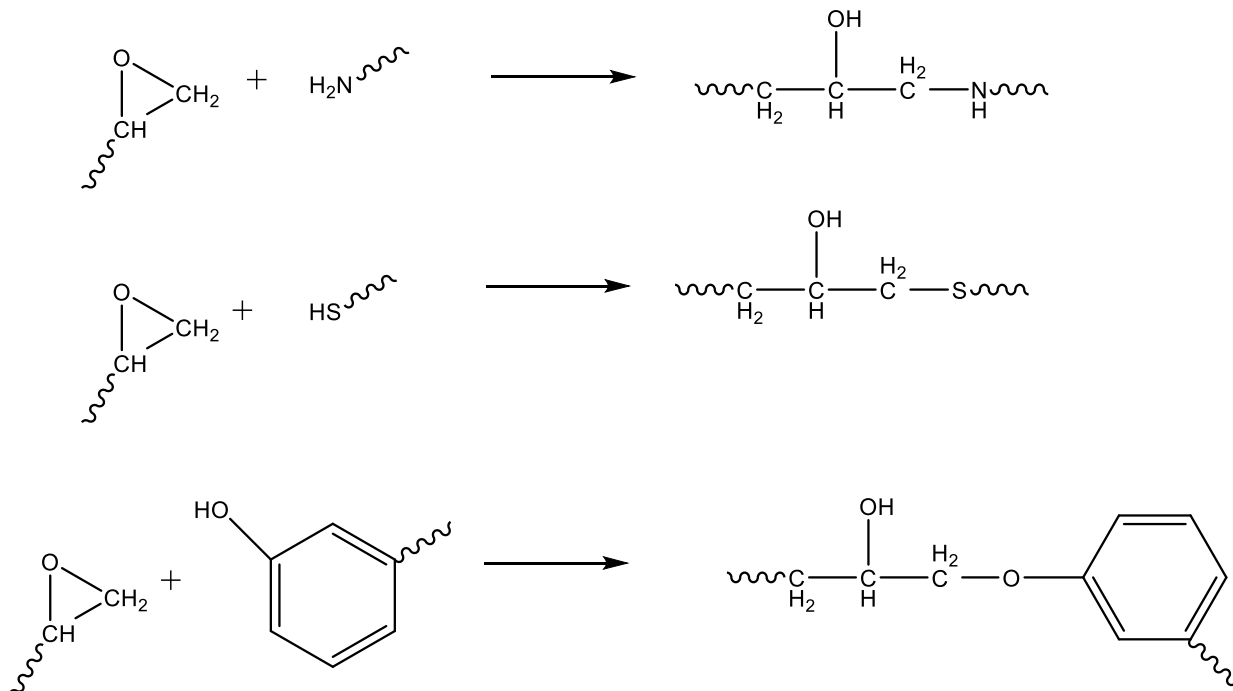
**Abstract**

Flame retardant (FR) properties of epoxy amine (EP) composites prepared by addition FR additive (modified graphene oxide (GO) with traditional FR materials) has been evaluated using cone calorimeter. A novel phosphorus/silicon (DOPO-V) and polysiloxane (PMDA) have been synthesized and covalently grafted onto the surface of graphene oxide (GO). The graphene-grafted phosphorus/silicon-containing flame retardant (GO-DOPO-V) and polysiloxane containing flame retardant (GO-PMDA) was obtained via one-step reduction of graphene oxide (GO). The FTIR, XPS, AFM and TGA measurements were used to confirm the structure and morphology of these GO grafted FR additives. DMA test indicated that the grafting of DOPO-V and PMDA improved the dispersion and solubility of GO sheets in the epoxy resin (EP) matrix. Furthermore, TGA and SEM measurement showed that GO-DOPO-V and GO-PMDA significantly enhanced the thermal stability and residual char strength of EP. Composites were prepared and analyzed by adding unmodified GO, DOPO-V and PMDA to the EP matrix in addition to the GO grafted FR additives, GO-DOPO-V and GO-PMDA. The effect of addition of unmodified GO, DOPO-V and PMDA were examined through cone calorimeter and compared with the GO grafted FR additives. It is very evident that grafting of inorganic moieties on GO improved the FR properties compared to unmodified counterparts. Incorporation of 2 wt% of GO-DOPO-V improved the FR properties of neat EP which had a decrease of 28.8% in peak heat release rate (PHR) and

15.6% in total heat release (THR). with the addition of 2wt% GO-PMDA we observed a decrease in PHR by 30.5 % and THR by 10.0% as compared to the neat EP. The morphology of the char obtained from the cone calorimeter was examined through scanning electron microscope. The char morphology of the composites containing GO grafted FR additives had a non-porous honey come structure, whereas the neat EP had a porous form of char morphology. From this it is evident that the grafting improved the non-porous char formation. The non-porous char improves the reduction in PHR and THR. This is attributed to the barrier effect of GO and phosphorus/silicon layer formation by DOPO-V. In case of GO-PMDA, polysilicone can create a stable silica layer on the char surface of EP, which reinforces the barrier effect of graphene. Thus a synergistic effect of GO and the grafted FR material improved the FR properties of epoxy-amine matrix.

## **5.1 Background**

Epoxy polymers are the most widely used in coatings, adhesives, composites and laminate materials, owing to its excellent properties such as high mechanical strength, outstanding chemical and heat resistance.<sup>217-220</sup> The versatile choice of available crosslinkers, as shown in scheme 5.1, makes epoxy networks to customize to a specific end application.<sup>221</sup> However, Epoxy networks, like all organic polymeric materials, are high flammable which is an unavoidable disadvantage.<sup>222</sup> In the previous chapter, we examined the effect of epoxy structure to its fire-resistant behavior. Nevertheless, satisfactory fire-resistant epoxy thermosets cannot be achieved only by tuning its chemical structure. The inclusion of flame-resistant molecules in the epoxy structure becomes essential to improve their resistance to fire.



Scheme 5.1 Epoxy curing reaction. Epoxide ring opens with any active proton donating monomers

Flame retardant(FR) materials are molecules which aid to reduce the ease of ignition or slow down the spread of the flame after ignition starts. The main aim of a fire retardant material is not to form a non-combustible material, but to reduce the risks associated with the ignition and to provide sufficient escape time by suppressing the smoke and heat released.<sup>223,224</sup>

Fire retardants can be classified in several ways: based on the mode of fire retardant action (condensed phase and gas phase mechanism) or based on the type of materials used (Halogenated and halogen-free). For the purpose of this chapter, we consider the classification based on the materials used.<sup>225</sup>

Halogenated FR are well known to inhibit fire in the gas phase. Halogenated FR degrades to form volatiles to release halogen radicals. These radicals abstract hydrogen

atoms from polymers to form hydrogen halides. These hydrogen halides act as flame inhibitor as they quench the radicals that cause chain branching propagation. Two mode of actions are known to happen: in the gas phase, as hydrogen halides dilute the combustible gas to reduce the temperature of flame. Secondly, in the condensed phase after abstracting the hydrogen which leads to unsaturated polymers what are known to be the precursors of char formation.<sup>226</sup> However, halogenated FR impose health risks and environmental hazard during combustion. The toxic smoke released is the primary cause of death while inhaled. Acid rain is formed when halogen hydride is released to the atmosphere and it can also bio-accumulated in soil and animals.<sup>72,225,227–229</sup> Owing to the overall risks associated with the use of halogenated FRs, halogen-free FR are being focused.

Several halogen-free FR can be classified broadly as follows.

- i. Inorganic and Nano: metal hydroxides, clay, boron based, layered double hydroxides, silicon-based materials
- ii. Nitrogen containing: Ammonium polyphosphate, melamine-based materials
- iii. Phosphorous containing: reactive and non-reactive FR

A comprehensive literature review on both halogen and halogen-free flame-retardant material and its mechanism is explained in chapter 6.

Phosphorous and siloxane-based compounds have gained recent interest among the halogen-free FRs due to the eco-friendly burning as compared to halogenated FRs. Based on the incorporation method, phosphorous and siloxane-based FR can be classified either by reactive FR (chemical bonding) and non-reactive FR (physical mixing).<sup>230–232</sup>

Among phosphorus-containing compounds, 9,10-dihydro-9-oxa-10-phosphaphenanthrene-10-oxide (DOPO) are one of the most promising halogen-free flame retardants, having high thermal stability, good oxidation and water resistance.<sup>233–235</sup> In recent years, a novel liquid compound (DOPO-V) containing DOPO and silicon was synthesized by allowing DOPO to react with vinyltrimethoxysilane (VTMS), and exhibited good compatibility with the epoxy matrix. However, a relatively high loading (10 wt%) was usually needed to achieve good flame-retardant effect.<sup>228,236–238</sup>

Silicon based compounds such as silicates, organ silicates and silsesquioxanes are considered as FR candidate owing to its high thermal stability and low toxicity or corrosive elements released during combustion. Siloxane materials acts in condense phase mechanism through char formation.<sup>182</sup>

Physical mixing of FR materials to the epoxy matrix has been considered due to its ease of mixing to a wide variety of polymer matrix. However, there are many disadvantages of non-reactive FRs not limited to the incompatibility, thermal stability at processing temperatures, leaching out of the matrix and high moisture uptake abilities which can lead to degradation of mechanical and electrical properties because of micro (or macro) phase separation. Chemical bonding within epoxy thermoset is achieved either by synthesizing FR monomers with either curative or epoxy reactive functional groups. The key issue is to uniformly disperse the FR materials in the matrix. Even though chemical bonding strategy is used as one of several strategies to achieve uniform dispersion, use of solubilizing compounds in order to improve the compatibility between the matrix and FR has also been used widely.<sup>234</sup>

Graphene, the two-dimensional  $sp^2$ -hybridized carbon is unique two-dimensional carbon-based material, has attracted a tremendous amount of attention in various application fields and has been widely studied as flame retardants.<sup>239–244</sup> Until recently, most studies of graphene-based nanocomposites focused on the incorporation of graphene, modified graphene, or graphene oxide (GO) into polymer matrixes. Because of their layered structures, graphene and GO can act as barriers reducing the heat released and insulating against the transfer of combustion gases into the inflammable polymer matrix.<sup>239,244–247</sup> However, due to the high surface area and strong Vander Waals force, the re-aggregating phenomenon is inclined to appear between graphene sheets, which limit its' use in polymer matrix.<sup>240,248</sup> The problem is usually solved by covalent functionalization. After oxidation, rich oxygen-containing groups (e.g., hydroxyl, epoxide, carboxyl and carbonyl groups, etc.) are brought to the surface of graphene sheets. Through further chemically functionalizing the GO, grafting the organic molecules on GO was widely adopted in improving the dispersion and thermal stability of GO.<sup>240,241,247–254</sup> POSS, phosphorus-containing molecule and intumescent flame retardant have been designed and covalently grafted onto the surface of graphene sheets to obtained a novel flame retardant.<sup>232,250,251,255,256</sup>

In this work, hydrophobic GO was synthesized by modifying hydrophilic GO with FR elements to improve the solubility thus improving the dispersion. This work is divided in two folds: a novel siloxane-based copolymer (PMDA) was synthesized via condensation polymerization which was grafted to GO. Secondly, a novel graphene-based phosphorus/silicon-containing flame retardant (GO-DOPO-V) was synthesized via one-step reduction of GO with DOPO-V. Both synthesized GO based nanomaterials were



added to epoxy amine thermosets to examine its FR properties along with mechanical properties. The structure and morphology were characterized and proved by the FTIR, XPS, AFM and TGA measurements. The GO modified nanocomposites along with individual components (GO, PMDA and DOPO-V) were compared for its fire retardant properties examining through cone calorimeter.

The novel flame retardant combined flame-retardant elements phosphorus and silicone together, with which the EP incorporated not only remarkably enhanced the amount of residual char but also obtained high flame retardancy at low loading of GO-DOPO-V. Graphene oxide aided in enhancement of uniform char formation with less porosity and hence it is necessary to functionalize the graphene with FR to improve the dispersion and enhance flame retardant efficiency.

## **5.2 Experimental**

### **5.2.1 Materials**

Graphite powders (spectrum pure), concentrated sulphuric acid (98%), phosphoric acid (85%), potassium permanganate, hydrogen peroxide (30%), tetramethylammonium hydroxide (TMAOH), methyltrimethoxysilane (MTMS), (3-aminopropyl)trimethoxysilane (APT), N,N'-dicyclohexylcarbodiimide (DCC), 2,2'-azobisisobutyronitrile (AIBN), and tetrahydrofuran (THF) were all purchased from Alfa Aesar Chemical Reagent Co. Ltd. Phenyltrimethoxysilane (PTMS) and dimethyldimethoxysilane (DMDS) were reagent grade and purchased from Gelest Chemical Reagent Co. Ltd. 9,10-dihydro-9-oxa-10-phosphaphenanthrene-10-oxide (DOPO) was purchased from TCI Development Co., Ltd. Vinyltrimethoxysilane (VTMS) and benzene were reagent grade and purchased from Sigma-Aldrich. Ethyl alcohol was

supplied by Decon. Chloroform ( $\text{CHCl}_3$ ) and hydrochloric acid was supplied by Fisher Scientific Chemical Co. EPON 826 with an epoxy equivalent weight of 178-186 grams was supplied by Hexion. The hardener, Jeffamine D230, with an amine equivalent weight of 60 grams, was supplied by Huntsman Corporation. All raw materials were used as received. The chemical structures of various monomers used in this study are shown in Figure 5.1.

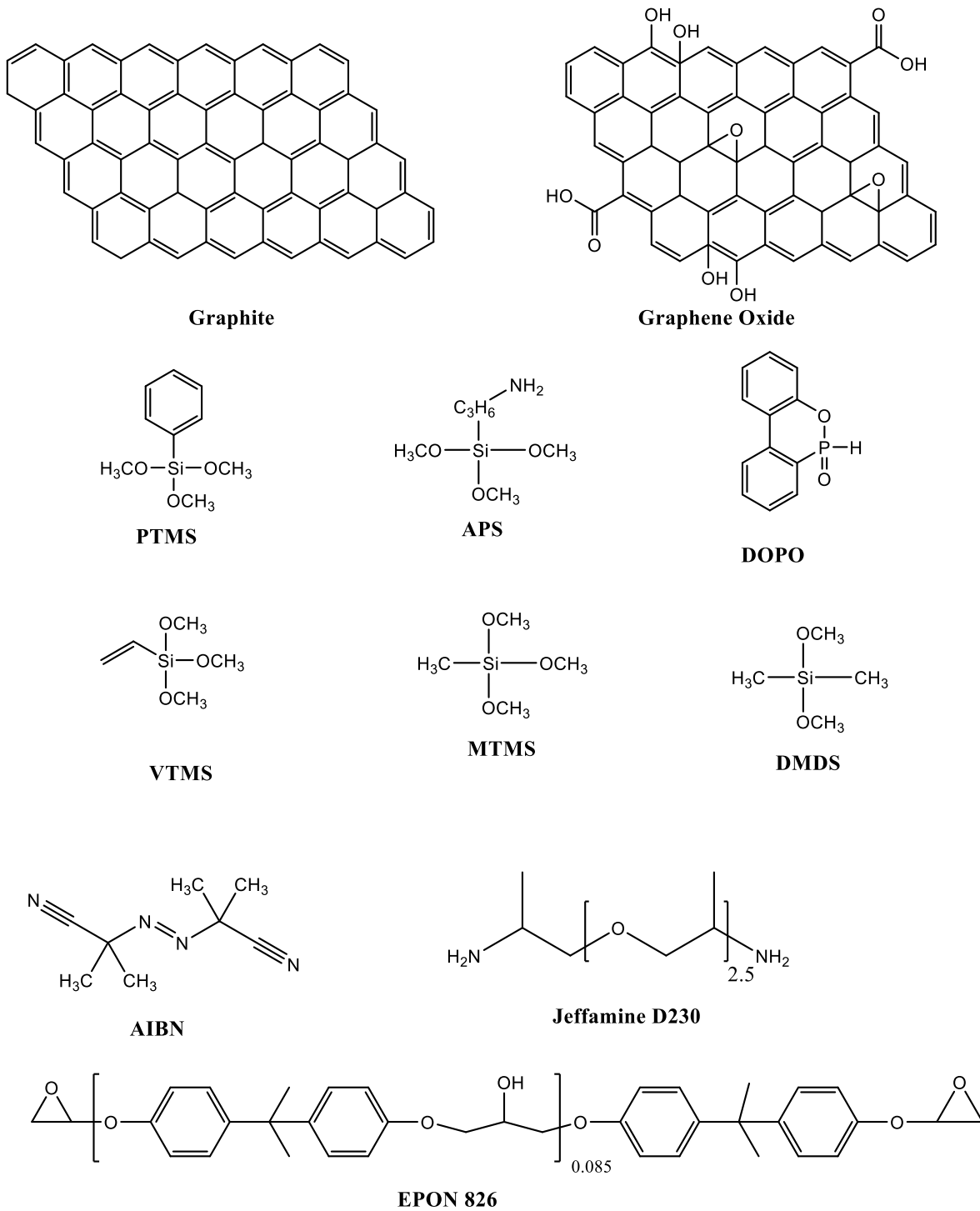
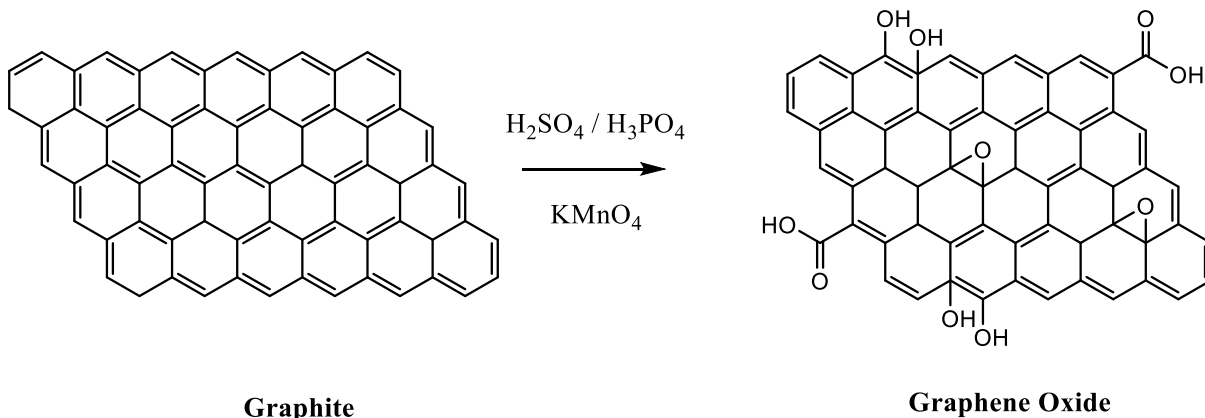


Figure 5.1 Chemical structures of monomers used in this work

### 5.2.2 Synthesis of graphene oxide

The graphene oxide was synthesized from graphite via Hummer's method as detailed below. One equivalent of graphite (3.0 gm) was mixed with 6 equivalents of potassium permanganate (18.0 gm) at room temperature. Concentrated sulfuric acid (360 mL) and phosphoric acid (40 mL) was mixed at a ratio of 9:1 separately and added dropwise to the above mixture under stirring. The temperature of the reaction kettle was maintained by keeping it in a water bath since addition of concentrated acid produced exotherm. The reaction mixture was then heated to 50°C and stirred for 12 hours. The reaction was then cooled to room temperature and poured onto a cooling mixture of ice (400 mL) with 30% H<sub>2</sub>O<sub>2</sub> (3 mL). For workup, the mixture was sifted through a metal U.S. standard testing sieve (300 um) and then filtered through polyester fiber. The filtrate was centrifuged and the supernatant was decanted away. The remaining solid material was then washed twice in succession with 200 mL of water, 200 mL of 30% HCl, and 200 mL of ethanol. For each wash, the mixture was sifted through the U.S. standard testing sieve and then filtered through polyester fiber with the filtrate being centrifuged and the supernatant was decanted each time. The washed material was then vacuum-dried overnight at room temperature to remove any residual unreacted components. The reaction is shown in Scheme 5.2.

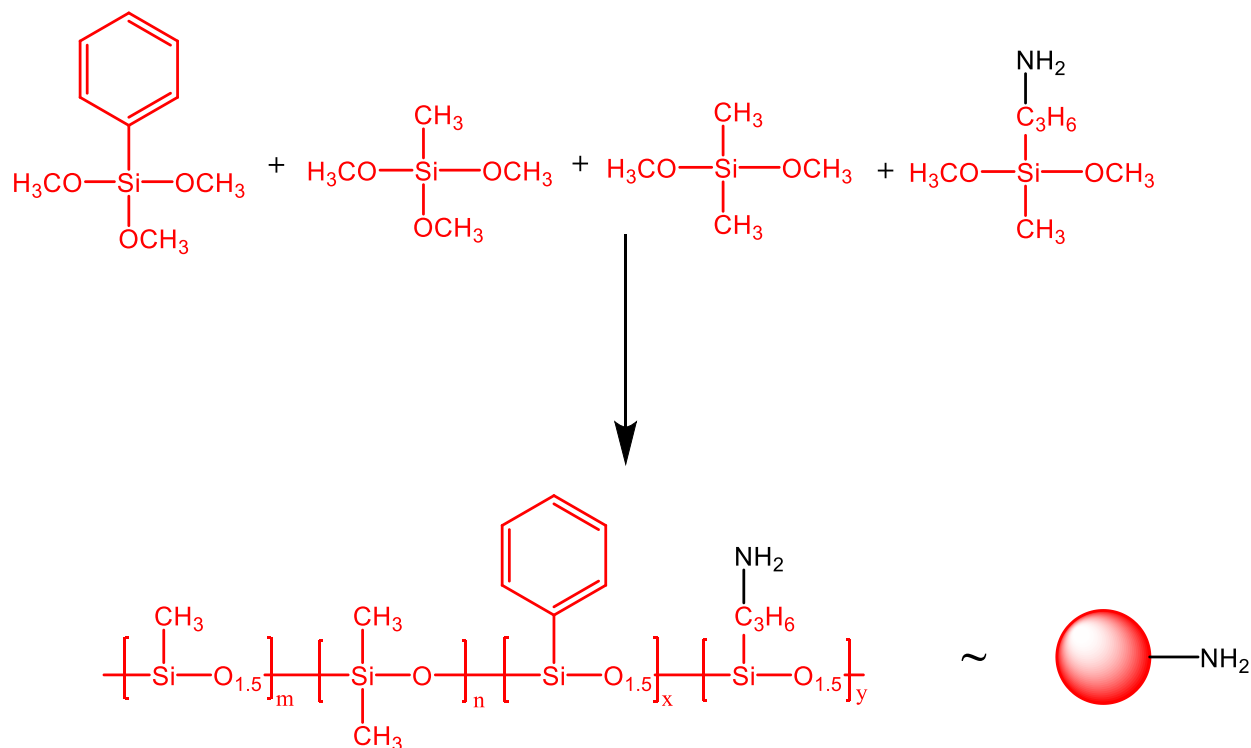


Scheme 5.2 Synthesis of graphene oxide from graphite via Hummer's method

### 5.2.3 Synthesis of Polysiloxane (PDMA):

Reactive polysiloxane monomer (PDMA) was synthesized via hydrolysis and condensation technique. Distilled water (25 ml) and ethyl alcohol (75 ml) were added to a round bottom flask equipped with a reflux condenser. 1 ml Tetramethylammonium hydroxide was added to the above mixture under stirring and maintained at a temperature of 70°C. Monomers, PTMS, MTMS, DMDS and APT were mixed at a mol ratio of 0.69 : 0.06 : 0.20 : 0.05 respectively and was added to the above solution dropwise. The total concentration of the monomers in the batch was targeted to approximately 10 wt%. The mixture was mixed for about 8 hours at 70°C and allowed to stand still overnight at room temperature. The resultant precipitated condensate was collected by decantation of the clear supernatant. This condensate was washed and dried in a vacuum filter using a mixture of distilled water-ethanol (1/3 v/v) followed by washing with ethanol. The resultant powder (PDMS) was dried in vacuum oven at 100°C for minimum 20 hours. The synthesized PDMS consisted of 60 mol% phenylsiloxane, 35 mol% methylsiloxane and 5 mol% aminosiloxane units. The extent of branches in polysiloxane was adjusted

through tuning the ratio of organic groups to silicon atoms (R/Si) and in our study, this was maintained to 1.2. The synthesis of reactive polysiloxane is shown Scheme 5.3.

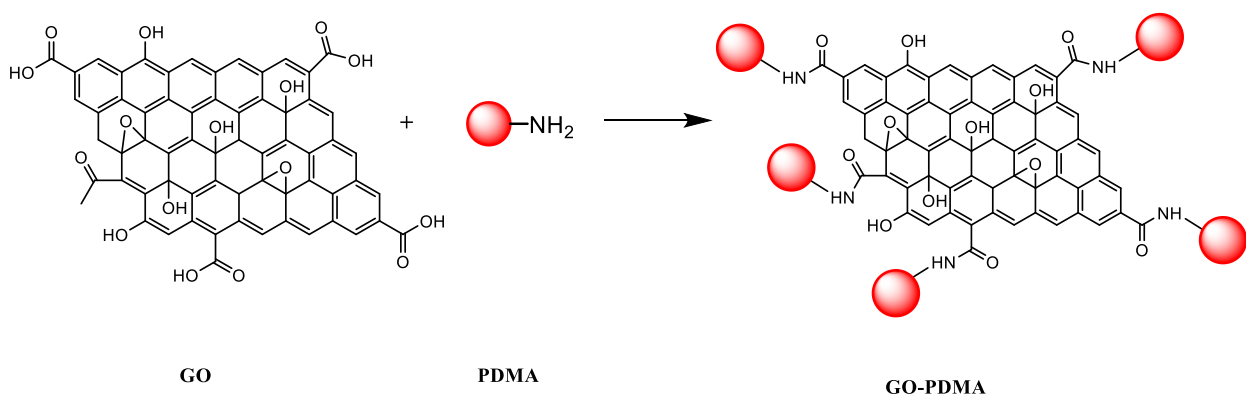


Scheme 5.3 Synthesis of reactive polysiloxane Oligomer. Color code is used to differentiate the synthesized oligomer in the rest of this work.

#### 5.2.4 Synthesis of polysiloxane (GO-PDMA) functionalized graphene oxide

Graphene oxide (GO) was synthesized from graphite using a modified Hummer's method described elsewhere.<sup>257</sup> The as-prepared GO (0.2 gm) was suspended in excess THF (200 ml) under ultra-sonification for 90 min. The synthesized PDMA (0.8 gm) was subsequently added to the above mixture in presence of N,N'-dicyclohexylcarbodiimide (0.1 gm) as catalyst and was subjected to ultra-sonification for 30 more min. The mixture was stirred and was heated to 65°C and refluxed for 20 hours under nitrogen atmosphere. The mixture was then subjected to centrifuge and thoroughly washed with anhydrous THF to remove the unreacted PMDA. The modified GO-PDMA was then dried in a

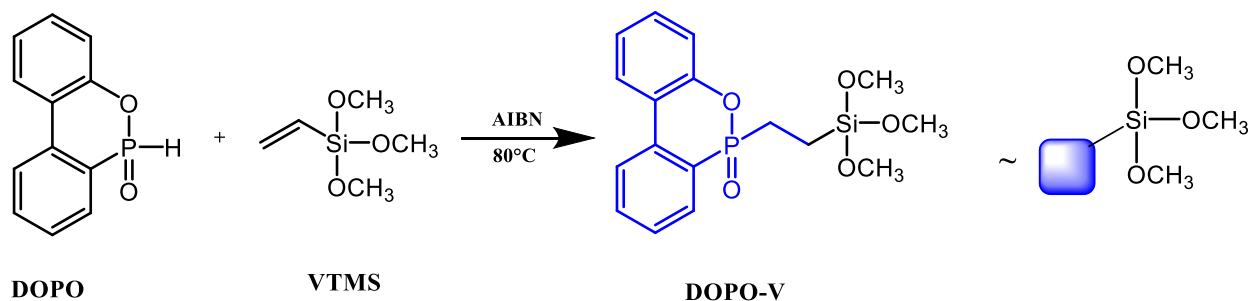
vacuum at room temperature for 12 hours to remove the residual solvent. The functionalization reaction of GO-PDMS is shown in Scheme 5.4.



Scheme 5.4 Functionalization of GO with PDMA

### 5.2.5 Synthesis of DOPO-V:

9,10-dihydro-9-oxa-10-phosphaphenanthrene-10-oxide (DOPO) was modified with Vinyltrimethoxysilane (VTMS) was achieved using the reaction explained below. The DOPO modified VTMS reaction scheme is shown in Scheme 3. 0.1 mol of DOPO (21.6 gm), 0.1 mol VTMS (14.8 gm) was added to a round bottom flask containing excess benzene (100 ml) equipped with a mechanical stirrer, flux condenser, dropping funnel and nitrogen inlet. The reaction mixture was heated to 80 °C to dissolve DOPO and VTMS completely to a homogeneous mixture. 0.1 gm of AIBN was dissolved in 50 ml of benzene and was added to the reaction vessel at a flow rate of 0.1 ml/min for about 2 hours. After the addition of AIBN, the reaction mixture was held at 80°C and stirred under nitrogen atmosphere for 24 hours. The resultant product was subjected to rotary evaporator to remove benzene and the resultant modified DOPO with VTMS was a colorless transparent liquid.<sup>231</sup>

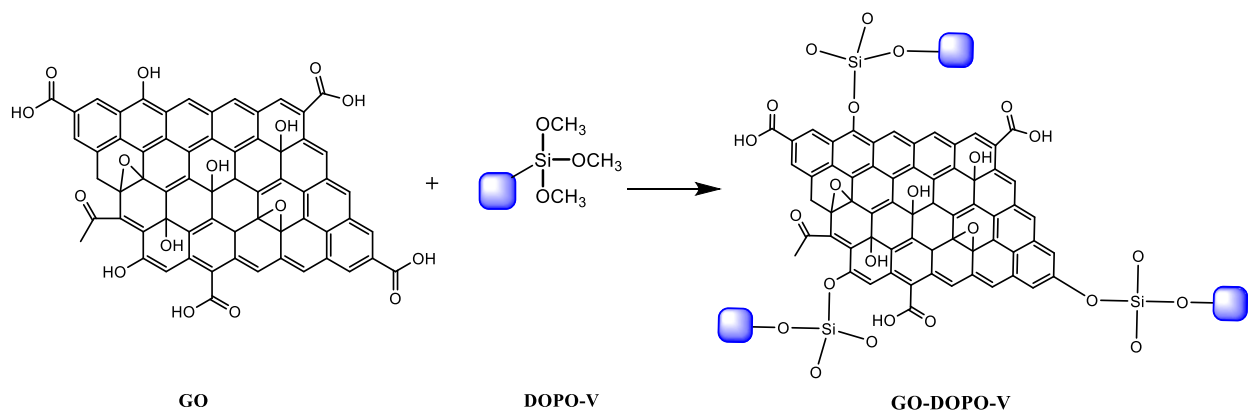


Scheme 5.5 Synthesis of DOPO-V. Color coded to differentiate the molecule from PMDA

### 5.2.6 Synthesis of DOPO-V functionalized graphene oxide

As mentioned earlier, graphene oxide was synthesized from graphite by modified Hummer's method.<sup>257</sup> The hydroxyl groups in the GO was used as active sites to modify with synthesized DOPO-V monomer as explained below. The as-prepared GO (0.2 gm) was suspended in excess THF as solvent under ultrasonication for about 90 minutes. The synthesized DOPO-V monomer (0.8 gm) was added to the GO mixture in presence of DCC (0.1 gm) as catalyst and subjected to ultrasonication for 30 min. The reaction mixture was then heated to 65 °C equipped with a reflux condenser under nitrogen atmosphere for 20 hours. The resulting mixture was subjected to centrifuge and the resultant precipitate was washed with anhydrous THF to remove unreacted DOPO-V. The resultant DOPO-V-functionalized graphene sheets GO-DOPO-V was dried in vacuum at room temperature for 12 hours to remove the residual solvent. The functionalization is illustrated in Scheme 5.6.





Scheme 5.6 Synthesis of GO-DOPO-V

### 5.2.7 Preparation of Epoxy Composite:

The 2wt % functionalized GO (GO-PDMA and GO-DOPO-V) containing epoxy-amine composites were prepared in two step process to investigate the effect on flame retardancy. In the first step, the functionalized GO (2 gm) was dispersed in acetone ( 1ml) and sonicated for 60 min to exfoliate the GO sheets. Then Epoxy matrix (EPON 826, 73.5 gm) was added to the above mixture and mechanically stirred for 30 min. Then mixture was then heated to 50 °C for 10 hours in vacuum oven to remove any acetone in the matrix. After cooling the mixture, the amine ( D230, 24.5 gm) was added and was subjected to stirring for 30 min. The mixture was degassed in vacuum oven to remove any trapped air bobbles and the samples were casted in a mold and cured at 80°C for 2 hours followed by a post cure at 135°C for 2 hours. Table 1 shows the components and the identity of the matrix which will be used to represent in the rest of the paper. For comparison, in addition to pure epoxy-amine matrix (containing no functionalized GO), matrixes with 2 wt% unmodified GO was also studied.

Table 5.1 Network Description

Identity	Components	Description
EP	Epon 826, Jeffamine D230	Pure Epoxy without additive
EP/GO	Epon 826, Jeffamine D230, Unmodified graphene oxide	Epoxy with GO
EP/GO-PDMA	Epon 826, Jeffamine D230, GO modified with synthesized siloxane oligomer	Epoxy with GO-PDMA
EP/DOPO-V	Epon 826, Jeffamine D230, DOPO as procured	Epoxy with DOPO
EP/GO-DOPO-V	Epon 826, Jeffamine D230, GO modified with synthesized DOPO modified siloxane	Epoxy with GO-DOPO-V

### 5.2.8 Characterization

The formation of oligomer (PDMA) and monomer (DOPO-V) was confirmed through Fourier transform infrared spectroscopy (FTIR) spectra of the dried samples using a Digilab Scimitar FTS-2000 IR spectrometer in reflectance mode. The synthesized samples were dried in vacuum oven and subjected to scans from wavelength ranging from 500 to 4000  $\text{cm}^{-1}$  in atmospheric air.

The chemical components were investigated using X-ray photoelectron spectroscopy (XPS) was carried out in a Thermo Scientific ESCALAB 250Xi X-ray photoelectron spectrometer equipped with a mono-chromatic Al  $K\alpha$  X-ray source (1486.6eV) located in Ningbo university of technology. The formation of chemical bonds before and after the functionalization step was also used as a technique to confirm the formation of monomer and oligomers.

Surface properties of the synthesized monomers were characterized using Atomic Force Microscopy (AFM). AFM observation was performed on the Bruker Dimension

Icon atomic force microscope in tapping-mode. The aqueous GO suspension and DMF suspension of functionalized GO (GO-PDMA and GO-DOPO-V) were spin-coated onto freshly cleaved silica surfaces.

The Thermal stability of the synthesized monomers were investigated using Thermogravimetric analysis (TGA) measurement on a TA instrument Q500 thermogravimetric analyzer. The sample (about 10 mg) was heated from 50 °C to 600 °C (or 700 °C for composites) at a 10 °C/min heating ramp rate in nitrogen atmosphere.

A Govmark cone calorimeter was used to investigate the fire properties of the networks in compliance with ASTM E 1354-90 horizontal burn test. A detailed description of Cone calorimeter is given in Chapter 1 of this thesis. The standard heat flux for this investigation was 50 kW/m<sup>2</sup> and the exhaust flow was set at 24L/sec. All cone specimens (sample size: 100 mm x 100 mm x 3 mm) were tested in a horizontal position. Typical results from cone calorimetry are reproducible to within about ± 10%; these uncertainties are based on many runs in which thousands of samples have been combusted.

The residual char obtained from cone calorimeter test was examined through scanning electron microscopy (SEM) using Quanta FEI 200. All samples were coated with a conductive layer of gold of around 5 nm using a Quorum Emitech K550X sputter coater to avoid charge build up on the specimen while imaging. Samples were charged under Argon gas and 25 mAmps for three minutes.

## **5.3 Results and discussion**

### **5.3.1 Characterization of synthesized monomers**

The synthesized monomers, (GO, PMDA, DOPO-V) and the grafted monomers, (GO-PDMA and GO-DOPO-V) were characterized before preparation of composite materials in epoxy-amine thermosets. Solubility analysis was chosen as a quick indication/ confirmation of the functionalization of graphene oxide (GO). GO is soluble in water due to the presence of carbonyl and hydroxyl groups leading to its hydrophilicity. Whereas, the modified monomers (GO-PMDA and GO-DOPO-V) introduces the hydrophobicity in the molecule through functional groups PMDA and DOPO-V respectively. When two immiscible liquids, H<sub>2</sub>O and CHCl<sub>3</sub>, were mixed, phase separation happened when the mixture was kept undisturbed. Synthesized GO, along with grafted GO-PMDA and GO-DOPO-V monomers, when added to the above mixture separately, the hydrophilic GO dissolved in H<sub>2</sub>O whereas hydrophobic GO-PMDA and GO-DOPO-V dissolved in CHCl<sub>3</sub> as shown in Figure 5.2. The mixture when agitated vigorously even after the dissolution of synthesized monomer, lead to phase separation which indicated the clear boundary of solubility of GO in water and functionalized GO monomer in CHCl<sub>3</sub> solvent.<sup>250,255</sup> The evolution of surface functionality during reaction usually leads to a change of the graphene oxide from hydrophilic into hydrophobic. Thus the monomer modification can be witnessed by the phase transfer of GO starting material from water phase into the CHCl<sub>3</sub> phase.

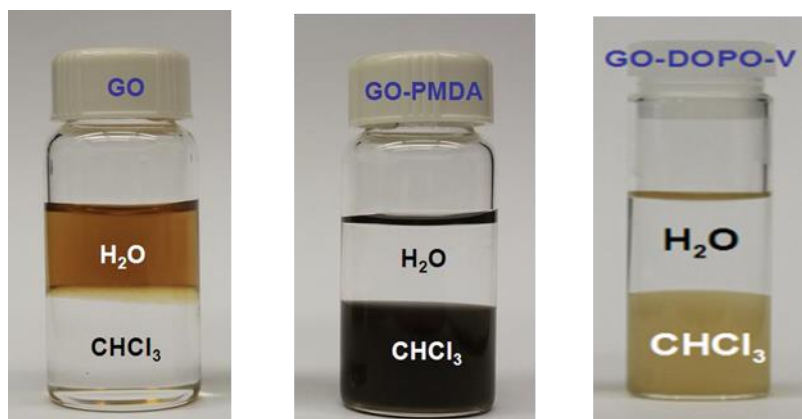


Figure 5.2 Solubility experiments indicating the solubility of hydrophilic GO in water and hydrophobic GO-PMDA and GO-DOPO-V soluble in CHCl<sub>3</sub>

The chemical structure of the synthesized monomer (GO, PMDA and DOPO-V) and grafted monomers (GO-PMDA and GO-DOPO-V) was characterized by FTIR spectroscopy. The modification of GO monomer can be confirmed through FTIR technique by looking for the signals corresponding to the stretching of new bonds. Figure 5.3 shows the FTIR spectrum for GO monomer, unmodified PMDA and DOPO-V as well as modified functional GO materials (GO-PMDA and GO-DOPO-V).

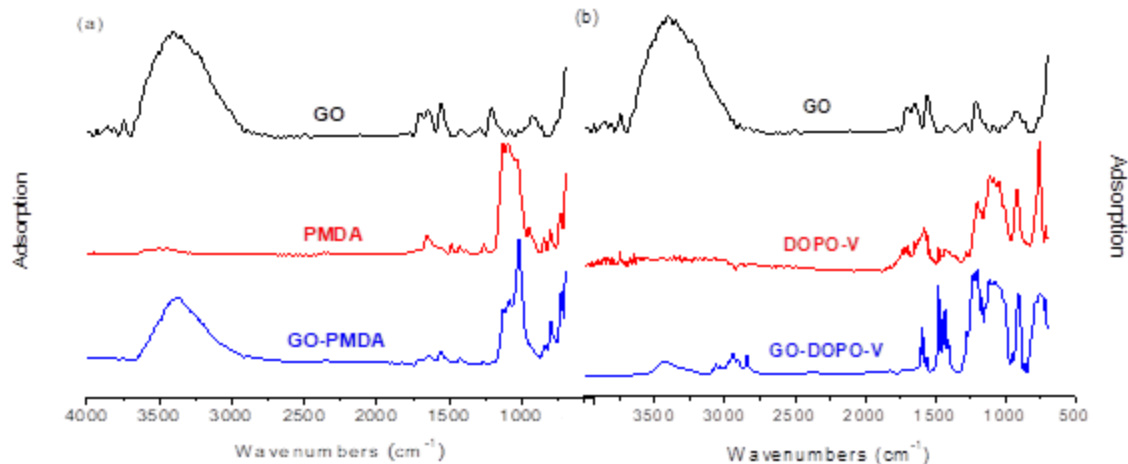


Figure 5.3 FTIR spectra showing the confirmation of monomer formation

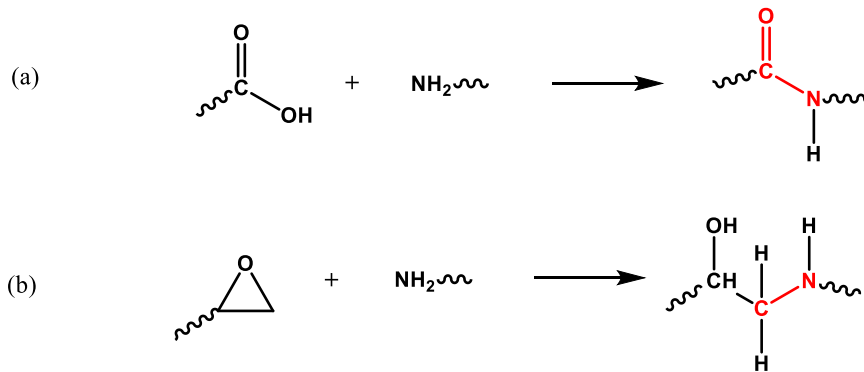
The FTIR spectra of GO shows significant contribution from -OH and C=O chemical groups, consistent with infrared spectra of GO presented elsewhere.<sup>258</sup> The strong absorption bands at about  $3406\text{ cm}^{-1}$  originated from stretching mode of -OH groups, C=O at  $1705\text{ cm}^{-1}$ , and C-O at  $1211\text{ cm}^{-1}$ , indicated the existence of oxygen-based functional groups  $\text{H}_2\text{O}$  and -COOH within GO.<sup>240,259</sup>

The intensities of the IR peaks decrease significantly after chemical attachment of PMDA and DOPO-V onto the GO. In Figure 5.3a (left), the strong peak at  $1200\text{-}1000\text{ cm}^{-1}$  corresponding the Si-O-Si stretching vibration in PMDA (indicated in red) is seen in the spectra of GO-PMDA (indicated in blue), indicating that PMDA has been successfully grafted onto GO.

The FTIR spectra of DOPO-V (Figure 5.3b-red shown on the right) showed that the characteristic peak at around  $1200\text{-}1000\text{ cm}^{-1}$  was belonged to Si-O-C and Si-O-Si structures.<sup>217,240</sup> The absorption peaks at  $902\text{ cm}^{-1}$ ,  $1274\text{ cm}^{-1}$  and  $1595\text{ cm}^{-1}$  correspond

to the stretching vibrations of P-O-Ph, Ph=O and P-Ph bonds, respectively. Those findings verify that the DOPO-V has been successfully prepared.<sup>231</sup> The FTIR spectra of GO-DOPO-V (Figure 2b-blue), contained the majority of absorption peaks appeared in both GO and DOPO-V, but the peaks intensity of -OH, C=O groups were decreased, which indicates the grafting of DOPO-V on GO.

X-ray photoelectron spectroscopy (XPS) was used to elucidate the surface composition of GO, and the functionalization of GO (GO-PMDA and GO-DOPO-V), which shed information on the chemical interaction between monomers. The survey spectra of GO, GO-PMDA and GO-DOPO-V is displayed in Figure 5.4. XPS survey spectra of GO indicates only the presence of C1s and O1s peaks. The survey spectra of GO-PMDA displayed N1s, Si2s and Si2p peaks in addition to the characteristic peaks of GO at O1s and C1s. Similarly, GO-DOPO-V survey spectra, along with O1s and C1s peaks corresponding to GO, they displayed the presence of Si2p (102 eV), P2p (133 eV), Si2s (154 eV) and P2s (191 eV) peaks. This confirms the covalent functionalization of GO with PMDA and DOPO-V. Furthermore, the ratio of O1s to C1s peaks is reduced upon modification, which also evidence the covalent bonding between PMDA and DOPO-V to GO. Since GO was synthesized through oxidation reactions, rich oxygen containing groups, such as hydroxyl, epoxide, carboxyl and carbonyl groups, are brought to the surface of graphene sheets. GO was chemically functionalized with PMDA through further grafting reaction with such oxygen rich carboxyl and epoxide group as shown in the reaction Scheme 5.7. Thus, the existence of N 1s band at 399.3 eV (C-N) and 402.6 eV (CO-N) shown in Figure 5.4b for GO-PMDA survey scans further confirms the covalent mode of modification of GO.



Scheme 5.7 Chemical functionalization of GO with PMDA via oxygen rich carboxyl and epoxide groups available on the surface of GO

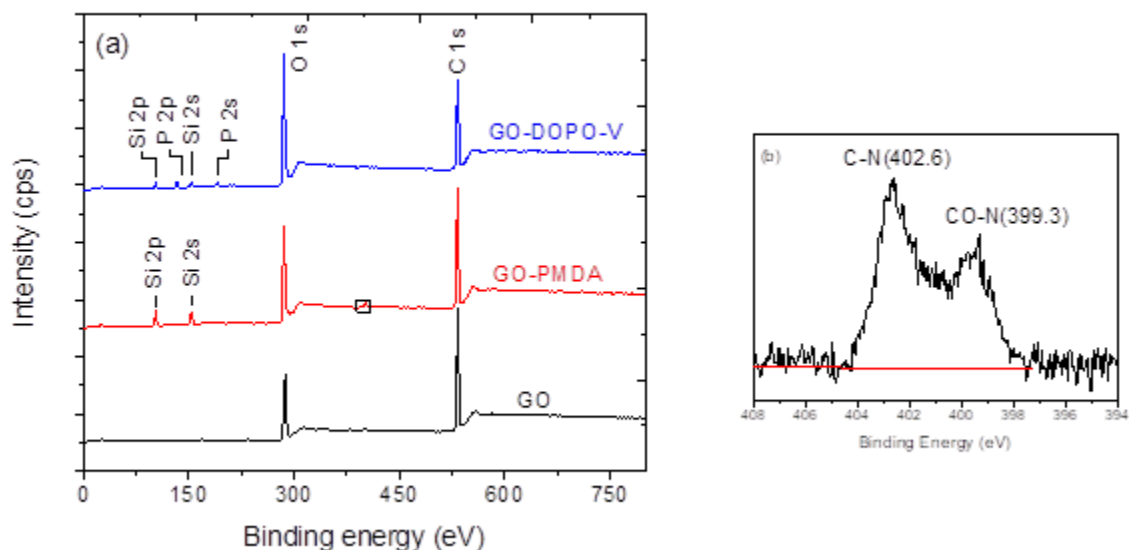


Figure 5.4 (a) XPS survey scans of GO (black), GO-PMDA (red) and GO-DOPO-V (blue) which confirms the covalent functionalization of GO. (b) high resolution XPS spectra of N 1s for GO-PMDA

The higher resolution of XPS spectra in C 1s region of (a) GO, (b) GO-PMDA and (c) GO-DOPO-V are shown in Figure 5.5. Figure 5.5b and 5.5c reproduces the high-resolution C 1s spectra for GO and GO-PMDA, respectively. The peaks for C-C (285.0



eV), C-O (287.0 eV), C=O (287.9 eV) and COO (289.0 eV) is clearly observed in C1s scan of GO (Figure 4a). As can be seen, the COO peak at 289.0 eV for GO-PMDA almost disappears upon the amide formation with the amine group of PMDA. The peak intensity of the C-O (287.0 eV) and C=O (287.9 eV) in GO-PMDA also significantly decreases (Figure 5.5b). This is because the nucleophilic substitution between GO and amine groups can cause deoxygenation and reduction of graphene oxide.<sup>250</sup> The high-resolution XPS spectra of C1s in Figure 3b and 3c shows the presence of four kinds of carbon in GO and GO-DOPO-V: C-C (285.0 eV), C-O (287.0 eV), C=O (287.9 eV) and COO (289.0 eV). In comparison of GO, the peaks of C-O, C=O and COO in the C1s scan of GO-DOPO-V are obviously decreased, which further confirmed that GO has been modified by the DOPO-V.

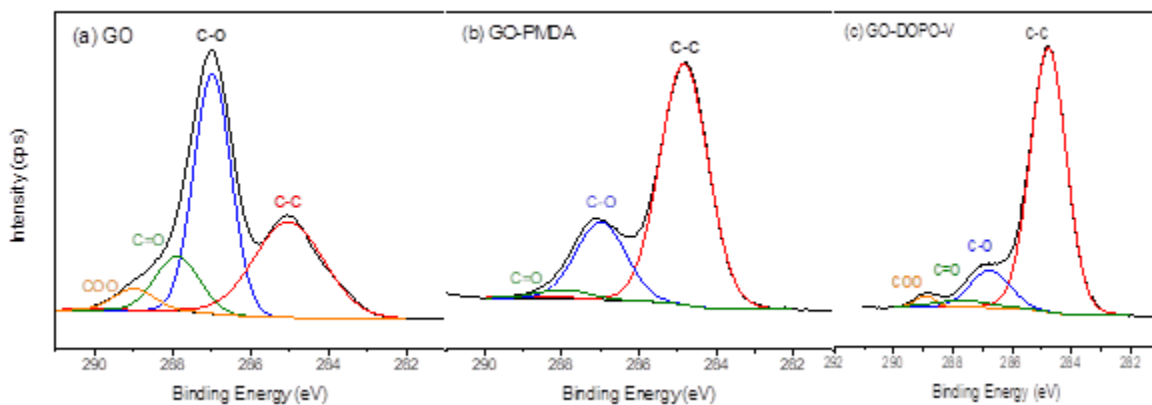


Figure 5.5 (a) XPS survey scans of GO (black), GO-PMDA (red) and GO-DOPO-V (blue) which confirms the covalent functionalization of GO. (b) high resolution XPS spectra of C1s for GO-PMDA

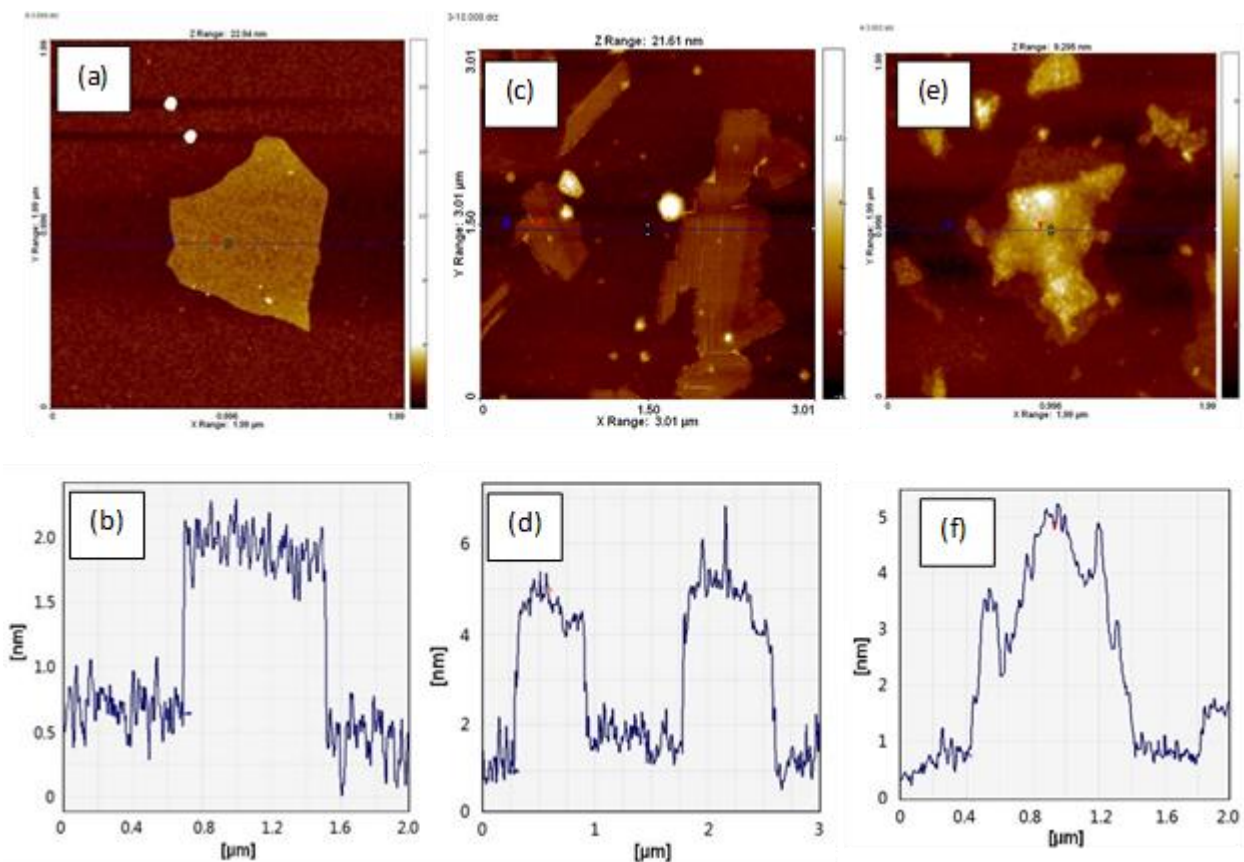


Figure 5.6 AFM images of GO, GO-PMDA and GO-DOPO-V with height profile

Atomic force microscopy (AFM) was used to investigate the morphology and thickness of the interface layer grafted on the GO sheet surface. Figure 5.6 represents the tapping mode AFM images of GO, GO-PMDA and GO-DOPO-V with the height profile. Figure 5.6a and Figure 5.6b represents the tapping mode AFM images of GO, showing the average height of  $\sim 1$  nm for a single-layer GO sheet. After grafting PMDA, the height of a single-layer GO-PMDA becomes  $\sim 4$  nm (Figure 5.6c and d), which is much higher than that of GO. The thicker sheets is possibly due to the PMDA chain grafted on GO sheet surface which indicate that the GO-PMDA is successfully obtained in our work. As

shown in the height profile in Figure 5.6e and f, the height of grafted DOPO-V onto the surface of GO sheet increases to 2~4 nm, comparing to 1 nm thickness of GO.

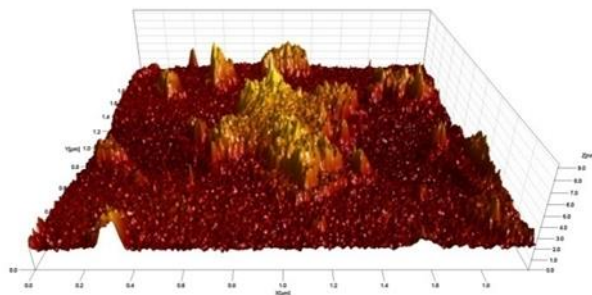


Figure 5.7 3D view of GO-DOPO-V which indicates a non-uniform surface morphology

Moreover, the 3D view of GO-DOPO-V (Figure 5.7) reveals that the surface of GO-DOPO-V is uneven, which is probably caused by the trimethoxy groups from DOPO-V molecular. The condensation reaction between DOPO-V molecules via methoxy groups can form the building blocks of polyorganosiloxanes<sup>260,261</sup> and subsequently leads to the non-uniform morphology of the surface of GO-DOPO-V sheet.

The thermal stability of synthesized monomers along with modified GO monomer was characterized using TGA. Figure 5.8 indicates the TGA plot of GO, PMDA, GO-PMDA, DOPO-V and GO-DOPO-V. GO along with synthesized monomers (PMDA and DOPO-V) and modified GO monomers (GO-PMDA and GO-DOPO-V) exhibits two step degradation process. Since GO contains hydrophilic elements on the surface, these materials tend to be hygroscopic which is removed at 100°C during the first step in TGA. The weight loss corresponded to the residual water was 7.6 wt%. The onset degradation temperature ( $T_{\text{onset}}$ ) of GO was recorded to 78.5 °C with maximum weight loss happening at 193.1°C and yielded a char of 16.5 wt% at 600 °C. At around 190°C there was a rapid

weight loss was observed which was associated with the decomposition of oxygen-containing functional groups to CO, CO<sub>2</sub>, and H<sub>2</sub>O.<sup>254</sup> The weight loss between 200 °C and 600 °C is about 8.5 wt%, associated with the removal of more thermally stable oxygen functionalities and thermal decomposition of GO.

When compared to GO, GO-PMDA and GO-DOPO-V exhibit much better thermal stability. The superior thermal stability of PMDA and DOPO-V which when grafted to the thermally less stable GO, the thermal stability of both modified monomers, GO-PMDA and GO-DOPO-V increased.

The TGA curve of GO-PMDA exhibits a much better thermal stability with both higher of  $T_{\text{onset}}$  (141.9 °C) and char yield (61.5 wt% at 600 °C) which is attributed to the presence of PMDA. The onset temperature of GO-DOPO-V and maximum weight loss rate were observed at 178.7 °C and 230.8 °C, respectively. It has been found that reduced GO is thermally stable and subject to minor mass loss in a nitrogen atmosphere, because most of the oxygen-containing groups on the surface of GO were removed in the reduction process.<sup>262</sup> More importantly, the amount of residue char at 600 °C also dramatically increased from 16.5 wt% for GO to 61.5 wt% for GO-PMDA and 54.6 wt% for GO-DOPO-V. It could be attribute to the presence of respective monomers, PMDA and DOPO-V, which has a high gas-phase activity and condensed-phase activity (through char formation).<sup>232,236</sup>

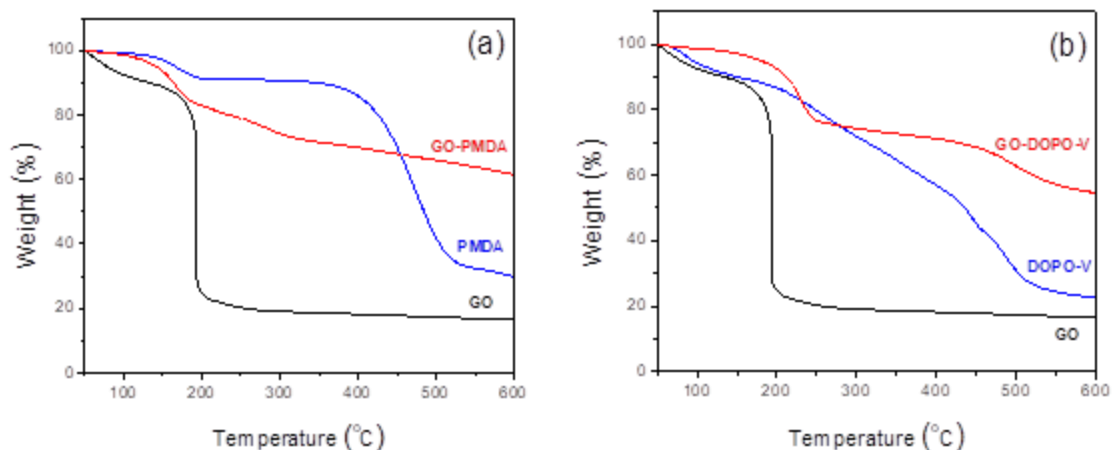


Figure 5.8 TGA curves of (a) PMDA, GO-PMDA and (b) DOPO, GO-DOPO displayed with unmodified GO for comparison

Composites in epoxy amine system were made via mixing the synthesized monomers, GO, GO-PMDA and GO-DOPO-V, and tested for its physical and fire properties. Since DOPO-V is also a popular flame retardant material, the composite was made by mixing DOPO-V in epoxy amine networks for comparison.

### 5.3.2 Analysis of composite materials

The thermal stability of neat epoxy-amine (EP), epoxy-amine-GO composite (EP/GO) and epoxy-amine-GO-PMDA (EP/GO-PMDA) under nitrogen atmosphere was measured through TGA and presented in Figure 5.9. All the composite materials and the neat EP exhibits one step degradation which is evident from the distinct single peak when weight loss rate is plotted as a function of temperature. The onset temperature ( $T_{\text{onset}}$ ) of EP/GO (322°C) is lower than EP (346°C) because of the presence of thermally unstable GO and the major weight loss in GO degradation occurred below 200°C arising from the decomposition of the oxygen-contained functional moieties as seen in thermal stability of

GO itself. The addition of GO-PMDA improves the  $T_{\text{onset}}$  as compared to GO by 15.4 °C. The  $T_{\text{max}}$  of the EP/GO and EP/GO-PMDA is similar to EP. However, peak degradation rate (PDR) of the EP/GO and EP/GO-PMDA, which indicates thermal degradation rates, were decreased compared to EP.

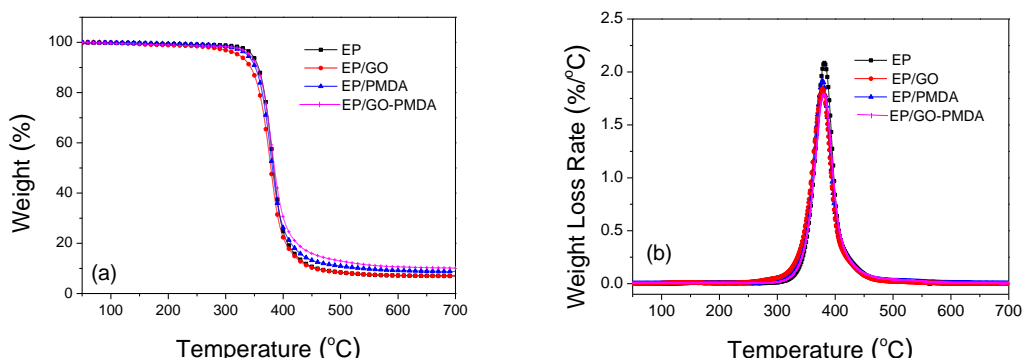


Figure 5.9 TGA curves of (a) PMDA, GO-PMDA and (b) DOPO, GO-DOPO shown along with unmodified GO

As shown in Figure 5.10, the effect of GO, DOPO-V and GO-DOPO-V on the thermal stability of EP has been investigated by TGA measurement, and corresponding data is summarized in Table 5.2. The  $T_{\text{onset}}$ ,  $T_{50\text{wt}\%}$  of EP/DOPO-V and EP/GO/DOPO-V exhibit similar values, but these values are still higher than that of EP/GO. Interestingly, the PDR and  $T_{\text{max}}$  of EP/GO-DOPO-V are both higher than those of EP/GO and EP/DOPO-V, which indicates that the synergistic effect of DOPO-V and GO. EP/GO-DOPO-V has higher thermal resistance because its high stability and high char forming capability as compared to EP/GO and EP/DOPO-V.

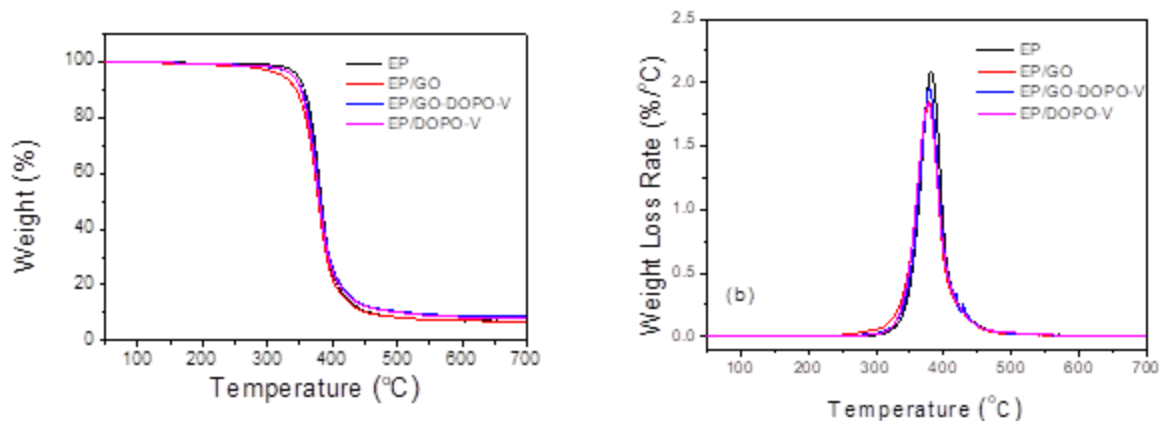


Figure 5.10 TGA curves of (a) PMDA, GO-PMDA and (b) DOPO, GO-DOPO shown along with unmodified GO

Interestingly, EP/GO possess the lowest residue. We hypothesize this is due to the low thermal stability of GO, however, this needs further investigation. The addition of GO-PMDA, DOPO-V and GO-DOPO-V exhibit an increase in the char residue as compared to GO. The residual char obtained from EP/GO-PMDA is higher than EP and EP/GO, which increased by 1.6 wt% with only 2 wt% addition and the residue char of EP/DOPO-V, EP/GO-DOPO-V is increased by 1.17 wt% and 1.50 wt%, respectively. The rich char yield formed during decomposition is due to the condensed phase flame retardant mechanism of silicon element in GO-PMDA, which can block the fuel and oxygen between composites and the environment as well as hinder the heat transfer. In case of DOPO-V and GO-DOPO-V, we hypothesize that since both Si and P elements have the function of promoting the char formation, the incorporation of DOPO-V in GO had a marked influence on the thermal decomposition behavior of EP. Interestingly, the presence of GO with DOPO-V yielded higher char and we hypothesize the early

degradation of GO helps promote the decomposition of DOPO-V which acts as a mechanism of higher char formation.

Table 5.2 TGA data of epoxy-amine / GO-DOPO-V/ GO-PMDA nano-composites

Sample	Temperature (°C)			PDR (wt%/°C)	Residues (wt%)
	$T_{onset}$	$T_{50wt\%}$	$T_{max}$		
EP	346.0	383.5	381.4	2.09	7.02
EP/GO	322.5	378.6	378.2	1.84	6.95
EP/PMDA	336.1	381.7	375.9	1.79	7.34
EP/GO-PMDA	337.9	381.3	378.2	1.92	8.76
EP-DOPO-V	338.7	380.2	376.8	1.84	8.19
EP/GO-DOPO-V	338.4	381.9	379.0	1.96	8.52

$T_{onset}$  – Onset temperature;  $T_{50\%}$  - Temperature at 50% degradation;  $T_{max}$  - Temperature at max degradation; PDR–peak degradation rate

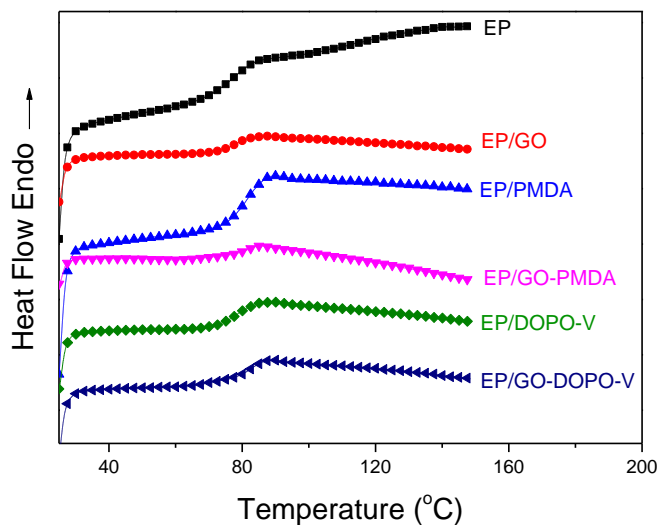


Figure 5.11 DSC thermograms of composites investigated in this work. Curves are offset vertically for clarity



DSC thermograms of the investigated networks along with nanocomposites are shown in Figure 5.11. The first heat (not shown) resembles the third heat shown here which indicates there is not unreacted monomers or any reactive nanocomposites present. It is very evident that the addition of nanocomposite did not affect the glass transition temperature indicating the nanocomposite did not alter the network structure.

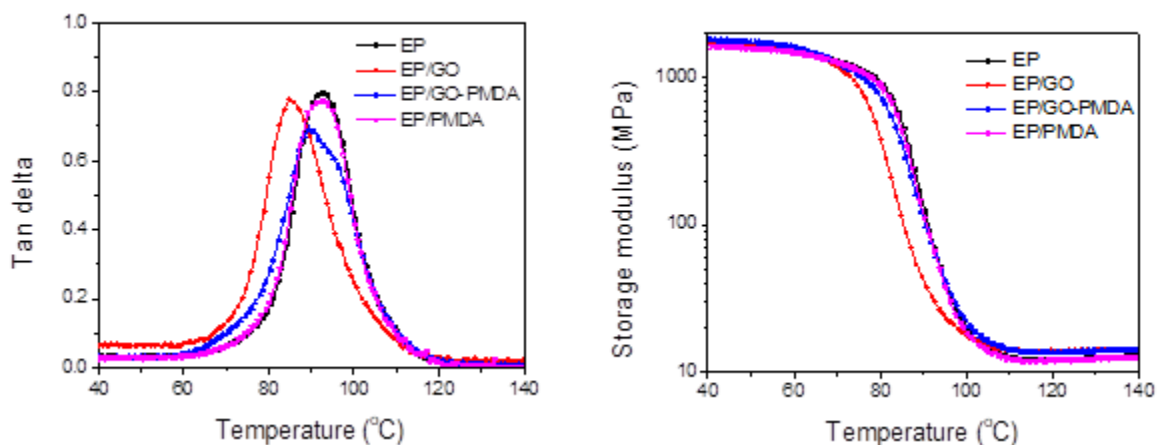


Figure 5.12 Storage modulus and Tan delta curves for EP, EP/GO and EP/GO-PMDA in the DMA test

DMA is a good technique to probe the interfacial interaction between additives and the polymer matrix. Figure 5.12 shows the temperature dependence of the storage modulus and tan delta of EP and its nanocomposites. The storage modulus of pure EP at 80 °C is 928.2 MPa. When adding 2 wt% of GO, the storage modulus of EP composites is decreased by 57.7% and reached 392.9 MPa below the  $T_g$ . The high hydrophilicity of GO and its large aspect ratio have a significant effect on the decrease of storage modulus. This is ascribed that GO affects the cross-linked structure between the EP molecular chains and the curing agent, and acts like a plasticizer role which increases the flexibility

of chain segments of EP matrix. This indicates the reduced cross-linking density of EP which lead to decreased mechanical properties.<sup>259</sup>

However, the storage modulus of EP/GO-PMDA shows much higher compared with EP/GO. The addition of 2 wt% GO decreases  $T_g$  of the EP matrix from 92.7 °C to 84.8 °C which confirms the plasticization effect of GO on EP. But with addition of GO-PMDA the  $T_g$  increases from to 89.5 °C. This indicates that the grafting of PMDA improves the dispersion and solubility of GO sheets in the EP matrix. A similar trend was observed with systems containing DOPO-V as nanocomposites.

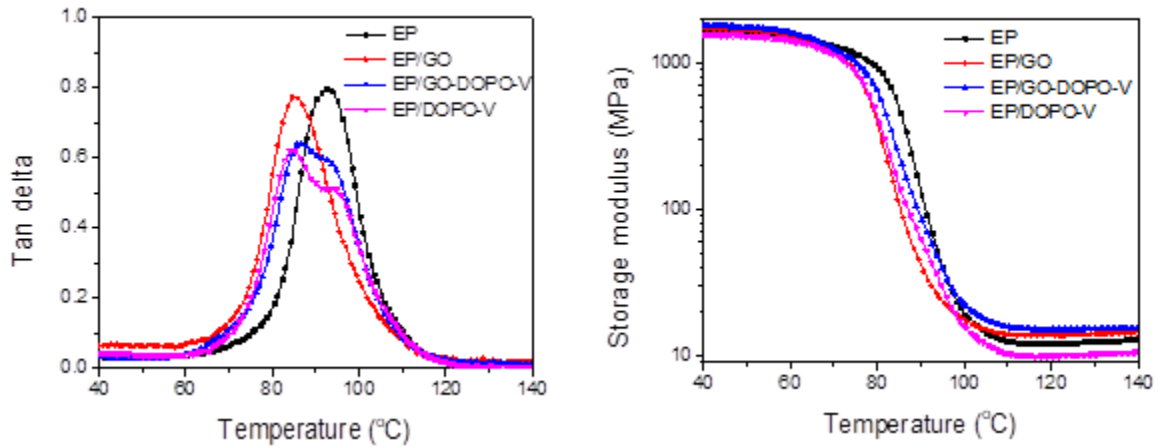


Figure 5.13 Storage modulus and Tan delta curves for EP, EP/GO and EP/GO-DOPO-V in the DMA test

The storage modulus as a function of temperature and ten delta of DOPO-V nanocomposites plotted as a function of temperature is shown in Figure 5.13a and Figure 5.13b respectively. As mentioned earlier, DOPO-V has been reported as flame retardant and hence addition of DOPO-V (without grafting on GO) has also been evaluated. The storage modulus of EP/DOPO-V is the lowest as compared to the GO based

nanocomposites. This primarily due to the agglomeration or inadequate dispersion of DOPO-V in EP matrix. Addition of nanocomposites tend to increase the storage modulus due to the reinforcing characteristics causing a decrease in relaxation amplitude of the polymer chain due to the polymer filler interactions. Thus addition of GO containing nanocomposites (GO, GO-DMPA and GO-DOPO-V) increases the storage modulus. Addition of GO-DOPO-V and DOPO-V in EP reduces the T<sub>g</sub> of the composite networks. But when only DOPO-V is added there exists two distinctiveness peak which indicates there exists two phases, which also points to the agglomeration. The addition of nanocomposites broadens the tan delta peak which indicates the better damping. Addition of GO containing nanocomposites, increased the T<sub>g</sub> when compared to just addition of only DOPO-V which proves the addition of GO facilitated better interaction between the filler and the matrix.

The cone calorimeter is one of the most effective methods to evaluate the flammability of various composites in real-world fire conditions. The heat release rate (HRR) and total heat release (THR) obtained from cone calorimeter have been found to be one of the important parameters to evaluate fire safety. Figure 5.14 shows the HRR and THR plotted as a function of time curves for EP, EP/GO and EP/GO-PMDA. In comparison to pure EP, the peak heat release rate (pHRR) and THR of nanocomposites with the incorporation of 2 wt% GO was reduced by 21.6% and 8.8% respectively. The time to ignition significantly reduces upon addition of GO and GO-PMDA based materials which is attributed to the highly flammable nature of organic content added. However, addition of nanocomposites to the epoxy matrix broadens the heat release curves which indicates the charring nature of the composites. The superior flame

retardancy of EP/GO over EP could be attributed to the barrier effect of GO, which retards the permeation of heat and the escape of volatile degradation products. Moreover, the pHRR of EP/GO-PMDA exhibits further reduction (30.5%, compared to EP), even though THR display little change (10.0%, compared to EP). The best flame-retardant properties of EP/GO-PMDA could be attributed to two aspects: firstly, the reduction of GO by PMDA helps converting GO into a more stable form, reduced-GO; secondly, PMDA can create a stable silica layer on the char surface of EP, which reinforces the barrier effect of graphene. Similar results have been reported on reduction and surface functionalization of graphene oxide with POSS in epoxy composites.<sup>250,254</sup>

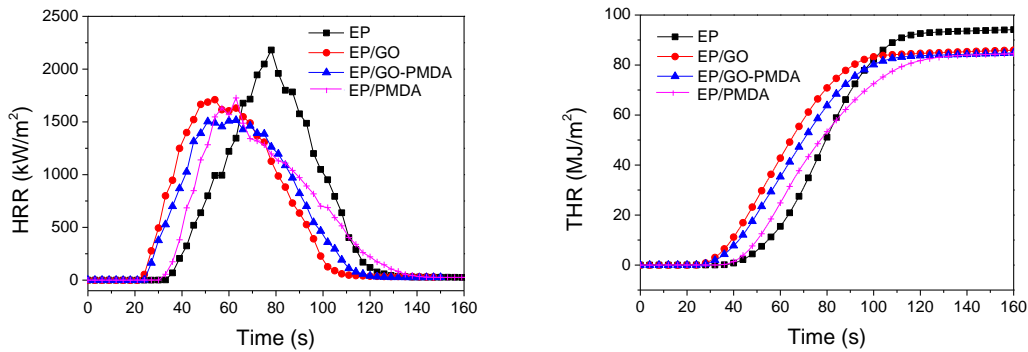


Figure 5.14 HRR and THR curves of EP, EP/GO, EP/PMDA and EP/GO-PMDA

The heat release rate (HRR) and total heat release (THR) of EP, EP/GO, EP/DOPO-V and EP/GO-DOPO-V is shown in Figure 5.15. As expected, the peak heat release rate (PHRR) and THR are both decreased compared to that of pure EP, and the maximum decreases of 28.8% in PHRR and 15.6% in THR are achieved by GO-DOPO-V. Interestingly, properties are different between DOPO-V and GO-DOPO-V based nanocomposites. The grafting of GO with DOPO-V (GO-DOPO-V) decreases the time to

ignition making it ignite faster, but the heat release curve of GO-DOPO-V shows higher char formation during combustion as compared to DOPO-V without GO. This is rationalized to two factors: first, GO aids in better dispersion of DOPO-V (avoiding agglomeration) and secondly the higher ignitability of GO which helps burning DOPO-V to produce char. As compared to GO and DOPO-V, GO-DOPO-V exhibits much better in improving the flame retardancy of EP.

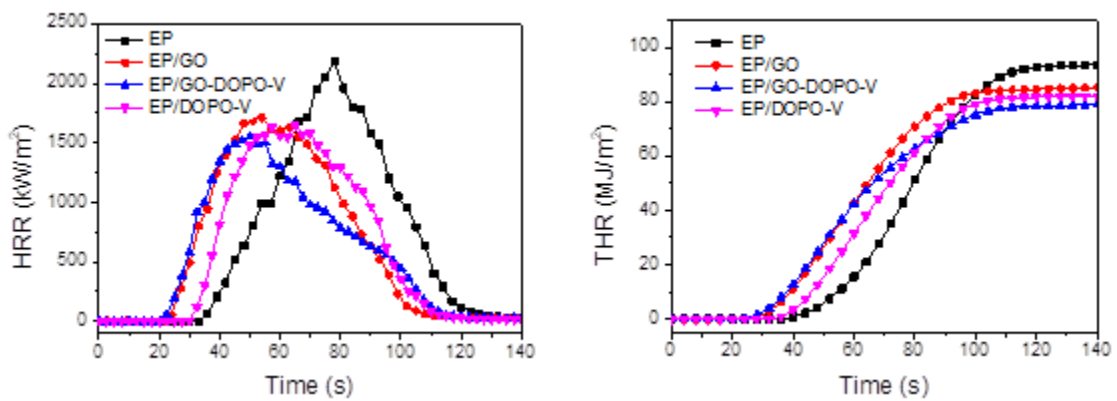


Figure 5.15 HRR and THR curves of EP, EP/GO, EP/DOPO-V and EP/GO-DOPO-V

Table 5.3 Cone calorimeter data for PMDA based nanocomposites (on the top set) and DOPO-V based nanocomposites (on the bottom)

Chemical Composition	T <sub>ig</sub> (sec)	PHRR (kW/m <sup>2</sup> )	T <sub>PHRR</sub> (sec)	Avg. HRR (kW/m <sup>2</sup> )	THR (MJ/m <sup>2</sup> )	Avg MLR (g/m <sup>2</sup> s)	Char yield [%]
EP	33	2180.8	78	465.3	94.2	20.1	1.56
EP/GO	21	1710.4	54	891.1	85.9	22.3	0.27
EP/GO-PMDA	24	1515.5	63	781	84.8	22.1	0.94
EP/PMDA	32	1726.5	63	670.7	84.5	19	2.47
EP/GO-DOPO-V	22.5	1552.8	50	821.6	79.3	19.7	9.83
EP/DOPO-V	30	1646.8	65	771.2	82.4	23	3.20

**Note:** T<sub>ig</sub> – time to ignition; Duration – total time for combustion; PHRR – peak heat release rate; T<sub>PHRR</sub> – time to PHRR; Avg. HRR – average heat release rate; THR – total hear release; Avg. MLR – average mass loss rate; char yield – amount of residue after combustion.

The residual char morphology obtained in cone calorimeter measurement was studied by SEM, as shown in Figure 5.16 and Figure 5.17.

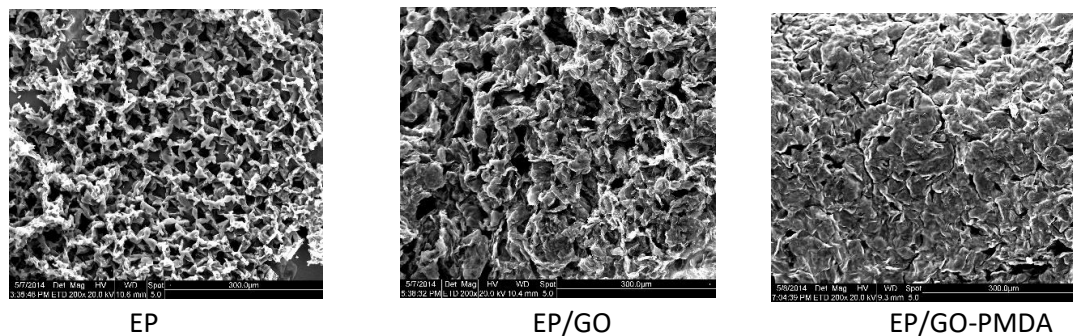


Figure 5.16 SEM images of residual char after cone calorimeter measurement

It was observed that EP is a highly flammable material and its residual char obtained showed a loose and multi-porous feature, and the inner morphology shows a honeycomb structure. The char obtained for EP/GO, honeycomb morphology was not observed, but there existed porous structure on the char layer. However, the char morphology of EP/GO-PMDA is quite different with that of EP/GO. Homogeneous outer char without any porous and dense structure is observed for the EP/GO-PMDA composites. The continuous and compact char surface are good barriers to protect the underlying polymers and inhibit the exchange of degradation products, combustible gases and oxygen. This is primarily due to the improved dispersion of nanocomposites in epoxy amine systems aided by the presence of GO. It indicates that the GO-PMDA can promote the formation of dense char layer and enhancing char stability.

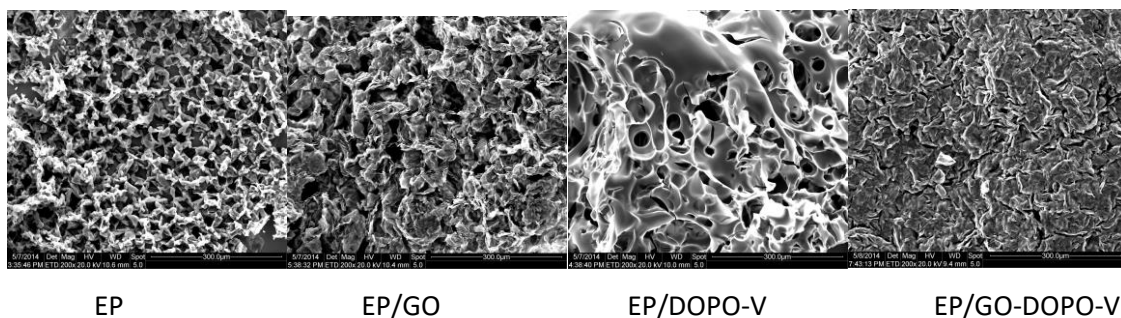


Figure 5.17 SEM images of residual char after cone calorimeter measurement

Char obtained for EP/GO and EP/DOPO-V is non-uniform and porous, which is caused by the released gaseous products during combustion, and the volatilization of these gases consequently lead to the formation of multi-porous interior chars.<sup>246,256</sup> For EP-GO-DOPO-V, homogeneous, continuous and compact residual char is formed. As

mentioned earlier, this can be attributed to better dispersion caused by the presence of GO which leads to barrier effect along with formation of phosphorus/silicon layer by DOPO-V molecules. Owing to the chemical combination and dispersibility of GO and DOPO-V during char formation, the strength of EP/GO-DOPO-V residual char is improved, which can protect the underlying polymer and inhibit exchange of degradation products, combustible gases and oxygen. Finally, the combustion behavior of EP is strongly enhanced, which is in accordance with the results obtained via TGA analysis and Cone measurements.

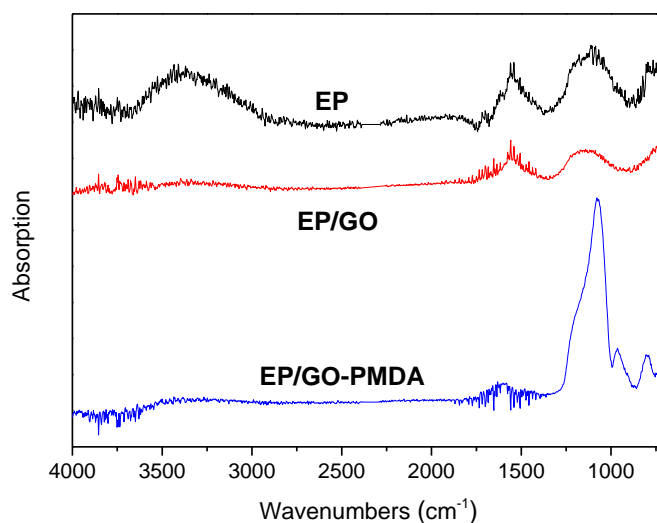


Figure 5.18 FTIR spectra of residual char after cone calorimeter measurement

The residual char of EP, EP-GO and EP/GO-PMDA after cone calorimeter measurement is further investigated by FTIR spectra (Figure 5.18). As can be observed, the FTIR spectra of EP and EP-GO exhibit similar shape, with two peaks at 1558 cm<sup>-1</sup> and 1110 cm<sup>-1</sup>. Distinctively, the FTIR spectra of EP/GO-PMDA shows the Si-O-Si



strong peak at  $1074\text{ cm}^{-1}$ , indicating the occurrence of partial cross-linking of PMDA to form a highly dense Si-O structure. As a result, the presence of the silica layer improves the thermal oxidative resistance of the protective char layer, which could effectively inhibit the heat and mass transmission, and the release of combustible gases from the matrix, which is in accord with the results showed in cone calorimeter and SEM measurement.

#### **5.4 Conclusion**

A novel flame-retardant nanocomposite was developed for epoxy-amine networks which contained phosphorous and siloxane moieties grafted on to a graphene oxide (GO). The uniform distribution of GO was achieved by siloxane and phosphorous modifications. The flame retardancy was greatly enhanced due to the synergistic effect of FR materials (phosphorous, siloxane and GO) along with the uniform distribution of GO within the matrix.

A modified Hummer's method was adopted to synthesize GO from graphite which let oxygen based functional groups on the surface. Synthesized siloxane-based copolymer with amine functional group was grafted to GO with the acid functional groups present on the GO surface. A phosphorous based compound, 9,10-dihydro-9-oxa-10-phosphaphenanthrene-10-oxide (DOPO) was modified with vinyltrimethoxysilane (VTMS) to synthesize DOPO-V. This was grafted on GO through the hydroxyl functional groups present on the surface of GO. FTIR, XPS and AFM was used to monitor the extent of monomer synthesis and grafting.

Composites were prepared by adding 2 wt% of GO modified nanocomposites, GO-PMDA and O-DOPO-V, in standard DEGBA based epoxy resin crosslinked with

polyether amine based curative. Thermal and mechanical properties of the composites were analyzed and compared with the composites prepared by mixing GO, PMDA and DOPO-V. The residue obtained from TGA measurements indicated that the grafted GO based nanocomposites lead to a higher char yield. DMA analysis revealed a slight increase in storage modulus with decrease in T<sub>g</sub> when nanocomposites based on grafted GO was added. This indicated an uniform dispersion along the matrix. On contrary, when pristine PMDA or DOPO-V was added, the storage modulus decreased as compared to the neat epoxy amine networks indicating the tendency of agglomeration.

The cone calorimetry results show a synergistic effect of GO and phosphorous and siloxane based on DOPO-V and PMDA moieties respectively. The effect of grafting PMDA and DOPO-V on GO on FR properties was compared and the effect of grafted nanocomposites were more pronounced than when added as individual component despite its potential fire-retardant capability. This is attributed to the efficient dispersion of nanocomposites which is aided through the functionalization of GO.

The residue obtained in cone calorimeter was analyzed in SEM. The char obtained for nanocomposites prepared from grafted GO left a dense (less porous char) as compared to the pristine nanocomposites. This indicates the grafted nanocomposites formed a thick layer of insulating char which acted as a barrier to both heat and transportation of molecules to aid the fire. Thus in addition to the synergistic effect of DOPO-V and PMDA with GO, grafting improved the dispersion leading to the formation of dense char further improving the flame resistance of the composites.

In conclusion, a uniform dispersion of FR material in the matrix improves the flame retardancy of the matrix. In this study, GO was made solubilized in the epoxy

systems through grafting the hydrophobic elements, PMDA and DOPO-V, on to the surface. The flame retardancy mechanism was from the synergistic effect of both contribution from the chemical elements along with improved dispersion.

### **5.5 Acknowledgements**

The author would like to thank Dr. Jiangbo Wang (Ningbo university of technology) for his initiative synthetic work and running XPS in his university. The authors would like to also acknowledge Dr. Emily Hoff, Patton research group at USM for running AFM measurements.

## CHAPTER VI METAL ORGANIC SALTS AS NEW INTUMESCENT FLAME RETARDANT MATERIALS.

### **Abstract**

Traditional flame retardants including halogenated, phosphorous and boron based materials possess high smoke release as their mechanism of fire scavenging. As a result, these materials are being phased out and there is a need of flame-retardant materials which are green. For the first time, we showed that the dissolved metal salt can greatly improve the flame retardancy as compared to a metal dispersed in the polymer phase. It was found that the primary and secondary amine aided in dissolution of metal salt in the polymer matrix. A two-step approach was chosen such that the first involved the preparation of small molecule additive by mixing amine with the metal salt. The synthesized small molecule additive was subsequently added to the polymer matrix. The dissolution was evidenced visually when the additive turned transparent along with checking for the loss in crystal structure of salt through wide angle x-ray analysis. As a proof of concept, we examined the flame-retardant effect of small molecule additive in epoxy-amine (EP), polyurethane (PU), polystyrene (PS) and polyethylene oxide (PEO) polymers. The cone calorimeter results indicated that the flame-retardant effect was seen when the additive concentration was as low as 0.1wt% of metal. Decrease in peak heat release rate (PHRR) compared to neat polymer matrix was chosen as a parameter to determine the flame-retardant effect of metal salt. We determined that the increasing concentrations of small molecule additive decreased the PHRR up to 12 wt% based on metal, beyond which the PHRR increased. This is possibly due to the increase in organic content arising from the tail portion of the metal salt. In a separate study, the effect of

addition of different metals in flame retardancy were compared. The effect on flame retardancy when the metal salt was dissolved was compared to the composites containing dispersed metal salt. It was very evident that the dissolved metal salt had higher reduction in PHRR values. A thick layer of continuous char was obtained for the composites that contained dissolved metal, whereas the char was porous non-continuous for the composites containing dispersed metal salt. This illustrated the importance of the dissolved metal salt. Surprisingly addition of small molecule additive induced plasticization effect. Differential scanning calorimeter (DSC) analysis revealed that addition of small molecule additive decreased the glass transition temperature with increasing content. Compressive tensile test was performed to verify the plasticization effect. The wide angle x-ray analysis was performed on the char obtained after the combustion which revealed the presence of oxide form of metal salt. In a separate study, stearate salts were heated above its melting temperature round 90°C to obtain a transparent mass which was added to the polymer matrix. This transparent composite also had improved flame-retardant properties compared to the neat polymer. Self-healing flame retardant composites were prepared by synthesizing an metal containing polyol crosslinked with an isocyanate. The co-ordination bond between the metal and the organic tail in the backbone imparted the self-healable nature to the polymer, whereas the presence of dissolved metal salt imparted the flame-retardant behavior.

## 6.1 Background

Polymers have found a wide variety of applications increasingly being used in the automotive, electronics and aerospace industries due to their high strength to weight ratios and high stiffness. The tunability of a polymer based on its constituents used such as improving corrosion resistance, thermal and electric insulation, adds advantage compared to other materials in use.<sup>263</sup> The major setback impeding polymers from extensive use is the flammable behavior. Since polymers are essentially organic molecules which are combustible, they decompose (bond-breaking) when exposed to sufficient heat generating flammable volatiles. These volatiles when mixed with air (oxygen), ignition occurs.<sup>206,264</sup> Thus, there is a necessity to improve the flame retardancy of polymers in order to take advantage of such versatile materials.

Polymer combustion process is a complex phenomenon involving a series of independent steps which occurs in condensed or gas phase along with the interphase between these two phases.<sup>206</sup> Flame retardancy does not mean that the polymeric material is resistant to burn, but rather it will be harder to burn. Flame retardant polymers avoid a sudden burst of heat energy and smoke aiding with the time to escape.<sup>223,264</sup> Polymers can be made fire resistant in different ways. The first obvious strategy is to break the fire triangle (oxygen, heat and fuel). The most common way to break the fire triangle by stopping the heat transfer and cut off oxygen is by using a FR material which forms char upon combustion.

Flame retardants (FR) can be classified in several ways. The classification can be based on the mode of addition (additive or reactive), based on the fire-retardant process (cooling, isolation and dilution) or based on the chemical nature (broadly halogenated

and halogen-free fire retardants).<sup>265</sup> There is no definite way of classifying FR materials and a single class of material can be assigned in multiple mechanistic ways. Also, two materials can be combined to synergistically improve the performance of FR material.

Classification based on the FR method of action include additive approach or reactive approach.<sup>266,267</sup> FR additives can be mixed with polymer matrix either during processing or post-processing stages. Care must be taken to ensure the homogeneous dispersion and aggregation free when added to the matrix. Adding flame retardants as additives can affect the physical and chemical properties of polymer. Reactive FRs are prepared by synthesizing monomers with the FR molecule. This has the advantage over additive FR to be permanently bonded to the polymer matrix along with use of relatively low quantities. However, obtaining reactive systems are more expensive because they require the development of a new polymer with specific chemical and physical properties. Recently, several researches have been focused in combing the above two methods by adding FR containing oligomers with reaction functional groups.<sup>268–270</sup>

The FR materials can act via physical or chemical mechanisms.<sup>265</sup> There are various potential ways in which flame retardants can react.

*Physical mechanism:*

- Cooling: FR materials can degrade endothermically cooling the substrate of the polymer to the temperature below its degradation or below the temperature required to sustain the combustion process. Examples include metal hydroxides.
- Isolation: Formation of layer of char on the surface during combustion, which acts as a thermal barrier reducing the heat transfer to the unburnt polymer surface. The char layer also isolates the volatiles formed reducing the fuel flow to the fire.

Intumescent systems and Nano-composites that form char upon combustion are contained in this category.

- Dilution: FR that releases inert gases or polymer matrix that contains inert substances diluting the fuel in the gaseous and solid phase respectively, reducing the volatile flammable compounds in the flame.

*Chemical mechanism:*

- Gas phase: Polymer materials during combustion produces species that react with atmospheric oxygen to reduce the propagation of fire. Usually, the exothermic process is reduced by the reactive radical quenching in the gas phase.

Phosphorous based and halogenated FR fall in this category of materials.

Depending on the nature of FR, the radicals may vary.

- Condensed phase: FR compounds during combustion can form a charring layer through the dehydrating leading to crosslinking reaction. As we know that char acts as a physical barrier from heat and mass transfer thus reducing the flammability of the system. Examples include boron and phosphorous based FR materials.

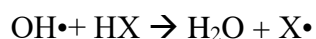
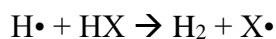
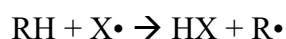
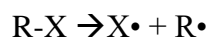
Broadly, FR materials can be broadly classified into halogenated and halogen-free materials based on the chemical identity. A brief overview of such FRs are discussed below.

*Halogenated FR:*

For several decades, halogen-based compounds serve as FR material when mixed with polymer matrix. Halogenated compounds, mostly brominated are often mixed in the polymer matrix as additives or by co-polymerization. Some research points that the



halide FR acts in condensed phase,<sup>271</sup> but most research indicates the retardant happens in the gas phase.<sup>180,272</sup> Highly reactive H• and OH• radicals are generated upon polymer degradation. Halogen based FR inhibit flame propagation in the gas phase by quenching these hydrogen and hydroxy radicals to form hydrogen halides. These hydrogen halides act as a flame inhibitor because they quench the radicals that cause chain branching propagation.<sup>271</sup>



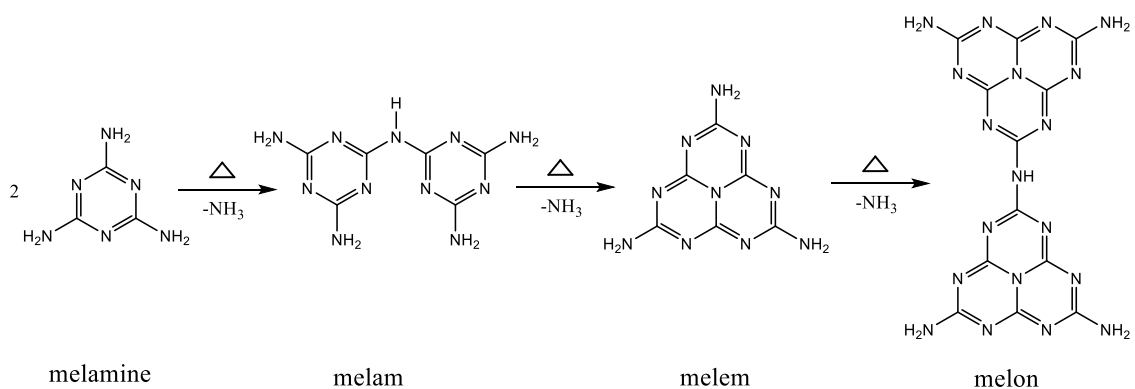
In the view of physical mechanism, the hydrogen halides dilute the concentration of combustible gases thus decrease the temperature of the flame. In the condensed phase, halogen radicals after abstracting the hydrogen atoms, newly unsaturated polymers with double bonds are formed which are known to be the precursors for char formation.<sup>272</sup>

Halogenated compounds represents a hazardous environment because of the increasing quantities of smoke and toxic decomposition products that are released during the combustion process. Moreover, they may also lead to formation of strong acid such as HCl and HBr which can be deteriorating both the polymer and the environment.<sup>225</sup> Thus halogenated compounds, despite of having good flame retardancy, with the growing concerns regarding human health and environmental safety, halogen-free FR being developed.

*Halogen-free FR:*

– Nitrogen based

Nitrogen based FR are becoming popular due to its relatively low toxicity compared to halogenated compounds. FR family containing nitrogen can be mainly divided in two families based on the mechanism.<sup>273</sup> One, endothermic decomposition caused by ammonia via dilution of the flammable gases in the gas phase. Second, melamine-based systems that enhances char formation in the condensed phase upon combustion. Guanidine, urea, ammonium polyphosphate (APP), ammonium pentaborate and sulfamate has been reported as effective FR materials in this family that acts in the gas phase. Melamine is the most popular compound with a melting point of 350°C that contains 67 wt% of nitrogen. In addition to the release of ammonia upon combustion which dilutes the combustion gas species, the decomposition reaction leads to the formation of thermally stable cross-linked phase known as melam, melem, and melon (Scheme 6.1) which is a precursor to form an incombustible insulating layer of char.<sup>274</sup> However, melamine-based polyphosphate compounds produce dripping during the combustion which limits its usage.



Scheme 6.1 Thermal decomposition of melamine-based products.

– Phosphorous based

Phosphorous based compounds constitute a large group of FRs which includes red phosphorous, phosphine oxide, phosphates, phosphonates and phosphinates (Figure 1).<sup>274</sup>

Phosphorous based FRs are known to act both in gas phase and in condensed phase.

Phosphoric acid is released during the decomposition which may catalyze the polymer degradation leading to double bond formation, subsequently leading to the char formation. Furthermore, phosphorous based FR forms active species such as  $\text{PO}_2\bullet$ ,  $\text{PO}\bullet$  and  $\text{HPO}\bullet$  which acts as scavengers for combustion products such as  $\text{H}\bullet$  and  $\text{OH}\bullet$ , thus reducing the flame spread. Reports are available in literature that phosphorous compounds produce radicals that are more effective than halogenated based radical scavengers.<sup>272,273</sup> Phosphorous based compounds can either be inorganic based (ammonium polyphosphate) or metal phosphinates (aluminum based phosphinates).<sup>275</sup>

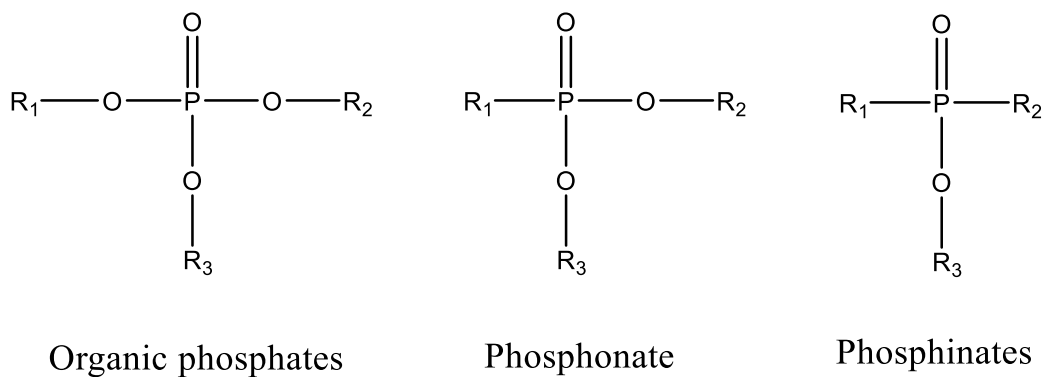


Figure 6.1 Phosphate based FR.

Phosphates can also be separated based on the incorporation method as reactive and non-reactive phosphate with either chemical or physical mixing respectively.<sup>273</sup>

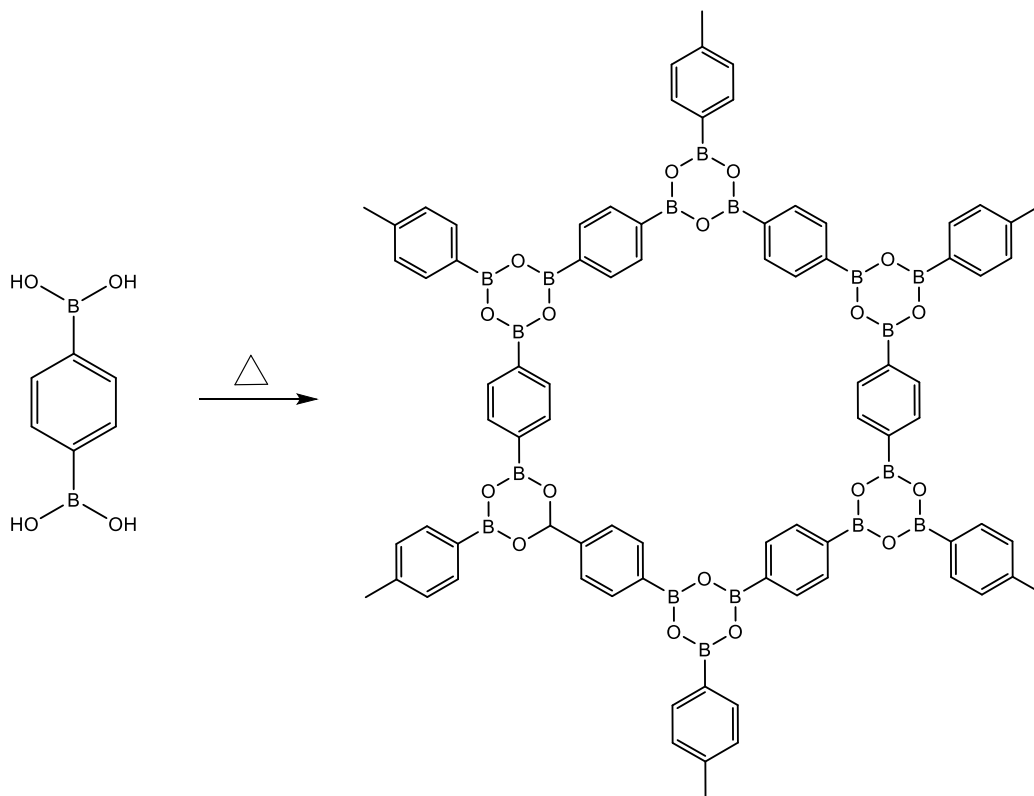
– Inorganic and Nano FR

Inorganic FRs which constitutes major of FR market consists of metal hydroxides, natural minerals, borates and layered double hydroxides. They are advantages because of its low cost, non-corrosive combustion products combined with the easy mixing to several polymer system, however certain drawbacks are associated to its high loading level which hampers the mechanical properties.<sup>276</sup> Nano particles with its high aspect ratio alters the desired property of the polymer matrix. Nanoclays,<sup>277</sup> graphene,<sup>278,279</sup> carbon nanotubes (CNTs),<sup>70</sup> metal oxides are few such examples that are used in improving the fire resistance of the polymer matrix.

Clay are referred to natural compounds with layered aluminum silicate containing cations such as Na<sup>+</sup> and Ca<sup>2+</sup> in between the layers which are exchangeable with other cations.<sup>277,280,281</sup> Montmorillonite (MMT) is typical clay used as a filler in the polymer matrix. In a certain study, the clays showed a synergistic effect after combining with phosphorous and halogenated compounds.<sup>173,282</sup> Modified clays were prepared by intercalating with hexyl-triphenyl-phosphonium bromide and then grafting with glycidyl-oxypropyl-trimethoxy silane.<sup>283</sup> It has been also reported that addition of Nanoclays up to 5 wt% improves both mechanical properties and FR properties.<sup>284</sup> These compounds create a protective layer of char during combustion which slows down the heat and mass transfer. Inorganic silicone nano particles have been also reported to exhibit FR properties without hampering the mechanical properties.<sup>18,36-38</sup>

Boric acid, boron oxide, zinc borates, melamine borate, boron phosphate and boron siloxanes are some of the boron-based compounds reported as FR.<sup>284-287</sup> Boron based FR acts mainly in condensed phase by favoring the carbon formation during

combustion rather than CO or CO<sub>2</sub> formation thus enhances the char formation which forms a barrier layer to prevent oxidation during combustion. The char formation relates to the thermal action of boronic acid with alcohol moieties in the polymer or during combustion. Scheme 6.2 demonstrates the formation of boroxine networks from boric acid as an example which enhances the char formation.<sup>288</sup>



Scheme 6.2 Formation of boroxine networks from boric acid, a precursor for char formation..

It has been reported that addition of boron-based FR leads to formation of boron oxide protective layer which further prevents degradation of the underneath polymer.

The other inorganic FR includes layered double hydroxides (LDH). LDHs are similar to metal hydroxides, but  $M^{2+}$  cations are replaced by  $M^{3+}$  and the excess positive

charged is balanced by intercalated anions and water molecules.<sup>289</sup> These materials follows a strong condensed phase mechanism with the formation of char layer in addition to diluting the flame due to the presence of water molecules. The ability of LDH to disperse arise from the charge present in the molecules.<sup>172,289-291</sup> The type of metal and the morphology also determines the char forming capability of LDH.

Silicone based materials such as silica, silicates, organ silanes and silsesquioxanes are widely used FR compounds.<sup>284</sup> These compounds have low toxicity, high thermal stability along with reduced corrosive r toxic compound release during combustion. These compounds are either added as an additive or as co-reactant in the networks. Siloxane based compounds acts in the condensed phase by enhancing the char formation which acts as the barrier layer for heat and mass transfer as explained before. Polydimethylsiloxane (PDMS), polyhedral oligomeric silsesquioxanes (POSS) and its derivatives are most commercially available FR compounds. Reports are available indicating the synergistic effect when used with phosphorous based compounds.<sup>292-294</sup> Recent studies in our lab indicated the effect of POSS structure on flame retardancy of thiol-ene networks. We found that incorporation of 5 wt% of aromatic POSS improved the FR properties of such networks.

Metal hydroxide form an important class of FR materials due to their dual mode of action: one the metal oxides to form a layer of char at the interface between the polymer and combustion. Secondly, the material acts as a heat sink due to the strong endothermic reaction that occurs during decomposition as shown in Scheme 3.<sup>295</sup> The water molecules that are released dilutes the flammable gases reducing the thermal transfer improving the flame retardancy.



Aluminum hydroxide (ATH) and magnesium hydroxide are major metal hydroxides that are used as FR. Several variants such as particle size (ranging from 1.5 micron to 35 micron), shapes are commercially available. The main advantages include low cost and low toxicity. The major drawback in using such FR is its higher loading which can be detrimental to the mechanical properties of the polymer. The other drawback is its tendency to form agglomerates which has been overcome by surface treatments to improve the dispersion.<sup>165,226,296</sup>

Recent work in our group demonstrated the potential use of hydrated metal salts such as zinc acetate and cobalt acetate as flame retardant agents for epoxy amine networks. We found that the char formed during the combustion trapped in the volatiles from feeding the fire, thus reducing the PHRR of the composite materials.<sup>74</sup>

In this work, we examined the potential use of several metal-based FR by dissolving in the polymer matrix. It was found that the dissolution of metal salt was the key aspect in achieving better flame-retardant properties. It was also found that the additive approach can be utilized in order to use the synthesized FR additive to several polymer including, epoxy-amine, polyurethane, polystyrene and polyethylene oxide, which showed greater performance than the pristine polymers. In a separate study, when these flame-retardant additives were added as a reactive component in a polyurethane system, we found that beyond certain concentration of dissolved salt, self-healing property was achieved.

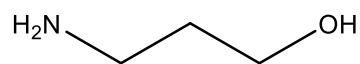
## 6.2 Experimental

### 6.2.1 Materials

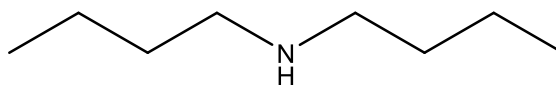
Amine based monomers, 3-amino-propanol, n-dibutyl amine, ethylene diamine and triethyl amine were procured from Sigma-Aldrich. All zinc salts (zinc acetate, zinc acrylate, zinc undecylenate, zinc stearate, zinc citrate and acetate salts of cobalt and nickel, and stearate salt of sodium, magnesium and nickel were also procured from Sigma-Aldrich. All metal salts had a reported characteristic particle size small than 50 nm. Laboratory grade stearic acid was procured from Fischer scientific. Chemical structures of all amine monomers and metal salts are reported in Figure 6.2 and Figure 6.3 respectively. Diglycidyl ether of Bisphenol-A based epoxy monomer, Epon 826 was supplied by Hexion Inc. and the polyether diamine based curing agent, Jeffamine D230 was provided by Huntsman. Polyurethane networks were prepared by reacting polyol with isocyanate. Sovermol 1092, a polyether ester based polyol was provided by BASF and the isocyanate, Desmodur W, was provided by Covestro. Since these compounds are provided by the industry, the exact structures are not known. However, since the properties were compared between metal based composites and the neat networks, the actual structure of the commercial monomers didn't affect this study. Polystyrene with  $M_w = 90,000$  and polyethylene oxide with  $M_w = 100,000$  were procured from Sigma-Aldrich. Monomers used in self-healing polyurethane studies, diethanol amine, methyl acrylate and hexanediol diacrylate were also procured from Sigma-Aldrich. All monomers were used as received. Solvents acetone and xylene which were used to in polyurethane networks were treated in a column of Zeolite 5A to remove any



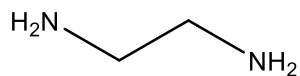
contaminated moisture. Small molecule additive and  $\beta$ -amino complex are used interchangeably and both indicate the dissolved metal salt.



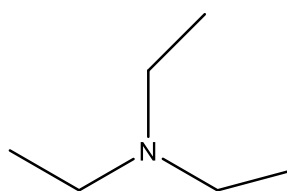
3-amino-propanol



n-dibutyl amine



Ethylene diamine



triethyl amine

Figure 6.2 Monomers used as dispersing agents for small molecule metal based additive

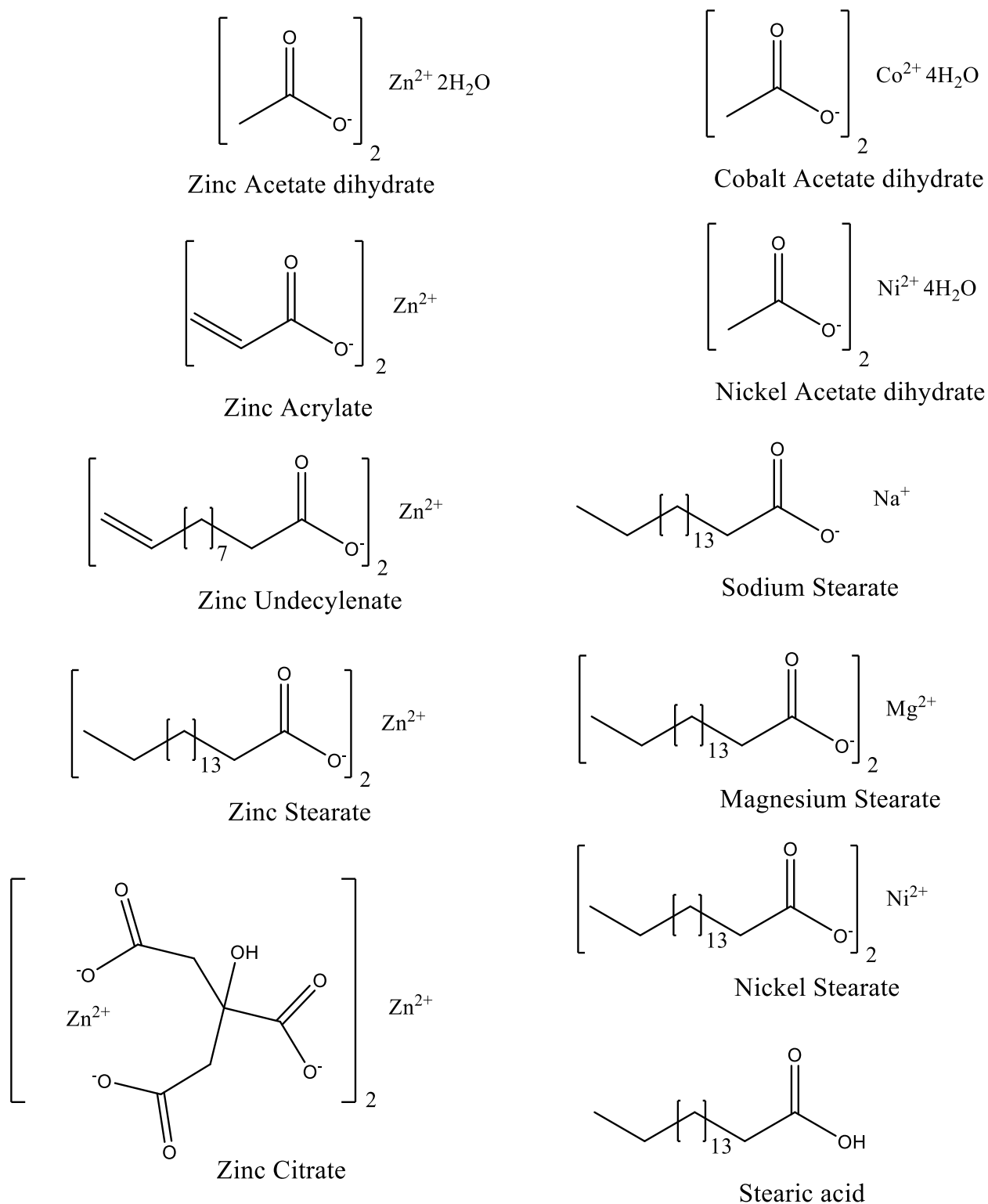
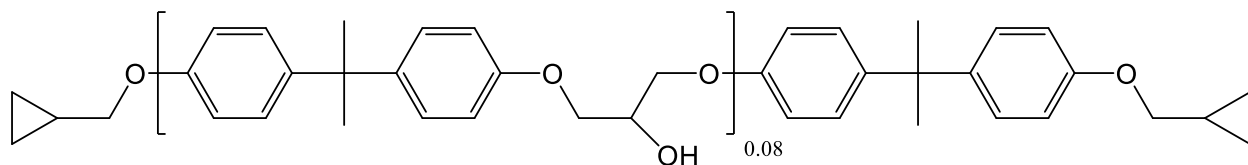
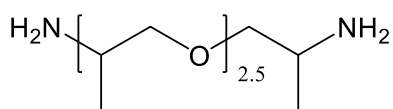


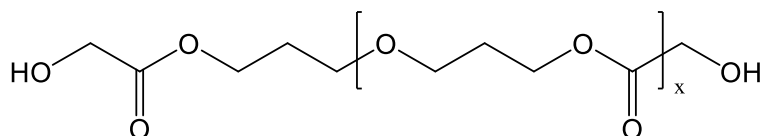
Figure 6.3 Metal salts used in this work



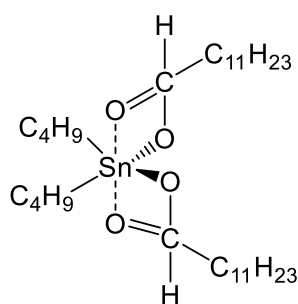
Epon 826 (DGEBA epoxy resin)



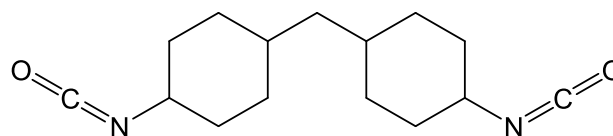
Jeffamine D230 (Polyether diamine)



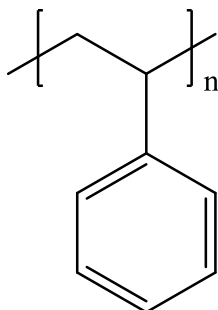
Sovermol 1092 (polyether-ester polyol)



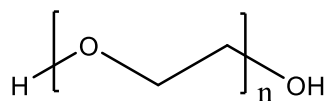
Dibutyl tin-dilaurate (catalyst)



Desmodur W (dicyclohexylmethane diisocyanate)



Polystyrene  
( $M_w = 90,000$ )



Polyethylene oxide  
( $M_w = 100,000$ )

Figure 6.4 Monomers / oligomers used as base to prepare composite materials

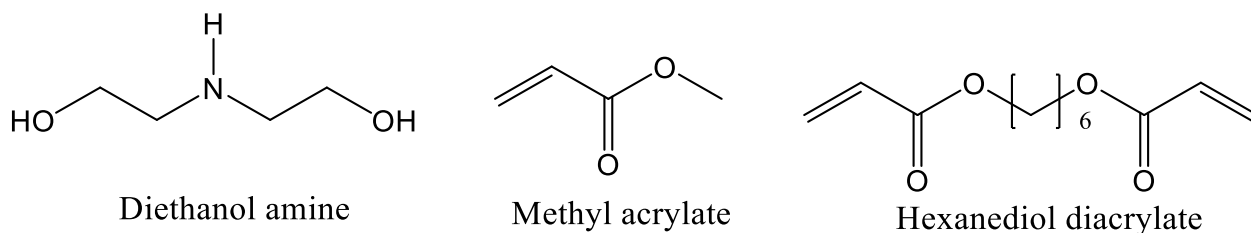
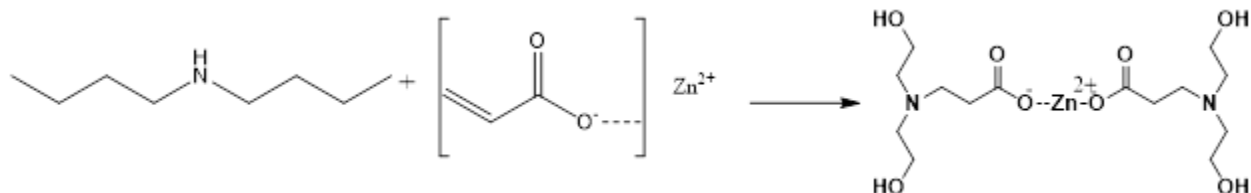


Figure 6.5 Monomers used to prepare flame-retardant self-healing material

### 6.2.2 Synthesis of small molecule additive / $\beta$ -amino complex

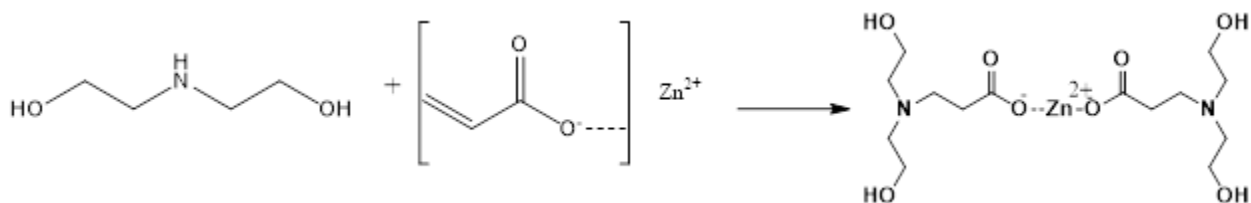
- i. For the work where, different zinc salts and different metal acetates dissolved in epoxy-amine, polyurethane and polystyrene, the following protocol was used. Small molecule metal containing additive was prepared by mixing the desired salt to an amine which is preheated to 65°C. Metal salts, were added slowly such that the added powder doesn't agglomerate in the amine. A stoichiometric ratio of 0.5:1 of metal salt to dibutyl amine was used to dissolve the metal salt to the amine. The reaction mixture was stirred continuously until it turned transparent. The confirmation of small molecule additive formation was carried out through the visual inspection for its transparency. The prepared small molecule additive was then cooled to room temperature gradually and then subsequently added to the desired polymer matrix. In certain instances, acetone was added in excess, to aid the mixing of metal salt in the amine. Dibutyl amine was chosen as a dispersing agent for the metal salts due to its solubility in common solvents for epoxy-amine, polyurethane and polystyrene. Special care was taken when additives were prepared to use with poly-isocyanate, since presence of moisture will result in polyurea when reacted. Thus, the solvent was poured through a column of zeolite 5Å to remove any trapped moisture in the solvent.

It is to be noted that even after removal of moisture from solvent and other monomers, there were certain instances we were not able to stop the formation of polyurea. Solubility was important to aid the miscibility of these prepared small molecule additive in those polymer matrices.



Scheme 6.3 Synthesis of small molecule additive using dibutyl amine and zinc acrylate

- ii. In case of small molecule additive which was added to water soluble polyethylene oxide, water soluble amine, ethylene diamine. Since NMR and preliminary miscibility test pointed the reaction between zinc acrylate and amine was Michael addition reaction, stoichiometric quantities were mixed such that for every replicable proton in nitrogen requires one electron rich double bond. Thus the stoichiometry between zinc acrylate to ethylene diamine was altered to 1:0.5 zinc acrylate to ethylene diamine. The prepared additive was checked for solubility in water and it was confirmed that the additive was completely miscible in water.



Scheme 6.4 Synthesis of small molecule additive with self-healing property

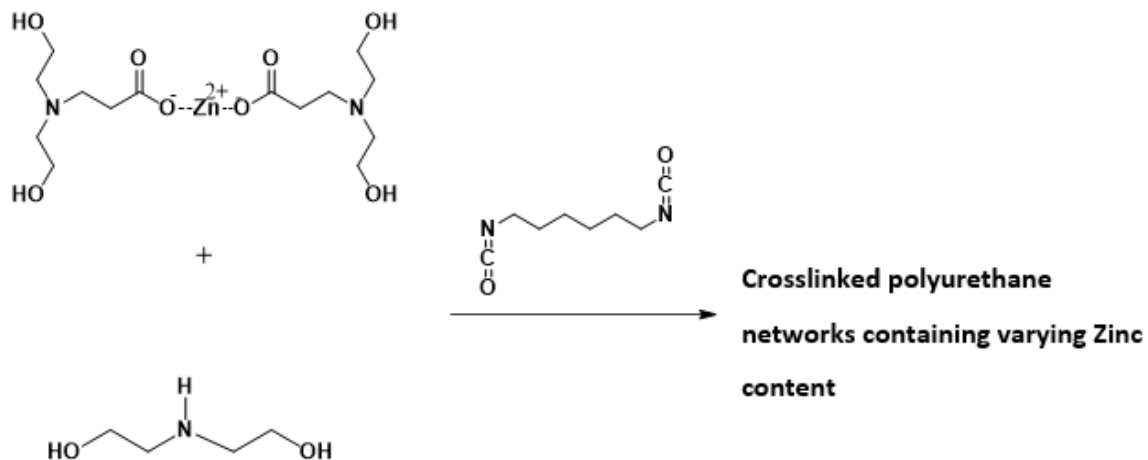
- iii. Small molecule additive preparation for self-healing polyurethanes involved the use of diethanol amine as dissolving agent. A similar protocol was chosen as mentioned earlier with a stoichiometry of 0.5: 1 zinc acrylate to diethanol amine. Since it was well established from earlier work in this chapter, the stoichiometric amounts were mixed and further used to prepare composites without NMR conformations.

### **6.2.3 Composite Preparation**

- i. Epoxy amine networks were prepared from standard diglycidyl ether of bisphenol-A (DGEBA) crosslinked with a diamine. Epon 826, a DGEBA epoxy resin was generously provided by Hexion Inc. and the crosslinker, Jeffamine D230, a polyether based diamine was provided by Huntsman. Epoxy amine networks were prepared by mixing Jeffamine D230 to Epon 826 at 1:1 stoichiometric quantities. Every epoxide group is reacted with the proton in nitrogen, hence Epon 826's functionality was 2, whereas the Jeffamine D230 functionality was 4. The composites were prepared by adding the synthesized small molecule additive to a preheated epoxy resin to 75 °C. Since Epon 826 was viscous in nature, preheating was necessary to facilitate the mixing. The mixture was then cooled down to 45°C and a stoichiometric quantities of Jeffamine D230 was added under string. The mixture was then degassed to remove any trapped air bubbles in a vacuum oven held at 60°C for about 10 minutes and subsequently casted in a desired mold. The liquid cast was then solidified by curing at 90°C for 12 hours. Neat crosslinked networks were prepared in a similar way except the addition of small molecule additive to epoxy resin.
- ii. Polyurethane composites were prepared by mixing the synthesized small molecule additive to the desired polyol which was then crosslinked through isocyanate. The

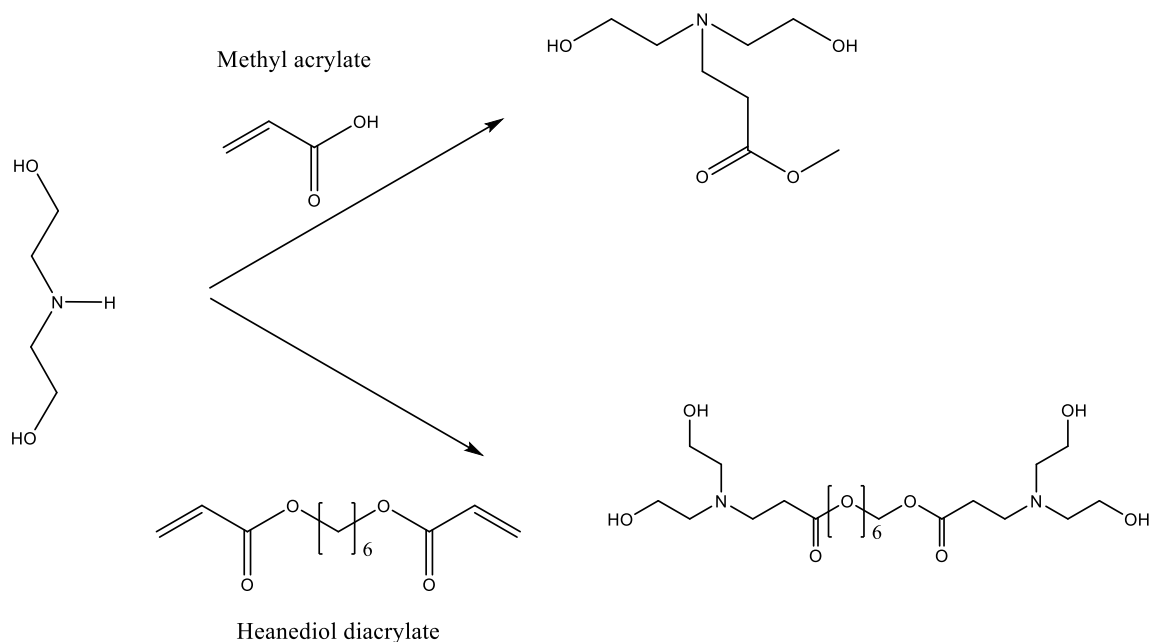
synthesized small molecule additive ( $\beta$ -amino complexes of zinc acrylate) was mixed with moisture free xylene to achieve a mixture containing 10 wt%, which was then added to poly-isocyanate prepolymer at room temperature. This mixture was slowly added in stoichiometric quantities to a polyol. this mixture was degassed in a vacuum oven maintained at room temperature for 10 min. Thermal environment was found to trigger the reaction between isocyanate and polyol and thus all premixing was done at room temperature in a moisture free environment. The mixture was then casted to a desired mold which was crosslinked at 85°C for 12 hours. It was very important to avoid the moisture ingress, either through added solvent or monomers, for polyurethane systems to avoid formation of polyurea.

- iii.** Polystyrene which were procured from Sigma-Aldrich was dissolved in methylene chloride under string. The synthesized small molecule additive was dissolved in excess methylene chloride and subsequently mixed with the dispersion of polystyrene in methylene chloride under stirring and casted in desired mold. The curing schedule was to bake at 65°C for 24 hours.
- iv.** Metal containing polyethylene oxide composites were prepared using water soluble small molecule additive prepared using ethylene diamine. Small molecule metal additive was dissolved in DI water and added to a solution of polyethylene oxide dispersed in DI water under mechanical stirring at 60°C. The composition was poured and casted in a mold of desired shape and let sit a room temperature for 7 days. The cast was then heated to 90°C for 30 min and tested for its properties.
- v.** Self-healing flame retardant was synthesized by adding the metal containing small molecule additive synthesized by adding zinc acrylate to diethanol amine. This small molecule was mixed with neat diethanol amine (alcohol part of polyurethane) at different proportions. Polyurethane composites were prepared by reacting this polyol with hexamethylene diisocyanate in stoichiometric quantities as described in scheme 1 below.



Scheme 6.5 Synthesis of self-healing flame-retardant compositions

Neat polyurethane systems containing no metal atoms were prepared by addition of synthesized small molecule additive using methyl acrylate and hexanediol diacrylate reacted with diethanol amine as depicted in Scheme 6.6.



Scheme 6.6 Neat polyurethane to compare with self-healing flame retardant polyurethane networks



#### 6.2.4 Characterization

The glass transition temperature of epoxy-amine networks and its composite prepared by adding metal salts were obtained using TA instrument Q1000 differential scanning calorimeter (DSC). The specimens were accurately weighed up to fourth decimal (approximately the sample was around 8 mg). All the samples were subjected to heat-cool-heat as follows: the sample was heated from room temperature to 200°C at 10°C/min to obtain the first heat flow. Next, the samples were cooled to 35°C/min at a rate of 10°C/min and then reheated to 200°C at again 10°C/min to obtain the second heat. The second heating scans are reported and the inflection point of the heat flow was assigned as glass transition temperature.

The thermal stability of the pure small molecule additive and the composites prepared using the small molecule additive along with the neat epoxy amine networks was studied via thermogravimetric analysis (TGA). The testing was performed on a TA instrument Q500 thermogravimetric analyzer under N<sub>2</sub> atmosphere. The sample gas purge flow rate was set at 60 mL/min. Samples weighing 6 mg were tested over a temperature range from room temperature to 650°C with a heating rate of 10°C/min.

Wide angle X-ray diffraction (WAXD) was used as a tool to confirm the dissolution of metal within the composites. WAXD were performed in transmission mode on a Xenocs Inc. Xeuss 2.0 beamline system with a X-ray wavelength of 1.54 Å (Cu-K $\alpha$  radiation). The composites prepared were mounted on a Pilatus 1M detector (Dectris Inc) with an exposure time of 10 min and processed using Foxtrot software. The WAXD patterns were analyzed to see the disappearance of the characteristic crystalline peaks of the metal salt after dissolving in polymer system to prepare composite materials.

The flame retardant properties were evaluated using cone calorimeter in compliance with ASTM D1354. Cone calorimeter is a laboratory scale fire testing instrument which provides a wealth of information on the combustion characteristics of polymer materials including time to ignition ( $T_{ig}$ ), heat release rate (HRR), peak heat release rate (PHRR), time to peak heat release rate ( $t_{PHRR}$ ), average mass loss rate (Avg. MLR) and total heat release (THR). Cone calorimeter can also quantify the smoke release, carbon monoxide and carbon dioxide release. Cone calorimeter was carried out using Govmark cone instrument (recently Deatak flammability test instruments). All samples weighing approximately  $35 \pm 3$  gm with dimension 100 x 100x 30 mm were exposed to an incident flux of  $50 \text{ kW/m}^2$  using a cone shaped heater and the exhaust flow rate was set at 24 L/s. The spark was turned on until the sample was ignited. Samples were contained in an aluminum foil to collect the remains after combustion for further analysis. Typically the data generated by cone are reproducible with an uncertainty which does not exceed  $\pm 10\%$ . All samples were run in triplicate and the average values are reported.

UL-94 test measures the ability of a sample to self-sustain ignition and propagation of flame in both vertical and horizontal spread configuration. UL-94 test in horizontal mode was conducted in a custom made set up where the samples were exposed to methane gas to evaluate the flammability, flame propagation and the dripping effect of different systems. In our study, the specimens were exposed only in horizontal way (ASTM D 5132) to compare and contrast the effect of increasing FR additive in the polymer matrix. ASTM D 5132 test method employs a standard test specimen (100 x 300 mm) with a thickness up to 13 mm, mounted on a clamp. The specimen is ignited with a

38-mm high flame at 45° for 15 seconds and the burning rate is determined by measuring the time taken to the horizontal flame to propagate between two marks separated at 200 mm, in relation to the time of burning (from the flame front reaching the first mark to the second one). The burning rate is calculated as follows.

$$B = \frac{D}{T} \cdot 60$$

Where, B is the burning rate (mm/min), D is the length the flame traveled, starting from the first line (mm) and the T is the time for the flame to travel distance D (seconds)

### **6.3 Experimental findings and discussion**

Nazarenko et al demonstrated the use of zinc acetate as a flame retardant component in epoxy amine systems.<sup>74</sup> A standard DGEBA based epoxy resin, Epon 826, crosslinked with polyether based diamine, Jeffamine D230, was used in their work. The protocol for preparing such composites materials included mixing the crystalline metal salt with epoxy and amine followed by curing at elevated temperatures. Surprisingly, the zinc acetate crystalline powder when added to epoxy resin turned into a dispersion of immiscible crystals in liquid, but when cured in oven with amine, the crystals partially dissolved yielding a composite with much lesser number of crystalline zinc acetate. However, it was not until later the importance of miscible composite was recognized.

This work was further extended to check which of the monomers of epoxy amine system was responsible for dissolution of powdered zinc salt. For this purpose, a scouting work was carried out by mixing zinc acetate in Epon 826 and Jeffamine D230 oligomers independently. It was found when zinc acetate was added to Jeffamine D230, the zinc acetate crystals started dissolving into the matrix.

### 6.3.1 Effect of different Zinc salts in Flame retardancy of Epoxy-amine networks

A two-step approach was adopted such that the prepared small molecule complex can be added as an additive to any polymeric system. Dibutyl amine (DBA) was selected as the amine part of the complex for three reasons. The first reason is that the low viscosity of DBA allowed the addition of more zinc acrylate to the mixture without adding a solvent such as acetone. The secondly we hypothesize that, since DBA has only one replicable hydrogen atom which requires two units of it per zinc acrylate, this results in a zinc acrylate complex with excellent compatibility with the organic polymer matrix. Lastly, the monomeric nature of DBA allowed to reduce the organic content in the small molecule which greatly reduces the flammability of the prepared molecule.

Several other zinc based organo salts including zinc acrylate, zinc citrate, zinc undecylenate, zinc stearate containing small molecule complex were prepared in similar proportions with dibutyl amine. This small molecule complex was further added to epoxy amine networks such that the total metal content in the composite was 2.25 wt% zinc metal.

The composites were visually examined, and the appearance is reported in Table 1. As seen, when the complex was prepared at 65 °C, except for zinc citrate and zinc stearate lead to an opaque composite while zinc acetate, zinc acrylate and zinc undecylenate formed a transparent composite. Wide angle x-ray diffraction (WAX) was used to characterize these composites for sharp diffraction peaks at specific angles that are indicative of crystal lattice spacing reported in Figure 6.6.

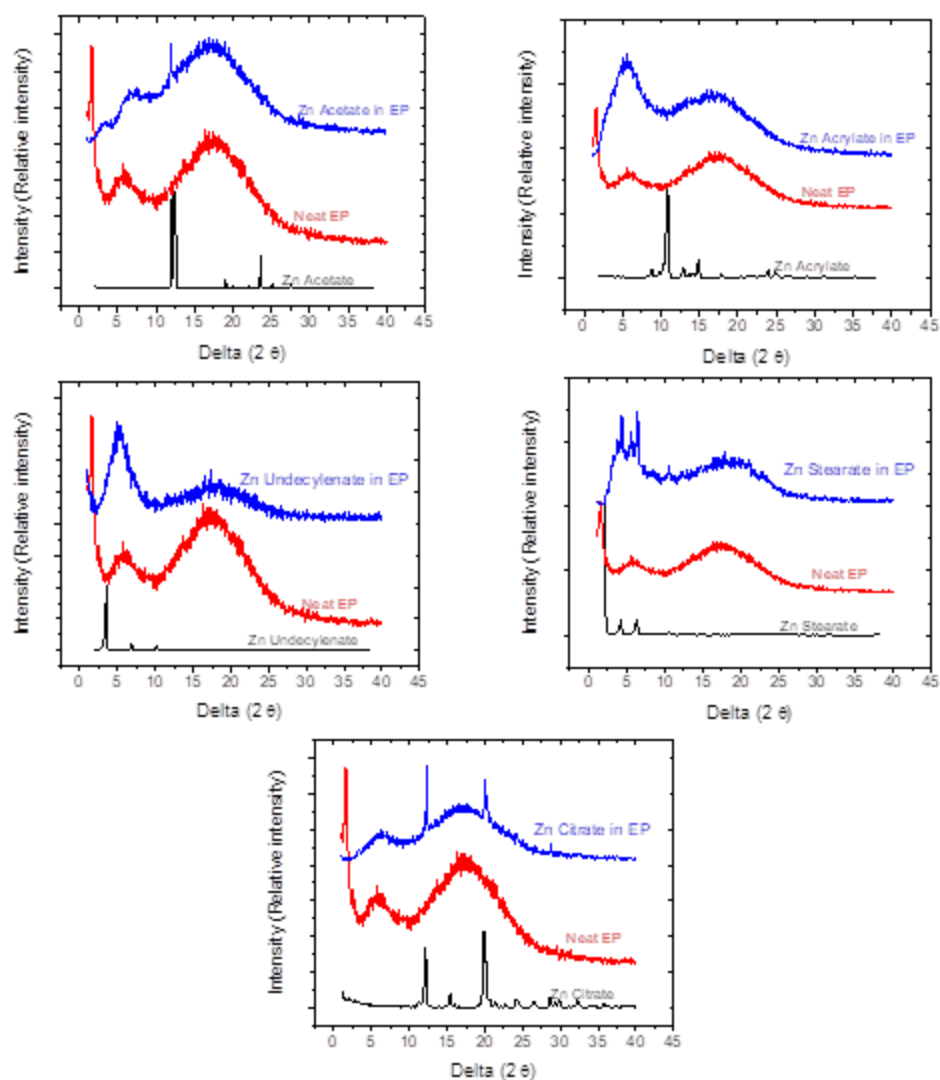


Figure 6.6 Wide angle X-ray analysis of prepared composites. Black spectrum indicates the powdered salt of zinc, red indicates the neat epoxy amine networks (without zinc) and blue indicates the composite made with metal salt in epoxy amine systems

Neat epoxy amine networks showed an amorphous halo indicating the absence of crystalline domains in the networks. Transparent composites containing small molecule additive with metal salts dissolved in the amine monomer showed a loss of crystalline diffraction peaks indicating the loss of crystal structure associated with the metal salt

within the polymer systems. However, zinc acetate showed a single diminished diffraction peak which indicated the existence of small amounts of crystalline zinc acetate in the systems. Regardless, the immiscible compounds (zinc citrate and zinc stearate) which yielded opaque or translucent composites showed a significant peak in the composites associated with the crystalline peaks of the metal salt. However, when zinc stearate prepared at elevated temperatures yielded transparent epoxy amine networks with no diffraction peaks which is explained later in this session. The WAX spectra along with the visual inspection for transparency was adopted as a means of checking the molecular level dispersion of metal in the epoxy amine networks. Dissolution of metal showed a transparent composite with amorphous halo, whereas dispersion of metal salt lead to opaque with characteristic peaks corresponding to the crystal lattice of metal salt.

The flame-retardant properties of the prepared composites were obtained via cone calorimeter and shown in Figure 6.7

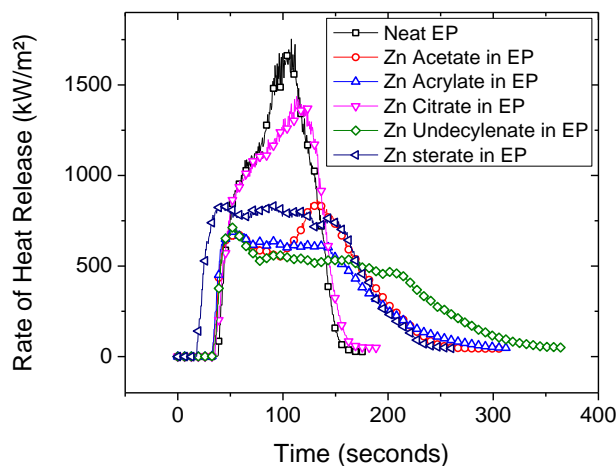


Figure 6.7 Heat release data obtained via cone calorimeter for the prepared composites. EP represents the epoxy amine networks. Small molecule additive was prepared with different metal salts prior to adding to the epoxy amine networks.

The cone calorimeter results, shown in Figure 6.7, peak heat release rate (PHRR) of the networks containing metal salts were lower as compared to the neat epoxy amine networks. Also, the composites where the metal salts are dissolved showed a significant reduction in PHRR compared to those composites where metal is just dispersed. The reduction in PHRR is attributed to the formed layer of zinc oxide char upon combustion. In case of dissolved metals, the reduction is significant due to the formation of continuous char between the unburnt polymer and the fire which acts as a barrier for the fuel to feed the combustion process. But with the metal dispersed composites, the char formed was porous and non-continuous which lets the molecules to feed the fire, but at much slower rate compared to the neat polymer systems. There was also an reduced time to ignition upon addition of small molecule metal complex. This might be due to the faster degradation tendency of the prepared small molecule which is due the presence of organic fragments as free chains.

The unburnt and burnt specimens was visually analyzed which is shown in Figure 6.8 and 6.8. As seen, the char obtained from transparent metal containing composites were continuous (non-porous), whereas the char obtained with opaque composites were non-continuous having a porous structure.

Char obtained from zinc stearate containing composites had a porous char on the top, but a dense continuous char underneath it. We hypothesize at high temperatures, wax like stearate-based compounds melts to form homogenous dispersion within the matrix before ignition. Analysis with stearate based metal compounds and different processing conditions are detailed later in this session.

Nevertheless, the neat epoxy that didn't contain any metal salt resulted in no char, and the highest heat release which indicates that all the polymeric molecules are broken into small fragments during combustion.

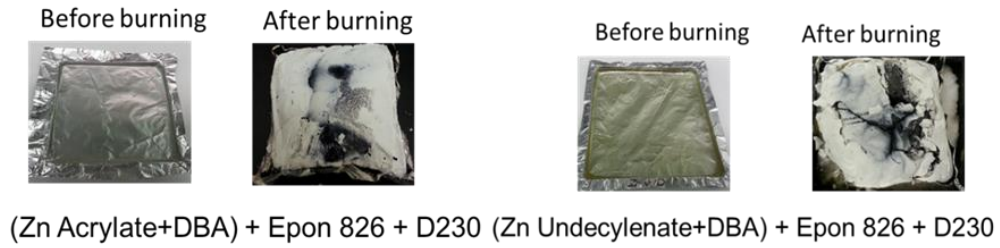
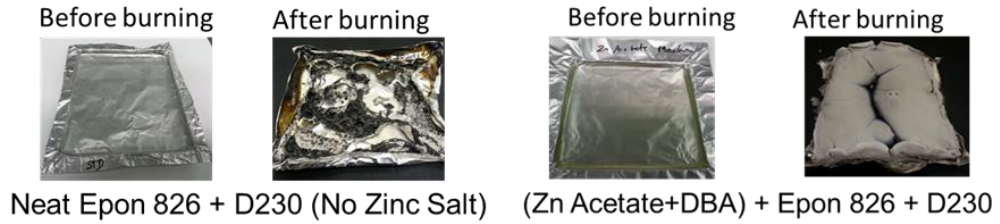


Figure 6.8 Pictures indicating the unburnt and burnt mold showing a continuous char formed for transparent composites prepared using zinc acetate, zinc acrylate, zinc undecylenate

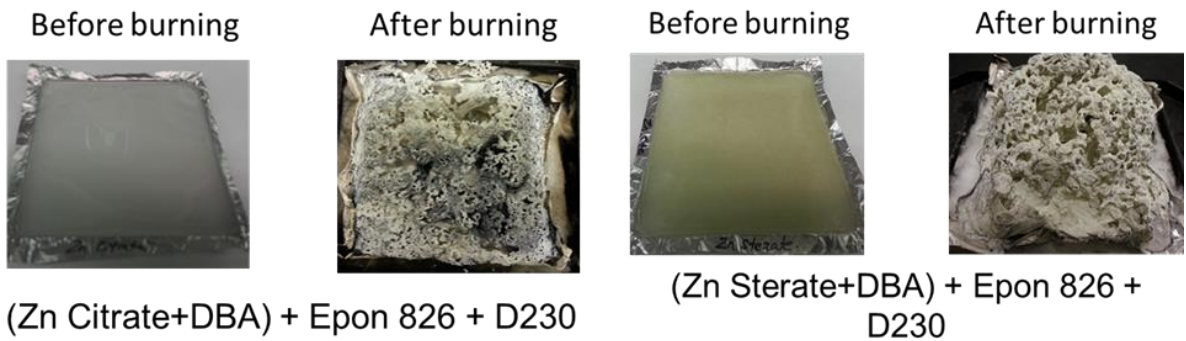


Figure 6.9 Pictures indicating the unburnt and burnt mold showing a continuous char formed for transparent composites prepared using zinc acetate, zinc acrylate, zinc undecylenate



Table 6.1 Cone calorimeter results of epoxy amine composites prepared with several small molecule additive based on zinc salts

Formulation	Neat epoxy amine (EP)	Zinc Acrylate in EP	Zinc Acetate in EP	Zinc Citrate in EP	Zinc Undecylenate in EP	Zinc Stearate in EP
Tig (s)	45.00	36.2	36.57	38.4	36.41	21.5
PHRR(KW/m <sup>2</sup> )	1754.20	703.4	866.60	1437.0	712.30	848.4
tPHRR(s)	108.00	54.0	132.50	113.0	52.00	90.0
THR (MJ/m <sup>2</sup> )	85.2	91.7	90.5	98.2	91.8	97.5
Physical state	Transparent	Transparent	Transparent	Opaque	Transparent	Opaque

The analysis was further extended to other bivalent metal including cobalt and nickel acetates by preparing a small molecule complex with dibutyl amine in a similar way described earlier. The WAX analysis of nickel and cobalt acetates along with neat epoxy amine and crystalline salts are reported in Figure 6.10.

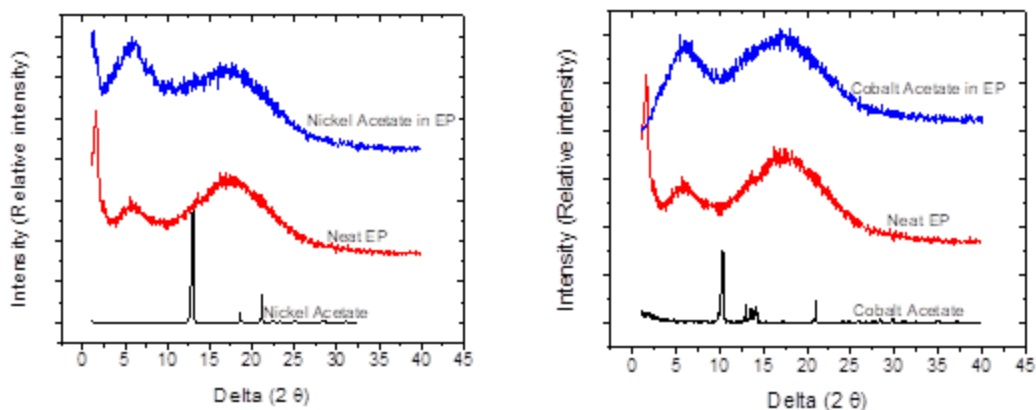


Figure 6.10 Wide angle X-ray analysis of prepared composites. Black spectrum indicates the powdered salt of zinc, red indicates the neat epoxy amine networks (without zinc) and blue indicates the composite made with metal salt in epoxy amine systems.

The WAX spectrum shows acetate salts of cobalt and nickel is dissolved in the epoxy amine matrix indicated by the absence of characteristic crystalline peaks of acetate salts (indicated in black in Figure 6.10 a and b).

### 6.3.2 Study of different metal acetates

To compare the flame retardancy between metals, ie., zinc, nickel and cobalt, the cone calorimetry results of zinc acetate is compared with cobalt acetate and nickel acetates as shown in Figure 6.11. As seen from the cone calorimeter data, the peak heat release is greatly reduced with addition of metal salts that dissolve within the matrix leading to transparent composite materials. A picture of burnt and unburnt composite of cobalt and nickel acetate is shown below. Each metal showed a characteristic color, cobalt acetate as intense magenta and nickel acetate as green. The char yield of nickel

acetate containing composite was low despite of dissolved metal, probably due to the low char forming capability of nickel metal.

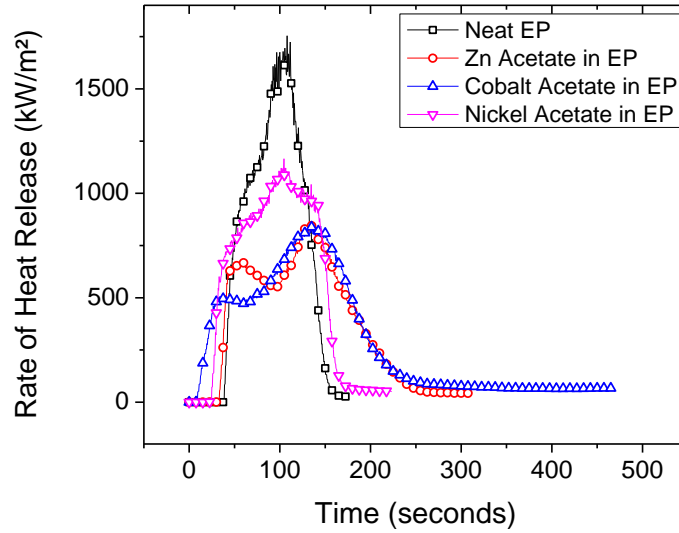


Figure 6.11 Heat release data obtained via cone calorimeter for the prepared composites.

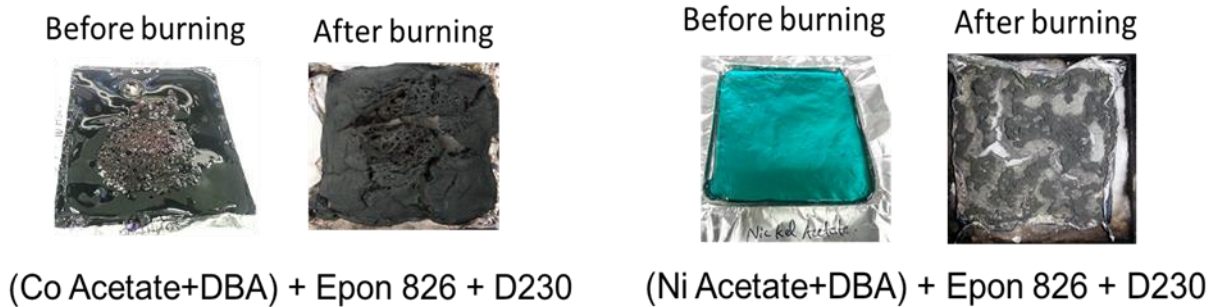


Figure 6.12 Pictures indicating the unburnt and burnt mold showing a continuous char formed for transparent composites prepared using cobalt acetate(left) and nickel acrylate (right)

Time to ignition and peak heat release rate were chosen as the justifiable parameters for comparing the flame-retardant effect of different zinc salts and with

different metals and reported in Figure 6.13. As seen, it is very evident that the composites that are transparent after metal salt addition shows better flame-retardant properties. Addition of metal complex made the composite to ignite faster as compared to the neat network systems. Among these composites, zinc acrylate and zinc undecylenate shows lower peak heat release rate. Comparatively within these two composites, the time to ignition for zinc acrylate is slightly delayed and hence hereafter in this work, zinc acrylate is chosen as the base material for further studies. But interestingly, zinc stearate also showed improvements in both time to ignition as well as peak heat release for the reasons mentioned before, and this has been investigated later in this work.

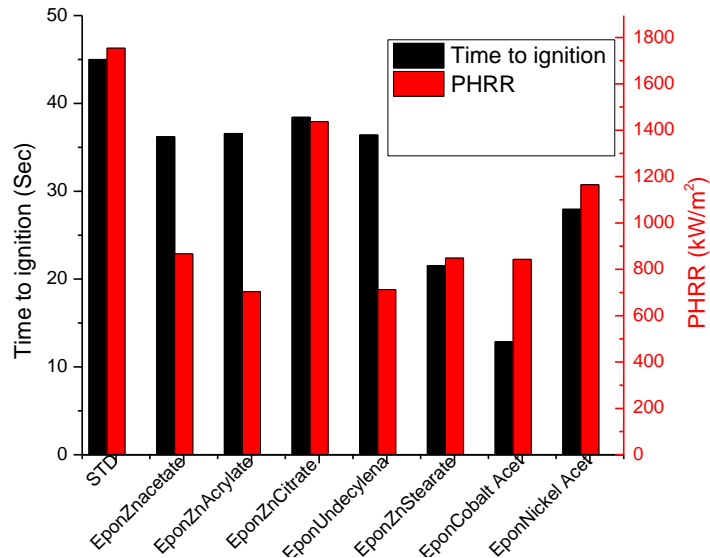


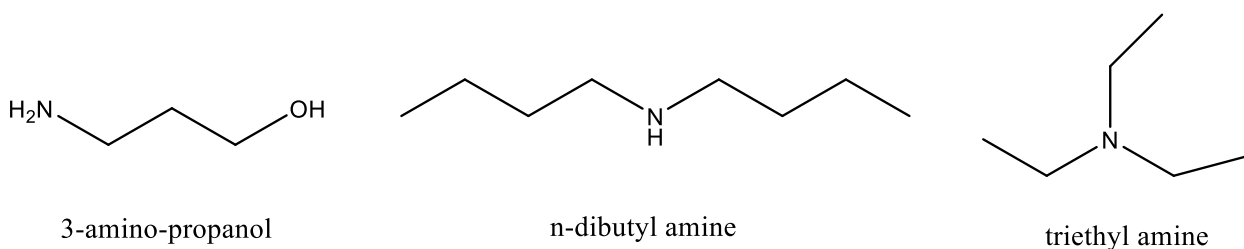
Figure 6.13 Comparison of time to ignition and peak heat release rate of the composites in this work

### 6.3.3 Analysis of small molecule additive/ $\beta$ -amino complex

In order to understand the dissolution mechanism, three types of amine-based compounds were used as dispersing agents and the small molecule additive was prepared to check its solubility.

3-amino propanol, n-dibutyl amine and triethyl amine were used as 1°, 2° and 3° amines respectively as dispersing agents. Small molecule additives were synthesized by mixing amines with zinc acrylate at 60°C under vigorous mechanical agitation.

Considering Michael addition reaction between the electron rich double bond of zinc acrylate and proton of amine, the ratio was chosen to be 1:1 stoichiometry between the difunctional zinc acrylate and the replaceable protons attached with nitrogen. For simplicity, the ratio between tertiary amine and zinc acrylate was taken to 1:1 wt%. All these small molecule additives were visually tested for miscibility.



Scheme 6.7 Chemical structures of primary (1°), secondary (2°) & tertiary (3°) amines.

The visual observation for solubility is reported through the digital pictures shown in Figure 6.14. Addition of zinc acrylate to a primary and secondary amine having hydrogen group attached to nitrogen leads to a soluble mass. When zinc acrylate is dissolved in triethyl amine (tertiary amine) with no hydrogen groups, the mixture tends to phase separate indicating the importance of the presence of hydrogen bearing nitrogen on

solubilizing the metal salt. This also confirms that the reaction occurring between the zinc acrylate and amine is Michael addition reaction.



Figure 6.14 Visual observation of solubility for checking the miscibility of 1°, 2° & 3° amines.

We intended to prepare a small molecule additive with no reactive groups, thus, our material of interest was narrowed down to dibutyl amine (a dispersing agent) and zinc acrylate as an organometallic salt which made the flame-retardant composition. The NMR spectra revealed the diminution of acrylate peaks indicating that the proton from the amine groups has been utilized to react with the acrylate component in the zinc acrylate. (Figure 6.15)

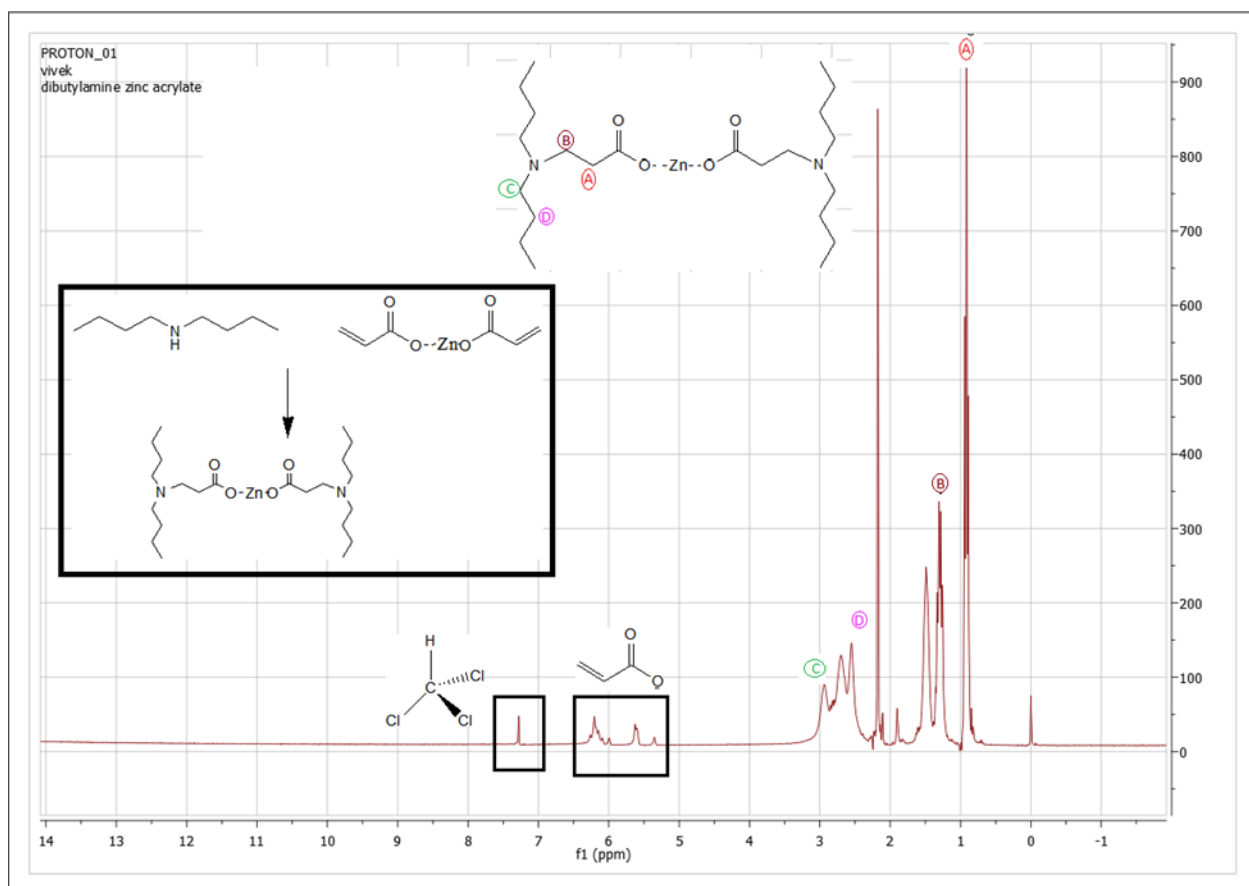


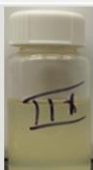


Figure 6.15 Proton NMR spectrum of the reaction product of zinc acrylate with stoichiometric quantities of dibutylamine.

The initial step was to optimize the amount of dibutyl amine required to form an additive that had dissolved metal salt in it. We intent to reduce the organic content in the additive thus maximizing the flame retardancy when these complexes are used. Hence zinc acrylate was mixed to dibutyl amine at increasing proportions ranging from 0.5:1 to 2:1 and checked for solubility of the mixture. The small molecule additive prepared at 0.5:1 stoichiometry lead to a transparent miscible solution.

Table 6.2 Solubility check of zinc acrylate with dibutyl amine at different proportions

Sl no	Mol ratio ZnAc : DBA	Zinc Acrylate %	Di butyl Amine %	Physical Appearance	
1	0.5:1	54.88	45.11		Completely Miscible
2	0.75:1	55.21	44.78		Hazy towards translucent
3	1:1	62.016	37.83		Immiscible
4	2:1	76.65	23.32		Can not mix

Additive approach was adopted such that the flame-retardant zinc-based compound can be added to any polymeric systems not limited to epoxy-amine, polyurethane, polystyrene, polyvinyl chloride and poly ethylene oxide. The choice of amine was selected such that the small molecule additive was compatible with the polymers of interest. For instance, metal-amine complex prepared using dibutyl amine showed a phase separation when mixed with water soluble polyethylene oxide, due to poor compatibility between the selected amine with the PEO. Thus, a preliminary test to for suitability in polymer system of interest was checked through determining the solubility of metal-amine complexes in various solvents and using basic concepts of solubility parameter theory, the amine monomer was selected to be miscible in particular



polymeric materials. In this test, the prepared small molecule additive was visually tested for its miscibility with various solvents. For example, small quantities of zinc acrylate-butylamino ester complex were transferred to vials and selected solvents were added to each vial in equal proportion to the complex under stirring. After a short time, the contents were inspected for dissolution of the small molecule additive in the selected solvent. The results are summarized in Table 6.3.

Table 6.3 Solubility analysis of small molecule additive prepared using zinc acrylate and dibutyl amine

Solvent	Miscible/ Immiscible
Acetone	Miscible
Water	Immiscible
Methylene Chloride	Miscible
THF	Miscible
Ethanol	Partially Soluble. but hazy
Xylene	Miscible

Hence the choice of amine (dispersing agent) can be tuned such that the complex formed is soluble in polymer's true solvent. For instance, since dibutyl amine was relatively non-polar compared to water, the small molecule additive prepared using dibutyl amine and zinc acrylate was not miscible with water as reported in Table 6.3. Hence, a water-soluble amine monomer, ethylene diamine was selected to prepared small

molecule additive in order to make compatible with water soluble polymer systems such as PEO.

Hence, a two step approach was followed in order to homogeneously incorporate the metal salt in the polymer systems. In the first step, small molecule additive (zinc acrylate-amine complex or  $\beta$ -amino complexes of zinc salts) was prepared separately by mixing a suitable amine compound with zinc acrylate along with excess solvent which was removed later through rotatory evaporator. The synthesized small molecule additive was added to the required polymer matrix. Several polymeric systems including, epoxy-amine, polyurethane, poly styrene, and polyethylene oxide were chosen, as a proof of concept, such that this new halogen free, phosphate free, soluble metal based compound can be used effectively as flame retardant.

### **6.3.4 Effect of small molecule additive on various polymer systems**

#### **6.3.4.1 Flame retardant for Epoxy-amine networks**

Zinc acrylate was added to the epoxy amine systems made with Epon 826 crosslinked with Jeffamine D230, in additive forms using the two step process as mentioned before. In the first step, a small molecule additive was prepared by dissolving zinc acrylate in dibutyl amine at 0.5:1 stoichiometric quantities. In the second step, the prepared small molecule additive was added to the epoxy amine networks such that the zinc metal content was 2.25 wt%

The neat epoxy-amine networks was transparent and upon the addition of commercial flame retardants such as zinc oxide or zinc borate, the epoxy resins became opaque, indicating that these oxides were insoluble in the polymer. (Figure 10). When incorporated at a concentration of 2.25 weight percent zinc, samples containing zinc

oxide or zinc borate (Firebrand® ZB Fine supplied by Borax(20 mule team)) showed a small reduction in the peak heat release rate upon burning in the cone calorimeter (Figure 6.16). The dibutyl amino complex with zinc acrylate, which is miscible in the epoxy amine resin, significantly improves the reduction in peak heat release rate.

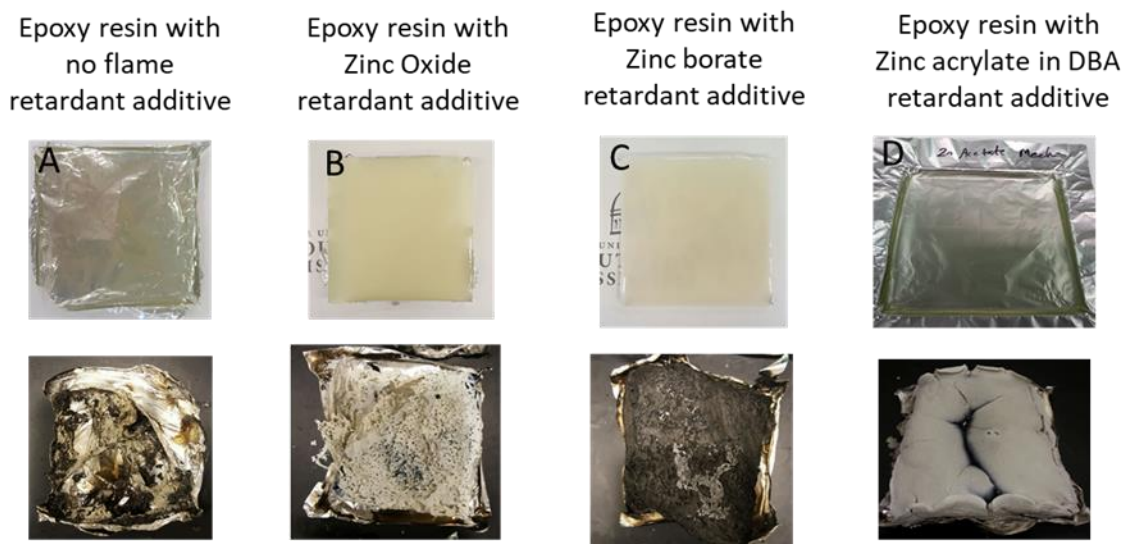


Figure 6.16 Photographs of samples of (a) epoxy resin, (b) Epoxy resin with zinc oxide, (c) epoxy resin with zinc borate and (d) zinc acrylate in DBA as additive in epoxy resin before and after burning in the cone calorimeter. Samples are shown above, and the corresponding char is shown beneath each sample.

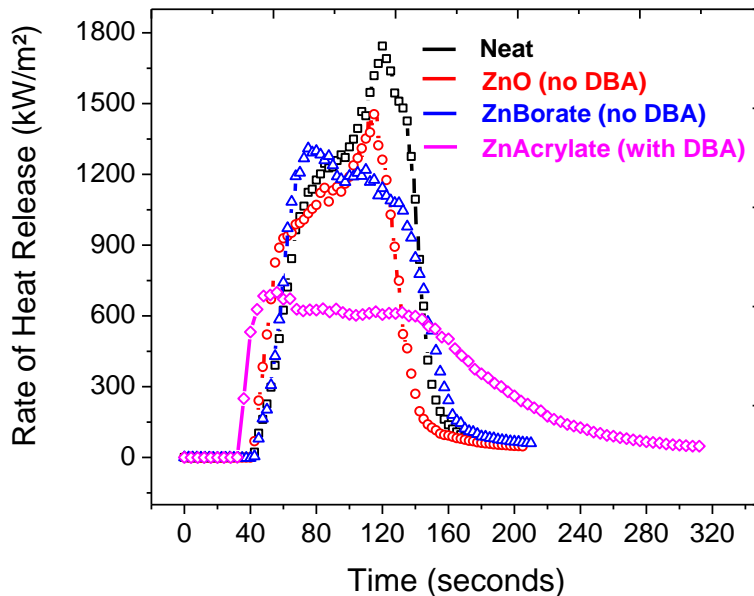


Figure 6.17 Heat release rate of prepared epoxy resins with different additives, zinc oxide, zinc borate and synthesized zinc acrylate in DBA.

The heat release rate of composites prepared using epoxy amine networks with added additives are reported in Figure 6.17. All the composites were prepared such that the zinc metal content was maintained to be 2.25 wt%. Unlike the commercial flame-retardants, zinc oxide and zinc borate, the reduction in HRR was significantly higher when the synthesized zinc acrylate ester complex was added to the network. This indicates a new generation metal based flame-retardant compounds prepared using zinc acrylate and an amine based dispersing agent is more effective than the commercial flame retardant additives.

#### 6.3.4.2 Flame retardant for polyurethane networks:

The  $\beta$ -amino complexes of zinc salts were prepared as described in a similar way described in small molecule additive preparation detailed in epoxy-amine systems.

Polyurethanes were synthesized by reacting the selected polyol with the selected isocyanate in the presence of dibutyl tin dilaurate as catalyst. The synthesized  $\beta$ -amino complexes of zinc salts were dissolved in xylene to achieve a mixture of about 10 wt% of solvent, and this mixture was then combined with the poly-isocyanate prepolymer. This mixture was then added slowly to stoichiometric quantities of polyol and degassed prior to casting in a desired mold to cure at 85°C for 12 hours. The samples were aged for at least 24 hours prior to test. The polyurethane sample that contained zinc acrylate only was opaque. The sample containing the dibutyl amine/zinc acrylate complex was transparent.

The composites were evaluated for fire-retardant performance in cone calorimeter. To compare the effect of dispersion and dissolution of zinc metal on flame retardancy, comparative example compositions were made using only zinc acrylate mixed with polyol-isocyanate complex and subsequently compared, by cone calorimetry, with compositions made using the zinc acrylate dibutylamine complex.

Cone calorimetry results for the polyurethane compositions with and without amine dispersing agent are shown in Figure 6.18 and Table 6.4. A dispersion of metal salt resulted when only zinc acrylate salt was added to polyurethane, whereas, the synthesized amine based complex led to dissolution of metal. The dispersed metal salt in polyurethane composition resulted in reduction of the peak heat release rate whereas addition of the zinc acrylate-dibutylamine complex resulted in a significantly more pronounced reduction of the peak heat release rate. These results demonstrate that dissolution of the metal component in polymer network substantially improves the fire-retardant performance over particulate dispersion of the metal component. As mentioned

earlier, the dissolved metal salts form a continuous layer of oxide layer of char which acts in two ways. One, it acts as an insulating layer reducing the heat transfer to the unburnt polymer surface and barrier layer trapping the volatiles from feeding the fire. In case of dispersed metal containing composites, porous non-continuous char is formed which can not trap the volatiles making it more flammable as compared to dissolved metals.

It is to be noted that the total heat release is not reduced, but it is increased because of the added extra organic molecule as an additive form. But by adding the additive, the sudden burst of energy is avoided which is seen the nature of the cone calorimeter curve. The addition of small molecule additive slows down the combustion process and hence we see a lengthier time of combustion in cone calorimeter.

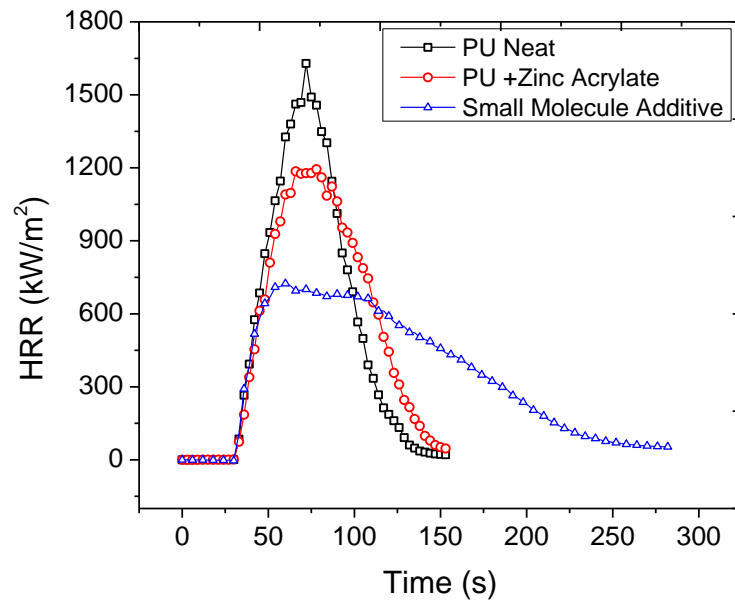


Figure 6.18 Cone calorimeter results of polyurethane systems. “PU+ Zinc acrylate” indicates the PU composites with metal dispersed and “small molecule additive in PU” indicates the dissolution of metal. Both composites correspond to an effective metal content to 2.25 wt% zinc.

Table 6.4 Cone calorimeter results comparing with and without dibutyl amine as dispersing agent for metal salt in polyurethane systems

<b>Formulation</b>	<b>Control (Polyurethane - 0% Zn metal)</b>	<b>(Polyurethane- 2.25% Zn metal as Acrylate) dispersion of metal</b>	<b>(Polyurethane - 2.5% Zn metal as B-amino complex of Zinc Acrylate)</b>
Tig (s)	32	30.5	31.5
PHRR (KW/m <sup>2</sup> )	1628.84	1237.33	726.909
tPHRR (s)	72	68	61
THR ( MJ/m <sup>2</sup> )	78	86.5	96.0
Physical state	Transparent	Opaque	Transparent

#### 6.3.4.3 Flame retardant for polystyrene polymers:

Polystyrene was cast via a solution casting method. The neat polymer was dissolved in methylene chloride under stirring. The zinc acrylate-dibutylamine complex, prepared as described earlier in epoxy amine session which was then diluted with methylene chloride and subsequently added to a solution of polystyrene under stirring. The mixture was then casted in a mold which was further evaluated for its flammability test. The composition was held in an oven for 24 hours at 65°C to evaporate the solvent and form a solid sample cast. The polystyrene cast containing only zinc acrylate was opaque which indicated the metal salt was dispersed in polystyrene. The polystyrene cast containing the butylamine/zinc acrylate complex was transparent indicating that the metal was dissolved in polystyrene. Polystyrene casts containing 2.25 weight percent zinc as zinc acrylate, with and without a stoichiometric amount of dibutylamine were prepared and tested by cone calorimetry. As seen from the cone calorimeter (Figure 6.19), the

reduction in peak heat release rate associated with the opaque polystyrene composites (without butyl amine) was less as compared to the transparent metal containing polystyrene composites. This is again due to the continuous char obtained from the composites where the metal is in dissolved state.

Table 6.5 Cone calorimeter results comparing with and without dibutyl amine as dispersing agent for metal salt in polystyrene systems

<b>Formulation</b>	<b>Polystyrene 0% Zn</b>	<b>Polystyrene- 2.25% Zn as zinc acrylate)</b>	<b>Polystyrene 2.5% Zn as <math>\beta</math>-amino complex of zinc acrylate)</b>
Tig (s)	38.5	35	29.5
PHRR (KW/m <sup>2</sup> )	1406.26	1148.42	819.74
tPHRR (s)	114.5	90	111.5
THR ( MJ/m <sup>2</sup> )	91	97.6	95.5
Physical State	Transparent	Opaque	Transparent



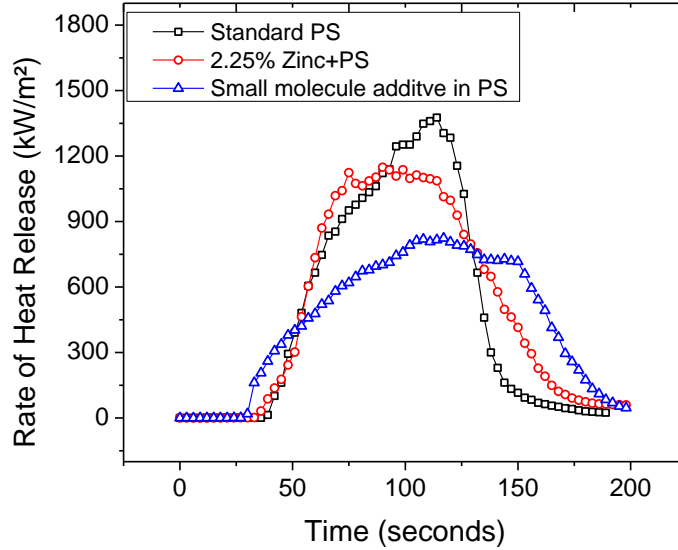


Figure 6.19 Cone calorimeter results of polystyrene (PS) systems. “PS+ Zinc acrylate” indicates the PU composites with metal dispersed and “small molecule additive in PS” indicates the dissolution of metal. Both composites correspond to an effective metal content to 2.25 wt% zinc

As seen in the heat release curves, the composites with dissolved metal had a delayed peak heat release due to its char forming capability. The observed char after the combustion indicated the continuous char formation for the composites with zinc dissolved. The dispersed zinc containing composites due to its porous char, the peak heat release rate was achieved at early stages of combustion.

#### 6.3.4.4 Flame retardant polyethylene oxide composites:

Polyethylene oxide was chosen to check if the method of adding metal based small molecule additive would improve the flame retardancy of such water-soluble polymers. Since dibutyl amine was insoluble in water, which would lead to phase

separation when added to a water soluble polymer, ethylene diamine (a water soluble amine) was chosen a dispersing agent. A similar method described in epoxy systems for the preparation of small molecule additive was followed, except for the use of ethylene diamine in stoichiometric amounts

Polyethylene Oxide compositions with Zinc Acrylate Amine complex was prepared as follows. Polyethylene Oxide was dissolved in water and under stirring at 60°C. The prepared zinc acrylate-amine complex was then mixed into the PEO solution until dissolved, and the composition was cast in a mold.

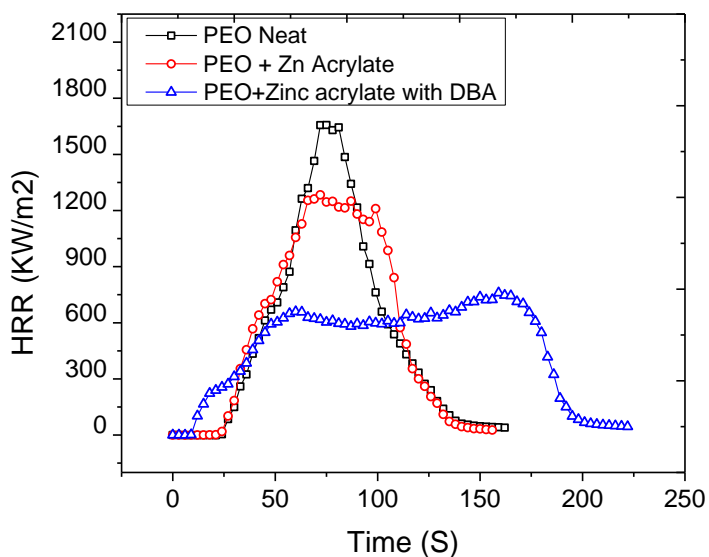


Figure 6.20 Cone calorimeter results of polyethylene oxide (PEO) systems. “PEO+ Zinc acrylate” indicates the PEO composites with metal dispersed and “small molecule additive in PEO” indicates the dissolution of metal. Both composites correspond to an effective metal content to 2.25 wt% zinc

The flame retardancy of polyethylene oxide casts containing 2.25 weight percent zinc as zinc acrylate, with and without a stoichiometric amount of ethylene diamine were

prepared and tested by cone calorimetry. Results are shown in Figure 6.20 and Table 6.6. As expected, the zinc acrylate added through soluble small molecule additive the peak heat release rate substantially more than the zinc acrylate alone. The char was observed which revealed that the soluble zinc metal lead to a continuous char, whereas the dispersion of zinc metal lead to non-continuous char. This also reveals that aqueous solutions of polyethylene oxide with a soluble zinc complex will retain fire retardancy after the solvent, water, has been depleted or removed by, for example, evaporation. More generally, this result demonstrates that aqueous solutions of polymers containing dissolved metal moieties can retain significant fire-retardant properties after the water has evaporated.

Table 6.6 Cone calorimeter results comparing with and without dibutyl amine as dispersing agent for metal salt in polyethylene oxide systems

<b>Formulation</b>	<b>Poly(ethylene oxide) 0% Zn</b>	<b>(Polyethylene oxide) - 2.25% Zn as zinc acrylate</b>	<b>(Polyethylene oxide) - 2.25% Zn as <u><math>\beta</math>-amino complex of zinc acrylate</u></b>
Tig (s)	23.9	21.76	15.5
PHRR (KW/m <sup>2</sup> )	1749.8	1136.71	759.6
tPHRR (s)	77	99.5	159
THR ( MJ/m <sup>2</sup> )	86	98.5	102.8
Physical State	Transparent	Opaque	Transparent

In summary, from the results obtained it is evident that the new metal based flame-retardant is much effective when it is present in the dissolved form rather than a dispersion in the polymer matrix. From the above studies, the flame retardancy is greatly

improved with dissolving the metal in a range of polymers including networks polymers (epoxy and polyurethane), thermoplastic polymers (polystyrene) and water soluble polymers (polyethylene oxide). Thus, this approach can be considered as next generation flame retardant due to its advantages over halogenated and phosphorous flame retardants, due to its eco-friendly and versatile applicability.

### 6.3.5 Effect of increasing content of small molecule additive

As an extension epoxy amine networks were chosen to evaluate the effect of incremental quantities of the prepared small molecule additive. We intent to check the flame-retardant effect at varying loading levels of zinc metal. These composites were evaluated for thermal, mechanical and flame retardant properties. The proportions of the complex were increased such that the effective zinc metal content in the network varied from 0.10 wt% to 18 wt%.

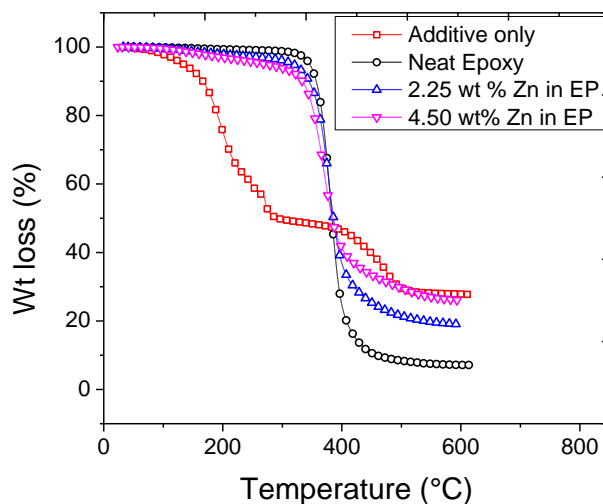


Figure 6.21 TGA analysis of epoxy amine networks with increasing small molecule additive concentrations.

Thermogravimetric analysis (TGA) in nitrogen atmosphere of synthesized small molecule additive along with prepared composites are reported in Figure 6.21. As seen the pure small molecule additive shows an early onset degradation temperature with two step degradation process. Since this small molecule additive contains organic tails with dissolved metal, we hypothesize that, the early degradation is caused by the organic fragments in the first step. The dissolved metal forms char which then breaks further under high temperature in the second degradation step. The prepared composites follow a single degradation step similar to neat epoxy amine networks. With increasing small molecule additive content, the onset degradation temperature decreased with increase in char yield at 600°C. It is evident that with the increase in metal content in the networks improved the char formation capability with a small reduction in onset temperature. We hypothesize that the early degradation temperature associated with the small molecule additive is responsible for effective conversion of organic molecules into char which further protects the polymer underneath. Table 7 indicates the TGA a decrease in onset temperature with an increase in char yield upon addition of small molecule additive to epoxy amine networks.

Table 6.7 TGA data for epoxy amine composites with increasing  $\beta$ -amino complexes content

Material	$T_{\text{onset}}(^{\circ}\text{C})$	$T_{10\%} (^{\circ}\text{C})$	$T_{50\%} (^{\circ}\text{C})$	Char	
				Yield(wt%)	$DT_{\text{max}}(^{\circ}\text{C})$
Small molécule additive	157.6	168.6	289.5	28.1	195, 270 & 475
Neat epoxy amine (EP)	361.7	357.8	383.6	6.6	381.7
2.25 wt% Zn in EP	350.9	346.3	385.5	18.8	377.4
4.50 wt% Zn in EP	340.0	335.2	384.7	25.1	369.5

$T_{\text{onset}}$  – Onset temperature;  $T_{10\%}$  - Temperature at 10% degradation;  $T_{50\%}$  - Temperature at 50% degradation;  $DT_{\text{max}}$  – Maxima of mass loss rate

Surprisingly, addition of small molecule additive to an epoxy amine networks induced plasticization to the network. Differential scanning calorimeter (DSC) analysis revealed that addition of small molecule additive decreased the glass transition temperature with increasing content and reported in Figure 6.22 and listed in Table 6.8. The clear transition also indicates the absence of phase separation within the networks even after addition of small molecule additive.

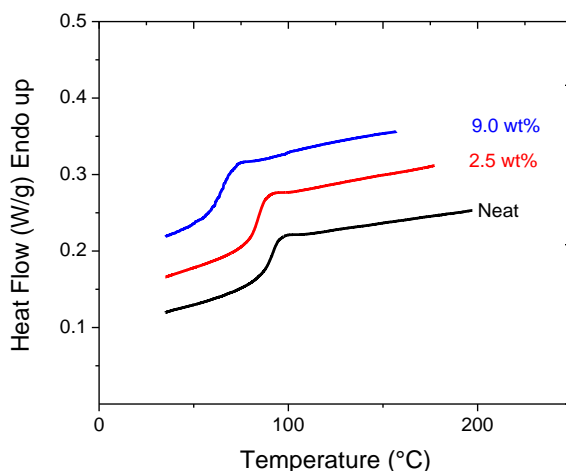


Figure 6.22 DSC thermograms of composites prepared using  $\beta$ -amino complexes in comparison with the neat epoxy amine networks. Thermograms are vertically offset for clarity

Table 6.8 Effect of  $\beta$ -amino complexes of zinc acrylate on the glass transition temperature of epoxy-amine resin as determined by differential scanning calorimetry

Zinc metal content of Epoxy Resin	T <sub>g</sub>
0	91°C
2.5 wt%	83°C
9 wt%	66°C

Addition of small molecule additive to the neat systems affects the long chain molecular motion which reflects through the T<sub>g</sub> of these composites. This needs further insight to understand the exact mechanism.

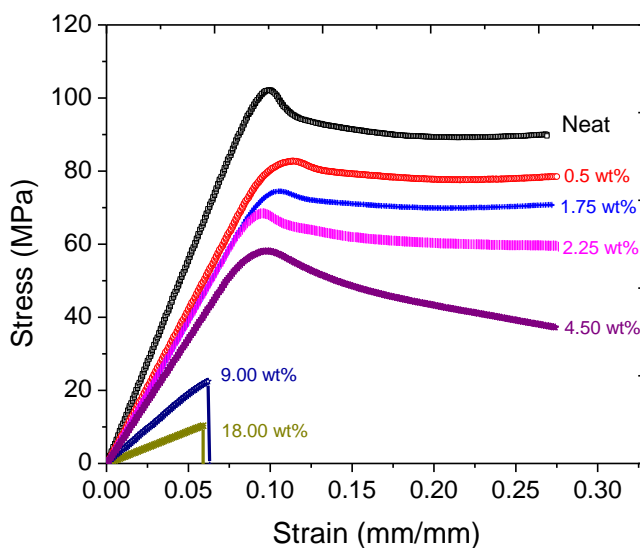


Figure 6.23 Tensile test (compression mode) of the prepared composites with increasing small molecule additive content

Plasticization of the epoxy resin was demonstrated by compressive tensile tests in which polymer cylinders were subjected to compression along the axis of the cylinder. The miscible  $\beta$ -amino complexes of zinc esters conferred a decrease in initial Young's Compressive Modulus followed by a distinct yield stress and plastic flow. (Figure 6.23 and Table 6.9) The value of the yield point decreased with increase in miscible zinc content. Polymers with miscible zinc contents of 9.1 weight percent and higher displayed brittle fracture when compressed. This phenomenon of fracture at higher loadings is still under investigation.

Table 6.9 Effect of  $\beta$ -amino complexes of zinc acrylate on the Young's Modulus and yield stress of epoxy resin as determined by compressive testing

Sample	Initial Modulus (Mpa)	Yield Stress (MPA)
Neat	1125	102
0.5 wt%	849	82
1.75 wt%	792	74
2.25 wt%	784	68
4.5 wt%	684	58
9.1 wt%	Shattered	-
18 wt%	Shattered	-



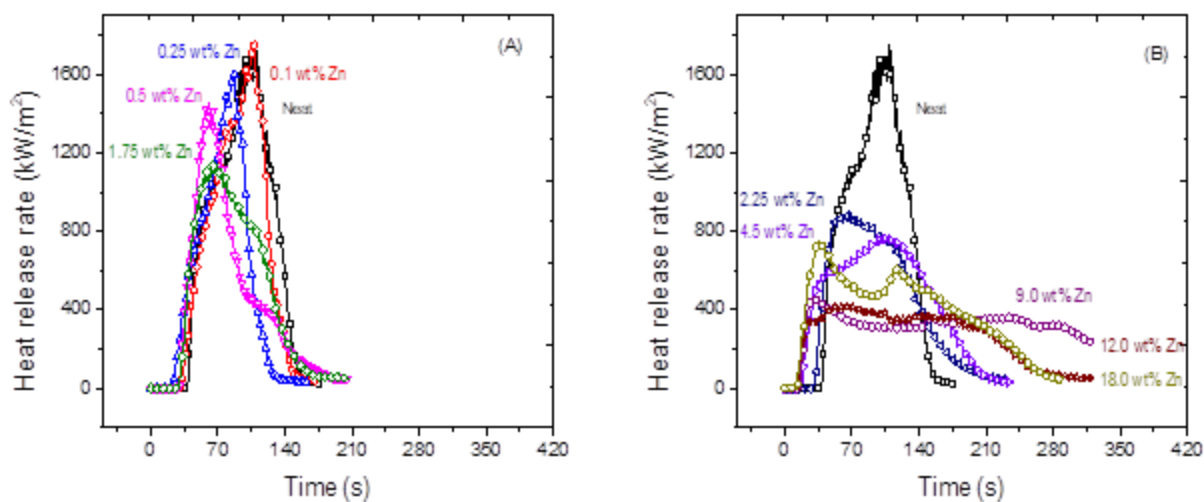


Figure 6.24 Heat release curves obtained via cone calorimeter for networks containing small molecule additive ranging from 0.1 wt% to 18 wt%. Both a and b curves represent the same serious burnt at similar conditions and separated for clarity.

Cone calorimetry results of Epoxy resin samples containing  $\beta$ -amino complexes of zinc acrylate ranging in concentration from 0.1 weight percent zinc to 18 percent zinc are presented in Figures 6.24 a and b. The addition of small molecule at 0.25 wt% zinc level showed a slight decrease in peak heat release rate (PHRR) of about only 2 %. But when the zinc content was increased to 2.25 wt%, a reduction of 45 % in PHRR was achieved. The maximum reduction in PHRR was achieved with 9 wt% (of about 71 %) beyond which addition of small molecule had a detrimental effect. This is because of the added organic content which feeds the fire. Thus the threshold limit for achieving efficient flame retardancy using this approach was found to be 9 at % of zinc metal.

Representative cone calorimeter data of selected composites is listed in Table 6.10. As seen, addition of metal based small molecule additive decreases the PHRR along with increasing the char yield up to 9 wt% of zinc metal. But at 18 wt% of zinc, there is

an increase in PHRR. It is important to note that addition of small molecule additive cause the composites to ignite early in the combustion process indicated by the decrease in time to ignition. Time to ignition also needs to be improved to be used as flame retardants in real world applications.

Table 6.10 Effect of concentration of  $\beta$ -amino complexes of zinc acrylate on fire retardancy of epoxy-amine compositions .

Formulation	Neat Epoxy - 0% Zn metal)	Epoxy -with 2.25% Zn metal)	Epoxy – with 4.5% Zn metal)	Epoxy with-9% Zn metal)	Epoxy with- 18% Zn metal)
Tig	29	32	20	18	11
PHRR	1629	896	778	468	752
tPHRR	72	68	108	31	36
THR (MJ/ m <sup>2</sup> )	79	91	98	112	109
Physical State	Transparent	Transparent	Transparent	Transparent	Transparent

The obtained char was analyzed through wide angle X-ray diffraction and reported in Figure 6.25. The peaks obtained through WAX corresponded to a standard Zinc oxide crystal lattice, which indicates that the dissolved metal in the matrix turns to zinc oxide while combustion.

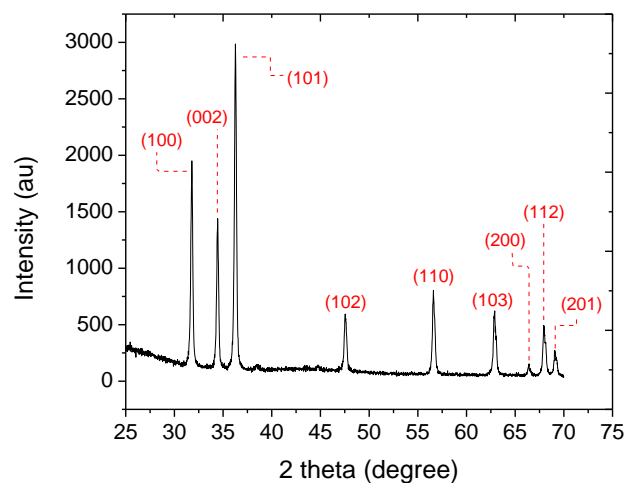


Figure 6.25 Wide angle x-ray analysis of obtained char from cone calorimeter. Crystal lattice represents the obtained char is zinc oxide

The American National Standards Institute; Underwriters' Laboratories. *Standard for Tests for Flammability of Plastic Materials for Parts in Devices and Appliances*, UL94-HB, describes a method to test the rate at which a standard horizontally oriented bar of material burns when it is ignited from one end. The standard flammability of epoxy-amine resins containing no zinc salts were compared with epoxy-amine resins containing miscible zinc acrylate-dibutylamine complex by testing according to ASTM method UL 94 HB. All samples passed the UL 94 HB test. The rate of burning was decreased for samples of epoxy-amine resin with the addition of miscible zinc acrylate-dibutylamine complex. Importantly, the samples containing the zinc acrylate complex did not drip during burning whereas the sample with no added zinc complex produced flaming drips as it burned. The results of the UL-94-HB test are shown in Table 6.11.

Table 6.11 ASTM method UL-94 HB testing of  $\beta$ -amino complexes of zinc acrylate on the standard flammability of epoxy-amine resin.

Sample Name	Time to reach Point	Time to reach Point	Linear Burning rate
	A (S)	B (S)	(mm/minute)
Control	40	281	21.4
0 wt % Zn			
2.5 wt% Zn	62	358	16.8
4.5 wt% Zn	69	494	12.1
6 wt% Zn	71	424	14.2
9.5 wt% Zn	70	379	15.8
18 wt % Zn	60	368	16.3

### 6.3.6 Effect of processing conditions of zinc stearate on FR properties

As mentioned earlier, epoxy resin containing  $\beta$ -amino complexes of zinc stearate yielded a char that was discontinuous on top with a continuous char beneath (Figures 6.8). Since stearic acid is essentially a long chain fatty acid, we hypothesized that heating to a temperature above the melting point would help dissolve these compounds in a homogeneous mixture. The melting point of zinc stearate powder was 90°C where the powder melts to a transparent solution when maintained at elevated temperatures. When cooled down, it started recrystallizing leading to its crystalline form. Thus small molecule additive with and without amine dispersing agent (dibutyl amine) was prepared at elevated temperature (at 90°C) and subsequently cured immediately without letting the molded composite below the melting point of crystalline zinc stearate salt.

Both the composites which were prepared with and without dibutyl amine appeared transparent. A post treatment method was also adopted where the opaque composite was prepared (protocol followed earlier) which was post cured at much higher temperature of 120°C. The post cure composites formed a granular type morphology which was due to the partially melted zinc stearate molecules due to such high temperature. The prepared composites via different protocol was exposed to cone calorimeter to evaluate the flame retardant properties. (Figure 6.26 and listed in Table 6.12)

Table 6.12 Effects of formulation temperature conditions on epoxy-amine compositions with zinc stearate.

<b>Sample identity</b>	<b>Epon+d230 (neat) (A)</b>	<b>Epon+d230+(DBA+ Zn stearate) 70°C prep cured @ 90°C (B)</b>	<b>Epon+d230+(DBA+ Zn stearate) + 70°C prep cured @ 90°C post treatment @ 120°C (C)</b>	<b>Epon+d230+(DBA+ Zn stearate) + 90°prep cured @ 90°C (D)</b>	<b>Epon+d230 Zn stearate alone 90°prep cured @ 90°C (E)</b>
<b>Tig (s)</b>	45.00	13.5	17	18	24.5
<b>PHRR(KW/m<sup>2</sup>)</b>	1754.20	797.14	805.7	815.7	728.8
<b>tPHRR(s)</b>	108.00	57.0	85	96	74.5
<b>THR (MJ/m<sup>2</sup>)</b>	85.2	96.6	97.1	92.1	88.25
<b>Physical state</b>	Transparent	Opaque	Small crystalline granules	Transparent	Transparent

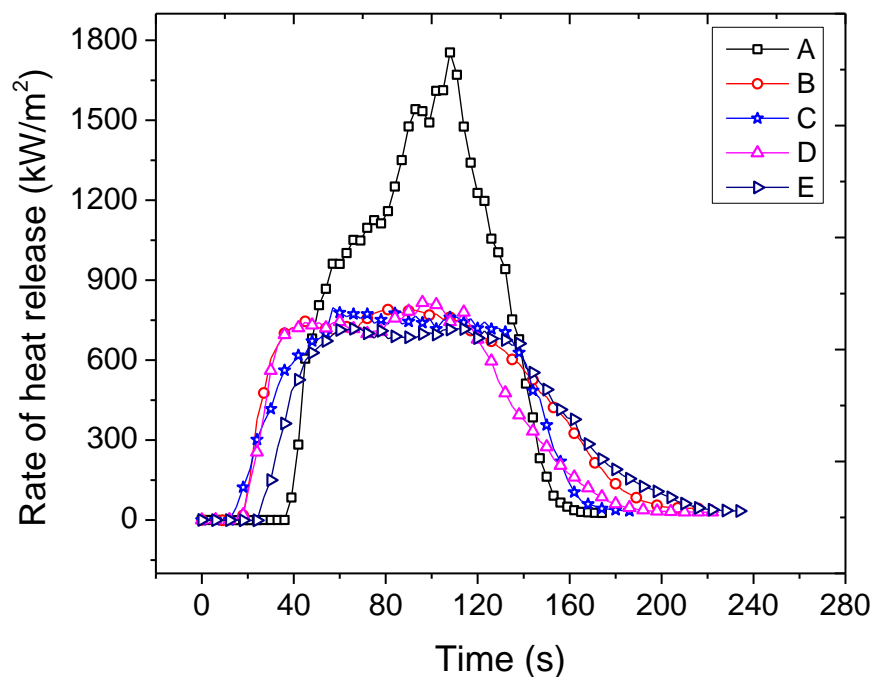


Figure 6.26 Heat release curves of composites prepared using zinc stearate prepared via different protocol. Labels A through E indicates different protocol listed in Table

The visual observation of the char obtained via cone calorimeter revealed that irrespective of the appearance of these composites, there existed a continuous char underneath a porous layer of char on the surface (Figure 6.27). The cone calorimeter results revealed that the heat release rate was significantly reduced with composites prepared irrespective of the prototype followed. This indicated that when the zinc stearate composites, exposed to high temperature above the melting point of zinc stearate salt, in cone during evaluation of flame retardancy test, turned into a soluble component. However, this needs to be further investigated.

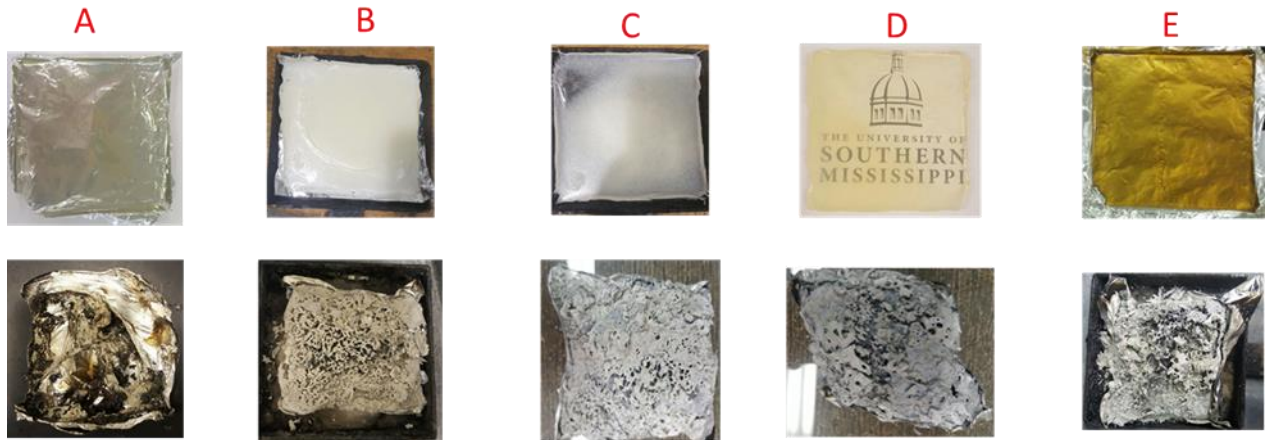


Figure 6.27 Burnt ( on top) and unburnt (bottom) of compositors containing zinc stearate prepared via different protocol. Transparent composites yielded a continuous char underneath a porous top surface

### 6.3.7 Effect of different stearate salts on FR properties

In a different study to compare the char forming capability of different metals, stearate salts of zinc was compared to sodium stearate, magnesium stearate, nickel stearate and stearic acid. Composites were prepared by mixing stearate salts at elevated temperatures ( 90°C) which was subsequently casted and crosslinked at 90°C.

With the above said protocol, magnesium stearate and zinc stearate formed a transparent while other compounds, stearic acid, sodium stearate formed opaque and nickel stearate turned to greenish translucent composites. The results obtained in cone calorimeter along with the physical appearance is listed in Table 6.13. The cone calorimeter results are shown in Figure 6.28.

Table 6.13 Flame resistance of stearate-based salts of zinc, nickel and magnesium determined via cone calorimeter

<b>Cone Calorimeter Measurement</b>	<b>Neat Epoxy Resin</b>	<b>Epoxy resin + Stearic Acid</b>	<b>Epoxy resin + Sodium Stearate</b>	<b>Epoxy resin + Magnesium Stearate</b>	<b>Epoxy resin + Nickel Stearate</b>	<b>Epoxy resin + Zinc stearate</b>
Time to ignition (secs)	42	24	24	21	22	25
Peak Heat Release Rate (Kw/sq.m)	1744	2016	1383	767	1081	729
time to Peak heat release (sec)	120	60	64	44	52	75
Total Heat Release (MJ/sq. m)	85.2	93.9	92	88	92	88
Appearance	Transparent	Opaque, waxy	Opaque with bubbles	Transparent	Greenish, translucent	Transparent

The cone calorimeter results indicated that the addition of metal salt resulted in reduction of PHRR compared to the neat systems. When stearic acid was added to the network, the PHRR was higher than the neat networks which is in agreement that with



added organic content in the system makes it more flammable. Also, stearic acid containing systems showed a sudden burst of energy due to the absence of char forming moieties in the compositions (shown in Figure 6.28). Different salts resulted in varying amounts of char yield at the end of the cone test. Magnesium and Zinc based stearate salts lead a dense continuous char while the sodium and nickel resulted in a non-continuous char. This study indicated that, even though nickel based stearate salt was partially soluble, the metal has to have char forming capability to achieve desired flame retardant properties. Thus magnesium and zinc based salts are suitable candidates to be used as flame retardant metal based compounds.

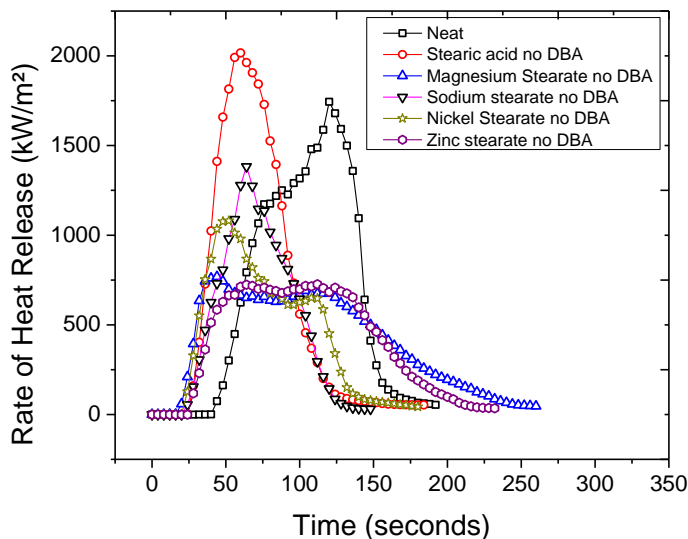


Figure 6.28 Heat release rates of stearate based salts examined with epoxy amine systems. Zinc and magnesium stearates resulted in lowest PHRR, whereas stearic acid increased the flammability.



Figure 6.29 Unburnt (top) and burnt (bottom) pictures of epoxy-amine composites of different stearate salts.

The wide-angle x-ray spectrum (WAX) of composites prepared with zinc, magnesium and nickel stearate is reported in Figure 6.30. The miscibility of metal salt in the networks can be determined via WAX spectrum. As expected, the zinc and magnesium based transparent composites didn't show any peaks characteristic to the metal salt, whereas nickel stearate composites showed the peaks associated with the crystal lattice in the composite materials. In addition to visual observations, WAX can be used as a tool to determine the miscibility of metal salt in the polymer matrix.

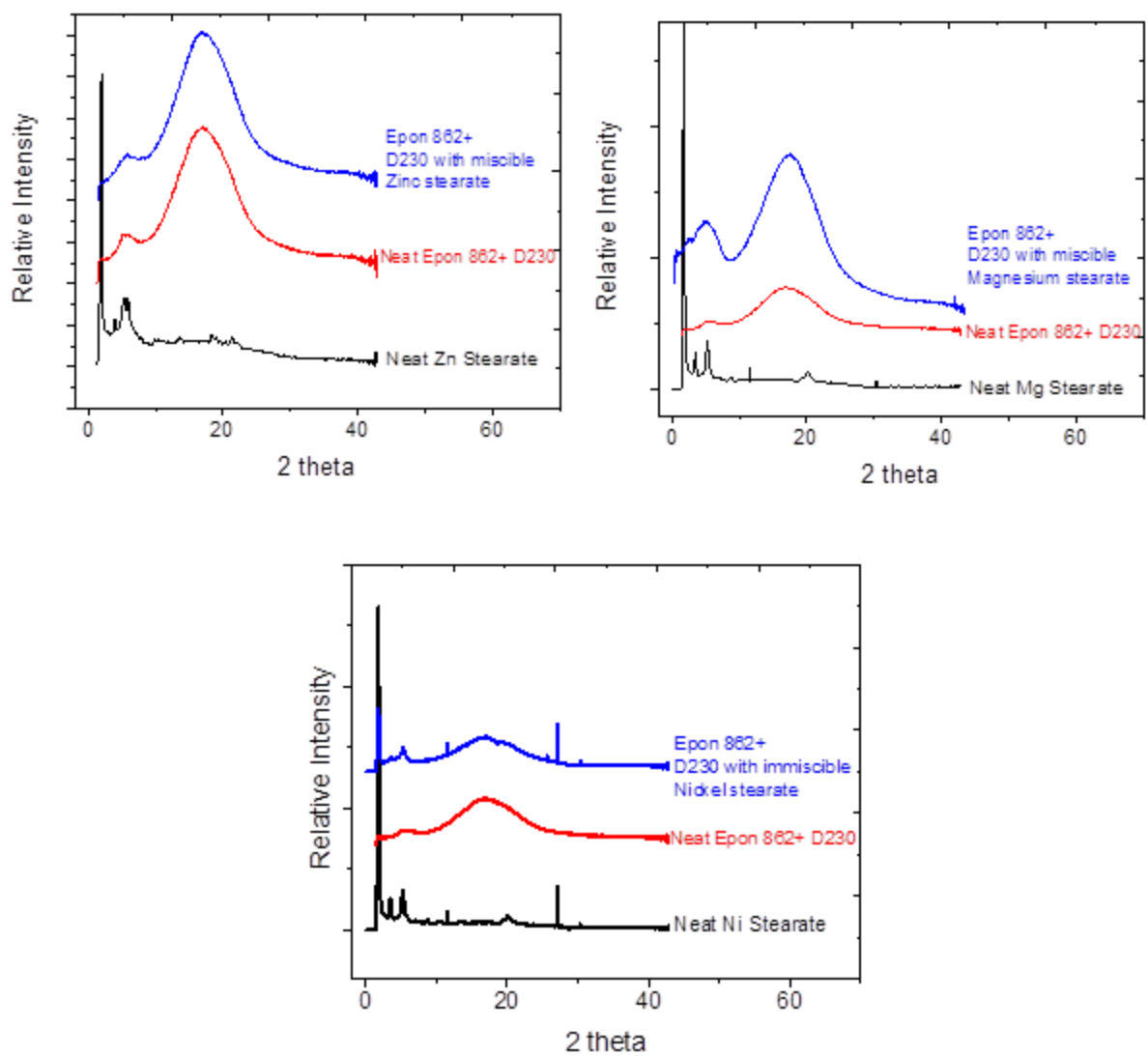


Figure 6.30 Wide angle x-ray spectrum of (a) miscible Zinc stearate, (b) miscible magnesium stearate & (c) immiscible nickel stearate composites in epoxy amine networks

### **6.3.8 Self-healing fire-retardant polymer networks comprising polymer chains crosslinked through coordination bonds with metal ions.**

Polymers with self-healing properties was prepared using coordination bonds as a site for crosslinking. several research has been carried out to achieve self healing property using ionic bonds. In this work, a small molecule additive was prepared using zinc acrylate and di-ethanol amine in a similar way described earlier. The prepared small molecule additive and di-ethanol amine was further crosslinked with a di-isocyanate to prepare a polyurethane based crosslinked systems with co-ordination bonds in the backbone of the polymer. This composition gave self healing property, through the co-ordination bond along with the flame-retardancy to the network systems. A detailed description of the monomer synthesis and network formation is detailed in the experimental session.

The composites containing metal dissolved in polyurethane exhibited self-healing property, whereas polyurethane prepared identically without zinc metal (using diacrylate) showed no bond reformation. Pictures indicating healable material prepared by incorporating zinc is shown in Figure 6.31.

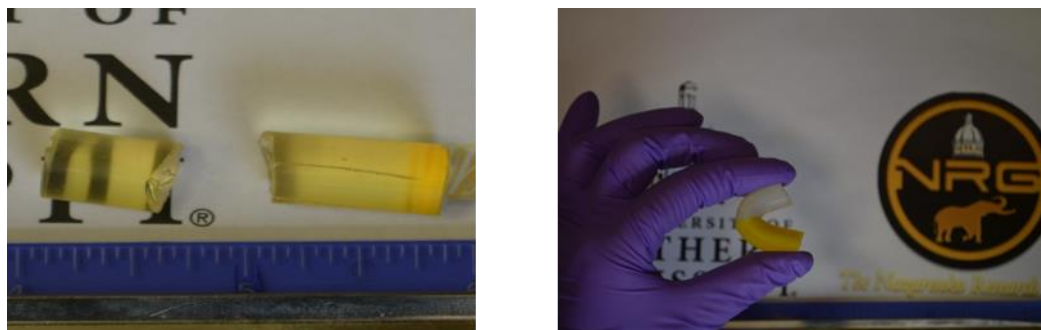


Figure 6.31 Polyurethane composites with (a) no Zinc metal on the left & (b) with zinc metal on the right. The composites without Zinc doesn't show the self-healing property, where is the composites with Zinc compound showed bond reformation

The flame-retardant properties of metal containing composites were tested in cone calorimeter and reported in Figure 6.32.

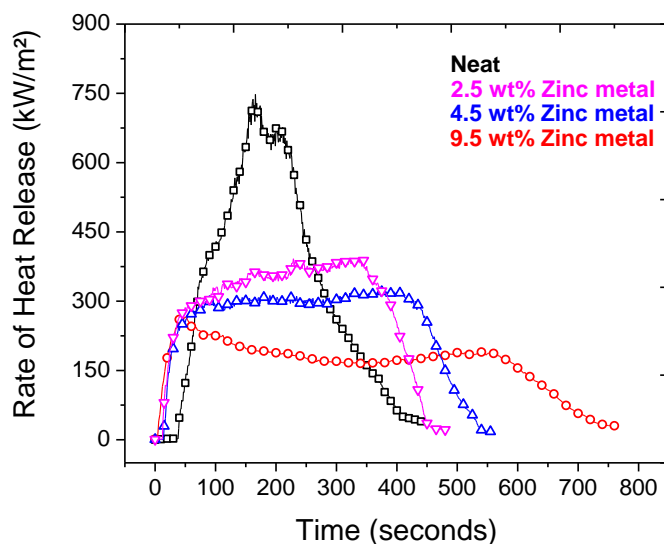


Figure 6.32 Heat release curves of polyurethane composites prepared with zinc acrylate in increasing concentrations

Calorimetry results for the polyurethane compositions are shown in Figure 6.33 for samples that contained respectively 2.5, 4.5 and 9.5 weight percent zinc. As seen in

Figure 25, with addition of small molecule additive, the time to ignition is reduced with decrease in PHRR. The observed char for compositions containing zinc metal formed a continuous char. Cone calorimetry results of polyurethane compositions prepared in a similar way with no metal is shown in Figure 6.33. Two types of control compositions were prepared, one containing methyl acrylate (which decreased the crosslink junction points) and the other composition contained diacrylate ( maintained the crosslinking points compared to zinc acrylate) was prepared. The cone calorimeter results of control polyurethanes showed a remarkable increase in PHRR and a short combustion time. Control samples with 4.5 wt% methyl acrylate showed higher PHRR as compared to the di-acrylate systems due to higher flammability associated with dangling methyl chains. All control polyurethane samples didn't show any char after the combustion which is due to the absence of char forming moieties in the networks.

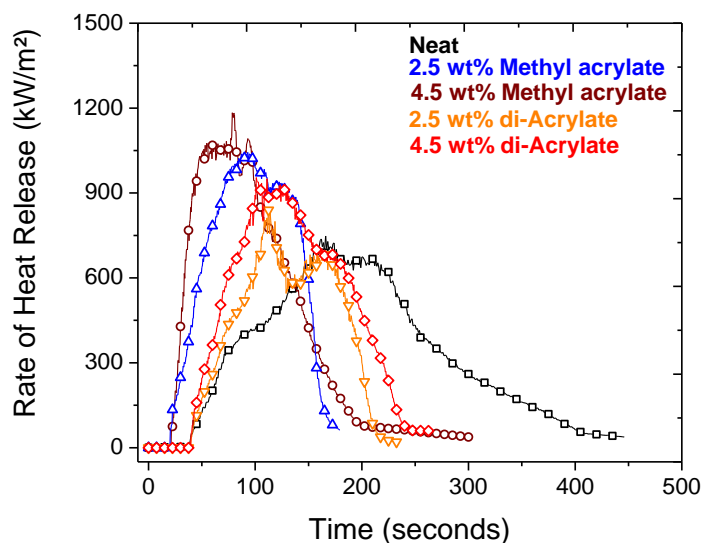


Figure 6.33 Heat release curves of polyurethane controls prepared with methyl acrylate and di-acrylate instead of zinc acrylate.

## 6.4 Conclusions and future directions

It has been discovered that the dissolution of metal in polymeric systems improves the flame retardancy by slowing the heat released and reducing the smoke. Dissolution of metal was achieved either by using amine-based compounds and or by using long chain metal salts at elevated temperatures. Excellent FR property was achieved at only 2.25 wt% of metal with several polymers including epoxy-amine, polyurethane, polystyrene and polyethylene oxide, thus proving its versatility in both solvent and water based polymers. In a different study to check the maximum possible loadings of such metal based compounds, it was found that the FR properties improved upto 9 wt%, beyond which it deteriorated. The addition of the small molecule imparted plasticization effect, but at higher loadings lead to increase in brittleness.

For the first time, a non-halogenated, non-phosphorous based flame retardant has been developed using metal salts and it has been proved to work with several systems. Even tough there are several unanswered questions, this approach is promising in terms of improving the flame retardancy of polymeric materials at low loading levels.

There are several unanswered questions such as the reaction mechanism happening to dissolve a metal salt in the polymer matrix, how does the metal salt lose its crystalline lattice structure upon addition to polymer matrix. It was noted that the time to ignition become faster upon addition of small molecule additive. We hypothesize that the faster ignitability causes the formation of char at an early stage of fire, which slows down the combustion of underneath layer of polymer. However, experimental evidence was not generated and hence need to be verified. This can be checked by preparing small

molecule additive with amines that burn at different rates. For example, long chain aliphatic amines or cyclo-aliphatic amines when used, the ignitability can be increased due to the increase in organic content. The ignitability can be reduced by the use of inorganic (siloxane) or aromatic amines.

## **6.5 Acknowledgements**

The author would like to thank Dr. Jianwei Tu from Wiggins research group for training and generously letting me use the MTS tensile tester. The author would also like to thank Dr. Robert Lochhead for his continuous support in filing a provision patent( No: 62-650,853)



## CHAPTER VII REFERENCES

- (1) Jacob, D. J. INTRODUCTION TO ATMOSPHERIC CHEMISTRY :  
SUPPLEMENTAL QUESTIONS AND PROBLEMS 5 Th EDITION. **2012**, No.  
August, 1–49.
- (2) IPCC. Climate Change 2007: The Physical Science Basis. *Intergov. Panel Clim. Chang.* **2007**, 446 (7137), 727–728.
- (3) Janssens-Maenhout, G.; Dentener, F.; Aardenne, J. Van; Monni, S.; Pagliari, V.; Orlandini, L.; Klimont, Z.; Kurokawa, J.; Akimoto, H.; Ohara, T.; et al. *EDGAR-HTAP: A Harmonized Gridded Air Pollution Emission Dataset Based on National Inventories*; 2012.
- (4) Kehrer, H. H. Fossil Fuel Combustion and the Major Sediment Cycle. *Science* (80- . ). **1971**, 173 (July), 233–235.
- (5) 2012, N. oceanic and atmospheric administration (NOAA). No Title  
<https://www.co2.earth>.
- (6) Figueroa, J. D.; Fout, T.; Plasynski, S.; McIlvried, H.; Srivastava, R. D. Advances in CO<sub>2</sub> Capture Technology—The U.S. Department of Energy’s Carbon Sequestration Program. *Int. J. Greenh. Gas Control* **2008**, 2 (1), 9–20.
- (7) Adewole, J. K.; Ahmad, A. L.; Ismail, S.; Leo, C. P. Current Challenges in Membrane Separation of CO<sub>2</sub> from Natural Gas: A Review. *Int. J. Greenh. Gas Control* **2013**, 17, 46–65.
- (8) Kusuma, V. A.; Gunawan, G.; Smith, Z. P.; Freeman, B. D. Gas Permeability of Cross-Linked Poly(Ethylene-Oxide) Based on Poly(Ethylene Glycol) Dimethacrylate and a Miscible Siloxane Co-Monomer. *Polymer (Guildf)*. **2010**, 51

- (24), 5734–5743.
- (9) Sun, Q.; Tian, H.; Li, Z.; Guo, X.; Liu, A.; Yang, L. Solubility of CO<sub>2</sub> in Water and NaCl Solution in Equilibrium with Hydrate. Part I: Experimental Measurement. *Fluid Phase Equilib.* **2016**, *409*, 131–135.
- (10) Cecchinato, L.; Corradi, M.; Fornasieri, E.; Zamboni, L. Carbon Dioxide as Refrigerant for Tap Water Heat Pumps: A Comparison with the Traditional Solution. *Int. J. Refrig.* **2005**, *28* (8), 1250–1258.
- (11) Spur, G.; Uhlmann, E.; Elbing, F. Dry-Ice Blasting for Cleaning: Process, Optimization and Application. *Wear* **1999**, *233–235*, 402–411.
- (12) Sakakura, T.; Choi, J.-C.; Yasuda, H. Transformation of Carbon Dioxide. *Chem. Rev.* **2007**, *107* (6), 2365–2387.
- (13) Paton, A. E.; Romack, T. J.; Betts, E.; Hill, C.; James, B.; C, N.; Ea, E. W. E. O. Extend McClain et Al .; Solution Properties of a CO-Soluble. **1999**, No. 19.
- (14) Watson, T. L.; Bachu, S. Evaluation of the Potential for Gas and CO<sub>2</sub> Leakage Along Wellbores. *E&P Environmental and Safety Conference*. Society of Petroleum Engineers: Galveston, Texas, U.S.A. 2007.
- (15) Primus, F. J.; Goldenberg, M. D.; Hills, S. United States Patent ( 19 ). **1991**, No. 19.
- (16) Pauling, L. *General Chemistry*; Courier Corporation, 1988.
- (17) Bhargava, B. L.; Balasubramanian, S. Probing Anion-Carbon Dioxide Interactions in Room Temperature Ionic Liquids: Gas Phase Cluster Calculations. *Chem. Phys. Lett.* **2007**, *444* (4–6), 242–246.
- (18) Rovira-Truitt, R.; Patil, N.; Castillo, F.; White, J. L. Synthesis and

- Characterization of Biopolymer Composites from the inside Out. *Macromolecules* **2009**, *42* (20), 7772–7780.
- (19) White, J. L.; Patil, N. Self-Assembled Biopolymer Nanocomposites. In *ABSTRACTS OF PAPERS OF THE AMERICAN CHEMICAL SOCIETY*; 2011; Vol. 242.
- (20) Patil, N. V; White, J. L. Sustainable Nanocomposites Based on Self-Assembly and End-Group Chemistry. In *ABSTRACTS OF PAPERS OF THE AMERICAN CHEMICAL SOCIETY*; 2011; Vol. 242.
- (21) Galand, N.; Wipff, G. Solvation of Benzene Derivatives in SC-CO<sub>2</sub>: A Molecular Dynamics Study of Fluorination Effects Electronic Supplementary Information (ESI) Available: Structures and Interaction Energies of X-Benz(CO<sub>2</sub>)<sub>n</sub> Aggregates in the Gas Phase and Table of Force Field Pa. *New J. Chem.* **2003**, *27* (9), 1319.
- (22) Cavenati, S.; Grande, C. A.; Rodrigues, A. E. Adsorption Equilibrium of Methane, Carbon Dioxide, and Nitrogen on Zeolite 13X at High Pressures. *J. Chem. Eng. Data* **2004**, *49* (4), 1095–1101.
- (23) Tan, L. S.; Lau, K. K.; Bustam, M. A.; Shariff, A. M. Removal of High Concentration CO<sub>2</sub> from Natural Gas at Elevated Pressure via Absorption Process in Packed Column. *J. Nat. Gas Chem.* **2012**, *21* (1), 7–10.
- (24) Buswell, A. M.; Mueller, H. F. Mechanism of Methane Fermentation. *Ind. Eng. Chem.* **1952**, *44* (3), 550–552.
- (25) NASA. Carbon Dioxide. **2016**, *4* (1).
- (26) Choi, S.; Drese, J. H.; Jones, C. W. Adsorbent Materials for Carbon Dioxide Capture from Large Anthropogenic Point Sources. *ChemSusChem* **2009**, *2* (9),

796–854.

- (27) Staudt-Bickel, C.; J Koros, W. Improvement of CO<sub>2</sub>/CH<sub>4</sub> Separation Characteristics of Polyimides by Chemical Crosslinking. *J. Memb. Sci.* **1999**, *155* (1), 145–154.
- (28) Han, S. H.; Lee, J. E.; Lee, K.-J.; Park, H. B.; Lee, Y. M. Highly Gas Permeable and Microporous Polybenzimidazole Membrane by Thermal Rearrangement. *J. Memb. Sci.* **2010**, *357* (1–2), 143–151.
- (29) Shekhawat, D.; Luebke, D. R.; Pennline, H. W. A Review of Carbon Dioxide Selective Membranes. *US Dep. Energy* **2003**.
- (30) He, X.; Hägg, M.-B. Energy Efficient Process for CO<sub>2</sub> Capture from Flue Gas with Novel Fixed-Site-Carrier Membranes. *Energy Procedia* **2014**, *63*, 174–185.
- (31) Brunetti, A.; Scura, F.; Barbieri, G.; Drioli, E. Membrane Technologies for CO<sub>2</sub> separation. *J. Memb. Sci.* **2010**, *359* (1–2), 115–125.
- (32) Aaron, D.; Tsouris, C. Separation of CO<sub>2</sub> from Flue Gas: A Review. *Sep. Sci. Technol.* **2005**, *40* (1–3), 321–348.
- (33) Merkel, T. C.; Lin, H.; Wei, X.; Baker, R. Power Plant Post-Combustion Carbon Dioxide Capture: An Opportunity for Membranes. *J. Memb. Sci.* **2010**, *359* (1–2), 126–139.
- (34) Cichowska-Kopczyńska, I.; Joskowska, M.; Dębski, B.; Łuczak, J.; Aranowski, R. Influence of Ionic Liquid Structure OnSupported Ionic Liquid Membranes Effectiveness InCarbon Dioxide/Methane Separation. *e-Journal Chem.* **2013**, *2013*, 1–10.
- (35) Van der Bruggen, B. *Membrane Technology*; 2017.

- (36) Patil, N.; Kelsey, J.; Fischer, J.; Grady, B.; White, J. L. Creating Polymer Templates and Their Use in the In-Situ Synthesis of Biodegradable Composite Networks. *Polym. (United Kingdom)* **2014**, *55* (10), 2332–2339.
- (37) Clough, A.; Sigle, J. L.; Tapash, A.; Gill, L.; Patil, N. V.; Zhou, J.; White, L. Component-Specific Heterogeneity and Differential Phase Partitioning in Gradient Copolymers Revealed by Solids NMR. **2014**.
- (38) Patil, N.; Kelsey, J.; White, J. L. Self-Assembled Polymer Nanocomposites and Their Networks. *J. Appl. Polym. Sci.* **2014**, *131* (22), 1–12.
- (39) Chung, T.-S.; Jiang, L. Y.; Li, Y.; Kulprathipanja, S. Mixed Matrix Membranes (MMMs) Comprising Organic Polymers with Dispersed Inorganic Fillers for Gas Separation. *Prog. Polym. Sci.* **2007**, *32* (4), 483–507.
- (40) Robeson, L. M. The Upper Bound Revisited. *J. Memb. Sci.* **2008**, *320* (1–2), 390–400.
- (41) Robeson, L. M.; Smith, Z. P.; Freeman, B. D.; Paul, D. R. Contributions of Diffusion and Solubility Selectivity to the Upper Bound Analysis for Glassy Gas Separation Membranes. *J. Memb. Sci.* **2014**, *453*, 71–83.
- (42) George, S. C.; Thomas, S. Transport Phenomena through Polymeric Systems. *Prog. Polym. Sci.* **2001**, *26* (6), 985–1017.
- (43) Lau, C. H.; Li, P.; Li, F.; Chung, T. S.; Paul, D. R. Reverse-Selective Polymeric Membranes for Gas Separations. *Prog. Polym. Sci.* **2013**, *38* (5), 740–766.
- (44) Eric, C.; Rideal, K. Permeation, Diffusion and Solution of gases in Organic Polymers. **1939**, No. 628, 628–643.
- (45) Murphy, T. M.; Offord, G. T.; Paul, D. R. Fundamentals of Membrane Gas

- Separation. *Membr. Oper. Innov. Sep. Transform.* **2009**, 63–82.
- (46) Bernardo, P.; Drioli, E.; Golemme, G. Membrane Gas Separation: 1 Review of State of the Art. *Ind. Eng. Chem. Res.* **2009**, 48 (10), 4638–4663.
- (47) Lin, H.; Freeman, B. D. Materials Selection Guidelines for Membranes That Remove CO<sub>2</sub> from Gas Mixtures. *J. Mol. Struct.* **2005**, 739 (1–3), 57–74.
- (48) Buonomenna, M. G.; Yave, W.; Golemme, G. Some Approaches for High Performance Polymer Based Membranes for Gas Separation: Block Copolymers, Carbon Molecular Sieves and Mixed Matrix Membranes. *RSC Adv.* **2012**, 2 (29), 10745.
- (49) Reijerkerk, S. R.; Knoef, M. H.; Nijmeijer, K.; Wessling, M. Poly(Ethylene Glycol) and Poly(Dimethyl Siloxane): Combining Their Advantages into Efficient CO<sub>2</sub> gas Separation Membranes. *J. Memb. Sci.* **2010**, 352 (1–2), 126–135.
- (50) Liu, S. L.; Shao, L.; Chua, M. L.; Lau, C. H.; Wang, H.; Quan, S. Recent Progress in the Design of Advanced PEO-Containing Membranes for CO<sub>2</sub> removal. *Prog. Polym. Sci.* **2013**, 38 (7), 1089–1120.
- (51) Patel, N. P.; Miller, A. C.; Spontak, R. J. Highly CO<sub>2</sub>-Permeable and -Selective Membranes Derived from Crosslinked Poly(Ethylene Glycol) and Its Nanocomposites. *Adv. Funct. Mater.* **2004**, 14 (7), 699–707.
- (52) Smith, A. R.; Klosek, J. A Review of Air Separation Technologies and Their Integration with Energy Conversion Processes. *Fuel Process. Technol.* **2001**, 70 (2), 115–134.
- (53) Hoyle, C. E.; Bowman, C. N. Thiol-Ene Click Chemistry. *Angew. Chemie - Int. Ed.* **2010**, 49 (9), 1540–1573.

- (54) Nair, D. P.; Podgórski, M.; Chatani, S.; Gong, T.; Xi, W.; Fenoli, C. R.; Bowman, C. N. The Thiol-Michael Addition Click Reaction: A Powerful and Widely Used Tool in Materials Chemistry. *Chem. Mater.* **2014**, *26* (1), 724–744.
- (55) Kwisnek, L.; Heinz, S.; Wiggins, J. S.; Nazarenko, S. Multifunctional Thiols as Additives in UV-Cured PEG-Diacrylate Membranes for CO<sub>2</sub> Separation. *J. Memb. Sci.* **2011**, *369* (1–2), 429–436.
- (56) Clark, T.; Kwisnek, L.; Hoyle, C. E.; Nazarenko, S. Photopolymerization of Thiol-Ene Systems Based on Oligomeric Thiols. *J. Polym. Sci. Part A Polym. Chem.* **2009**, *47* (1), 14–24.
- (57) Hoyle, C. E.; Lee, T. Y.; Roper, T. Thiol-Enes: Chemistry of the Past with Promise for the Future. *J. Polym. Sci. Part A Polym. Chem.* **2004**, *42* (21), 5301–5338.
- (58) Neil B. Cramer, †; J. Paul Scott, † and; Christopher N. Bowman\*, †,‡. Photopolymerizations of Thiol–Ene Polymers without Photoinitiators. **2002**.
- (59) Hoyle, C. E.; Hensel, R. D.; Grubb, M. B. Temperature Dependence of the Laser-Initiated Polymerization of a Thiol-Ene System. *J. Polym. Sci. Polym. Chem. Ed.* **1984**, *22* (8), 1865–1873.
- (60) Hoyle, C. E.; Hensel, R. D.; Grubb, M. B. Laser-Initiated Polymerization of a Thiol-Ene System. *Polym. Photochem.* **1984**, *4* (1), 69–80.
- (61) Kloxin, C. J.; Scott, T. F.; Bowman, C. N. Stress Relaxation via Addition–Fragmentation Chain Transfer in a Thiol-Ene Photopolymerization. *Macromolecules* **2009**, *42* (7), 2551–2556.
- (62) Morgan, A. B.; Bundy, M. Cone Calorimeter Analysis of UL-94 V-Rated Plastics. *Z.* **2007**, No. November, 257–283.

- (63) Grand, A. F.; Wilkie, C. A. *Fire Retardancy of Polymeric Materials*; CRC Press, 2000.
- (64) Dollimore, D.; Phang, P. Thermal Analysis. *Anal. Chem.* **2000**, 72 (12), 27–36.
- (65) Scholar.
- (66) Beetsma Jochum. Alkyd Emulsion Paints: Properties, Challenges and Solutions. *Pigment Resin Technol.* **1998**, 27 (1), 12–19.
- (67) HASEEBUDDIN, S.; PATIL, N. V. Renewable Materials in Surface Coatings. *Paintindia* **2006**, 56 (12).
- (68) Hu, N. V. P.; Weiguo. Dynamic Mechanical Relaxations in Ultra-High Molecular Weight Polyethylene Fibers Probed by Solid-State NMR. In *Proceedings of a meeting held 22-26 March 2015, Denver, Colorado, USA. Preprints Submitted for Papers Presented at the 249th National American Chemical Society Meeting*; 2015; Vol. 112.
- (69) Patil, N.; Hu, W. Dynamic Mechanical Relaxations in Ultrahigh Molecular Weight Polyethylene Fibers Probed by Solid-State NMR. In *ABSTRACTS OF PAPERS OF THE AMERICAN CHEMICAL SOCIETY*; 2015; Vol. 249.
- (70) Laoutid, F.; Bonnaud, L.; Alexandre, M.; Lopez-Cuesta, J. M.; Dubois, P. New Prospects in Flame Retardant Polymer Materials: From Fundamentals to Nanocomposites. *Mater. Sci. Eng. R Reports* **2009**, 63 (3), 100–125.
- (71) Levchik, S. V. Introduction to Flame Retardancy and Polymer Flammability. *Flame Retard. Polym. nanocomposites* **2007**, 1–29.
- (72) Rakotomalala, M.; Wagner, S.; Döring, M. Recent Developments in Halogen Free Flame Retardants for Epoxy Resins for Electrical and Electronic Applications.



- Materials (Basel)*. **2010**, 3 (8), 4300–4327.
- (73) Schartel, B.; Hull, T. R. Development of Fire-Retarded Materials - Interpretation of Cone Calorimeter Data. *Fire Mater.* **2007**, 31 (5), 327–354.
- (74) Manzi-nshuti, C.; Wu, Y.; Nazarenko, S. A Comparative Study of the Fire Retardant Effect of Several Metal-Based Compounds Added to an Epoxy-Amine Thermoset. **2012**.
- (75) Grady, B. P.; Paul, A.; Peters, J. E.; Ford, W. T. Glass Transition Behavior of Single-Walled Carbon Nanotube–Polystyrene Composites. *Macromolecules* **2009**, 42 (16), 6152–6158.
- (76) Troitzsch, J. H. Overview of Flame Retardants. *Chimica Oggi*. 1998, pp 18–24.
- (77) Zheng, X.; Wilkie, C. A. Nanocomposites Based on Poly ( $\epsilon$ -Caprolactone) (PCL)/Clay Hybrid: Polystyrene, High Impact Polystyrene, ABS, Polypropylene and Polyethylene. *Polym. Degrad. Stab.* **2003**, 82 (3), 441–450.
- (78) Bourbigot, S.; Gilman, J. W.; Wilkie, C. A. Kinetic Analysis of the Thermal Degradation of Polystyrene-Montmorillonite Nanocomposite. *Polym. Degrad. Stab.* **2004**, 84 (3), 483–492.
- (79) Li, Y.; Ishida, H. Solution Intercalation of Polystyrene and the Comparison with Poly(Ethyl Methacrylate). *Polymer (Guildf)*. **2003**, 44 (21), 6571–6577.
- (80) Suin, S.; Khatua, B. B. Exfoliated and Optically Transparent Polycarbonate / Clay Nanocomposites Using Phosphonium Modified Organoclay : Preparation and Characterizations. *Ind. Eng. Chem. Res.* **2012**, No. 51, 15096–15108.
- (81) Floyd, J. Coupling a Network HVAC Model to a Computational Fluid Dynamics Model Using Large Eddy Simulation. *Fire Saf. Sci.* **2011**, 10 (3), 459–470.

- (82) Index, O.; Index, O. Oxygen Index 操作手順. **2013**, 1–14.
- (83) Burning, H. UL-94. **2014**, No. November, 1–7.
- (84) Requirements, C. Specifications - UL Test Procedures Procedure for Obtaining UL Listing of Device Specifications - UL Test Procedures. 24–26.
- (85) Lindholm, J.; Brink, A.; Hupa, M. Cone Calorimeter – a Tool for Measuring Heat Release Rate. *Finnish-Swedish Flame Days 2009* **2009**, No. August 2008, 4B.
- (86) Costa, L.; Camino, G.; Bertelli, G.; Borsini, G. Mechanistic Study of the Combustion Behaviour of Polymeric Materials in Bench-Scale Tests. *Fire Mater.* **1995**, 19 (March), 133–142.
- (87) Mouritz, A. P. Simple Models for Determining the Mechanical Properties of Burnt FRP Composites. *Mater. Sci. Eng. A* **2003**, 359 (1–2), 237–246.
- (88) Le Lay, F.; Gutierrez, J. Improvement of the Fire Behaviour of Composite Materials for Naval Application. *Polym. Degrad. Stab.* **1999**, 64 (3), 397–401.
- (89) Schartel, B.; Perret, B.; Dittrich, B.; Ciesielski, M.; Krämer, J.; Müller, P.; Altstädt, V.; Zang, L.; Döring, M. Flame Retardancy of Polymers: The Role of Specific Reactions in the Condensed Phase. *Macromol. Mater. Eng.* **2016**, 301 (1), 9–35.
- (90) Gilman, J. W.; Kashiwagi, T.; Harris, R. H.; Lomakin, S.; Lichtenhan, J. D.; Bolf, A.; Jones, P. Char Enhancing Approaches to Flame Retarding Polymers. *Chemistry and Technology of Polymer Additives*. 1999, pp 135–150.
- (91) Mwanthi, M. A.; Kimani, V. N. Agrochemicals Pose Health Risks to Coffee Factory Workers in Githuguri (Kenya). *Int. J. Environ. Health Res.* **1993**, 3 (2), 73–81.

- (92) Finzel, M. C.; Delong, J.; Hawley, M. C. Effect of Stoichiometry and Diffusion on an Epoxy/Amine Reaction Mechanism. *J. Polym. Sci. Part A Polym. Chem.* **1995**, *33* (4), 673–689.
- (93) Thomas, A. The Versatility of Ambient Curing Waterborne. **2017**, No. December.
- (94) Chen, W. Y.; Wang, Y. Z.; Chang, F. C. Study on Curing Kinetics and Curing Mechanism of Epoxy Resin Based on Diglycidyl Ether of Bisphenol A and Melamine Phosphate. *J. Appl. Polym. Sci.* **2004**, *92* (2), 892–900.
- (95) Jin, F. L.; Li, X.; Park, S. J. Synthesis and Application of Epoxy Resins: A Review. *J. Ind. Eng. Chem.* **2015**, *29*, 1–11.
- (96) Fisch, W.; Hofmann, W.; Koskikallio, J. Mechanism of Epoxy Resins. *J. Appl. Chem.* **1956**, *6* (10), 429–441.
- (97) Quiz, P.; Reading, R. Polycondensation and Curing Of. **2014**, 1–12.
- (98) DUŠEK, K. Cross-Linking of Epoxy Resins. **1984**, 3–14.
- (99) Dabestani, R.; Ivanov, I. N. ( Cure Kinetics ) of Model.
- (100) Baxter, R.; Hastings, N.; Law, a.; Glass, E. J. . [ No Title ]. *Anim. Genet.* **2008**, *39* (5), 561–563.
- (101) Nitin V Patil, W. H. Glass Transitions Associated with Nanodomains in Phase-Mixed Poly(Urethane Urea) Elastomers Investigated by Solid-State NMR. In *ABSTRACTS OF PAPERS OF THE AMERICAN CHEMICAL SOCIETY*; 2015; Vol. 249.
- (102) Patil, N. V; White, J. L. Polymerizable Structure-Directing Agents for in-Situ Synthesis of Nanocomposite Networks. In *ABSTRACTS OF PAPERS OF THE AMERICAN CHEMICAL SOCIETY*; 2013; Vol. 245.

- (103) Guo, C.; Zhou, L.; Lv, J. Effects of Expandable Graphite and Modified Ammonium Polyphosphate on the Flame-Retardant and Mechanical Properties of Wood Flour-Polypropylene Composites. *Polym. Polym. Compos.* **2013**, *21* (7), 449–456.
- (104) Kawakami, M.; Iwanaga, H.; Hara, Y.; Iwamoto, M. Gas Permeabilities of Cellulose Nitrate / Poly ( Ethylene Glycol ) Blend Membranes. **1982**, *27*, 2387–2393.
- (105) Li, J.; Wang, S.; Nagai, K.; Nakagawa, T.; Mau, A. W. H. Effect of Polyethyleneglycol (PEG) on Gas Permeabilities and Permselectivities in Its Cellulose Acetate (CA) Blend Membranes. *J. Memb. Sci.* **1998**, *138* (2), 143–152.
- (106) Patel, N. P.; Spontak, R. J. Gas-Transport and Thermal Properties of a Microphase-Ordered Poly(Styrene- b -Ethylene Oxide- b -Styrene) Triblock Copolymer and Its Blends with Poly(Ethylene Glycol). *Macromolecules* **2004**, *37* (8), 2829–2838.
- (107) Yave, W.; Car, A.; Funari, S. S.; Nunes, S. P.; Peinemann, K. V. CO<sub>2</sub>-Philic Polymer Membrane with Extremely High Separation Performance. *Macromolecules* **2010**, *43* (1), 326–333.
- (108) Car, A.; Stropnik, C.; Yave, W.; Peinemann, K. V. Pebax®/Polyethylene Glycol Blend Thin Film Composite Membranes for CO<sub>2</sub>separation: Performance with Mixed Gases. *Sep. Purif. Technol.* **2008**, *62* (1), 110–117.
- (109) Li, J.; Nagai, K.; Nakagawa, T.; Wang, S. Preparation of Polyethyleneglycol (PEG) and Cellulose Acetate (CA) Blend Membranes and Their Gas Permeabilities. *J. Appl. Polym. Sci.* **1995**, *58* (9), 1455–1463.

- (110) Julian, H. Polysulfone Membranes for CO<sub>2</sub>/CH<sub>4</sub> Separation: State of the Art. *IOSR J. Eng.* **2012**, 02 (03), 484–495.
- (111) Barbi, V.; Funari, S. S.; Gehrke, R.; Scharnagl, N.; Stribeck, N. SAXS and the Gas Transport in Polyether- b Lock -Polyamide Copolymer Membranes. *Macromolecules* **2003**, 36 (3), 749–758.
- (112) Bondar, VI , Freeman, B. D. , Pinnau, I. Gas Sorption and Characterization of Poly (Ether-b-Amide ). *J. Polym. Sci. Part B Polym. Phys.* **1999**, 37, 2463–2475.
- (113) Reijerkerk, S. R.; Wessling, M.; Nijmeijer, K. Pushing the Limits of Block Copolymer Membranes for CO<sub>2</sub> Separation. *J. Memb. Sci.* **2011**, 378 (1–2), 479–484.
- (114) Lin, H.; Freeman, B. D. Gas Solubility, Diffusivity and Permeability in Poly(Ethylene Oxide). *J. Memb. Sci.* **2004**, 239 (1), 105–117.
- (115) Reijerkerk, S. R.; Ijzer, A. C.; Nijmeijer, K.; Arun, A.; Gaymans, R. J.; Wessling, M. Subambient Temperature Co<sub>2</sub>and Light Gas Permeation through Segmented Block Copolymers with Tailored Soft Phase. *ACS Appl. Mater. Interfaces* **2010**, 2 (2), 551–560.
- (116) Car, A.; Stropnik, C.; Yave, W.; Peinemann, K. V. PEG Modified Poly(Amide-b-Ethylene Oxide) Membranes for CO<sub>2</sub>separation. *J. Memb. Sci.* **2008**, 307 (1), 88–95.
- (117) Metz, S. J.; Mulder, M. H. V; Wessling, M. Gas-Permeation Properties of Poly(Ethylene Oxide) Poly(Butylene\rterephthalate) Block Copolymers. *Macromolecules* **2004**, 37, 4590–4597.
- (118) Reijerkerk, S. R.; Arun, A.; Gaymans, R. J.; Nijmeijer, K.; Wessling, M. Tuning of

Mass Transport Properties of Multi-Block Copolymers for CO<sub>2</sub>capture Applications. *J. Memb. Sci.* **2010**, 359 (1–2), 54–63.

- (119) De Lorenzo, L.; Tocci, E.; Gugliuzza, A.; Drioli, E. Pure and Modified Co-Poly(Amide-12-b-Ethylene Oxide) Membranes for Gas Separation Studied by Molecular Investigations. *Membranes (Basel)*. **2012**, 2 (3), 346–366.
- (120) Bondar, V. I.; Freeman, B. D.; Pinnau, I. Gas Transport Properties of Poly(Ether-b-Amide) Segmented Block Copolymers. *J. Polym. Sci. Part B Polym. Phys.* **2000**, 38 (15), 2051–2062.
- (121) Husken, D.; Visser, T.; Wessling, M.; Gaymans, R. J. CO<sub>2</sub>permeation Properties of Poly(Ethylene Oxide)-Based Segmented Block Copolymers. *J. Memb. Sci.* **2010**, 346 (1), 194–201.
- (122) Yoshino, M.; Ito, K.; Kita, H.; Okamoto, K. I. Effects of Hard-Segment Polymers on CO<sub>2</sub>/N<sub>2</sub> Gas-Separation Properties of Poly(Ethylene Oxide)-Segmented Copolymers. *J. Polym. Sci. Part B Polym. Phys.* **2000**, 38 (13), 1707–1715.
- (123) Lin, H.; Kai, T.; Freeman, B. D.; Kalakkunnath, S.; Kalika, D. S. The Effect of Cross-Linking on Gas Permeability in Cross-Linked Poly(Ethylene Glycol Diacrylate). *Macromolecules* **2005**, 38 (20), 8381–8393.
- (124) Raharjo, R. D.; Lin, H.; Sanders, D. F.; Freeman, B. D.; Kalakkunnath, S.; Kalika, D. S. Relation between Network Structure and Gas Transport in Crosslinked Poly(Propylene Glycol Diacrylate). *J. Memb. Sci.* **2006**, 283 (1–2), 253–265.
- (125) Lin, H.; Freeman, B. D. Gas and Vapor Solubility in Cross-Linked Polyethylene Glycol Diacrylate. *Macromolecules* **2005**, 38 (20), 8394–8407.
- (126) Lin, H.; Kai, T.; Freeman, B. D.; Kalakkunnath, S.; Kalika, D. S. The Effect of

- Cross-Linking on Gas Permeability in Cross-Linked Poly(Ethylene Glycol Diacrylate). *Macromolecules* **2005**, *38* (20), 8381–8393.
- (127) Kusuma, V. A.; Freeman, B. D.; Smith, S. L.; Heilman, A. L.; Kalika, D. S. Influence of TRIS-Based Co-Monomer on Structure and Gas Transport Properties of Cross-Linked Poly(Ethylene Oxide). *J. Memb. Sci.* **2010**, *359* (1–2), 25–36.
- (128) Hirayama, Y.; Kase, Y.; Tanihara, N.; Sumiyama, Y. Permeation Properties to CO<sub>2</sub> and N<sub>2</sub> of Poly ( Ethylene Oxide ) -Containing and Crosslinked Polymer <sup>®</sup> Lms. **1999**, *160*.
- (129) Scholes, C. A.; Chen, G. Q.; Lu, H. T.; Kentish, S. E. Crosslinked PEG and PEBAX Membranes for Concurrent Permeation Ofwater and Carbon Dioxide. *Membranes (Basel)*. **2015**, *6* (1), 1–10.
- (130) Kwisnek, L.; Goetz, J.; Meyers, K. P.; Heinz, S. R.; Wiggins, J. S.; Nazarenko, S. PEG Containing Thiol-Ene Network Membranes for CO<sub>2</sub> Separation: Effect of Cross-Linking on Thermal, Mechanical, and Gas Transport Properties. *Macromolecules* **2014**, *47* (10), 3243–3253.
- (131) Kwisnek, L.; Goetz, J.; Meyers, K. P.; Heinz, S. R.; Wiggins, S.; Nazarenko, S. PEG Containing Thiol – Ene Network Membranes for CO<sub>2</sub> Separation: E Ff Ect of Cross-Linking on Thermal, Mechanical, and Gas Transport Properties. **2014**, 1–43.
- (132) Sekelik, D. J.; Stepanov, E. V.; Nazarenko, S.; Schiraldi, D.; Hiltner, A.; Baer, E. Oxygen Barrier Properties of Crystallized and Talc-Filled Poly(Ethylene Terephthalate). *J. Polym. Sci. Part B Polym. Phys.* **1999**, *37* (8), 847–857.
- (133) Tao, S. J. Positronium Annihilation in Molecular Substances. *J. Chem. Phys.* **1972**,

56 (11), 5499–5510.

- (134) Kirkegaard, P.; Eldrup, M.; Mogensen, O. E.; Pedersen, N. J. Program System for Analysing Positron Lifetime Spectra and Angular Correlation Curves. *Comput. Phys. Commun.* **1981**, *23* (3), 307–335.
- (135) Bevington, P. R.; Robinson, D. K. Data Reduction and Error Analysis for the Physical Sciences, 2nd Edn. *Computers in Physics*. 1992, p 324.
- (136) Roose, P.; Fallais, I.; Vandermiers, C.; Olivier, M. G.; Poelman, M. Radiation Curing Technology: An Attractive Technology for Metal Coating. *Prog. Org. Coatings* **2009**, *64* (2–3), 163–170.
- (137) Scott, T. F.; Kloxin, C. J.; Draughon, R. B.; Bowman, C. N. Nonclassical Dependence of Polymerization Rate on Initiation Rate Observed in Thiol–Ene Photopolymerizations. *Macromolecules* **2008**, *41* (9), 2987–2989.
- (138) Hoyle, C. E.; Lee, T. Y.; Roper, T. Thiol–Enes: Chemistry of the Past with Promise for the Future. *J. Polym. Sci. Part A Polym. Chem.* **2004**, *42* (21), 5301–5338.
- (139) Daniliuc, A.; Deppe, B.; Deppe, O.; Friebel, S.; Kruse, D.; Philipp, C. New Trends in Wood Coatings and Fire Retardants: Biobased Monomers and High Performance Coatings. *Eur. Coatings J.* **2012**, No. 7–8, 20–25.
- (140) Remzi Becer, C.; Hoogenboom, R.; Schubert, U. S. Click Chemistry beyond Metal-Catalyzed Cycloaddition. *Angew. Chemie - Int. Ed.* **2009**, *48* (27), 4900–4908.
- (141) Opsteen, J. A.; Van Hest, J. C. M. Modular Synthesis of Block Copolymers via Cycloaddition of Terminal Azide and Alkyne Functionalized Polymers. *Chem. Commun.* **2005**, No. 1, 57–59.



- (142) Sumerlin, B. S.; Vogt, A. P. Macromolecular Engineering through Click Chemistry and Other Efficient Transformations. *Macromolecules* **2010**, *43* (1), 1–13.
- (143) Wisian-neilson, P.; Bailey, L.; Bahadur, M. Hydrophobicity. **1994**, 7713–7717.
- (144) Lu, H.; Carioscia, J. A.; Stansbury, J. W.; Bowman, C. N. Investigations of Step-Growth Thiol-Ene Polymerizations for Novel Dental Restoratives. *Dent. Mater.* **2005**, *21* (12), 1129–1136.
- (145) Kwisnek, L.; Nazarenko, S.; Hoyle, C. E. Oxygen Transport Properties of Thiol - Ene Networks. **2009**, 7031–7041.
- (146) Shin, J.; Nazarenko, S.; Hoyle, C. E. Effects of Chemical Modification of Thiol-Ene Networks on Enthalpy Relaxation. *Macromolecules* **2009**, *42* (17), 6549–6557.
- (147) Zhang, P.; Song, L.; Dai, K.; Shan, X.; Lu, H.; Wang, J. Preparation and Thermal Properties of the UV-Cured Epoxy Acrylate / Microencapsulated Phase-Change Material. *Composites* **2011**, 785–790.
- (148) Hu, W.; Patil, N. V.; Hsieh, A. J. Glass Transition of Soft Segments in Phase-Mixed Poly (Urethane Urea) Elastomers by Time-Domain 1H and 13C Solid-State NMR. *Polymer (Guildf)*. **2016**, *100*, 149–157.
- (149) Chen, L. J.; Tai, Q. L.; Song, L.; Xing, W. Y.; Jie, G. X.; Hu, Y. Thermal Properties and Flame Retardancy of an Ether-Type UV-Cured Polyurethane Coating. *Express Polym. Lett.* **2010**, *4* (9), 539–550.
- (150) Xing, W.; Song, L.; Hu, Y.; Lv, X.; Chen, L. Combustion and Thermal Behaviors of the Novel UV-Cured Intumescent Flame Retardant Coatings Containing

- Phosphorus and Nitrogen. *Sci. Technol.* **2010**, No. 063, 1–11.
- (151) Senyurt, A. F.; Wei, H.; Hoyle, C. E.; Piland, S. G.; Gould, T. E. Ternary Thiol-Ene/Acrylate Photopolymers: Effect of Acrylate Structure on Mechanical Properties? *Macromolecules* **2007**, *40* (14), 4901–4909.
- (152) Gmbh, W. V.; Ccc, W. 1 © 2002. **2002**, *8*, 1–8.
- (153) Schroeder, W. F.; Auad, M. L.; Barcia Vico, M. A.; Borrajo, J.; Aranguren, M. I. Thermodynamic, Morphological, Mechanical and Fracture Properties of Poly(Methyl Methacrylate)(PMMA) Modified Divinylester(DVE)/Styrene(St) Thermosets. *Polymer (Guildf)*. **2005**, *46* (7), 2306–2319.
- (154) Jackson, M.; Kaushik, M.; Nazarenko, S.; Ward, S.; Maskell, R.; Wiggins, J. Effect of Free Volume Hole-Size on Fluid Ingress of Glassy Epoxy Networks. *Polymer (Guildf)*. **2011**, *52* (20), 4528–4535.
- (155) Rico, M.; López, J.; Bouza, R.; Bellas, R. Thermal Behavior of Blends Based on a Thermoplastic-Modified Epoxy Resin with a Crosslinking Density Variation. *J. Therm. Anal. Calorim.* **2011**, *105* (2), 599–606.
- (156) Liang, H.; Shi, W. Thermal Behaviour and Degradation Mechanism of Phosphate Di/Triacrylate Used for UV Curable Flame-Retardant Coatings. *Polym. Degrad. Stab.* **2004**, *84* (3), 525–532.
- (157) Li, L.; Zhong, Y.; Li, J.; Chen, C.; Zhang, A.; Xu, J.; Ma, Z. Thermally Stable and Solvent Resistant Honeycomb Structured Polystyrene Films via Photochemical Cross-Linking. *J. Mater. Chem.* **2009**, *19* (39), 7222–7227.
- (158) Yao, H.; Wilkie, C. A. Cross-Linking of Polystyrene by Friedel-Crafts Chemistry : A Review Cross-Linking of Polystyrene by Friedel-Crafts Reaction. **1881**, 125–

135.

- (159) Rabek, J. F.; Lucki, J. Crosslinking of Polystyrene under Friedel-Crafts Conditions in Dichloroethane and Carbon Tetrachloride Solvents through the Formation of Strongly Colored Polymer-AlCl<sub>3</sub>-Solvent Complexes. *J. Polym. Sci. Part A Polym. Chem.* **1988**, *26* (9), 2537–2551.
- (160) Li, J.; Wilkie, C. A. Improving the Thermal Stability of Polystyrene by Friedel-Crafts Chemistry. *Polym. Degrad. Stab.* **1997**, *57* (3), 293–299.
- (161) Wang, Z.; Jiang, D. D.; McKinney, M. A.; Wilkie, C. A. Cross-Linking of Polystyrene by Friedel-Crafts Chemistry to Improve Thermal Stability. *Polym. Degrad. Stab.* **1999**, *64* (3), 387–395.
- (162) Of, S.; Retardation, F.; Polymers, I. N. Chapter 1 Introduction 1.1 Significance of Flame Retardation in Polymers.
- (163) Handelsman-Benory, E.; Botoshansky, M.; Greenberg, M.; Shteiman, V.; Kaftory, M. Methyl Rearrangement of Methoxy-Triazines in the Solid- and Liquid-State. *Tetrahedron* **2000**, *56* (36), 6887–6897.
- (164) Huggett, C. Estimation of Rate of Heat Release by Means of Oxygen Consumption Measurements. *Fire Mater.* **1980**, *4* (2), 61–65.
- (165) Morgan, A. B. A Review of Transition Metal-Based Flame Retardants: Transition Metal Oxide/Salts, and Complexes; Wilkie, C. A., Morgan, A. B., Nelson, G. L., Eds.; American Chemical Society: Washington, DC, 2009; Vol. 1013, pp 312–328.
- (166) Lu, H.; Hu, Y.; Xiao, J.; Kong, Q.; Chen, Z.; Fan, W. The Influence of Irradiation on Morphology Evolution and Flammability Properties of Maleated Polyethylene/Clay Nanocomposite. *Mater. Lett.* **2005**, *59* (6), 648–651.

- (167) Lyon, R. E. *Solid-State Thermochemistry of Flaming Combustion*; Marcel Dekker, Inc., NY, 2000.
- (168) Lyon, R. E. Solid-State Thermochemistry of Flaming Combustion. **2000**, *0* (1), 1–5.
- (169) Petrella, R. V. The Assessment of Full-Scale Fire Hazards from Cone Calorimeter Data. *J. Fire Sci.* **1994**, *12* (1), 14–43.
- (170) Gilman, J. W. Flammability and Thermal Stability Studies of Polymer Layered-Silicate (Clay) Nanocomposites. *Appl. Clay Sci.* **1999**, *15* (1–2), 31–49.
- (171) Manzi-Nshuti, C.; Songtipya, P.; Manias, E.; Jimenez-Gasco, M. M.; Hossenlopp, J. M.; Wilkie, C. A. Polymer Nanocomposites Using Zinc Aluminum and Magnesium Aluminum Oleate Layered Double Hydroxides: Effects of LDH Divalent Metals on Dispersion, Thermal, Mechanical and Fire Performance in Various Polymers. *Polymer (Guildf)*. **2009**, *50* (15), 3564–3574.
- (172) Manzi-Nshuti, C.; Hossenlopp, J. M.; Wilkie, C. A. Comparative Study on the Flammability of Polyethylene Modified with Commercial Fire Retardants and a Zinc Aluminum Oleate Layered Double Hydroxide. *Polym. Degrad. Stab.* **2009**, *94* (5), 782–788.
- (173) Manzi-Nshuti, C.; Hossenlopp, J. M.; Wilkie, C. A. Fire Retardancy of Melamine and Zinc Aluminum Layered Double Hydroxide in Poly(Methyl Methacrylate). *Polym. Degrad. Stab.* **2008**, *93* (10), 1855–1863.
- (174) Straka, P.; Náhunková, J.; Brožová, Z. Kinetics of Copyrolysis of Coal with Polyamide 6. *J. Anal. Appl. Pyrolysis* **2004**, *71* (1), 213–221.
- (175) Marney, D. C. O.; Russell, L. J.; Wu, D. Y.; Nguyen, T.; Cramm, D.; Rigopoulos,

- N.; Wright, N.; Greaves, M. The Suitability of Halloysite Nanotubes as a Fire Retardant for Nylon 6. *Polym. Degrad. Stab.* **2008**, *93* (10), 1971–1978.
- (176) Frisch, K. C. Thermal Stability of Isocyanate-Based Polymers. 2. Kinetics. **1987**, 2077–2083.
- (177) Stovall, B. K. D.; Hoyle, C. E.; Otaigbe, J. U. Comparative Study of Novel Thiol-Ene Resins and Composites. **2004**.
- (178) Anderson, D. R.; Holovka, J. M.; Corporation, X. Thermally Resistant Polymers Containing the S-Triazine Ring. *J. Polym. Sci. Part A Polym. Chem.* **1966**, *4*, 1689–1702.
- (179) Mouritz, A. P.; Feih, S.; Kandare, E.; Mathys, Z.; Gibson, A. G.; Des Jardin, P. E.; Case, S. W.; Lattimer, B. Y. Review of Fire Structural Modelling of Polymer Composites. *Compos. Part A Appl. Sci. Manuf.* **2009**, *40* (12), 1800–1814.
- (180) Boryniec, S. Polymer Combustion Processes . 3 . Flame Retardants for Polymeric Materials. **2001**, *27* (10), 127–148.
- (181) Kuo, P. Y.; De Assis Barros, L.; Sheen, Y. C.; Sain, M.; Tjong, J. S. Y.; Yan, N. Thermal Degradation of Extractive-Based Bio-Epoxy Monomer and Network: Kinetics and Mechanism. *J. Anal. Appl. Pyrolysis* **2016**, *117*, 199–213.
- (182) Nishizawa, H. Flame Retardant Polymeric Materials : II . The Basics & Recent Trends in Studies of Flame Retardant Mechanisms. **2014**, No. 9, 23–30.
- (183) Alae, M. An Overview of Commercially Used Brominated Flame Retardants, Their Applications, Their Use Patterns in Different Countries/Regions and Possible Modes of Release. *Environ. Int.* **2003**, *29* (6), 683–689.
- (184) Lewin, M.; Mey-Marom, A.; Frank, R. Surface Free Energies of Polymeric

- Materials, Additives and Minerals. *Polym. Adv. Technol.* **2005**, *16* (6), 429–441.
- (185) Tour, J. M. Synthesis and Testing of New Flame Retardant Monomers and Polymer Additives. No. 02, 1–69.
- (186) Chen, L. J.; Tai, Q. L.; Song, L.; Xing, W. Y.; Jie, G. X.; Hu, Y. Thermal Properties and Flame Retardancy of an Ether-Type UV-Cured Polyurethane Coating. **2010**, *4* (9), 539–550.
- (187) *Handbook for Corrosion Protection of Steel Surfaces by Painting.*
- (188) Zhang, X.; He, Q.; Gu, H.; Colorado, H. A.; Wei, S.; Guo, Z. Flame-Retardant Electrical Conductive Nanopolymers Based on Bisphenol F Epoxy Resin Reinforced with Nano Polyanilines. *ACS Appl. Mater. Interfaces* **2013**, *5* (3), 898–910.
- (189) Zhang, B. Synthesis of Microencapsulated Zinc Stannate and Its Application in Flame - Retardant Poly ( Vinyl Chloride ) Membrane Material. **2017**, No. April, 1–10.
- (190) Scott, G. *Properties of Polymers. Their Correlation with Chemical Structure; Their Numerical Estimation and Prediction from Additive Group Contributions;* 1992; Vol. 16.
- (191) *Polyimides*; 1984.
- (192) Report, F. Calculating Polymer Flammability From Molar Group Contributions. **2001**, No. September.
- (193) Walters, R. N. Molar Group Contributions to the Heat of Combustion. *Fire Mater.* **2002**, *26* (3), 131–145.
- (194) Reilly, T.; Beard, a. Additives Used in Flame Retardant Polymer Formulations:

Current Practice & Trends. **2009**.

- (195) Sirjean, B.; Glaude, P.-A.; Ruiz-Lopez, M. F.; Fournet, R. Theoretical Kinetic Study of the Ring Opening of Cyclic Alkanes. **2009**, 1–6.
- (196) Sirjean, B.; Glaude, P. A.; Ruiz-Lopez, M. F.; Fournet, R. Detailed Kinetic Study of the Ring Opening of Cycloalkanes by CBS-QB3 Calculations. *J. Phys. Chem. A* **2006**, *110* (46), 12693–12704.
- (197) Inversion, P. Bicyclo[3.2.0]Hept-2-Ene. *Society* **1988**, *1*, 479–480.
- (198) Szekeres, G.; Siklos, P.; Nagy, L.; Jelinek, L. Thermal Dimerization of Cyclopentadiene and Its Reaction with Isoprene. **1976**, 13–26.
- (199) Hamerton, I.; Thompson, S.; Howlin, B. J.; Stone, C. A. New Method to Predict the Thermal Degradation Behavior of Polybenzoxazines from Empirical Data Using Structure Property Relationships. *Macromolecules* **2013**, *46* (19), 7605–7615.
- (200) Duann, Y. F.; Liu, T. M.; Cheng, K. C.; Su, W. F. Thermal Stability of Some Naphthalene- and Phenyl-Based Epoxy Resins. *Polym. Degrad. Stab.* **2004**, *84* (2), 305–310.
- (201) Lyon, R. E.; Safronava, N.; Crowley, S. Thermal Analysis of Polymer Ignition. *Fire Mater.* **2018**, *42* (6), 668–679.
- (202) Sinclair, J. W. Effects of Cure Temperature on Epoxy Resin Properties. *J. Adhes.* **1992**, *38* (3–4), 219–234.
- (203) Mamleev, V.; Bourbigot, S.; Le Bras, M.; Lefebvre, J. Three Model-Free Methods for Calculation of Activation Energy in TG. *J. Therm. Anal. Calorim.* **2004**, *78* (3), 1009–1027.

- (204) Sauerbrunn, S.; Gill, P. {Decomposition} {Kinetics} {Using} {Tga}. *Am. Lab.* **1994**, 26 (1), 29.
- (205) Carraher, C. Carraher's Polymer Chemistry. **2003**, 902.
- (206) Llc, S. U. S.; York, N. Introduction To Flame Flammability. 1–30.
- (207) Lyon, R. E.; Rilipczak, R.; Walters, R. N.; Crowley, S.; Stoliarov, S. I. Thermal Analysis of Polymer Flammability. *U.S. Department Transp.* **2007**, No. April, 1–44.
- (208) Lyon, R. E.; Takemori, M. T.; Safronava, N.; Stoliarov, S. I.; Walters, R. N. A Molecular Basis for Polymer Flammability. *Polymer (Guildf)*. **2009**, 50 (12), 2608–2617.
- (209) Tsai, K. C.; Drysdale, D. Flame Height Correlation and Upward Flame Spread Modelling. *Fire Mater.* **2002**, 26 (6), 279–287.
- (210) Quang Dao, D.; Luche, J.; Richard, F.; Rogaume, T.; Bourhy-Weber, C.; Ruban, S. Determination of Characteristic Parameters for the Thermal Decomposition of Epoxy Resin/Carbon Fibre Composites in Cone Calorimeter. *Int. J. Hydrogen Energy* **2013**, 38 (19), 8167–8178.
- (211) Sonnier, R.; Otazaghine, B.; Iftene, F.; Negrell, C.; David, G.; Howell, B. A. Predicting the Flammability of Polymers from Their Chemical Structure: An Improved Model Based on Group Contributions. *Polymer (Guildf)*. **2016**, 86, 42–55.
- (212) Lyon, R. E. STANDARD TEST METHOD FOR FLAMMABILITY  
SCREENING OF AC MATERIALS Standard Test Method for Flammability  
Screening of AC Materials. *City* **2006**.



- (213) Kauskik, M.; Jackson, M.; Heinz, S; Wiggins, J.S.; Nazrenko, S. S. I. S. P. No Title; Wichita, KS, 2009.
- (214) Tucker, S. J.; Wiggins, J. S. Study of 3,3' vs. 4,4' DDS Isomer Curatives on Physical Properties and Phenyl Ring Motions of DGEBA EPOXY via Molecular Dynamics, Deuterium NMR, and Dielectric Spectroscopy. *Polym. Sci. Eng.* **2010**, *PhD* (December), 243.
- (215) Achorn, P. J.; Ferrillo, R. G. Comparison of Thermal Techniques for Glass Transition Measurements of Polystyrene and Cross-linked Acrylic Polyurethane Films. *J. Appl. Polym. Sci.* **1994**, *54* (13), 2033–2043.
- (216) Characterization of Epoxy Reinforced Glass by DSC and DMA. 66.
- (217) Rao, A. V.; Kulkarni, M. M.; Amalnerkar, D. P.; Seth, T. Surface Chemical Modification of Silica Aerogels Using Various Alkyl-Alkoxy/Chloro Silanes. *Appl. Surf. Sci.* **2003**, *206* (1–4), 262–270.
- (218) Yang, S.; Wang, J.; Huo, S.; Wang, M.; Wang, J.; Zhang, B. Synergistic Flame-Retardant Effect of Expandable Graphite and Phosphorus-Containing Compounds for Epoxy Resin: Strong Bonding of Different Carbon Residues. *Polym. Degrad. Stab.* **2016**, *128*, 89–98.
- (219) You, G.; Cheng, Z.; Tang, Y.; He, H. Functional Group Effect on Char Formation, Flame Retardancy and Mechanical Properties of Phosphonate–Triazine-Based Compound as Flame Retardant in Epoxy Resin. *Ind. Eng. Chem. Res.* **2015**, *54* (30), 7309–7319.
- (220) Gu, A.; Liang, G. Thermal Degradation Behaviour and Kinetic Analysis of Epoxy/Montmorillonite Nanocomposites. *Polym. Degrad. Stab.* **2003**, *80* (2), 383–

391.

- (221) Ashcroft, W. R. Curing Agents for Epoxy Resins. In *Chemistry and Technology of Epoxy Resins*; Springer Netherlands: Dordrecht, 1993; pp 37–71.
- (222) Wang, Q.; Shi, W. Kinetics Study of Thermal Decomposition of Epoxy Resins Containing Flame Retardant Components. *Polym. Degrad. Stab.* **2006**, *91* (8), 1747–1754.
- (223) F.J.MARTIN, C. P. F. and. Flammability of Polymers. *Flammabl. Polym.* **1965**, *1*, 135–139.
- (224) Beyler, C. A Brief History of the Prediction of Flame Extinction Based upon Flame Temperature. *Fire Mater.* **2005**, *29* (6), 425–427.
- (225) Mauerer, O. New Reactive, Halogen-Free Flame Retardant System for Epoxy Resins. *Polym. Degrad. Stab.* **2005**, *88* (1), 70–73.
- (226) Wilkie, C. A. *Fire Retardancy of Polymers*; 2009; Vol. 12.
- (227) Randoux, T.; Vanovervelt, J. C.; Van den Bergen, H.; Camino, G. Halogen-Free Flame Retardant Radiation Curable Coatings. *Prog. Org. Coatings* **2002**, *45* (2–3), 281–289.
- (228) Hu, Z.; Chen, L.; Zhao, B.; Luo, Y.; Wang, D.-Y.; Wang, Y.-Z. A Novel Efficient Halogen-Free Flame Retardant System for Polycarbonate. *Polym. Degrad. Stab.* **2011**, *96* (3), 320–327.
- (229) Song, L.; Hu, Y.; Lin, Z.; Xuan, S.; Wang, S.; Chen, Z.; Fan, W. Preparation and Properties of Halogen-Free Flame-Retarded Polyamide 6/Organoclay Nanocomposite. *Polym. Degrad. Stab.* **2004**, *86* (3), 535–540.
- (230) Weil, E. D.; Levchik, S. A Review of Current Flame Retardant Systems for Epoxy

Resins. *Journal of Fire Sciences*. 2004.

- (231) Qian, X.; Pan, H.; Yi Xing, W.; Song, L.; Yuen, R. K. K.; Hu, Y. Thermal Properties of Novel 9,10-Dihydro-9-Oxa-10-Phosphaphenanthrene 10-Oxide-Based Organic/Inorganic Hybrid Materials Prepared by Sol–Gel and UV-Curing Processes. *Ind. Eng. Chem. Res.* **2012**, *51* (1), 85–94.
- (232) Liu, S.; Fang, Z.; Yan, H.; Wang, H. Superior Flame Retardancy of Epoxy Resin by the Combined Addition of Graphene Nanosheets and DOPO. *RSC Adv.* **2016**, *6* (7), 5288–5295.
- (233) Levchik, S. V.; Weil, E. D. A Review of Recent Progress in Phosphorus-Based Flame Retardants. *J. Fire Sci.* **2006**, *24* (5), 345–364.
- (234) Wang, X.; Hu, Y.; Song, L.; Xing, W.; Lu, H.; Lv, P.; Jie, G. Flame Retardancy and Thermal Degradation Mechanism of Epoxy Resin Composites Based on a DOPO Substituted Organophosphorus Oligomer. *Polymer (Guildf)*. **2010**, *51* (11), 2435–2445.
- (235) Šehić, A.; Tomšič, B.; Jerman, I.; Vasiljević, J.; Medved, J.; Simončič, B. Synergistic Inhibitory Action of P- and Si-Containing Precursors in Sol–gel Coatings on the Thermal Degradation of Polyamide 6. *Polym. Degrad. Stab.* **2016**, *128*, 245–252.
- (236) Qian, X.; Pan, H.; Yi Xing, W.; Song, L.; Yuen, R. K. K.; Hu, Y. Thermal Properties of Novel 9,10-Dihydro-9-Oxa-10-Phosphaphenanthrene 10-Oxide-Based Organic/Inorganic Hybrid Materials Prepared by Sol–Gel and UV-Curing Processes. *Ind. Eng. Chem. Res.* **2012**, *51* (1), 85–94.
- (237) Wang, L.; Jiang, J.; Jiang, P.; Yu, J. Synthesis, Characteristic of a Novel Flame

- Retardant Containing Phosphorus, Silicon and Its Application in Ethylene Vinyl-Acetate Copolymer (EVM) Rubber. *J. Polym. Res.* **2010**, *17* (6), 891–902.
- (238) Qian, X.; Song, L.; Wang, B.; Hu, Y.; Yuen, R. K. K. Synthesis of Organophosphorus Modified Nanoparticles and Their Reinforcements on the Fire Safety and Mechanical Properties of Polyurea. *Mater. Chem. Phys.* **2013**, *139* (2–3), 443–449.
- (239) Wang, X.; Song, L.; Yang, H.; Lu, H.; Hu, Y. Synergistic Effect of Graphene on Antidripping and Fire Resistance of Intumescent Flame Retardant Poly(Butylene Succinate) Composites. *Ind. Eng. Chem. Res.* **2011**, *50* (9), 5376–5383.
- (240) Wang, X.; Xing, W.; Zhang, P.; Song, L.; Yang, H.; Hu, Y. Covalent Functionalization of Graphene with Organosilane and Its Use as a Reinforcement in Epoxy Composites. *Compos. Sci. Technol.* **2012**, *72* (6), 737–743.
- (241) Li, Y.-L.; Kuan, C.-F.; Chen, C.-H.; Kuan, H.-C.; Yip, M.-C.; Chiu, S.-L.; Chiang, C.-L. Preparation, Thermal Stability and Electrical Properties of PMMA/Functionalized Graphene Oxide Nanosheets Composites. *Mater. Chem. Phys.* **2012**, *134* (2–3), 677–685.
- (242) Zhu, Y.; Murali, S.; Cai, W.; Li, X.; Suk, J. W.; Potts, J. R.; Ruoff, R. S. Graphene and Graphene Oxide: Synthesis, Properties, and Applications. *Adv. Mater.* **2010**, *22* (35), 3906–3924.
- (243) Georgakilas, V.; Otyepka, M.; Bourlinos, A. B.; Chandra, V.; Kim, N.; Kemp, K. C.; Hobza, P.; Zboril, R.; Kim, K. S. Functionalization of Graphene: Covalent and Non-Covalent Approaches, Derivatives and Applications. *Chemical Reviews*. American Chemical Society November 14, 2012, pp 6156–6214.

- (244) Kim, H.; Abdala, A. A.; Macosko, C. W. Graphene/Polymer Nanocomposites. *Macromolecules* **2010**, *43* (16), 6515–6530.
- (245) Shi, Y.; Li, L.-J. Chemically Modified Graphene: Flame Retardant or Fuel for Combustion? *J. Mater. Chem.* **2011**, *21* (10), 3277–3279.
- (246) Bao, C.; Guo, Y.; Yuan, B.; Hu, Y.; Song, L. Functionalized Graphene Oxide for Fire Safety Applications of Polymers: A Combination of Condensed Phase Flame Retardant Strategies. *J. Mater. Chem.* **2012**, *22* (43), 23057.
- (247) Huang, X.; Qi, X.; Boey, F.; Zhang, H. Graphene-Based Composites. *Chem. Soc. Rev.* **2012**, *41* (2), 666–686.
- (248) Yu, B.; Wang, X.; Xing, W.; Yang, H.; Song, L.; Hu, Y. UV-Curable Functionalized Graphene Oxide/Polyurethane Acrylate Nanocomposite Coatings with Enhanced Thermal Stability and Mechanical Properties. *Ind. Eng. Chem. Res.* **2012**, *51* (45), 14629–14636.
- (249) Qian, X.; Yu, B.; Bao, C.; Song, L.; Wang, B.; Xing, W.; Hu, Y.; Yuen, R. K. K. Silicon Nanoparticle Decorated Graphene Composites: Preparation and Their Reinforcement on the Fire Safety and Mechanical Properties of Polyurea. *J. Mater. Chem. A* **2013**, *1* (34), 9827.
- (250) Wang, X.; Song, L.; Yang, H.; Xing, W.; Kandola, B.; Hu, Y. Simultaneous Reduction and Surface Functionalization of Graphene Oxide with POSS for Reducing Fire Hazards in Epoxy Composites. *J. Mater. Chem.* **2012**, *22* (41), 22037.
- (251) Yu, B.; Shi, Y.; Yuan, B.; Qiu, S.; Xing, W.; Hu, W.; Song, L.; Lo, S.; Hu, Y. Enhanced Thermal and Flame Retardant Properties of Flame-Retardant-Wrapped

- Graphene/Epoxy Resin Nanocomposites. *J. Mater. Chem. A* **2015**, *3* (15), 8034–8044.
- (252) Yang, H.; Li, F.; Shan, C.; Han, D.; Zhang, Q.; Niu, L.; Ivaska, A. Covalent Functionalization of Chemically Converted Graphene Sheets via Silane and Its Reinforcement. *J. Mater. Chem.* **2009**, *19* (26), 4632.
- (253) Huang, G.; Chen, S.; Tang, S.; Gao, J. A Novel Intumescent Flame Retardant-Functionalized Graphene: Nanocomposite Synthesis, Characterization, and Flammability Properties. *Mater. Chem. Phys.* **2012**, *135* (2–3), 938–947.
- (254) Xue, Y.; Liu, Y.; Lu, F.; Qu, J.; Chen, H.; Dai, L. Functionalization of Graphene Oxide with Polyhedral Oligomeric Silsesquioxane (POSS) for Multifunctional Applications. *J. Phys. Chem. Lett.* **2012**, *3* (12), 1607–1612.
- (255) Liao, S.-H.; Liu, P.-L.; Hsiao, M.-C.; Teng, C.-C.; Wang, C.-A.; Ger, M.-D.; Chiang, C.-L. One-Step Reduction and Functionalization of Graphene Oxide with Phosphorus-Based Compound to Produce Flame-Retardant Epoxy Nanocomposite. *Ind. Eng. Chem. Res.* **2012**, *51* (12), 4573–4581.
- (256) Wang, X.; Xing, W.; Feng, X.; Yu, B.; Song, L.; Hu, Y. Functionalization of Graphene with Grafted Polyphosphamide for Flame Retardant Epoxy Composites: Synthesis, Flammability and Mechanism. *Polym. Chem.* **2014**, *5* (4), 1145–1154.
- (257) Marcano, D. C. D.; Kosynkin, D. D. V.; Berlin, J. M. J.; Sinitskii, A.; Sun, Z.; Slesarev, A.; Alemany, L. B.; Lu, W.; Tour, J. M. Improved Synthesis of Graphene Oxide. *ACS Nano* **2010**, *4* (8), 4806–4814.
- (258) Çiplak, Z.; Yildiz, N.; Çalimli, A. Investigation of Graphene/Ag Nanocomposites Synthesis Parameters for Two Different Synthesis Methods. *Fullerenes Nanotub.*

- Carbon Nanostructures* **2015**, 23 (4), 361–370.
- (259) Wang, Z.; Wei, P.; Qian, Y.; Liu, J. The Synthesis of a Novel Graphene-Based Inorganic–organic Hybrid Flame Retardant and Its Application in Epoxy Resin. *Compos. Part B Eng.* **2014**, 60 (60), 341–349.
- (260) Baney, R. H.; Itoh, M.; Sakakibara, A.; Suzuki, T. Silsesquioxanes. *Chem. Rev.* **1995**, 95 (5), 1409–1430.
- (261) Laine, R. M.; Zhang, C.; Sellinger, A.; Viculis, L. Polyfunctional Cubic Silsesquioxanes as Building Blocks for Organic/Inorganic Hybrids. *Appl. Organomet. Chem.* **1998**, 12 (10–11), 715–723.
- (262) Qian, X.; Yu, B.; Bao, C.; Song, L.; Wang, B.; Xing, W.; Hu, Y.; Yuen, R. K. K. Silicon Nanoparticle Decorated Graphene Composites: Preparation and Their Reinforcement on the Fire Safety and Mechanical Properties of Polyurea. *J. Mater. Chem. A* **2013**, 1 (34), 9827.
- (263) Hiorns, R. Polymer Handbook, 4th Edn, Edited by J Brandup, EH Immergut and EA Grulke, Associate Editors A Abe and DR Bloch, John Wiley and Sons, New York, 1999, Pp 2250, Price  $\diamond$ 210 ISBN 0-471-16628-6. *Polym. Int.* **2000**, 49 (7), 807–807.
- (264) Quintiere, J. G. A Theoretical Basis for Flammability Properties. *Fire Mater.* **2006**, 30 (3), 175–214.
- (265) Lewin, M.; Weil, E. . Fire Retardant Materials. In *In Fire Retardant Materials*; 2001; pp 31–68.
- (266) Lu, S.-Y.; Hamerton, I. Recent Developments in the Chemistry of Halogen-Free Flame Retardant Polymers. *Prog. Polym. Sci.* **2002**, 27 (8), 1661–1712.

- (267) Edbon, J.R.; Jones, M. . *Concise Polymeric Materials Encyclopedia*; 1996.
- (268) Biswas, B.; Kandola, B. K. The Effect of Chemically Reactive Type Flame Retardant Additives on Flammability of PES Toughened Epoxy Resin and Carbon Fiber-Reinforced Composites. *Polym. Adv. Technol.* **2011**, 22 (7), 1192–1204.
- (269) Marosi, G.; Szolnoki, B.; Bocz, K.; Toldy, A. Reactive and Additive Phosphorus-Based Flame Retardants of Reduced Environmental Impact. *Polym. Green Flame Retard.* **2014**, 181–220.
- (270) Chen, L.; Wang, Y.-Z. A Review on Flame Retardant Technology in China. Part I: Development of Flame Retardants. *Polym. Adv. Technol.* **2009**, 21 (1), n/a-n/a.
- (271) Costa, L.; Luda, M. .; Trossarelli, L. Mechanism of Condensed Phase Action in Flame Retardants. Synergistic Systems Based on Halogen-Metal Compounds. *Polym. Degrad. Stab.* **2000**, 68 (1), 67–74.
- (272) Rakotomalala, M.; Wagner, S.; Döring, M. Recent Developments in Halogen Free Flame Retardants for Epoxy Resins for Electrical and Electronic Applications. *Materials (Basel)*. **2010**, 3 (8), 4300–4327.
- (273) Morgan, A. B.; Wilkie, C. A. *Non-Halogenated Flame Retardant Handbook*.
- (274) Laoutid, F.; Bonnaud, L.; Alexandre, M.; Lopez-Cuesta, J.-M.; Dubois, P. New Prospects in Flame Retardant Polymer Materials: From Fundamentals to Nanocomposites. *Mater. Sci. Eng. R Reports* **2009**, 63 (3), 100–125.
- (275) GRAND, A. F. & WILKIE, C. A. *Fire Retardancy of Polymeric Materials*; 2000.
- (276) Lawson, D. F.; Kay, E. L.; Roberts, D. T. Mechanism of Smoke Inhibition by Hydrated Fillers. *Rubber Chem. Technol.* **1975**, 48 (1), 124–131.
- (277) Kashiwagi, T. Flame Retardant Mechanism of Polyamide 6–clay Nanocomposites.



- Polymer (Guildf)*. **2004**, 45 (3), 881–891.
- (278) Cho, J. H.; Vasagar, V.; Shanmuganathan, K.; Jones, A. R.; Nazarenko, S.; Ellison, C. J. Bioinspired Catecholic Flame Retardant Nanocoating for Flexible Polyurethane Foams. *Chem. Mater.* **2015**, 27 (19).
- (279) Kim, H.; Kim, D. W.; Vasagar, V.; Ha, H.; Nazarenko, S.; Ellison, C. J. Polydopamine-Graphene Oxide Flame Retardant Nanocoatings Applied via an Aqueous Liquid Crystalline Scaffold. *Advanced Functional Materials*. 2018, p 1803172.
- (280) Jin Zhu, †; Alexander B. Morgan, §,¶; Frank J. Lamelas, ‡,⊥ and; Charles A. Wilkie\*, †. Fire Properties of Polystyrene–Clay Nanocomposites. **2001**.
- (281) Li, Y.-C.; Schulz, J.; Mannen, S.; Delhom, C.; Condon, B.; Chang, S.; Zammarano, M.; Grunlan, J. C. Flame Retardant Behavior of Polyelectrolyte–Clay Thin Film Assemblies on Cotton Fabric. *ACS Nano* **2010**, 4 (6), 3325–3337.
- (282) Gilman, J. W.; Jackson, C. L.; Morgan, A. B.; Harris, R.; Manias, E.; Giannelis, E. P.; Wuthenow, M.; Hilton, D.; Phillips, S. H. Flammability Properties of Polymer - Layered-Silicate Nanocomposites. Polypropylene and Polystyrene Nanocomposites. *Chem. Mater.* **2000**, 12 (7), 1866–1873.
- (283) Wang, W. S.; Chen, H. S.; Wu, Y. W.; Tsai, T. Y.; Chen-Yang, Y. W. Properties of Novel Epoxy/Clay Nanocomposites Prepared with a Reactive Phosphorus-Containing Organoclay. *Polymer (Guildf)*. **2008**, 49 (22), 4826–4836.
- (284) Horrocks, A. R.; Price, D.; Institute of Materials, M. *Advances in Fire Retardant Materials*; Woodhead Pub, 2008.
- (285) Marosi, G.; Márton, A.; Szép, A.; Csontos, I.; Keszei, S.; Zimonyi, E.; Toth, A.;

- Almeras, X.; Le Bras, M. Fire Retardancy Effect of Migration in Polypropylene Nanocomposites Induced by Modified Interlayer. *Polym. Degrad. Stab.* **2003**, *82* (2), 379–385.
- (286) Unlu, S. M.; Dogan, S. D.; Dogan, M. Comparative Study of Boron Compounds and Aluminum Trihydroxide as Flame Retardant Additives in Epoxy Resin. *Polym. Adv. Technol.* **2014**, *25* (8), 769–776.
- (287) Bourbigot, S.; Duquesne, S. Fire Retardant Polymers: Recent Developments and Opportunities. *J. Mater. Chem.* **2007**, *17* (22), 2283.
- (288) Sacristán, M.; Hull, T. R.; Stec, A. A.; Ronda, J. C.; Galià, M.; Cádiz, V. Cone Calorimetry Studies of Fire Retardant Soybean-Oil-Based Copolymers Containing Silicon or Boron: Comparison of Additive and Reactive Approaches. *Polym. Degrad. Stab.* **2010**, *95* (7), 1269–1274.
- (289) Wang, D. Y.; Leuteritz, A.; Wang, Y. Z.; Wagenknecht, U.; Heinrich, G. Preparation and Burning Behaviors of Flame Retarding Biodegradable Poly(Lactic Acid) Nanocomposite Based on Zinc Aluminum Layered Double Hydroxide. *Polym. Degrad. Stab.* **2010**, *95* (12), 2474–2480.
- (290) Zammarano, M.; Franceschi, M.; Bellayer, S.; Gilman, J. W.; Meriani, S. Preparation and Flame Resistance Properties of Revolutionary Self-Extinguishing Epoxy Nanocomposites Based on Layered Double Hydroxides. *Polymer (Guildf)*. **2005**, *46* (22), 9314–9328.
- (291) Manzi-nshuti, C.; Songtipya, P.; Manias, E.; Jimenez-gasco, M.; Hossenlopp, J. M.; Wilkie, C. A. Polymer Nanocomposites Using Zinc Aluminum and Magnesium Aluminum Oleate Layered Double Hydroxides : Effects of the

- Polymeric Compatibilizer and of Composition on the Thermal and Fire Properties of PP / LDH Nanocomposites. *Polym. Degrad. Stab.* **2009**, *94* (11), 2042–2054.
- (292) Wesolek, D.; Gasiorowski, R.; Rojewski, S.; Walentowska, J.; Wojcik, R. New Flexible Flame Retardant Coatings Based on Siloxane Resin and Ethylene-Vinyl Chloride Copolymer. *Polymers (Basel)*. **2016**, *8* (12).
- (293) Tang, Z.; Li, Y.; Zhang, Y. J.; Jiang, P. Oligomeric Siloxane Containing Triphenylphosphonium Phosphate as a Novel Flame Retardant for Polycarbonate. *Polym. Degrad. Stab.* **2012**, *97* (4), 638–644.
- (294) Zhou, T.; He, X.; Guo, C.; Yu, J.; Lu, D.; Yang, Q. Synthesis of a Novel Flame Retardant Phosphorus/Nitrogen/Siloxane and Its Application on Cotton Fabrics. *Text. Res. J.* **2015**, *85* (7), 701–708.
- (295) Schartel, B.; Knoll, U.; Hartwig, A.; Pütz, D. Phosphonium-Modified Layered Silicate Epoxy Resins Nanocomposites and Their Combinations with ATH and Organo-Phosphorus Fire Retardants. *Polym. Adv. Technol.* **2006**, *17* (4), 281–293.
- (296) González, A.; Dasari, A.; Herrero, B.; Plancher, E.; Santarén, J.; Esteban, A.; Lim, S. H. Fire Retardancy Behavior of PLA Based Nanocomposites. *Polym. Degrad. Stab.* **2012**, *97* (3), 248–256.